

# Numerical Investigations on Two-phase Flow in Polymer Electrolyte Fuel Cells

## Numerieke modellering van twee-fase storming in Polymer Electrolyte brandstof cellen

(met een samenvatting in het Nederlands)

### PROEFSCHRIFT

ter verkrijging van de graad van doctor aan de Universiteit Utrecht op gezag van de rector  
magnificus, prof.dr. G.J. van der Zwaan, ingevolge het besluit van het college voor promoties  
in het openbaar te verdedigen op maandag 4 juni 2012 des middags te 4.15 uur  
door

**CHAOZHONG QIN**

geboren op 25 september 1982 te HENAN, China

Promoter: Prof. dr. ir. S.M. Hassanizadeh

Co-promoter: Dr.-Ing. D. Rensink

## The Reading Committee

Prof. Dr.-Ing. R. Helmig, Stuttgart University, Germany.

Prof. Dr.-Ing. U. Nieken, Stuttgart University, Germany.

Prof. Dr. R. Schotting, Utrecht University, The Netherlands.

Prof. Dr. O. Iliev, Fraunhofer Institute for Industrial Mathematics (ITWM), Germany.

Prof. Dr. W. Lehnert, Forschungszentrum Jülich, Germany.

Copyright©2012 by C. Z. Qin

All rights reserved. No part of this material may be copied or reproduced in any way without the prior permission of the author.

---

ISBN:	978-90-6266-299-9
Title:	Numerical Investigations on Two-phase Flow in Polymer Electrolyte Fuel Cells
Author:	Qin, C. Z.
Publisher:	Utrecht University, Geosciences Faculty, Earth sciences department
Number of pages:	160

---

❖ This thesis was accomplished with financial support from GM Alternative Propulsion Europe, Adam Opel AG.

# Acknowledgments

---

I would like to acknowledge a number of people who have encouraged and helped me to fulfill my doctoral research over the past few years.

I am very grateful to GM Alternative Propulsion Europe, Adam Opel AG, financing my doctoral research and giving me the opportunity to work in such a fantastic project.

I would like to thank my academic supervisor, Prof. Dr. Majid Hassanizadeh, and my co-supervisor, Dr. Dirk Rensink for their constant inspiration and invaluable guidance. Each year, I stayed in Majid's group at Utrecht University for three months. Through our numerous discussions, I gained a lot of knowledge on physics of fluid and multiphase flow in porous media. Especially, he taught me how to motivate and conduct scientific studies. I also appreciate that he always encouraged and supported me to attend conferences and workshops. In the rest time, I worked at Adam Opel AG. I am deeply thankful to my co-supervisor Dr. Dirk Rensink for his mentorship. He gave me enormous supports on not only my research but also my living in Germany. I could benefit a lot from his rich experience and knowledge on fuel cells and numerical modeling. His careful editing also contributed considerably to the production of this thesis.

I am very grateful to Dr. Stephan Fell for his constructive comments and discussion on my research. I would like to thank all my colleagues in the group of CAE Advanced Propulsion, GM Alternative Propulsion Europe. I really appreciate having had the opportunity to work with you. I want to specially thank Dr. Rainer Immel, who helped me to develop MATLAB code, which led to the production of Chapter 7. Sincere gratitude to Dr. Philip Klaus, Dr. Dirk Kehrwald, Dr. Suman Basu, Dr. Christian Wieser and Andre Mack-Gardner for the fruitful discussions on fuel cells and FLUENT software. I also would like to thank Steffen Boehm, Andrea Werner, Dr. Elena Schneider, Dominic Thier, Andrea Wesche, Dr. Valentin Schultheis and Armin Schneider for your help, I enjoyed the time with all of you.

I had a good time at Utrecht University. First of all, many thanks to Margreet, who helped me much in administrative tasks. I would like to thank Prof. Schotting for nice parties in your house and your wonderful lectures. Thanks are also given to my colleagues at the university, Qiulan, Li Shuai, Imran, Vahid, Amir, Nikos, Brijesh, Reza, Mojtaba, Wouter, Manuel and many other Chinese friends in Utrecht. In particular, I would like to acknowledge Margreet and Wouter for the Dutch summary translation.

Most of all, my heartfelt thanks to my family in China for their unconditional support and encouragement throughout all the years of my education. This thesis would not have been possible without you.

# Contents

Acknowledgments .....	III
Chapter 1 - Introduction .....	1
1.1 Background and motivation .....	1
1.2 Structure of the thesis.....	2
Chapter 2 - Two-phase Flow in Polymer Electrolyte Fuel cells: A Review.....	4
2.1 Introduction.....	4
2.2 Water generation and transfer in an operating PEFC.....	6
2.2.1 Components of a typical PEFC .....	7
2.2.2 Operating principles.....	9
2.2.3 Water movement.....	10
2.3 Numerical modeling of two-phase flow in PEFCs.....	11
2.3.1 Two-phase flow in GCs .....	11
2.3.2 Two-phase flow in diffusion layers .....	14
2.3.3 Interface treatment.....	22
2.4 Experimental observations of two-phase flow in PEFCs.....	23
2.4.1 Optical photography .....	24
2.4.2 X-ray technique.....	25
2.4.3 Neutron radiography.....	26
2.5 Summary .....	27
References .....	28
Chapter 3 - Pore-scale simulation of the cathode gas diffusion layer of a polymer electrolyte fuel cell .....	32
Abstract.....	32
3.1 Introduction.....	32
3.2 Gas diffusion layer generation .....	34
3.3 Numerical method.....	36
3.3.1 Governing equations.....	36
3.3.2 Boundary conditions .....	37
3.3.3 Numerical implementation.....	38

3.4 Results and discussion .....	39
3.4.1 Intrinsic permeability calculation.....	39
3.4.2 Pore-scale simulation.....	42
3.5 Conclusions.....	46
References .....	48
Chapter 4 - Two-phase Flow Modeling for the Cathode Side of a Polymer Electrolyte Fuel Cell .....	53
Abstract.....	53
4.1 Introduction.....	53
4.2 Two-phase flow model.....	55
4.2.1 Governing equations of gas phase.....	56
4.2.2 Liquid water transport equation.....	57
4.2.3 Constitutive correlations and source terms .....	58
4.2.4 Boundary conditions and numerical implementation .....	60
4.3 Results and discussion .....	61
4.3.1 Modeling of GC flooding.....	61
4.3.2 Immobile saturation effect.....	66
4.4 Conclusions.....	67
References .....	68
Chapter 5 - Polymer Electrolyte Fuel Cell Modeling with Emphasis on the Effect of Gas Diffusion Layer Anisotropy.....	72
Abstract.....	72
5.1 Introduction.....	72
5.2 Mathematical model.....	74
5.2.1 Electrochemical kinetics.....	75
5.2.2 Gas phase transport .....	77
5.2.3 Water transport .....	78
5.2.4 Heat transport .....	81
5.3 Boundary conditions and implementation .....	82
5.4 Results and discussion .....	83
5.4.1 Base case study.....	83
5.4.2 Effect of GDL anisotropy.....	87
5.5 Conclusions.....	88
References .....	91

Chapter 6 - Direct Simulation of Liquid Water Dynamics in the Gas Channel of a Polymer Electrolyte Fuel Cell .....	96
Abstract.....	96
6.1 Introduction.....	96
6.2 Numerical method.....	99
6.2.1 Computational domain.....	99
6.2.2 Governing equations.....	100
6.2.3 Boundary and initial conditions.....	102
6.2.4 Mesh and numerical implementation.....	102
6.3 Results and discussion .....	103
6.3.1 Droplet dynamics .....	104
6.3.2 Film dynamics .....	108
6.3.3 Competition between film and droplet flows .....	111
6.4 Conclusions.....	114
References .....	115
Chapter 7 - One-dimensional Phenomenological Model for Liquid Water Flooding in Cathode Gas Channel of a Polymer Electrolyte Fuel Cell .....	118
Abstract.....	118
7.1 Introduction.....	118
7.2 Physical model.....	120
7.2.1 Assumptions .....	120
7.2.2 Governing equations.....	120
7.3 Numerical model .....	124
7.3.1 Simplifications of governing equations.....	124
7.3.2 Boundary conditions and numerical implementation .....	127
7.4 Results and discussion .....	128
7.4.1 Base case study .....	128
7.4.2 Effect of droplets in the GC .....	130
7.4.3 Effect of operating conditions .....	132
7.5 Conclusions.....	134
References .....	135
Appendix 7A.....	137
Chapter 8 - Numerical study on liquid water flooding in gas channels used in polymer electrolyte fuel cells.....	142
Abstract.....	142

8.1 Introduction.....	142
8.2 Mathematical model.....	144
8.2.1 Governing equations.....	145
8.2.2 Source terms and geometrical information .....	146
8.2.3 Closure equations .....	148
8.3 Boundary conditions .....	149
8.4 Results and discussion .....	150
8.4.1 Base case .....	150
8.4.2 Effect of relative humidity.....	152
8.4.3 Effect of net water transfer coefficient.....	152
8.4.4 Effect of half corner angle .....	154
8.5 Conclusions.....	155
References .....	157
Chapter 9 - Summary and future works .....	160
9.1 Summary .....	160
9.2 Future works.....	161



# Chapter 1 - Introduction

---

## 1.1 Background and motivation

### Background

With the increase of environmental concerns and depletion of fossil fuels, polymer electrolyte fuel cells (PEFC) have been receiving much attention over the past two decades. They convert chemical energy in fuels (e.g.  $H_2$ ) to electricity by means of electrochemical reactions, with the advantages of high efficiency, low/zero pollution, and quick startups.

As new power sources, PEFCs have the high potential to be widely applied in automotive section in the near future. However, before this can occur, several technical challenges of PEFCs must be solved, such as cell performance, durability, fuel storage, generation and delivery, as well as system cost to ensure a proper market penetration.

Hundreds of PEFC units are connected in series for providing useful power. The structure of each PEFC unit is relatively simple, which comprises flow field, gas diffusion layer, and catalyst layer on each side, as well as the membrane acting as an electrical insulator. To complete full electrochemical reactions in a PEFC, several key transport processes are involved simultaneously, like diffusion of gaseous reactants, gas-water two-phase flow in diffusion layers and gas channels, as well as electrical and ionic transport. As a consequence, water management plays a significant role in the improvement of cell performance and durability, which is also interrelated to heat management very much.

Water balance is critical to the operation of PEFCs, since the membrane needs to attain sufficient water for effective ionic conduction. On the other hand, too much water accumulating in PEFCs would result in mass transport limitations, which is termed as liquid water flooding. In most cases, liquid water flooding occurs in porous diffusion layers and micro gas channels at the same time. This can limit the cell performance and detract the durability of PEFCs. It needs to be noted that water content in the membrane is intricately coupled with water activity in the catalyst layers. In order to obtain optimized operating conditions and increase cell performance, a complete understanding of liquid water transport mechanisms in PEFCs is indispensable.

### Motivation

In the past few years, tremendous efforts have been contributed to the understanding of liquid water transport in PEFCs. In experiments, optical observations using modified transparent PEFCs have provided remarkable insights into water dynamics in gas channels. In addition, several noninvasive techniques, like X-ray and neutron radiography, have been extensively used to visualize and quantify water content distribution in diffusion layers and the membrane.

Numerical modeling can be the other promising tool to explore two-phase flow in PEFCs; to this end, several key transport processes as mentioned above should be taken into account in the modeling. What's more, they need to be described properly.

The cathode side of a PEFC is prone to being flooded first, since water is generated in the cathode catalyst layer (CL) due to chemical reactions. Excessive liquid water penetrates through the porous layers into gas channels (GCs). Typically, a GC is confined by three walls from the bipolar plate which are hydrophilic, and the surface of the gas diffusion layer (GDL) which is hydrophobic. When liquid water breaks through the GDL-GC interface, water droplets and film slugs form on the GDL surface and along hydrophilic GC corners, respectively. It is obvious that under flooding situations, liquid water transport on the cathode side can occur in both porous layers and GCs simultaneously.

In computational fluid dynamics (CFD) simulations of the liquid water transport in a PEFC, two major challenges lie in how to effectively mimic the liquid water transport in the GC, and how to couple the liquid water transport between the GDL and GC. Even though some interface tracking methods have been extensively used to investigate water dynamics in the GC, they all suffer from heavy computational efforts, and cannot be applied to a large level. In addition, these methods are based on a much smaller spatial scale than that in the GDL, where the averaged two-phase Darcy's law is commonly employed to describe the liquid water transfer.

This thesis herein is motivated by the following major expectations: (1) to develop a full PEFC model, addressing the influences of immobile saturation, GC flooding and GDL anisotropy on water transfer in PEFCs; (2) to investigate liquid water dynamics in a GC, providing insights into the development of a macro GC flooding model; (3) to develop a macro phenomenological model for liquid water flooding in GCs, including the effect of droplet population.

## 1.2 Structure of the thesis

The thesis is structured as follows:

1. In chapter 2, a comprehensive overview of numerical models for two-phase flow in PEFCs is given, including interface treatments between different layers. For completeness, several advanced imaging techniques used in PEFCs and obtained results are also presented briefly (*Preparation for Journal of Power Sources*).
2. Based on a virtually created GDL, chapter 3 is devoted to the study of its anisotropic permeability. In addition, we investigate pore-scale species transport in the microstructure of a GDL (*Submitted to International Journal of heat and mass transfer*).
3. Liquid water flooding in micro GCs is an important issue in the water management of PEFCs. In chapter 4, the GC is assumed to be a structured porous medium and a two-phase flow model for the cathode side of a PEFC is developed. The liquid water flooding in the GC and its impact on the liquid water distribution in diffusion layers are explored in detail. Furthermore, the effect of the immobile saturation on the predicted liquid water distribution in the diffusion layers is studied (*Journal of Power Sources 197 (2012) 136-144*).
4. In chapter 5, we develop a three-dimensional non-isothermal PEFC model to investigate the liquid water flooding in diffusion layers and the associated heat transfer. More importantly,

we illustrate the necessity of considering the GDL anisotropy in the PEFC modeling, which has been neglected in most previous numerical studies (*Under review, Electrochim Acta*).

5. In chapter 6, we propose a novel geometrical setup to conduct a series of direct simulations of the liquid water dynamics in a GC. The droplet dynamics, corner film dynamics, and the competition between the film and droplet flows in the GC are explored in detail. The results from this work also serve to provide insights into the development of a phenomenological model for the liquid water flooding in GCs (*Journal of the Electrochemical Society 159 (4) B434-B443, 2012*).
6. The mathematical description of the liquid water flooding in the GC of a PEFC at the macro scale has remained a challenge up to now. The mist flow assumption in the GC has been commonly used in previous numerical studies. In chapter 7, a one-dimensional macroscale phenomenological model for the liquid water flooding in the cathode GC is developed based on several reasonable assumptions (*Journal of the electrochemical society 159 (6) B737-B745, 2012*).
7. In chapter 8, we introduce a non-equilibrium phase change model into the previously developed one-dimensional channel flooding model, which enables the consideration of partially humidified inlet gas. In addition, we extend this model into the anode side, and connect the channel flooding on both sides by the so-called net water transfer coefficient (*Submitted to Chemical Engineering Science*).
8. In the last chapter, we summarize the conclusions in this thesis and propose some future works.

# Chapter 2 - Two-phase Flow in Polymer Electrolyte Fuel cells: A Review

---

## 2.1 Introduction

Nowadays, polymer electrolyte fuel cells (PEFCs) are attracting more and more attention due to their striking attributes, like low/zero emission, high efficiency, quick startup and power output, as well as low operation temperatures<sup>1-3</sup>. This type of fuel cell is regarded as one of the most promising alternative power sources in the near future, which can be broadly employed in stationary, automotive and portable sections<sup>4</sup>. However, in order to be successfully introduced into commercialization, a number of efforts are still needed to improve cell performance, durability and stability<sup>5</sup>. Meanwhile, the cost should be reduced considerably<sup>6</sup>.

Inside a PEFC unit, various transport processes are intricately coupled, along with electrochemical reactions in the catalyst layers (CLs). As a consequence, water and heat issues are always ineluctable. On the one hand, the membrane should attain high water content to transport protons towards the cathode CL with a low ohmic resistance. Therefore, gaseous reactants (e.g. H<sub>2</sub>, O<sub>2</sub>) are normally humidified before being fed into fuel cells. On the other hand, excessive liquid water accumulating in fuel cells would hinder reactants transport into reactive sites resulting in the so-called flooding situation, and also deteriorates the cell performance. It is evident there exist two conflicting requirements for water. To achieve an optimal cell performance, it is essential to bring about a dedicate water balance to ensure that the membrane is fully hydrated for high protonic conductivity, while severe flooding is avoided, especially on the cathode side<sup>7</sup>.

It is widely recognized that the flow of two immiscible phases (i.e. gas mixture and liquid water) in PEFCs is extremely complex, since a PEFC consists of four distinctive constituents, namely, gas channel (GC), gas diffusion layer (GDL), CL, and electrolyte membrane. When PEFCs are operating under certain conditions (e.g. high current densities and cold startup), two-phase flow is probably involved in all components simultaneously. The mechanism of liquid water transport in respective constituent is totally different from each other. In addition, the coupling of liquid water transport between adjacent layers needs to be taken into account as well. In general, two-phase flow in a PEFC could be categorized into three sub-processes<sup>8</sup>, namely, (1) liquid water accumulation and transport in the CL, (2) two-phase flow in the GDL, along with interfacial coverage at the GDL-GC interface, and (3) liquid water transport in the GC, more recently, which received more and more attention. Generally speaking, above mentioned three sub-processes all place detrimental impacts on the cell performance. Meanwhile, these processes

are inevitable in an operating PEFC, particularly for automotive applications. For instance, during the first sub-process, excessive water accumulating in the CL would cover catalyst pellets, acting as an additional barrier to reactants transport into reactive sites. Based on the preceding descriptions of water transport, we can see that a proper water management plays a central role in the development and commercialization of PEFCs.

Over the past two decades, two-phase flow and flooding phenomenon in PEFCs has been extensively investigated via both experimental and numerical methods, which have been utilized successfully and made appreciable progresses in PEFCs. In addition, they provided useful guidelines for developing innovative materials and architectures. As for experimental studies, high-resolution techniques for imaging liquid water evolution in PEFCs are widely utilized to obtain insights into the water management. Optical photography<sup>9-11</sup> using modified transparent PEFCs, has been proposed to visualize liquid water emergence from GDL and dynamics in GCs. Although direct optical observations can provide high temporal and spatial resolutions of liquid water transfer, liquid water behaviors in other layers (e.g. GDL and CL) are inaccessible. Moreover, modified PEFCs may invoke other unpredictable material effects, such as surface wettability and roughness. Besides optical visualization, another two well-known techniques are also widely employed to study liquid water transport in an operating PEFC, namely, X-ray and neutron radiography<sup>12, 13</sup>. X-ray and neutron beams can easily penetrate the opaque materials of PEFCs, and have the capability to quantify the water content within fuel cells. As they both have reasonable spatial and temporal resolutions, which are two greatly important factors to guarantee useful insights from experimental data, the obtained experimental results can reveal realistic water transport mechanisms and validate numerical models. Compared to experimental studies, numerical modeling has several distinguishing advantages, like arbitrarily accessible to detailed information within the resolved domain, strictly controllable operating parameters and low cost. However, as mentioned above, two-phase flow phenomenon in PEFCs is complex; it is difficult to describe them mathematically. For example, the issue how to effectively treat two-phase coupling at the GDL-GC interface is still unresolved, since liquid water dynamics in the GC can exhibit several dissimilar flow regimes such as film flow, slug flow and droplet flow<sup>14</sup>. To date, a multitude of numerical models have been developed to address two-phase flow in PEFCs, they may vary from one-dimensional to three-dimensional, from simple to comprehensive. More details are given in section 2.3.

The present chapter is mainly devoted to giving an overview of available numerical models on two-phase flow in PEFCs, including interface treatments between different layers. For completeness, several advanced imaging techniques used in PEFCs and obtained results are also briefly presented, which can provide valuable insights into water transport mechanisms within fuel cells and validate numerical models.

This review is organized as follows: in section 2.2, we describe the detailed water transfer processes in a PEFC with focus on water transport in the diffusion layers and GCs. Then, several prevalent two-phase models are reported and an emphasis is placed on the predictive abilities and limitations of these models in section 2.3. In general, numerical studies of two-phase flow in PEFCs can be simply classified into macroscopic and pore-scale modeling. Pore-scale models have the potential to shed light on the fundamentals of two-phase flow and provide constitutive relationships, i.e. capillary pressure saturation and relative permeability saturation curves, which

are essential to macroscopic models. However, a literature survey shows that macroscopic models are predominant due to the ease of incorporating electrochemical reactions and computational efficiency, as well as free from detailed geometric constructions. Greater detail is given in section 2.3. In section 2.4, main experimental achievements regarding two-phase flow in PEFCs are summarized. At last some conclusions and remarks on further studies of two-phase flow in PEFCs are presented in section 2.5.

## 2.2 Water generation and transfer in an operating PEFC

Water management is one of the most critical issues in the development and optimization of PEFCs, proper water management is essential to improve the cell performance, reliability and durability. In order to manage water effectively, obviously complete understanding of water generation and transport within an operating PEFC is indispensable. Nevertheless, due to the opaque feature of the constituents of a PEFC and its tiny volume, it is extremely hard to directly observe and quantify the water content and transfer. In this section, we focus on water generation and transport from a physical perspective (i.e. phenomenological description of water generation and transport), which always forms the fundamentals of macroscopic two-phase flow models in PEFCs. We divide this section into three subsections: first the components of a typical PEFC are introduced, followed by the description of its operating principles; in the third subsection, the detailed water generation and movement in a PEFC are presented, including phase change between water vapor and liquid water.

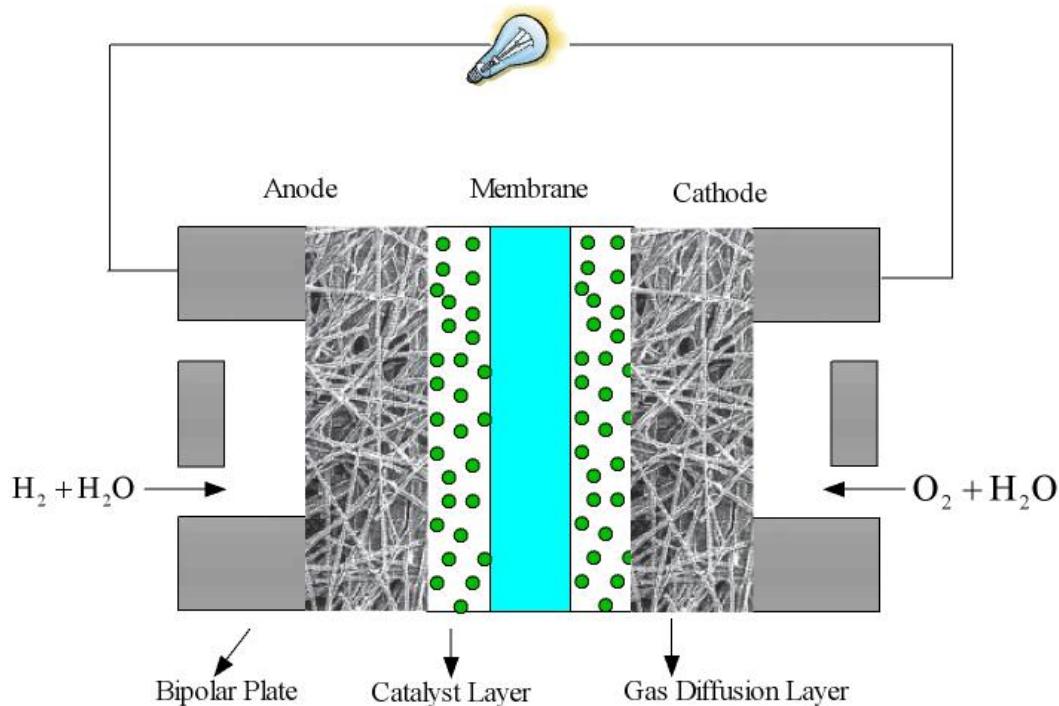


Figure 2-1: Schematic of a PEFC (consisting of four distinct components: membrane, CLs on both sides of the membrane, GDLs next to the CLs, and BPs).

## 2.2.1 Components of a typical PEFC

In practice, a number of PEFC units connected in series constitute a fuel cell stack, which can provide useful power for various applications. Unless otherwise stated, in this review, a PEFC is referred to as a single cell unit. A typical PEFC consists of four main components, as shown in Fig. 2-1, namely, electrolyte membrane, CL, GDL or PTL (porous transport layer) and BP (bipolar plate). The heart of a PEFC is the membrane; we also can see it from the name of this kind of fuel cells. On each side of the membrane there are diffusion layers including CL and GDL. Technically, the CL should be a part of the membrane or part of the GDL depending on manufacturing processes<sup>5</sup>, which is used to facilitate chemical reactions. The multilayer assembly of the membrane sandwiched by two CLs is called the MEA (membrane electrode assembly). In the following, the constituents of a PEFC are presented in more detail.

### Polymer electrolyte membrane

The strong interest in PEFCs stems from the benefit of utilizing a solid polymer electrolyte membrane with a typical thickness of 18-25  $\mu\text{m}$ . This layer is very thin but acts as a profound electrical insulator, and gas barrier preventing fuel and air crossover between electrodes while holding high proton conductivity. At the same time, electrons have to travel via external circuit to do useful works. However, for high performance of PEFCs, it is pivotal to keep the membrane fully humidified, since the ionic conductivity depends directly on its water content (or water uptake). Higher water content gives rise to higher ionic conductivity, in turn lower ohmic resistance and higher cell voltage at the same current density. The most commonly used electrolyte material is Nafion<sup>TM</sup>, a member of the perfluorosulfuric acid (PFSA) family. The chemical structure of Nafion comprises two primary parts: a Teflon-like backbone (hydrophobic) providing mechanical support and a sulfonic acid (hydrophilic) part used to transport protonic ions; for more detail, one can refer to the reference<sup>3</sup>.

It is worth noting that the membrane thickness has a big impact on the cell performance. In general, a thin membrane renders a low protonic ohmic loss, which is one of the several main attributions to the voltage losses in an operating PEFC. Nevertheless, if the membrane is too thin, it cannot provide enough structural strength, as well as allows for reactants crossover through the membrane, especially on the anode side due to the high diffusivity of hydrogen. Therefore, it is highly necessary to optimize the membrane thickness for better cell performance.

Nafion possesses several distinctive advantages in PEFC applications, like stationary, high protonic conductivity and strong mechanical stability. However, its high cost hampers the commercialization of PEFCs. More importantly, its noticeable property of high protonic transport entails the presence of excessive liquid water in PEFCs resulting in the so-called water flooding problem, which is even worse at high current densities. Due to this unavoidable drawback, water management plays an important role in the usage of this sort of polymer electrolyte. For this reason, recently many attempts have been made to develop new materials alternative to Nafion and the similar polymers. In general, the goals are to (1) reduce the material cost and (2) develop new solid proton exchange membranes which have the potential to effectively operate at high temperatures. It means that the fuel cells employing this kind of membranes are free from water management issue, and in turn could enhance the performance, durability and stability

dramatically. Even though some progresses have been achieved over the past few years, it is still not ready to replace the Nafion-type membranes. Therefore, nowadays, most research works relevant to PEFCs are still based on the Nafion-type membranes.

### Catalyst layer

Due to low operating temperatures (60-90°C), catalyst is required to enhance the sluggish chemical reactions in PEFCs. Depending on different MEA manufacturing processes, the CL with thickness of 5-30 µm may be applied on each side of the membrane, or coated directly on the surface of the GDL. Normally the CL is comprised of ionomer and platinum pellets supported by black-carbon particles. Electrochemical reactions take place on the catalyst surface, which is also known as three-phase boundary. Protons are transported by Nafion, reactants transport through the void pores, and electrons can also reach the catalyst surface via carbon particles which are effectively in contact with the GDL. Therefore, the CL is always referred to as porous media and mainly responsible for gaseous reactants transport, protonic and electrical conductions, as well as water and heat removals relevant to water and heat managements, which are introduced in the following sections. It is evident that several different transport processes occur in the CL simultaneously. This indicates that some optimizations can be facilitated to improve the cell performance, especially for the CL on the cathode side, which plays a significant role in the performance losses of PEFCs because of extremely sluggish oxygen reduction reaction (ORR) compared to hydrogen oxidation reaction (HOR) on the anode side.

Over the past few years, many efforts have been paid to this issue. Song et al.<sup>15</sup> conducted numerical optimizations of the cathode CL in terms of several design parameters: Nafion content, void space, CL thickness and platinum loading by using a one-dimensional model. They concluded that the CL performance was very sensitive to its thickness, and the best optimal performance could be achieved by adjusting the layer thickness and platinum loading. Qi and Kaufman<sup>16</sup> experimentally investigated the effects of Pt loading and Nafion content on the cathode performance. There are also a number of studies relating to the CL degradation in PEFCs, since it is one of the most critical factors affecting the durability of PEFCs. For more information, one can refer to the review<sup>17</sup> on platinum-based CL degradations.

### Gas diffusion layer

The GDL used in PEFCs is typically multi-layered and carbon-based porous media containing a macro porous layer (conventional GDL) and micro porous layer (MPL). In order to avoid confusing notations, the GDL refers to as conventional GDL in the following sections. The GDL with thickness of 150-400 µm, as one of the crucial components of a PEFC, has a significant impact on the cell performance, as its basic functions include: (1) transporting gaseous reactants from GCs to reactive sites, (2) draining out excessive liquid water from the CL to GCs under flooding situations, (3) keeping the membrane from dehydration, and (4) conducting electrons and heat with low resistance. In addition, the GDL also supports the mechanical structure of a PEFC.

Due to the importance of GDL in PEFCs, a vast amount of papers regarding the GDL study have been published in the open literature over the past two decades. Recently, Cindrella et al.<sup>18</sup> provided a comprehensive review on the GDL for PEFCs. Up to now, two most commonly used GDLs in PEFCs are carbon paper and woven carbon cloth. In general, they can be characterized by

porosity, pore morphology, wettability and permeability. In order to remove liquid water effectively, the GDL is always coated with polytetrafluoroethylene (PTFE) to make it hydrophobic. Analysis of the polarization curve of an operating PEFC shows that three main factors contribute to the voltage losses as increasing the current density, namely, activation loss, ohmic loss and mass concentration loss. It is a recognized fact that the most promising improvements can be achieved by optimizing the GDL to enhance its mass transfer ability, such as reactants transport into the CL and liquid water removal out of the CL. The optimization of the GDL is only possible by understanding several key transport processes in the GDL, like reactants diffusion, liquid water and heat transfer. It is believed that the development of GDL can promise a lot of potentials for higher power output, reliability and longevity.

The MPL with thickness of 5-20  $\mu\text{m}$ , originally developed to enhance the electrical contact between GDL and CL, is normally used to assist in water management in PEFCs with pore size of 100-500 nm. Although the exact functions of MPL are not yet clear now, it can improve cell performance noticeably at high current densities. One reason is that the MPL enhances thermal and electrical contacts between CL and GDL by offering a more continuous interface. Another reason may be that the MPL can serve as a capillary barrier to liquid water entering into the GDL and force liquid water to penetrate into the anode side. For the time being, researches on the MPL are still undergoing intensively.

#### Bipolar plate

Over the past few years, developing advanced BP materials and manufacturing techniques has been an active research subject in PEFCs. Micro GCs (i.e. flow fields) are machined on both sides of BP providing reactants distribution and transport, while the land facilitates electrical conduction and heat removal. The BP has the following main functions: reactants distribution and transport, liquid water removal, and electrical and thermal conductions. Due to these functions, it is seen that the optimization of BP design could improve the cell performance considerably. For more information, one can refer to some fuel cell handbooks<sup>3,5</sup>.

### 2.2.2 Operating principles

Fig. 2-1 shows the schematic of a PEFC. Humidified hydrogen (or hydrogen-rich gas) and oxygen (or air directly) streams are delivered into the flow fields on the anode and cathode sides separately. Hydrogen diffuses through the anode GDL into the CL, where each hydrogen molecule splits into two electrons and two protons according to the following reaction:



This half reaction is called HOR. The protons migrate into the cathode CL via the membrane, while the electrons have to travel through external circuit to do useful works. On the cathode side, oxygen transports into the cathode CL as well, where it combines with the protons from the membrane and the electrons from external circuit to form liquid water and heat, as expressed by Eq. 2-2:



This half reaction is referred to as ORR. Therefore, the overall reaction in a PEFC can be written as:



Note that Eq. 2-1 and Eq. 2-2 only indicate the main reaction steps in the CLs. In fact, lots of intermediate steps are involved on the catalyst surface, which are neglected here for simplicity. Although the operating principles of a PEFC are quite simple, several transport processes (reactants transport, liquid water movement, heat and electron conductions, etc) occur simultaneously inside its tiny volume, influencing the cell performance and durability. In what follows, we focus on describing water movement in an operating PEFC.

### 2.2.3 Water movement

Water management is critical to the performance of PEFCs. The membrane needs high water content to conduct protons effectively, whereas excessive water would block gas pathways and cover catalyst sites, resulting in reactant starvation and cell degradation. In this subsection, a first impression of water movement inside an operating PEFC is given, which could serve as a basis for the subsequent overview of two-phase flow in PEFCs.

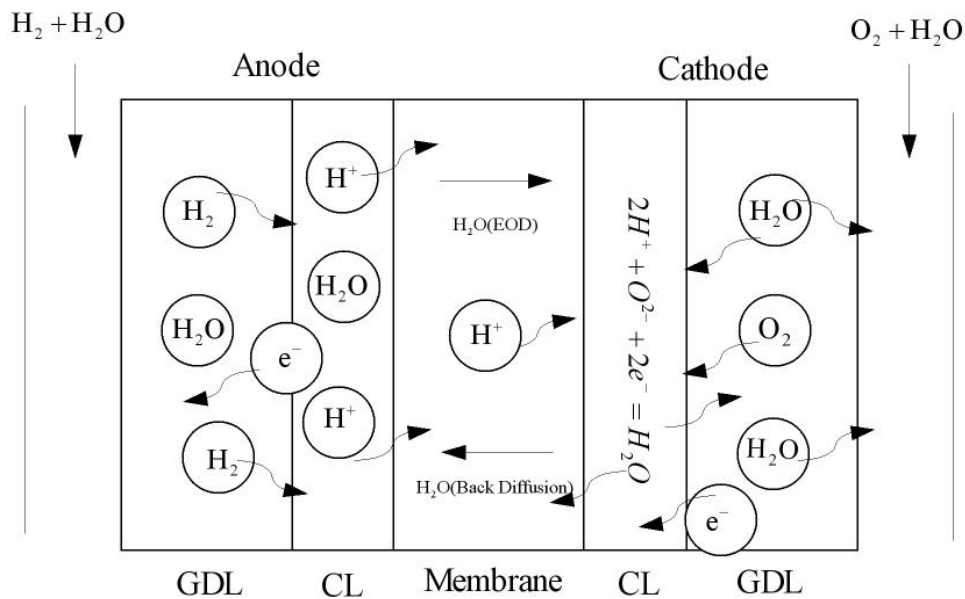


Figure 2-2: Schematic of the water movement inside a PEFC.

Fig. 2-2 schematically shows the water movement inside a PEFC. Water vapor is delivered into the GCs on both sides along with reactants, and subsequently diffuses into the CLs. Three types of water transport mechanisms can coexist in the membrane: (1) electro-osmotic drag (EOD) from the anode to the cathode associated with proton migration; (2) back diffusion normally from the cathode to the anode due to water concentration difference; (3) convective transport due to

pressure gradient (note that this mechanism is less dominant in contrast with EOD and back diffusion). In the cathode CL, water is generated because of ORR. When water vapor pressure exceeds its saturated value, water vapor would condense into liquid form, which always happens under high current densities. Under the action of capillary force, liquid water in the cathode CL penetrates into the GC through the GDL from high water saturation to the low. As a result, in PEFC experiments [10], we often observe lots of water droplets and slugs in GCs, which are finally removed out of the channels mainly under gas shear force and capillary force. The same phenomenon occurs on the anode side under flooding situations. Excessive liquid water in the anode CL would penetrate through the GDL into the anode GC, and then is swept out of the channel.

Overall liquid water transport inside diffusion layers of PEFCs is dominated by capillary action except for interdigitated flow fields<sup>19</sup>, which are designed to enhance convective transport in the GDL. In GCs, liquid water dynamics may exhibit different forms depending on several parameters, such as gas flow rates, channel dimensions, and wettabilities; more information is given in section 2.3.

## 2.3 Numerical modeling of two-phase flow in PEFCs

As mentioned above, numerical modeling of PEFCs holds several advantages, such as short developing cycle, low cost and easy control of simulation parameters. However, to obtain meaningful and reliable numerical results, a rigorous mathematical depiction of the physical processes occurring within fuel cells is needed. Over the past two decades, numerical modeling of PEFCs has received more and more attention with a focus on liquid water transfer. Based on the distinct components of a typical PEFC, water flow can be divided into three parts, namely, dissolved water transport in the membrane, liquid water transport in the diffusion layers (CL, GDL) and transport in the GCs. In general, two-phase flow in a PEFC refers to liquid water and gas mixture transport inside the diffusion layers and GCs. In this section, currently available numerical models of the two-phase flow in PEFCs are reviewed, particularly addressing their predictive abilities and limitations. For different scales and flow domains, we have different numerical treatments on the description of two-phase flow. For the sake of coherence, we divide this section into three subsections: subsection 2.3.1 is devoted to the review of two-phase flow in micro GCs; two-phase flow in diffusion layers is presented in subsection 2.3.2; and interface treatment is discussed in detail in subsection 2.3.3.

### 2.3.1 Two-phase flow in GCs

Two-phase flow in micro channels has attracted much attention for various applications, such as PEFCs, microelectronic cooling systems and biomedical instruments. For PEFC applications, there are two aims to study the two-phase flow in micro GCs: (1) understanding the liquid water dynamics in GCs and (2) incorporating the two-phase channel flooding into a PEFC model. First, a better understanding of dynamic behaviors of liquid water emerging from the GDL into the GC is indispensable. Several engineering parameters can affect the liquid water removal in the GC, including channel geometry and dimensions, wettabilities of channel side walls and GDL surface, and inlet gas velocities. Several interface-tracking numerical models have been extensively employed to investigate liquid water dynamics in GCs and provide guidelines for channel designs.

Theodorakakos et al.<sup>20</sup> incorporated the volume of fluid (VOF) method<sup>21</sup> with Navier-Stokes equations flow solver to study the detachment of liquid droplets from different GDL surfaces used in PEFCs. Parametric studies were conducted to emphasize the relevant importance of various factors influencing the detachment of liquid droplets from a GDL surface. Zhu et al.<sup>22-24</sup> adopted the VOF method in FLUENT to study the physical mechanism of a water droplet emerging from a GDL pore. Various parametric simulations including the effects of gas flow velocity, water injection velocity and dimensions of the pore were performed with a highlight on the effect of the wettabilities of GDL surface and micro channel surface. In addition, the effect of channel geometry on water droplet dynamics in the GC was also reported, and the results showed that the friction coefficient increased by a factor of 2-4 in the presence of liquid water. The upside-down trapezoid GC yielded the maximum coverage ratio and water saturation, while the rectangle with a curved bottom wall resulted in the minimum values. Cai et al.<sup>25</sup> utilized VOF method in FLUENT to study water droplet and film behaviors in the micro channels of a PEFC. It was reported that a hydrophilic channel side wall with a hydrophobic GDL surface could avoid water accumulation on the GDL surface. Jiao et al.<sup>26, 27</sup> performed the numerical investigations of air-water flow in micro-parallel-channels and serpentine flow channels with inlet and outlet manifolds of PEFCs using FLUENT. Their results showed that for straight-channels, excessive and unevenly distributed liquid water could cause blockage of the airflow and uneven distribution of air along the different flow channels, and the outlet manifolds were prone to being blocked severely. Most recently, Qin et al.<sup>28</sup> conducted a series of direct simulations of liquid water dynamics (i.e. water droplet and film dynamics) in a GC based on a proposed novel geometrical setup. The authors simplified the GDL by means of three connected water conducting pathways, which was supported by experimental observations. In addition, they studied the competing mechanisms of liquid water flow from conducting pathways in the GDL to the GC. This would give us the possibility to regulate liquid water flow into GCs, and maybe lead to a better water management in GCs.

Besides the widely applied VOF method, Lattice Boltzmann Method (LBM) is another effective numerical approach to modeling the two-phase flow in micro GCs. Hao and Cheng<sup>29</sup> used multiphase free-energy LBM to study the formation and subsequent movement of a water droplet. Recently, Choi and Son<sup>30</sup> employed the level set method to investigate the droplet motion in a micro channel with different contact angles. Kumbur et al.<sup>31</sup> performed theoretical studies of the effect of controllable engineering parameters, including surface PTFE coverage, channel geometry, droplet chord length and height, and air flow rate on the liquid droplet deformation and detachment in micro GCs. Based on the above literature review, we can see that GC flooding issue has received much attention due to its importance in the water management of PEFCs. Severe channel flooding results in large pressure drop along GCs, reactant starvation and maldistribution in CLs.

Although aforementioned interface-tracking models have been used to investigate water dynamics in GCs, they are computationally expensive and have not yet been ready to be integrated with a macroscopic PEFC model. Furthermore, these models always entail simplified water-inlet boundaries, such as suspended water droplets in the GC or emerged droplets from a structured GDL pore. But, the fact is that liquid water generated in the CL transfers into the GC through the GDL under combined capillary and viscous forces. It is evident that a strong interaction exists at the interface between GC and GDL. To fully reveal liquid water flooding in

PEFCs, we could not isolate the GC or the diffusion layers in numerical studies. It means that a complete two-phase model for an entire PEFC is required. Due to the complicated dynamics of gas-liquid two-phase flow in GCs, to date, the biggest challenge is how to mathematically describe liquid water flooding in GCs at the macro scale. Mist flow model (tiny droplets) and film flow model have been used for the extreme situations of high gas velocity (liquid water saturation < 0.1%) and low gas velocity/highly hydrophilic channel surface (liquid water saturation > 10%) respectively<sup>32</sup>. Wang et al.<sup>33</sup> proposed to model the two-phase flow in GCs by using the two-phase Darcy's law. They regarded a micro GC as structured and ordered porous media. According to the well-known Hagen-Poiseuille equation, a nominal permeability of the GC could be assumed as:

$$K_{GC} = c \frac{d^2}{32} \quad (2-4)$$

where  $K_{GC}$  denotes the nominal permeability of the GC,  $d$  represents the hydraulic diameter of the GC, and  $c$  is the shape factor determined by the cross-section of the GC.

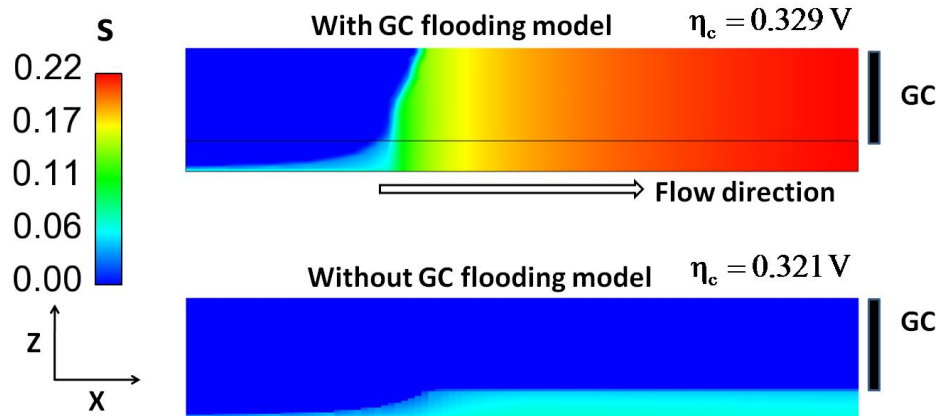


Figure 2-3: Distributions of the liquid water saturation at the middle cross-section of the cathode side with GC flooding model (upper one) and without GC flooding model (lower one) (operating conditions:  $RH = 66\%$ ,  $\xi_c = 2.0$ , and  $I_{ave} = 0.2 \text{ A cm}^{-2}$ ).

Later on Basu et al.<sup>8</sup> implemented this assumed two-phase channel model into an entire PEFC. Their numerical results showed a good agreement with experimental data in terms of pressure drops along GCs and wet areas at the GDL-GC interface. What is more, they investigated GDL intrusion effect and maldistribution of reactants due to the water flooding in GCs. Qin et al.<sup>7</sup> developed a two-phase flow model for the cathode side of a PEFC. They also assumed the GC to be a structured porous medium with the porosity of 1.0. The two-phase Darcy's law was applied to both GC and diffusion layers. More liquid water was found in the diffusion layers due to the water coverage effect at the GDL-GC interface when including the GC flooding model, as shown in Fig. 2-3. In addition, they showed that proper estimation of the gas drag force is crucial to the assumed GC flooding model. When the GC is assumed to be a structured porous medium, the

nominal relative permeability for each phase cannot be only a function of water saturation, but also of other variables (e.g. gas flow rate and current density).

Most recently, Qin et al.<sup>34,35</sup> developed a one-dimensional phenomenological model for the liquid water flooding in GCs. They idealized the liquid water distribution in the GC as shown in Fig. 2-4. It is seen that film flow was assumed at the GC corners due to the hydrophilic sidewalls, while water droplet was assumed in the middle due to the hydrophobic GDL surface. They further presumed that the existence of droplets in the GC solely influenced the configuration of the GC cross-section. As a result, the droplet population along the GC should be given in advance. Their numerical results showed that the gas drag force at the film-gas interface significantly enhanced the film flow along GC corners. A proper selection of the GC sidewall contact angle was found to be critical to a better water management in the GC. However, we note that further studies are still needed to make this phenomenological model more comprehensive and robust. On the one hand, we need to track the droplet dynamics explicitly in order to capture several key processes, like water clogging in the GC and mass exchange between droplet and film. On the other hand, efforts should be paid to the treatment of the GDL-GC interface. In other words, it is essential to determine that how much liquid water goes into the film flow and how much liquid water feeds the droplet.

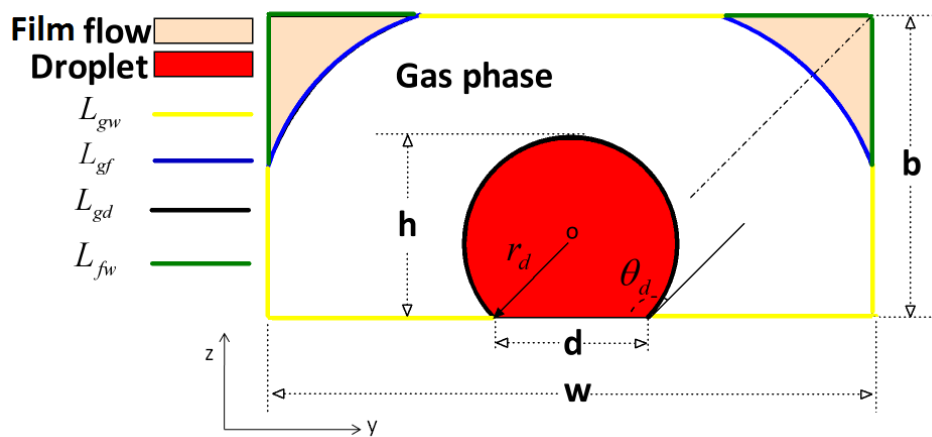


Figure 2-4: Assumed liquid water distribution in the GC, including the film flow at the corners and the water droplet sitting at the center.

### 2.3.2 Two-phase flow in diffusion layers

Under some operating conditions (e.g. startup, humid environments and high current densities), liquid water generated in the CL penetrates through the GDL into the GCs, resulting in the gas-liquid two-phase regimes in the diffusion layers. Excessive liquid water accumulation in diffusion layers would block gas pathways and cover catalyst pellets. To mitigate water flooding in PEFCs, a complete understanding of liquid water transfer and distribution inside diffusion layers is necessary. Over the past few years, numerical modeling of the two-phase immiscible flow in porous media<sup>36</sup> has given a remarkable contribution to this field. In principle, two

different modeling scales are available, namely, macro scale and pore scale. To some extent, information obtained from pore-scale studies can be used to complement macroscopic models. In the following, both macroscopic and pore-scale models for the two-phase flow in diffusion layers are reviewed in detail.

### 2.3.2.1 Macroscopic approach

Since detailed pore structure of porous media is usually unknown or hard to be established, modeling of two-phase flow at the pore scale would be extremely difficult. For this reason, two-phase flow in porous media is normally modeled at the macro scale, which is much greater than a pore diameter but much less than the simulation domain<sup>37</sup>. Macroscopic models can considerably reduce computational efforts. Meanwhile, the reconstruction of pore structure of porous media is avoidable. In general, two-phase flow in porous media is potentially the combined result of capillary, viscous and gravitational forces. Their relative magnitudes govern the two-phase flow regimes and distribution. In the absence of buoyancy forces, Lenormand et al.<sup>38</sup> found that the immiscible two-phase flow in porous media was dominated by two dimensionless numbers: capillary number,  $Ca$  and viscosity ratio,  $M$  :

$$Ca = \frac{\mu_{nw} u_{nw}}{\sigma} \quad M = \frac{\mu_{nw}}{\mu_w} \quad (2-5)$$

in which the subscripts  $_{nw}$  and  $_w$  denote the non-wetting and wetting respectively,  $u_{nw}$  is the total Darcy velocity of the non-wetting phase,  $\sigma$  is the surface tension and  $\mu$  denotes the dynamics viscosity. Depending on the relative magnitudes of capillary number and viscosity ratio, two-phase flow in porous media can exhibit three different regimes<sup>39</sup>, namely, viscous fingering, stable displacement and capillary fingering. In diffusion layers of PEFCs, the capillary number is pretty small ( $10^{-8}$ ). Thus, liquid water transport is dominated by capillary action.

Porous media can be characterized by its porosity, permeability and tortuosity, etc., which serve as essential input parameters for macroscopic models. Due to the difficulty in upscaling of two-phase flow in porous media from the pore scale to the macroscopic scale, a straightforward way is to empirically extend the single-phase Darcy's law to the two-phase flow similarly (i.e. the so-called two-phase Darcy's law), accounting for the effect of the presence of the other phase in porous media. According to our knowledge, most of macroscopic CFD (computational fluid dynamics) models for the two-phase flow in diffusion layers of PEFCs are based on the two-phase Darcy's law. In the following, for simplicity, the two-phase Darcy's law is introduced without considering species transport as well as electrochemistry inside a PEFC. First, the mass conservation equations for both gas and liquid phases<sup>40</sup> are given as:

$$\frac{\partial[(1-s)\varepsilon\rho_g]}{\partial t} + \nabla \cdot (\rho_g \bar{V}_g) = \dot{S}_g \quad (2-6)$$

$$\frac{\partial(\varepsilon s \rho_l)}{\partial t} + \nabla \cdot (\rho_l \bar{V}_l) = \dot{S}_l \quad (2-7)$$

where the subscripts  $g$  and  $l$  denote the gas and liquid water phases, respectively,  $\bar{V}$  is the Darcy velocity,  $s$  represents the liquid water saturation defined as the fraction of pore space occupied by the liquid phase,  $\varepsilon$  denotes the porosity, and  $\dot{S}_g$  and  $\dot{S}_l$  are the volumetric source terms for gas and liquid phases, respectively, which are used to account for chemical reactions in CLs and phase change. The two-phase Darcy equation for each phase is given as:

$$\bar{V}_g = -\frac{k_{rg}k_0}{\mu_g}(\nabla p_g - \rho_g \bar{g}) \quad (2-8)$$

$$\bar{V}_l = -\frac{k_{rl}k_0}{\mu_l}(\nabla p_l - \rho_l \bar{g}) \quad (2-9)$$

where  $\nabla p$  is the pressure gradient,  $k_0$  is the intrinsic permeability, and  $k_{rg}$  and  $k_{rl}$  denote the relative permeabilities for the gas and liquid phases, respectively. The difference between these two equations and the single-phase form stems from the presence of relative permeability, which designates the influence of the reduced void space for each phase due to the existence of the other phase. In addition, capillary pressure is introduced to express the pressure difference between the gas and liquid phases:

$$p_c(s) = p_g - p_l \quad (2-10)$$

To close the above governing equations, two constitutive correlations are needed, namely, capillary pressure-saturation and relative permeability-saturation relationships. The traditional two-phase flow theory in porous media presumes that the capillary pressure is solely functional of the saturation. Hassanizadeh and Gray<sup>41</sup> claim that, based on a rigorous thermodynamic derivation, the capillary pressure is not only a function of saturation but also of the specific areas of the three interfaces for the two-phase flow in porous media. However, to date, this model is still hard to be integrated with current CFD codes, since it involved several additional variables. Another weakness in the traditional capillary pressure-saturation correlation lies in the lack of the consideration of dynamic effect indicated by recent studies<sup>42</sup>. We can see that capillary pressure and relative permeabilities play an important role in the description of multiphase flow in porous media. In PEFC modeling, an empirical relationship between capillary pressure and saturation is always used. Wang et al.<sup>43</sup> proposed an expression based on the following Leverett  $J(s)$  function:

$$P_c = \sigma \cos\theta \left( \frac{\varepsilon}{k_0} \right)^{1/2} J(s) \quad (2-11)$$

in which  $\theta$  is the static contact angle of porous media. Note that  $J(s)$  function is not general and depends on the wettability and the morphological properties of porous media<sup>44</sup>. Udell's<sup>45</sup> correlation has been frequently employed to evaluate  $J(s)$  in PEFC modeling, given as:

$$J(s) = \begin{cases} 1.42(1-s) - 2.12(1-s)^2 + 1.26(1-s)^3 & \text{for } \theta \leq 90^\circ \\ 1.42s - 2.12s + 1.26s & \text{for } \theta > 90^\circ \end{cases} \quad (2-12)$$

It needs to be pointed out that the Udell's correlation is originally derived for geological porous media, which is highly hydrophilic. It cannot distinguish the difference between sand and diffusion layers. Based on the above governing equations of two-phase flow in porous media, apparently the capillary function has a big impact on the prediction of two-phase models<sup>46</sup>. Therefore, a straightforward way is to obtain capillary pressure-saturation curves experimentally. Nguyen et al.<sup>47</sup> employed volume displacement technique to measure the capillary pressure and the corresponding liquid water saturation in both GDL and CL in association with neutron imaging technique. Later on Ye and Nguyen<sup>44</sup> incorporated these experimental data into a three-dimensional two-phase flow model to investigate liquid water behaviors in a PEFC.

On the other hand, still due to the lack of experimental data, a cubic correlation is used for the relative permeabilities. Note that this relationship comes from sand/rock-type porous media with a typical porosity of 0.1-0.4<sup>44</sup>. So, the gas and liquid permeabilities can be expressed as:

$$k_{rg} = (1-s)^{n_1} \quad k_{rl} = s^{n_2} \quad (2-13)$$

where both exponents  $n_1$  and  $n_2$  can be regarded as material properties. Recently, Hussaini and Wang<sup>123</sup> experimentally determined air and water relative permeabilities as functions of water saturation for several typical GDLs used in PEFCs. The authors fitted some expressions for in-plane relative permeabilities. However, it was found that measurements of through-plane relative permeabilities exhibited large uncertainties.

In the two-phase Darcy's law, a full set of conservation equations are solved for each phase; and two phases are coupled by capillary pressure. However, in PEFC modeling, modified Navier-Stokes equation (Darcy's source term is added) or Brinkman equation has been commonly used which could circumvent the interface treatment between GC and GDL because of the same order of momentum equations in both domains. Up to now, only a few researchers have employed this model to mimic the two-phase flow in PEFCs, since it requires a multiphase solver, and should be able to couple species transport, phase change and electrochemical reactions simultaneously. As a consequence, this multi-fluid model necessitates lots of computational efforts and produces numerical instabilities. Berning and Djilali<sup>48</sup> developed a three-dimensional multi-fluid multi-component model to study the two-phase flow in the GDL of a PEFC based on a commercial solver CFX 4.3, accounting for the phase change and heat transfer. In their model, the CL and membrane were assumed to be an infinitely thin interface and a heat-conducting solid, separately, with the mist flow assumption inside the GCs. Jain et al.<sup>49</sup> developed a two-fluid model for water transport in a PEFC based on a commercial CFD solver, CFD-ACE+, a notable feature of their model was allowing for the prediction of water transport in GCs. Song et al.<sup>50</sup> developed a 1D non-isothermal multi-fluid model to conduct transient analysis for the cathode GDL. The effects of four parameters, namely, liquid water saturation at the GC-GDL interface (i.e. water coverage effect), contact angle, current density and proportion of inlet liquid water to all of the water generated in the CL were examined. More recently, Berning et al.<sup>51</sup> established a 3D multiphase multi-fluid model for the cathode diffusion layers to study the effects of various

material parameters on the predicted liquid water distribution. The authors included the irreducible saturation for each layer. In addition, an expression of the GDL-GC interface condition for liquid water transport was developed.

Another model, called unsaturated flow theory<sup>52, 53</sup> (UFT), has also received much attention over the past few years in PEFC modeling. In this model, gas phase pressure is assumed to be constant throughout porous media, i.e. the effect of gas drag force on liquid water transport is negligible. As a result, the liquid water transport equation can be derived as:

$$\frac{\partial(\varepsilon s \rho_l)}{\partial t} + \nabla \cdot \left( \rho_l \frac{k_{rl} k_0}{\mu_l} \frac{dp_c}{ds} \nabla s \right) = \dot{S}_l \quad (2-14)$$

Interestingly the above liquid water transport equation can be easily implemented into a general CFD code by regarding liquid water as somewhat solute transport without convective term<sup>53</sup>. Since this sort of model does not consider gas drag force on liquid water transport, no momentum equation for gas phase is needed which makes calculations stable and fast. Natarajan and Nguyen<sup>54</sup> employed the UFT to investigate the influence of various operating parameters on liquid water removal. In their simulations, only the GDL was considered by assuming the CL as a thin interface. The capillary pressure was the only driving force for liquid water flow. Later on, Lin et al.<sup>55, 56</sup> further developed this model. They included the CL represented by a thin-film/agglomerate approach and membrane. More recently, Wang and Nguyen<sup>57</sup> extended this model to elucidate the effect of the cathode MPL on the cell performance. However, it should be noted that GCs were not included in all these simulations, and gas pressure was assumed to be constant. Pasaogullari and Wang<sup>52</sup> compared the predicted liquid water distributions from the UFT and so-called multiphase mixture model. It was found that the UFT underestimated the water saturation in the GDL for fully humidified air inlet.

To account for gas drag force on liquid water transport, Ye and Nguyen<sup>44</sup> presented a liquid water transport equation derived from the two-phase Darcy's law. The modified Navier-Stokes equation was used for the gas phase flow in the diffusion layers of a PEFC. Two phases were coupled by the phase change between water vapor and liquid water; and the effect of the presence of liquid water on the gas flow was taken into account only by correcting gaseous species diffusivities. Wu<sup>58</sup> used the same methodology to investigate the dynamic performance of PEFCs. Qin et al.<sup>59</sup> studied the effect of GDL anisotropy on the liquid water flooding as well as heat transfer in a PEFC.

Aside from the aforementioned approaches, the multiphase mixture ( $M^2$ ) model has been employed extensively by many fuel cell researchers<sup>60-71</sup> as well. Based on the two-phase Darcy's law, the  $M^2$  model for multiphase, multi-component transport in capillary porous media was firstly developed by Wang and Cheng<sup>72</sup>. Compared to the classical multiphase approach, the  $M^2$  model holds the following advantages: (1) it strongly resembles the single-phase flow theory; (2) it requires fewer nonlinear and coupled differential equations; (3) it can deal with the coexistence of single- and two-phase regimes conveniently; (4) it is a reformulation of the classical multiphase model into a single-phase system without involving any additional assumptions; (5) and it does not smear out the intrinsic characteristics of individual phases. Zhang et al.<sup>43</sup> first introduced the  $M^2$  model into PEFC modeling. The  $M^2$  model for the cathode side of a PEFC was developed to

investigate the water flooding effect on the cell performance. Pasaogullari and Wang<sup>52</sup> used a 1D multiphase mixture formalism for the cathode side of a PEFC to address the effect of gas shear force on liquid water flow in the diffusion layers. The authors demonstrated that a MPL between the GDL and CL could enhance water back-diffusion across the membrane as well as reduce water saturation in the CL. Later on, Pasaogullari et al.<sup>67</sup> further developed the previous model<sup>52</sup> into a 3D full PEFC model to investigate the MPL effect on water management in detail. The results showed that the water back-flow through the membrane increased with increasing the MPL hydrophobicity and thickness, and decreasing its pore size and porosity. Wang and Wang<sup>62</sup> incorporated non-isothermal effect into the M<sup>2</sup> model including irreversible heat, entropic heat, Joule heat and latent heat owing to phase change. The authors studied the complex interactions between two-phase flow and heat transfer. They illustrated that the vapor-phase diffusion and capillary-driven liquid water transport aid each other in the water removal along the through-plane direction under the channel area, however oppose each other along the in-plane direction between the channel and land. Wang and Wang<sup>73</sup> extended this non-isothermal model to be transient, and studied the GDL de-wetting problem. Ju<sup>63</sup> addressed the effect of anisotropic GDL on heat and water transfer in a PEFC by employing a 3D, non-isothermal M<sup>2</sup> model. Later the author<sup>61</sup> reformulated the M<sup>2</sup> model to facilitate the immobile liquid water saturation influence in the diffusion layers of a PEFC. Most Recently, Basu et al.<sup>74</sup> studied the phase-change phenomenon in the cathode GDL of a PEFC based on a steady-state, non-isothermal M<sup>2</sup> model. They demonstrated that the phase-change-driven removal of product water and heat from a PEFC could be dominant in an operating PEFC. Finally, we note that the M<sup>2</sup> model lumps water vapor and liquid water into one water concentration variable, and recovers them in the post-processing, which entails local phase equilibrium assumption.

To sum up, macroscopic modeling of two-phase flow in PEFCs has attracted much attention over the past few years. However, it cannot take morphology of diffusion layers into account. On the other hand, two-phase coupling mechanisms between GC and GDL still remain challenging for macroscopic approaches. For the time being, more and more researchers resort to the pore-scale modeling for revealing fundamentals of two-phase flow in PEFCs. In the following, pore-scale studies on the two-phase flow in the GDL of a PEFC are reviewed in detail.

### 2.3.2.2 Pore-scale approach

Pore-scale modeling, as an effective tool, has been widely used to shed light on the fundamentals of multiphase flow in porous media<sup>75</sup>. In general, according to applied methodologies, pore-scale models can be divided into rule-based and first-principle-based models<sup>76</sup>. Rule-based models, such as pore network (PN) and full morphology (FM), rely on imposing some essential rules representing fundamental physics on an idealized network representation of porous media. First-principle-based models resolve the underlying governing equations directly based on the microstructure of porous media. Note that LBM is regarded as one of the principle-based models. The first step in pore-scale modeling is to describe the pore structure of porous media. Up to now, several mathematical and experimental methods have been available to represent detailed pore structure<sup>77</sup>, such as stochastic method, X-ray and micro-CT tomography techniques.

PN modeling was first proposed by Fatt<sup>78-80</sup> who computed capillary pressure and relative permeability in a network of interconnected pores. In PN modeling, macroscopic equations, such as the Darcy's law, are not involved directly, but emerge from averaging the relevant pore-scale physics. For this reason, PN modeling is quite different from traditional simulation approaches for transport in porous media, where the macroscopic constitutive relationships are assumed a priori<sup>81</sup>. In PN models, porous media is discretized by a network of pore bodies connected by narrow regions called pore throats. For simplicity one can assume a random distribution of pore bodies and throats calibrated by macroscopic properties of porous media, or more precisely, a realistic microstructure of porous media could be used to establish the pore network.

Over the past few years, PN modeling has been employed by some researcher to obtain capillary pressure-saturation and relative permeability-saturation relationships and gain insights into the fundamentals of two-phase liquid-gas flow in the GDL of a PEFC. Sinha and Wang<sup>77</sup> developed a dynamic PN model to study the liquid water flooding in a GDL. In their model, the pore structure of GDL was represented by both pore bodies cubic in shape and pore throats of square cross-section. Their radii were assigned by a cut-off log normal distribution function. Note that film flow in pore throats was ignored for simplicity. Later on, the authors<sup>82</sup> extended this model to account for the mix-wettability effect of GDL, which consisted of both hydrophilic and hydrophobic pores. Koido et al.<sup>83</sup> used the PN modeling to predict capillary pressure-saturation curve of the GDL, which served as an important input for traditional continuum models. Gostick et al.<sup>84</sup> also developed a PN model to compute the pore-scale distribution of liquid water and gas under drainage conditions using an invasion percolation algorithm. The relative permeability and effective gas diffusivity were computed as functions of water saturation. Lee et al.<sup>85</sup> developed a dynamic PN model to study the liquid water transport in a hydrophobic GDL. The pore structure of GDL was represented by a regular cubic network of pores connected by throats. In addition, film flow at corners was considered. Rebai and Prat<sup>86</sup> studied the scale effect on liquid water transport and distribution in a GDL, which illustrated poor predictions of liquid water distribution obtained from continuum models. Additionally, inlet boundary conditions for the GDL, coverage effect of channel land and GDL compression effect were investigated. Most recently, Luo et al.<sup>87</sup> developed a steady-state topologically equivalent PN model. The salient feature was that they extracted pore networks directly from GDL microstructures. They found that GDL morphology affected water transport characteristics strongly.

From the above review of PN modeling, we can see that this method has received more and more attention in PEFCs owing to its computational effectiveness and powerful predictive abilities. However, one should be concerned with the pore structure difference between fibrous GDL used in PEFCs and normal rock- and sand-type porous media. One necessary consideration is that whether the pore structure of GDL can be represented by a network of pore bodies and throats. Scanning electron microscopy (SEM) images of a GDL show no evident pore throats connecting pore bodies. Another limitation of PN models used in PEFC modeling arises from the fact this pore-scale modeling cannot couple the liquid water transfer between the GDL and GC.

Besides PN models, the LBM, regarded as a novel computational approach for a wide spectrum of fluid transport phenomenon<sup>88, 89</sup>, has been widely applied to multiphase flow in porous media, two-phase flow with phase change, and chemical reactions in microscopic flow, as well as electro-kinetic transport<sup>90-92</sup>. LBM is a modeling approach based on kinetic theory of

molecular/particle motion, tracking movements of particle ensembles along prefixed paths where the velocities are determined by a finite set of vectors. The governing equation is the well-known Boltzmann transport equation, in which a probability distribution function is used to describe the particle population. The time-evolution of the distribution function depends on molecular interaction forces. It is shown that macroscopically LBM is equivalent to a continuity equation and the Navier-Stokes equation for incompressible flow. LB models holds two salient advantages: convenient and flexible incorporation for complex boundary conditions and simple computational algorithm. However, it should be noted that LB models are very computationally expensive, requiring efficient parallel implementations of the algorithms and access to high-performance computers in order to obtain meaningful results<sup>93</sup>. To date, several types of LB models used to model multiphase flow in porous media have been available. For more detail, one can refer to<sup>93</sup>.

The LBM has been successfully adopted by fuel cell researchers to investigate liquid water flooding in the GDL of a PEFC, and obtain constitutive correlations critical to macroscopic PEFC models<sup>94, 95</sup>. Mukherjee et al.<sup>76, 94</sup> developed a two-phase LB model, on the basis of the S-C approach<sup>96</sup>, to mimic liquid water flow through the GDL of a PEFC. The pore structure was virtually reconstructed by the stochastic method<sup>97</sup>. Some insights into liquid water transport mechanism in fibrous GDLs were presented; and the effect of surface wettability of GDL was investigated as well. It needs to be noted that, in their model, the assumption of equal density and viscosity values for both gas and liquid was involved because of numerical instabilities arising from spurious currents at the phase interface. This is an intrinsic weakness in the S-C approach. Park et al.<sup>92</sup> developed a multiphase LB model to study liquid water droplet motion in the GDL of a PEFC. Niu et al.<sup>95</sup> presented a multiphase multiple-relaxation-time LB model to delineate water-gas transport processes in the GDL of a PEFC. This proposed model was based on the mean-field interface theory and could deal with the multiphase flow with large density ratios and various viscosities, which released the limitation of the models based on the normal S-C approach. The authors also examined the saturation-related transport properties in the GDL, such as relative permeability and capillary pressure. In comparison with PN modeling, LB models are based on fundamental physics of fluid dynamics, and can be conducted on the basis of realistic pore structures directly without any additional treatments. However, they always entail heavy computational efforts.

Direct simulations can also be employed to study two-phase flow in the GDL of a PEFC based a reconstructed pore structure. This first-principle-based method resolves the governing partial differential equations directly, which are discretized on a computational grid using finite volume or finite element CFD techniques in association with proper boundary and initial conditions. For single-phase flow, Navier-Stokes equation is calculated explicitly, while the VOF method can be used for multiphase flow, which is a popular interface-tracking methodology as mentioned in the section 3.1<sup>21</sup>. One may encounter triple difficulties in the application of direct simulations, namely, reconstruction of pore structures, pore structure meshing and expensive calculations, especially for complicated porous media. Wang et al.<sup>98</sup> reconstructed a carbon-paper GDL stochastically<sup>99</sup> and used direct simulations to address the pore-scale transport phenomenon in the GDL. However, in their simulations, liquid water was assumed to be absent. To reveal exact liquid transport mechanism and evaluate liquid droplet coverage effect on water flooding in diffusion layers, Rensink et al.<sup>100</sup> employed the VOF method to mimic liquid water transport in a

GDL and dynamic process of droplet emergence from the GDL into GCs. The results showed that liquid droplets at the GDL-GC interface had a profound impact on the water saturation in the GDL. However, we note that the authors did the calculations based on 2D cross-sections of the GDL for saving computational efforts. Whether a fibrous GDL can be represented by its 2D cross-sections is still pending.

In conclusion, several pore-scale numerical models have been successful used to shed light on water transport mechanisms in GDLs. Some guidelines have been provided to optimize GDL structures aiming at enhancing reactants transfer into reactive sites and mitigating water flooding in PEFCs. However, according to this literature survey, currently available pore-scale models more or less involved some assumptions, which may detract the final interpretations of obtained results. For instance, GDL pore structures were greatly simplified by some researchers<sup>84, 85, 89</sup>. A more realistic pore structure<sup>97, 99, 100</sup> based on stochastic generation process also involved a few assumptions, such as overlapping of fibers and excluding binder effect. For this reason, additional efforts concerning true geometry construction of GDLs are still needed. Maybe the straightforward way resolving the above problems is to draw GDL pore structures from experimental data (e.g. CT tomography), which has been adopted in other types of porous media. In addition to the reconstruction of GDL pore structures, one should pay attention to some other specific features of GDLs used in PEFCs, which are needed to be integrated into pore-scale simulations. For instance, water transport inside the GDL is always affected by its adjacent components in an operating PEFC. This means that interface effects must be taken into account for a comprehensive PEFC modeling. PN modeling fails to predict these interface influences. Maybe LB modeling and direct simulations could contribute to this issue. In what follows, we focus on the discussion on interface treatments in PEFC modeling.

### 2.3.3 Interface treatment

Under water flooding situations in PEFCs, liquid water emerges from diffusion layers into GCs in the form of small droplets and slugs, especially on the cathode side. As a result, with respect to the two-phase flow modeling in a PEFC, mainly two different interfaces can be involved simultaneously, namely, CL-GDL and GDL-GC interfaces. The CL-GDL interface is relatively easy to handle in the context of macroscopic modeling, since both CL and GDL are porous layers. In general, a continuous capillary pressure is enforced across the CL-GDL interface. Due to the different material properties between CL and GDL, a discontinuity of water saturation at the CL-GDL interface can be obtained<sup>51</sup>. When a MPL is included between CL and GDL, Kang and Ju<sup>101</sup> assigned a high entry pressure to the MPL due to its fine pore structure. Their numerical results showed that the high liquid-entry pressure of the MPL prevented any liquid water from entering the MPL. Consequently, this liquid-free MPL enhanced the water back-flow across the membrane into the anode side. Most recently, Hizir et al.<sup>102</sup> used optical profilometry to characterize the MPL and CL surfaces for a better understanding of their surface morphologies. They indicated that the CL-MPL interface could result in a significant interfacial water storage capability due to its roughness. Therefore, this interface effect can be regarded as an additional resistance for liquid water transport in the through-plane direction, which should be considered in further numerical studies.

In macroscopic PEFC modeling, more difficulties can arise from the treatment of GDL-GC interface for two main reasons: lacking effective channel flooding model and coupling liquid water transport between porous media (GDL) and free flow (GC). As a result, the mist flow assumption has been employed in most previous numerical models<sup>51, 58-60</sup>, in which zero water saturation (i.e. zero capillary pressure) is assigned at the GDL-GC interface. However, experimental observations<sup>9, 10</sup> showed that water droplets and slugs prevailed in GCs under flooding situations, particularly at low gas flow rates. These droplets and slugs cover the GDL surface and block GCs, in turn, influence the flooding level in the diffusion layers. In order to capture this physical phenomenon, interactive mechanisms between GDL and GC much be incorporated into a full PEFC model.

Up to now, only a few researchers have numerically addressed the GDL-GC interface effect on water management in PEFCs<sup>51, 103-105</sup>. Song et al.<sup>50</sup> developed a 1D non-isothermal two-phase model to address the effect of liquid water saturation at the GDL-GC interface on the transient behavior of liquid water transport in the cathode GDL. The results showed that this parameter had a big impact on the water saturation inside the GDL. A more elaborate interfacial coverage model was proposed by Meng and Wang<sup>9</sup>. They assumed the interfacial water saturation at the GDL-GC interface to be a function of the GDL surface contact angle, current density, as well as gas inlet velocity with the mist flow assumption in the GC. The results showed that the interfacial coverage effect deteriorated the flooding level in the diffusion layers considerably. Berning et al.<sup>51</sup> separated the GDL from the GC, and prescribed an interface boundary condition which was not affected by the channel flow. This interface boundary condition was extracted from the interior of the GDL based on the Hagen-Poiseuille equation. The authors assumed that liquid water must overcome a pressure barrier to penetrate into the GC, corresponding a non-zero liquid water saturation or capillary pressure at the interface. Recently some researchers<sup>7, 32, 33, 106</sup> proposed to model water flooding in GCs by the two-phase Darcy's law. If so, the two-phase coupling between GDL and GC became straightforward. However, it should be noted that only the two-phase Darcy's law is incompetent to simulate complicated two-phase flow in GCs ranging from the mist flow to droplets and slug flows. The validation of this model is still controversial. It is evident that a proper treatment of GDL-GC interface is critical to the reliable predictive ability of a PEFC model. Neglecting this interfacial coverage effect would lead to underestimating the flooding level in both diffusion layers and GCs, in turn, overestimating the cell performance.

## 2.4 Experimental observations of two-phase flow in PEFCs

Revealing water evolution and transport in PEFCs is critical to improve their performance and durability, which is referred to as water management. As reviewed in the last section, many studies have been focused on theoretical and numerical modeling of two-phase flow in PEFCs over the past two decades. In reality, complex architectures and material characteristics of PEFC components inherently prevent a complete mathematical description of water evolution and transport. Some essential assumptions have to be involved in PEFC modeling which may detract the physical interpretations of obtained results. Fortunately, to date, several advanced experimental techniques have been successfully applied to visualize water content and transport in both diffusion layers and GCs, including optical photography<sup>14, 9-11, 107</sup>, X-ray technique<sup>12, 108-111</sup>, and neutron radiography and tomography<sup>13, 112-116</sup>. They all have their advantages and

disadvantages based on the considerations of cost, temporal and spatial resolutions, etc. In the following these three in situ and promising visualization techniques are discussed in detail. Some recently obtained insights into water evolution in PEFCs are reviewed. We note that besides the abovementioned techniques, multiple other methods also have been used to measure water content in an operating PEFC, such as magnetic resonance imaging (MRI), ionic resistance, infrared absorption, and residence time distribution<sup>117</sup>.

### 2.4.1 Optical photography

Optical photography using transparent fuel cells has been widely employed to study liquid water dynamics in GCs. This technique has excellent spatial and temporal resolutions depending upon the combination of optics and recording systems, and is easily accessible (low cost). However, it requires the modification of GCs in order to accommodate optical observations. This modification can result in different material properties, which in turn affects the cell performance and water distribution. What's more, only liquid water in GCs can be imaged directly by means of this method. Ge and Wang<sup>10</sup> optically observed liquid water formation and transport in the anode GC, and found that condensed water could wick into the hydrophilic GDL and mitigated the anode channel flooding. Yang et al.<sup>9</sup> summarized dynamic water transport process in the GC of an operating PEFC, starting from droplet emergence from the GDL, droplet growth and subsequent detachment, to the two-phase flow regime. The authors found that liquid water emerged from preferential locations on the GDL surface, and surface tension played a predominant role in the water removal out of the GC. When the sidewalls of the GC were highly hydrophilic, coalescence of water droplets and flow along the GC corners were attributed as the main water removal mechanism. Zhang et al.<sup>107</sup> also reported two models of water removal in a GC based on the magnitude of gas inlet velocity. When the gas velocity was high, the water droplet size was small and mainly swept by the drag force imposed by the gas flow; under the low gas flow rate, emerged droplet would grow to a critical size comparable to the channel dimensions, and then wicked into the sidewalls under surface tension force. In addition, the authors fitted a semi-empirical relationship between droplet detachment diameter and gas velocity in the GC. Spornjak et al.<sup>11</sup> employed a transparent single-serpentine PEFC to qualitatively examine the water removal effectiveness of several types of GDLs, since under the same operating condition, water flooding level in the GC could reflect the water removal capacity of GDLs. High amount of water appearing in the GC indicated high efficiency of water removal in GDLs. In addition, the MPL effect on water transport was also evaluated in terms of the two-phase flow in the GC by the authors. Akhtar et al.<sup>118</sup> isolated the GC to address the channel geometry effect on its water removal ability. Note that liquid water was introduced manually in this work, not generated in an operating fuel cell. Most recently, Hussaini and Wang<sup>14</sup> presented a flow map illustrating various two-phase flow patterns in the GC. A new parameter named wetted area ratio was proposed to address the liquid water coverage on the GDL surface, which would affect the liquid water distribution and transport inside the GDL, as well as hinder reactants diffusion into reactive sites.

It is evident that optical observations employing transparent fuel cells can provide useful insights into liquid water dynamics in GCs and on the GDL surface, assisting in the optimization and development of GCs, as well as understanding water flooding in fuel cells. However, the above reviewed works are limited to the two-phase flow in GCs due to the opaque feature of a

PEFC. To visualize liquid water flow in the GDL optically, Lister et al.<sup>119</sup> employed fluorescence microscopy associated with optical photography to visualize liquid water transport through the GDL. In their work, a dye solution was pumped into the GDL through the bottom, and water transport was imaged by fluorescence microscopy. This novel technique allowed for the tracking of two-phase interface explicitly, and informed the liquid water transport pathways and mechanisms inside the fibrous GDL. The authors observed a fingering and channeling transport model for liquid water against the capillary-tree-like model previously proposed by Pasaogullari and Wang<sup>68</sup>. Later on, Bazylak<sup>120, 121</sup> used the same apparatus and method to study the liquid water transport behaviors in the Toray GDL under the effect of compression, and the water droplet dynamics emerging from the GDL into the GC. However, fluorescence microscopy can only visualize liquid water flow as it emerged from few-micrometer locations below the GDL surface. Another drawback of this method lies in the employment of unrealistic operating conditions for a PEFC (e.g. prescribed water inlet boundary for the GDL).

## 2.4.2 X-ray technique

X-ray imaging technique also has been successfully used to investigate liquid water distribution and transport in PEFCs by a number of researchers. Sinha et al.<sup>111</sup> first evaluated the viability of using X-ray micro-tomography to quantify liquid water saturation in the GDL of a PEFC with a high spatial resolution ( $10\ \mu\text{m}\times 10\ \mu\text{m}\times 13.4\ \mu\text{m}$ ). However, as a first attempt, just the GDL was taken into account in the authors' work. Lee et al.<sup>109</sup> reported a high spatial resolution of  $9\ \mu\text{m}$  to quantify liquid water content in an operating PEFC by means of X-ray imaging technique. Recently, Manke et al.<sup>108</sup> employed synchrotron X-ray radiography to investigate water evolution and transport in the through-plane direction of an operating PEFC. A spatial resolution as high as  $3\text{-}7\ \mu\text{m}$  was reported with a temporal resolution of about  $4.8\ \text{s}$ ,  $1\ \text{s}$  for exposure and  $3.8\ \text{s}$  for data readout. Quantitative measurements of liquid water content were present. According to the quantitative analysis and observations of water evolution, the authors proposed a new model for water transport in GDLs combining the continuous capillary-tree-like model<sup>68</sup> and eruptive transport mechanism<sup>119</sup>. Hartnig et al.<sup>12, 110</sup> from the same group also used this synchrotron X-ray facility to study water content distribution along the cross-sectional direction, as well as dynamics of primary water clusters transport through the GDL. Liquid Water distribution in the respective component of an operating PEM fuel cell was quantitatively visualized under a series of operating current densities varying from low to high. Their experimental results showed that under low current densities ( $<420\text{mA cm}^{-2}$ ) liquid water trended to flood the cathode side. With increasing the current density, more and more liquid water emerged in both anode and cathode sides, mainly accumulating near the channel ribs and near MPL-GDL and MPL-CL interfaces. This indicates that some gaps and cracks may be present at both interfaces, which have the potential to store considerable liquid water. The authors also presented transient water behaviors inside the cell at a relatively large time scale (i.e. several minutes), while changing the current density from one value to another immediately. A compact cluster flow in the GDL and eruptive mechanism from the GDL to GCs were proposed to explain the pore-scale liquid water transport.

Synchrotron X-ray, owing to its high energy density, is capable of achieving high spatial resolution and acceptable temporal resolution, which can ensure insightful experimental results regarding to water distribution and transport in an operating PEFC. However, the scarcity of X-ray apparatus limits its wide applications in PEFCs. In addition, during beam exposure<sup>122</sup>, severe

degradation of cell performance can occur in a few minutes due to the change of material properties. This maybe question the possibility of using X-ray to illustrate the water transport mechanisms in PEFCs. Another issue we need to care about is the temporal resolution of X-ray technique. In contrast to optical observations, X-ray visualization can only present a time-averaged water transport within fuel cells, failing to shed light on the transient dynamics of liquid water with a high temporal resolution.

### 2.4.3 Neutron radiography

Since neutrons are strongly attenuated by water relative to PEFC materials, this technique is ideally suited to interrogate an operating PEFC for liquid water transport. Over the past decade, neutron technique has been extensively employed to study water management issue in PEFCs, including GDL flooding, membrane dehydration, and ice formation during subfreezing operations. Recently, Mukundan and Borup<sup>112</sup> gave a detailed review of visualizing liquid water in PEFCs by means of neutron imaging. In what following, some important results obtained from neutron experiments regarding water management in PEFC are briefly reviewed. Compared to the synchrotron X-ray reviewed above, in general neutron imaging has lower spatial and temporal resolutions limited by low neutron fluence rates. However, high-resolution neutron imaging was made possible recently with the advent of neutron-sensitive micro-channel plates (MCP). Trabold et al.<sup>114</sup> visualized water content in GCs of an operating PEFC in the through-plane direction, and a masking method was used to isolate gas channels from other constituents. Krama et al.<sup>113</sup> also employed neutron imaging to investigate the water accumulation in GCs. In addition, the water content in the GDL only underneath the land was quantitatively visualized in spite of less accuracy. Bellows et al.<sup>116</sup> used neutron imaging to measure water gradient profiles in the Nafion of an operating PEFC. Satija et al.<sup>115</sup> reported a relatively high temporal resolution (1 s) of neutron radiography with a low spatial resolution of about 100  $\mu\text{m}$ . They visualized water content distribution in the through-plane direction varying with the operating time, and the masking technique was adopted to isolate the flow fields. Most recently, Hickner et al.<sup>13</sup> reported a relatively high spatial resolution of neutron radiography up to 16.4  $\mu\text{m} \times 16.4 \mu\text{m}$  at the cost of extremely low temporal resolution, which enabled quantitative observations of water content distribution through the cross-section of an operating PEFC. The authors found that the water content within MEA kept more or less constant over the range of current densities from 0.25 to 1.00  $\text{A cm}^{-2}$ . The water content was minimal at the low current densities below 0.25  $\text{A cm}^{-2}$  because of little water production. However, when the current densities exceeded 1.00  $\text{A cm}^{-2}$ , the water content reduced again due to the enhanced heat generation and water evaporation. It is evident that water and heat managements in PEFCs are closely coupled together. In addition, they also investigated the effects of cell temperature and gas feed rate on the water content in an operating PEFC.

To sum up, in this section we provide a quick review of recent achievements in experimental visualization of liquid water transport in PEFCs, such as newly proposed liquid water transport models in the GDL, water content distribution under different operating conditions, as well as liquid water dynamics in GCs. As a matter of face, spatial and temporal resolutions are two most important factors determining the quality of obtained results for in situ non-destructive imaging techniques, such as X-ray, neutron technique, and MRI. Normally, one high resolution is based on the low resolution of the other one. For optical technique, although it provides excellent

temporal and spatial resolutions simultaneously, it involves modified material to assist in optical observations; what is more, this technique is incapable of visualizing liquid water content within the MEA. Despite some disadvantages, experimental studies regarding liquid water flooding issue in PEFCs can offer guidelines and validations for analytical and numerical models of multiphase multi-component transport processes. So, we believe that in the future experimental investigations (e.g. liquid water visualization) will continue to play an important role in the development of PEFCs.

## 2.5 Summary

In this chapter, two-phase flow (i.e. immiscible gas mixture and liquid water) in PEFCs has been reviewed based on an extensive literature survey. We mainly focus on the review of modeling two-phase flow in PEFCs, including two-phase flow in GCs and two-phase flow in diffusion layers. In addition, we address the importance of treating interfaces between different components of a PEFC when modeling liquid water transfer. At last, we give a quick review of experimental visualization of water distribution and transport inside an operating PEFC for completeness. We also note that experimental studies could continue to play an important role in not only illustrating realistic water transport mechanisms in PEFCs, but also validating numerical models.

Two-phase flow in GCs, as a significant part of water management in PEFCs, has been receiving more and more attention. However, compared to extensive experimental observations of liquid water dynamics in transparent GCs, more efforts are still needed to develop a comprehensive macro channel flooding model, which is computationally effective and can be applied to a large scale.

Most of macroscopic models for two-phase flow in PEFC are based on the well-known two-phase Darcy's law. They have been widely employed to investigate two-phase flow in PEFCs as well as optimize cell operating conditions due to their computational effectiveness. However, macroscopic models failed to provide insights into the fundamental mechanisms of liquid water transport in PEFCs, since they did not take into account the pore morphology of diffusion layers. Recently, several pore-scale models were employed to mimic liquid water transport through a fibrous GDL, like PN models and LBM. In PN modeling, one critical consideration lies in whether we can represent the fibrous pore structure of a GDL by a network of pore bodies and throats. In addition, PN models are incapable of capturing the interactive liquid water transport through the GDL-GC interface. LB models can resolve liquid water dynamics in the realistic pore structure of a GDL. However, to reduce computational efforts and stabilize calculations, both arbitrary water density and viscosity were used in previous numerical studies, which may impact interpretations of obtained numerical results. Therefore, additional efforts are still needed to make pore-scale modeling more reliable and comprehensive.

Several interfaces are also involved in the modeling of two-phase flow in PEFCs, like GDL-GC and CL-GDL. Strong dynamic interactions occur at the GDL-GC interface during liquid water transport. A proper treatment of GDL-GC interface is critical to the reliable prediction of a PEFC model. Neglecting this interfacial coverage effect would lead to underestimating the flooding level in diffusion layers. What's more, recent experimental studies showed that gaps and cracks

present at the CL-MPL interface, which have the potential to trap considerable liquid water. As a consequence, it can result in additional resistance for liquid water transfer in the through-plane direction, which should be included in further numerical studies.

## References

- [1] H. Li, Y.H. Tang, Z.W. Wang, *J. Power Sources* 178 (2008) 103-117.
- [2] N. Demirdöven, J. Deutch, *Science* 305 (2004) 974-976.
- [3] M.M. Mench, *Fuel Cell Engines*, John Wiley & Sons, 2008.
- [4] C.Y. Wang, *Chem. Rev.* 104 (2004) 4727–4765.
- [5] G. Hoogers, *Fuel Cell Technology Handbook*, CRC Press, 2003.
- [6] G. Wu, K.L. More, C.M. Johnston, P. Zelenay, *Science* 332 (2011) 443-447.
- [7] C.Z. Qin, D. Rensink, S. Fell, S.M. Hassanizadeh, *J. Power Sources* 197 (2012) 136-144.
- [8] S. Basu, J. Li, C.Y. Wang, *J. Power Sources* 187 (2009) 431-443.
- [9] X.G. Yang, F.Y. Zhang, A.L. Lubawy, C.Y. Wang, *Solid-State Lett.* 7 (2004) A408-A411.
- [10] S. Ge, C.Y. Wang, *J. Electrochem. Soc.* 154 (2007) B998-B1005.
- [11] D. Spornjak, A.K. Prasad, S.G. Advani, *J. Power Sources* 170 (2007) 334-344.
- [12] C. Hartnig, I. Manke, R. Kuhn, N. Kardjilov, J. Banhart, W. Lehnert, *Appl. Phys. Lett.* 92 (2008) 134106.
- [13] M.A. Hickner, N.P. Siegel, K.S. Chen, D.S. Hussey, D.L. Jacobson, M. Arif, *J. Electrochem. Soc.* 155 (2008) B427-B434.
- [14] I.S. Hussaini, C.Y. Wang, *J. Power Sources* 187 (2009) 444-451.
- [15] D. Song, Q. Wang, Z. Liu, T. Navessin, M. Eikerling, S. Holdcroft, *J. Power Sources* 126 (2004) 104-111.
- [16] Z. Qi, A. Kaufman, *J. Power Sources* 113 (2003) 37-43.
- [17] S. Zhang, X.Z. Yuan, J. Hin, H. Wang, K.A. Friedrich, M. Schulze, *J. Power Sources* 194 (2009) 588-600.
- [18] L. Cindrella, A.M. Kannan, J.F. Lin, K. Saminathan, Y. Ho, C.W. Lin et al., *J. Power Sources* 194 (2009) 146-160.
- [19] J.S. Yi, T.V. Nguyen, *J. Electrochem. Soc.*, 146 (1999) 38-45.
- [20] A. Theodorakakos, T. Ous, M. Gavaises, J.M. Nouri, N. Nikolopoulos, H. Yanagihara, *J. Colloid Interface Sci.* 300 (2006) 673-687.
- [21] T. Waclawczyk, T. Koronowicz, *J. Theor. App. Mech.* 46 (2008) 325-345.
- [22] X. Zhu, Q. Liao, P.C. Sui, N. Djilali, *J. Power Sources* 195 (2010) 801-812.
- [23] X. Zhu, P.C. Sui, N. Djilali, *J. Power Sources* 172 (2007) 287-295.
- [24] X. Zhu, P.C. Sui, N. Djilali, *J. Power Sources* 181 (2008) 101-115.
- [25] Y.H. Cai, J. Hu, H.P. Ma, B.L. Yi, H.M. Zhang, *J. Power Sources* 161 (2006) 843-848.
- [26] K. Jiao, B. Zhou, P. Quan, *J. Power Sources* 157 (2006) 226-243.
- [27] K. Jiao, B. Zhou, P. Quan, *J. Power Sources* 154 (2006) 124-137.
- [28] C.Z. Qin, D. Rensink, S.M. Hassanizadeh, S. Fell, *J. Electrochem. Soc.* 159 (2012) B1-B10.
- [29] L. Hao, P. Chen, *J. Power Sources* 190 (2009) 435-446.
- [30] J. Chio, G. Son, *J. Mech. Sci. Technol.* 22 (2008) 2590-2599.
- [31] E.C. Kumbur, K.V. Sharp, M.M. Mench, *J. Power Sources* 161 (2006) 333-345.

- [32] S. Basu, Channel Two-Phase Flow and Phase Change in Polymer Electrolyte Fuel Cells, PhD Thesis, The Pennsylvania State University (2008).
- [33] Y. Wang, S. Basu, C.Y. Wang, *J. Power Sources* 179 (2008) 603-617.
- [34] C.Z. Qin, D. Rensink, S.M. Hassanizadeh, S. Fell, submitted to *J. Electrochem. Soc.* (2012), under review.
- [35] C.Z. Qin, D. Rensink, S.M. Hassanizadeh, S. Fell, Preparation for submitting to *J. Electrochem. Soc.* (2012).
- [36] A.Z. Weber, J. Newman, *Chem. Rev.* 104 (2004) 4679-4726.
- [37] G.F. Pinder, W.G. Gray, *Essentials of Multiphase Flow and Transport in Porous Media*, John Wiley & Sons, 2008.
- [38] R. Lenormand, E. Touboul, C. Zarcone, *J. Fluid Mech.* 189 (1998) 165-187.
- [39] R. Lenormand, *J. Phys.: Condens. Matter* 2 (1990) SA79-SA88.
- [40] N. Djilali, *Energy* 32 (2007) 269-280.
- [41] S.M. Hassanizadeh, W.G. Gray, *Adv. Water Resour.* 13 (1990) 169-186.
- [42] S.M. Hassanizadeh, M.A. Celia, H.K. Dahle, *Vadose Zone J.* 1 (2002) 38-57.
- [43] Z.H. Wang, C.Y. Wang, K.S. Chen, *J. Power Sources* 94 (2001) 40-50.
- [44] Q. Ye, T.V. Nguyen, *J. Electrochem. Soc.* 154 (2007) B1242-B1251.
- [45] K.S. Udell, *Int. J. Heat Mass Transfer* 28 (1985) 485-495.
- [46] X. Wang, T.V. Nguyen, *J. Electrochem. Soc.* 155 (2008) B1085-B1092.
- [47] T.V. Nguyen, G. Lin, H. Ohn, X. Wang, *ECS Trans.* 3 (2006) 415-423.
- [48] T. Berning, N. Djilali, *J. Electrochem. Soc.* 150 (2003) A1589-A1598.
- [49] K. Jain, J.V. Cole, S. Kumar, A. Gidwani, N. Vaidya, *ECS Trans.* 16 (2008) 45-56.
- [50] D. Song, Q. Wang, Z.S. Liu, C. Huang, *J. Power Sources* 159 (2006) 928-942.
- [51] T. Berning, M. Odgaard, S.K. Kær, *J. Electrochem. Soc.* 156 (2009) B1301-B1311.
- [52] U. Pasaogullari, C.Y. Wang, *Electrochim. Acta* 49 (2004) 4359-4369.
- [53] S. Lister, N. Djilali, Chapter 5, *Transport Phenomenon in Fuel Cells*, WIT Press, 2005, 175-123.
- [54] D. Natarajan, T.V. Nguyen, *J. Electrochem. Soc.* 148 (2001) A1324-A1335.
- [55] G. Lin, T.V. Nguyen, *J. Electrochem. Soc.* 151 (2004) A1999-A2006.
- [56] G. Lin, T.V. Nguyen, *J. Electrochem. Soc.* 153 (2006) A372-A282.
- [57] X. Wang, T.V. Nguyen, *ECS Trans.* 16 (2008) 3-12.
- [58] H. Wu, *Mathematical Modeling of Transient Transport Phenomena in PEM Fuel Cells*, PhD Thesis, University of Waterloo (2009).
- [59] C.Z. Qin, D. Rensink, S.M. Hassanizadeh, S. Fell, Preparation for submitting to *J. Power Sources* (2012).
- [60] Y. Wang, *J. Power Sources* 185 (2008) 261-271.
- [61] H. Ju, *J. Power Sources* 185 (2008) 55-62.
- [62] Y. Wang, C.Y. Wang, *J. Electrochem. Soc.* 153 (2006) A1193-A1200.
- [63] H. Ju, *J. Power Sources* 191 (2009) 259-268.
- [64] H. Meng, C.Y. Wang, *J. Electrochem. Soc.* 152 (2005) A1733-A1741.
- [65] H. Ju, G. Luo, C.Y. Wang, *J. Electrochem. Soc.* 154 (2007) B218-B228.
- [66] C.Y. Wang, *Electrochem. Solid-State Lett.* 12 (2009) S2-S3.
- [67] U. Pasaogullari, C.Y. Wang, K.S. Chen, *J. Electrochem. Soc.* 152 (2005) A1574-1582.
- [68] U. Pasaogullari, C.Y. Wang, *J. Electrochem. Soc.* 152 (2005) A380-A390.

- [69] C.Y. Wang, Handbook of Fuel Cells-Fundamentals, Technology and Applications, John Wiley & Sons, 2003, Volume 3, Part 3, 337-347.
- [70] S. Basu, Int. J. Hydrogen Energy 36 (2011) 9855-9863.
- [71] S. Basu, C.Y. Wang, K.S. Chen, Chem. Eng. Sci. 65 (2010) 6145-6154.
- [72] C.Y. Wang, P. Cheng, Int. J. Heat Mass Transfer 39 (1996) 3607-3618.
- [73] Y. Wang, C.Y. Wang, J. Electrochem. Soc. 154 (2007) B636-B643.
- [74] S. Basu, C.Y. Wang, K.S. Chen, J. Electrochem. Soc. 156 (2009) B748-B756.
- [75] M. Piri, M.J. Blunt, Phys. Rev. E 71 (2005) 026301.
- [76] P.K. Sinha, P.P. Mukherjee, C.Y. Wang, J. Mater. Chem. 17 (2007) 3089-3103.
- [77] P.K. Sinha, C.Y. Wang, Electrochim. Acta 52 (2007) 7936-7945.
- [78] I. Patt, Trans. AIME 207 (1956) 144.
- [79] I. Patt, Trans. AIME 207 (1956) 160.
- [80] I. Patt, Trans. AIME 207 (1956) 164.
- [81] M.J. Blunt, M.D. Jackson, M. Piri, P.H. Valvatne, Adv. Water Resour. 25 (2002) 1069-1089.
- [82] P.K. Sinha, C.Y. Wang, Chem. Eng. Sci. 63 (2008) 1081-1091.
- [83] T. Koido, T. Furusawa, K. Moriyama, J. Power Sources 175 (2008) 127-136.
- [84] J.T. Gostick, M.A. Ioannidis, M.K. Fowler, M.D. Pritzker, J. Power Sources 173 (2007) 277-290.
- [85] K.J. Lee, J.H. Nam, C.J. Kim, Electrochim. Acta 54 (2009) 1166-1176.
- [86] M. Rebai, M. Prat, J. Power Sources 192 (2009) 534-543.
- [87] G. Luo, Y. Ji, C. Y. Wang and P. K. Sinha, Electrochim. Acta 55 (2010) 5332-5341.
- [88] Y. Tabe, Y. Lee, T. Chikahisa, M. Kozakai, J. Power Sources 193 (2009) 24-31.
- [89] J. Park, X. Li, ECS Trans. 12 (2008) 81-92.
- [90] S.P. Dawson, S. Chen, G.D. Doolen, J. Chem. Phys. 98 (1993) 1514-1523.
- [91] X. He, N. Li, Comput. Phys. Commun. 129 (2000) 129-158.
- [92] J. Park, K.Y. Huh, X. Li, J. Electroanal. Chem. 591 (2006) 141-148.
- [93] C. Pan, M. Hilpert, C.T. Miller, Water Resour. Res. 40 (2004) W01501.
- [94] S. Mukherjee, J.V. Cole, K. Jain, A. Gidwani, ESC Trans. 16 (2008) 67-77.
- [95] X.D. Niu, T. Munekata, S.A. Hyodo, K. Suga, J. Power Sources 172 (2007) 542-552.
- [96] X. Shan, G.D. Doolen, Phys. Rev. E 54 (1993) 3614.
- [97] K. Schladitz, S. Peters, D. Reinel-Bitzer, A. Wiegmann, J. Ohser, Comput. Mater. Sci. 38 (2006) 56-66.
- [98] Y. Wang, S. Cho, R. Thiedmann, V. Schmidt, W. Lehnert, X. Feng, Int. J. Heat Mass Transfer 53 (2010) 1128-1138.
- [99] R. Thiedmann, F. Fleischer, C. Hartnig, W. Lehnert, V. Schmidt, J. Electrochem. Soc. 155 (2008) B391-B399.
- [100] D. Rensink, J. Roth, S. Fell, Liquid water transport and distribution in fibrous porous media and gas channels, Proc. 6th Int. ASME Conf. On Nanochannels, Microchannels and Minichannels (2008), ICNMM2008-62087.
- [101] K. Kang, H. Ju, J. Power Sources 194 (2009) 763-773.
- [102] F.E. Hızir, S.O. Ural, E.C. Kumbur, M.M. Mench, J. Power Sources 195 (2010) 3463-3471.
- [103] H. Meng, C.Y. Wang, J. Electrochem. Soc. 152 (2005) A1733-A1741.
- [104] V. Gurau, T.A. Zawodzinski, J.A. Mann, J. Fuel Cell Sci. Technol. 5 (2008) 021009.
- [105] A.Z. Weber, J. Newman, J. Electrochem. Soc. 152 (2005) A667-A688.

- [106] K.H. Wong, K.H. Loo, Y.M. Lai, S.C. Tan, C.K. Tse, *Int. J. Hydrogen Energy* 36 (2011) 3941-3955.
- [107] F.Y. Zhang, X.G. Yang, C.Y. Wang, *J. Electrochem. Soc.* 153 (2006) A225-A232.
- [108] I. Manke, C. Hartnig, M. Grünerbel, W. Lehnert, N. Kardjilov, A. Haibel et al., *Appl. Phys. Lett.* 90 (2007) 174105.
- [109] S.J. Lee, N.Y. Lim, S. Kim, G.G. Park, C.S. Kim, *J. Power Sources* 185 (2008) 867-870.
- [110] C. Hartnig, I. Manke, R. Kuhn, S. Kleinau, J. Goebbels, J. Banhart, *J. Power Sources* 188 (2009) 468-474.
- [111] P.K. Sinha, P. Halleck, C.Y. Wang, *Electrochem. Solid-State Lett.* 9 (2006) A344-A348.
- [112] R. Mukundan, R.L. Borup, *Fuel Cells* 5 (2009) 499-505.
- [113] D. Kramer, J. Zhang, R. Shimoi, E. Lehmann, A. Wokaun, K. Shinohara et al., *Electrochim. Acta* 50 (2005) 2603-2614.
- [114] T.A. Trabold, J.P. Owejan, D.L. Jacobson, M. Arif, P.R. Huffman, *Int. J. Heat Mass Transfer* 49 (2006) 4712-4720.
- [115] R. Satija, D.L. Jacobson, M. Arif, S.A. Werner, *J. Power Sources* 129 (2004) 238-245.
- [116] R.J. Bellows, M.Y. Lin, M. Arif, A.K. Thompson, D. Jacobson, *J. Electrochem. Soc.* 146 (1999) 1099-1103.
- [117] A. Bazylak, *Int. J. Hydrogen Energy* 34 (2009) 3845-3857.
- [118] N. Akhtar, A. Qureshi, J. Scholta, C. Hartnig, M. Messerschmidt, W. Lehnert, *Int. J. Hydrogen Energy* 34 (2009) 3104-3111.
- [119] S. Lister, D. Sinton, N. Djilali, *J. Power Sources* 154 (2007) 95-105.
- [120] A. Bazylak, D. Sinton, N. Djilali, *J. Power Sources* 176 (2008) 240-246.
- [121] A. Bazylak, *Liquid Water Transport in Fuel Cell Gas Diffusion Layer*, PhD thesis, University of Victoria (2008).
- [122] A. Schneider, C. Wieser, J. Roth, L. Helfen, *J. Power Sources* 195 (2010) 6349-6355.
- [123] I.S. Hussaini, C.Y. Wang, *J. Power Sources* 195 (2010) 3830-3840.

# Chapter 3 - Pore-scale simulation of the cathode gas diffusion layer of a polymer electrolyte fuel cell

---

## Abstract

*The intrinsic permeability of gas diffusion layer (GDL) serves as one of the critical material properties in macroscopic modeling of polymer electrolyte fuel cells (PEFCs). In this work, we reconstruct a carbon-paper GDL numerically by means of stochastic method. Its fibrous structure is represented by real geometries. Navier-Stokes (N-S) equations are solved to calculate the in-plane and through-plane permeability of the GDL. The obtained permeability matches well with existing numerical and experimental results in literature. The in-plane permeability shows a higher value than the through-plane one. The anisotropic factor of permeability for the carbon-paper GDL is found to be about 1.5. We have also conducted pore-scale simulations of reactants transport inside a cathode GDL. The area-averaged flow velocities at the GC-GDL interface for two different GC inlet velocities are calculated. Our results show that the three-dimensional fibrous structure of carbon-paper GDL does not invoke large local variations of species distributions. As to the slip phenomenon at the GC-GDL interface, the area-averaged x-component slip velocities along the flow direction have the highest values:  $8.199 \times 10^{-3}$  m/s, and  $1.606 \times 10^{-2}$  m/s for the 0.1 m/s and 0.2 m/s GC inlet velocities, respectively. It is found that this velocity is doubled when the GC inlet velocity is doubled. A similar trend is observed for the area-averaged y-component slip velocities, although they are very small. Regarding the z-component velocities, their magnitudes are mainly affected by the mass flow from the CL to the GC, and insensitive to the GC inlet velocity.*

## 3.1 Introduction

Nowadays, polymer electrolyte fuel cells are capturing more and more attention due to their favorable properties, such as low/zero emission, high efficiency, quick start-up and power output, as well as low operating temperature. This type of fuel cell is regarded as one of the most promising alternative power sources in the future, which would be broadly employed in stationary, automotive, and portable applications<sup>1, 2</sup>. However, in order to be successfully commercialized, additional efforts are still in need to improve cell performance, durability and stability. Moreover, the cost has to be reduced considerably.

A typical PEFC unit, as shown in Fig.3-1, consists of four main components: PEM (Polymer Electrolyte Membrane), CL (Catalyst Layer), GDL (Gas Diffusion Layer) or PTL (Porous Transport Layer) and BP (Bipolar Plate), which contains the gas channel. The heart of a PEFC is the polymer

electrolyte membrane. We also can see it from the name of this kind of fuel cell. On each side of the membrane there is a porous electrode including CL and GDL. The GDL used in PEM fuel cells is typical of multi-layered and carbon-based porous material containing a macro porous layer (conventional GDL), and a micro porous layer (MPL). The conventional GDL (which is referred to as the GDL in the rest of this work) with a thickness of 150-400  $\mu\text{m}$ , is one of the crucial components of a PEFC. It has a profound impact on cell performance, as its main functions are: (1) delivering gaseous reactants from gas channel to reactive sites effectively; (2) discharging excessive liquid water from catalyst layer to gas channel under flooding situations<sup>3-5</sup> and keeping membrane from dehydration; (3) conducting electrons and heat with a low resistance. Additionally, it also provides mechanical support to the cell. For detail, one is referred to the review of gas diffusion layer for PEFCs<sup>6</sup>.

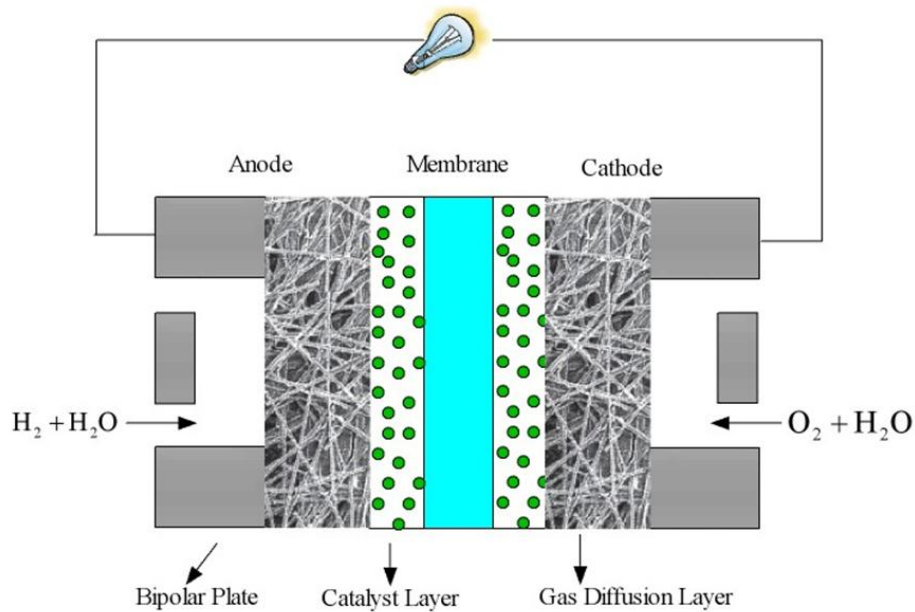


Figure 3-1: 2D schematic of a typical PEFC (consisting of four distinct components: polymer electrolyte membrane, catalyst layers on both sides of the membrane, gas diffusion layers adjacent to the catalyst layers, and bipolar plates with grooved gas channels).

Over the past two decades, numerical models<sup>7-17</sup> have played an important role in the development of PEFCs, ranging from simplified single-phase flow to more comprehensive multi-component multi-phase flow. Several physical transport mechanisms coexist inside the GDL of an operating PEFC, such as gaseous reactants transport, electrical and thermal conduction, and water-gas two-phase flow. Therefore, more and more attention has been paid to the accurate description of GDL numerically. Since detailed microstructure of GDL is usually unknown or hard to be established due to its complexity, modeling of transport processes at the pore scale is extremely difficult. As a result, species transport in the GDL is commonly modeled at the macroscopic scale, which is much greater than a pore diameter but much less than the simulation domain<sup>18</sup>. To the best of our knowledge, only a few researchers<sup>19, 20</sup> have conducted direct simulations of reactants transport or two-phase flow inside stochastically reconstructed GDL. In

the macroscopic modeling of GDL, Darcy's law or extended two-phase Darcy's law is employed to relate mass flux and the corresponding pressure gradient through determined macroscopic material properties, like intrinsic and relative permeability, porosity, as well as tortuosity. Feser et al.<sup>21</sup> measured the in-plane intrinsic permeability of GDL at different levels of compression, and concluded that woven and non-woven samples had significantly higher in-plane permeability compared to the carbon fiber paper (i.e. TGP-60-H) at similar solid volume fractions. Gostick et al.<sup>22</sup> measured in-plane and through-plane gas permeability of several common GDLs used in PEFCs. They reported that most materials had higher in-plane permeability than through-plane permeability, the permeability in the two-perpendicular in-plane directions was also found to show significant anisotropy. In addition to experimental measurements, Hao<sup>23</sup> and Schulz<sup>19</sup> reconstructed nonwoven carbon paper GDL using a stochastic generation method<sup>24</sup>, and calculated the in-plane and through-plane permeability by employing Lattice Boltzmann Method (LBM). Jaganathan et al.<sup>25</sup> converted the experimental structure data of fibrous porous media into computational tetrahedral cells, and used commercial solver FLUENT to calculate its permeability based on Navier-Stokes (N-S) equations.

Even though macroscopic modeling has been widely utilized in PEFC studies, it ignores local variations of variables of interest in a representative elementary volume (REV)<sup>18</sup>. Furthermore, whether the REV concept is applicable to the GDL is still unclear due to its small thickness along the through-plane direction. Wang et al.<sup>20</sup> conducted direct numerical simulation of species, electron and heat transport inside the GDL. However, the authors did not take into account the gas flow filed delivering reactants into reactive sites via GDL, and only assumed uniform reactant concentrations at the upper surface of GDL and no slip velocity at the interface between GDL and GC.

In this chapter, we use stochastic method to generate the pore-structure of a carbon-paper GDL. Instead of voxel-based geometry, we represent the reconstructed GDL so that its exact geometric information is kept. However, we need to generate unstructured computational mesh additionally. Based on the generated GDL, we calculate the in-plane and through-plane permeability. Moreover, the pore-scale reactive species (i.e. water vapor and oxygen) transport inside the GDL is simulated and discussed. The slip phenomenon at the GC-GDL interface is also addressed.

## 3.2 Gas diffusion layer generation

Detailed geometry of the GDL is required to conduct pore-scale simulations. For the time being, two approaches are popular for obtaining the pore structure of porous media of interest. They are noninvasive experimental techniques such as X-ray and magnetic resonance computed tomography, and numerical reconstructions with aid of high-performance digital computers<sup>26</sup>. Fig. 3-2 shows the microscopic images of carbon-paper GDL used in PEFCs. The long fibers with nearly uniform diameter are randomly oriented more or less in the in-plane directions, which are connected by resin binder. This special feature leads carbon-paper GDL to hold highly anisotropic transport properties, like anisotropic permeability, electrical and thermal conductivities along the in-plane and through-plane directions<sup>27, 28</sup>. Taking this special structure into account, carbon-paper GDL can be generated by means of stochastic method in the absence of experimental data. Since reconstruction of the exact GDL is still difficult, our generation in this work is based on the

following assumptions: (1) fibers are assumed to be long enough to cross the whole block under the study; (2) fibers are mainly aligned in the in-plane directions with a controllable small orientation in the through-plane direction; (3) fibers are represented by cylinders all with the same uniform diameter; (4) fibers are allowed to overlap, and binder and PTFE (a hydrophobic polymer added into the GDL to increase its hydrophobicity) are not taken into account.

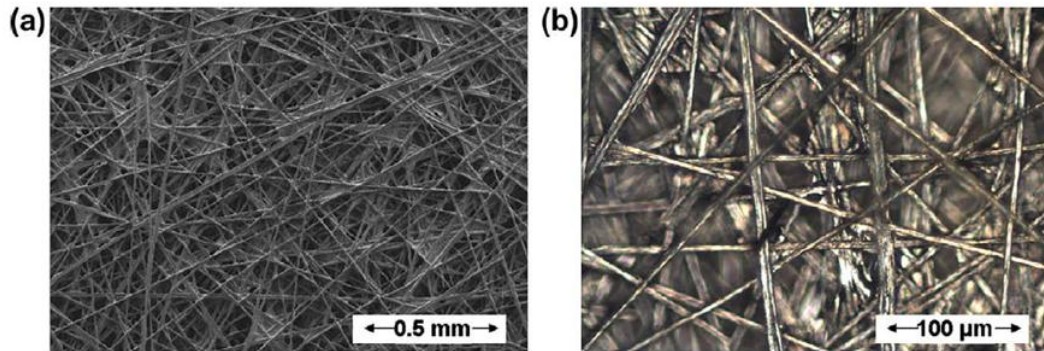


Figure 3-2: Microscopic images of Carbon paper GDL used in PEFCs [20].

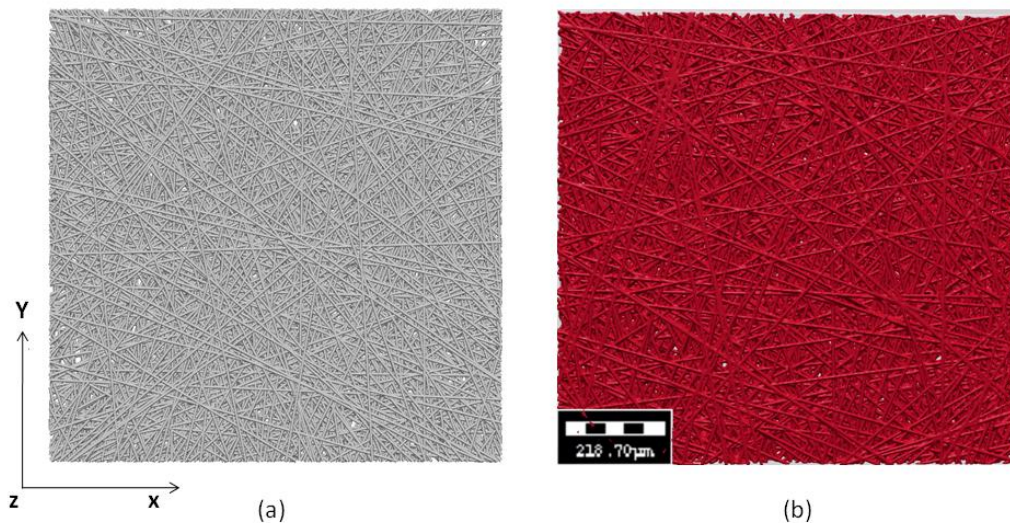


Figure 3-3: Virtually created GDL with dimensions of  $1\text{mm}\times 1\text{mm}\times 0.15\text{mm}$  along  $x$ ,  $y$  and  $z$  directions (note  $x$ ,  $y$  are in-plane directions, while  $z$  is the through-plane direction) respectively, and input parameters are: porosity 0.82, fiber diameter  $7\ \mu\text{m}$ , through-plane orientation zero degree: (a) generated in this work, (b) generated by Geodict.

In this work three parameters are needed to numerically construct a carbon-paper GDL, namely, porosity, fiber diameter, and fiber orientation in the through-plane direction. Fig. 3-3a displays a virtually-created GDL with dimensions of  $1\text{mm}\times 1\text{mm}\times 0.15\text{mm}$  along  $x$ ,  $y$  and  $z$  directions, respectively. Three input parameters are porosity of 0.82, fiber diameter of  $7\ \mu\text{m}$ , and zero through-plane orientation. Note that Fig. 3-3b shows the carbon-paper GDL generated by

commercial software Geodict<sup>28</sup>, which is very similar to the one in Fig. 3-3a. One distinctive feature of the GDL generated in this work is that all fibers are represented by real geometries rather than voxel approximations (as done by Geodict). Consequently, high-resolution of the pore structure of GDL is kept, even if the generation of computational mesh based on this complex geometry is not easy.

### 3.3 Numerical method

#### 3.3.1 Governing equations

The computational domain in the present study consists of three parts: GC, virtually created carbon-paper GDL, and CL assumed to be a two-dimensional interface, as shown in Fig. 3-4a. First, a large GDL block (see Fig. 3-3a) with dimensions of 1mm×1mm×0.15mm along x, y and z directions is generated. Note that, x and y are the in-plane directions and z is the through-plane direction. From this block, we cut off a smaller GDL with dimensions of 1mm×0.1mm×0.15mm along x, y and z directions, to be used in our pore-scale simulations. Here, one may argue that the y direction (0.1mm) does not satisfy the REV size requirement. However, as a first attempt, our focus is on the species transport along the GC. We have to reduce computational efforts to make pore-scale simulations feasible.

To keep the membrane well hydrated, in practice humidified air stream is delivered into the flow field on the cathode side, and then diffuses through the GDL into the cathode CL, where it combines with protons from the electrolyte and electrons from the external circuit to form water and heat, as expressed by Eq. (3-1):



When excessive liquid water accumulates in the cathode CL, it would penetrate into the cathode GDL under capillary action from high saturation to low saturation, and finally removed out of the GC by gas drag force. In fact, up to now the questions how the liquid water is formed in the CL and how it transports inside the GDL are still unclear. Both experimental observations and two-phase numerical modeling<sup>29, 30</sup> are contributing to this field. However, in this work, we concentrate on the single-phase multi-component transport inside the virtually-created GDL for simplicity.

In the GC and the void space of GDL, the steady-state N-S equations are used to describe gas flow:

$$\nabla \cdot (\rho \bar{u}) = 0 \quad (3-2)$$

$$\nabla \cdot (\rho \bar{u} \bar{u}) = -\nabla p + \nabla \cdot [\mu (\nabla \bar{u} + \nabla \bar{u}^T)] \quad (3-3)$$

Here,  $p$  is the pressure,  $\mu$  denotes the dynamic viscosity of gas mixture, which is assumed to be constant in this work for simplicity, and  $\rho$ , the density of gas mixture, is related to the species mass fractions according to ideal mixture gas law:

$$\rho = \frac{P}{RT \sum_i \frac{C_i}{M_i}} \quad (3-4)$$

In addition to the mass and momentum conservations, we also need species transport equations. Normally, in PEFCs used in automotive applications we have water vapor, oxygen, and nitrogen gaseous species at the cathode side. The steady-state gaseous species transport equation can be expressed as:

$$\nabla \cdot (\rho C_i \bar{u}) = \nabla \cdot (\rho D_i \nabla C_i) + S_i \quad (3-5)$$

Here, the subscript  $i$  represents each reactive species, water vapor or oxygen. Since the summation of mass fractions of the three species in the gas mixture equals to unity, nitrogen is regarded as an inert component, which is not necessary to be modeled.  $S_i$  is the species source term, which is zero in this work due to the assumed CL interface,  $D_i$  is the species diffusivity in the gas mixture, which can be calculated based on the following empirical expressions<sup>12</sup>:

$$D_{H_2O} = 0.2982 \times 10^{-4} (T/333)^{1.75} (101325/p) \quad (3-6)$$

$$D_{O_2} = 0.2652 \times 10^{-4} (T/333)^{1.75} (101325/p) \quad (3-7)$$

Note that in macroscopic modeling of species diffusion in porous media, Bruggeman correlation<sup>31</sup> is normally employed to account for the effect of pore structure on species diffusivity.

Due to the small temperature variation in an operating PEFC<sup>32</sup> and the membrane is excluded in this study, we assume isothermal conditions. Energy equation is not included. In what follows, we describe the imposed boundary conditions and numerical implementation including the mesh issue.

### 3.3.2 Boundary conditions

At the GC inlet (see Fig. 3-4a), the gas mixture is fed into the fuel cell at a constant flow rate. Thus, a uniform gas velocity normal to the boundary and mass fractions of species are specified as follows:

$$C_{O_2} = C_{O_2}^{in} \quad C_{H_2O} = C_{H_2O}^{in} \quad \mathbf{u} = \mathbf{u}^{in} \quad (3-8)$$

At the GC outlet, zero gauge pressure is specified. Note that in this study, the operating pressure is set to be 1 bar.

As stated earlier, to reduce computational effort, the y direction of computational domain is only 0.1mm. Therefore, symmetrical boundary conditions are applied to the sidewalls of GC and GDL to minimize this dimensional effect.

Oxygen reduction reaction (ORR) (see Eq. (3-1)) takes place at the triple-phase boundary in the cathode CL, which can be described by the well-known Butler-Volmer equation<sup>1</sup>:

$$j_c = \alpha i_0^{ref} \left\{ \exp\left[\frac{a_a F \eta}{RT}\right] - \exp\left[\frac{a_c F \eta}{RT}\right] \right\} \quad (3-9)$$

where  $\alpha$  is the cathode catalyst specific area,  $i_0^{ref}$  denotes the reference exchange current density at reference temperature and pressure, which is determined by the catalyst electrochemical kinetics, and  $a_a$  and  $a_c$  are the anodic and cathodic charge transfer coefficients, respectively. Because in this work the CL is assumed to be an interface, the simplified Tafel equation is employed to relate the current density and local oxygen concentration<sup>33</sup>:

$$j_c = \alpha i_0^{ref} \frac{C_{O_2}}{Y_{O_2,ref}} \frac{\rho}{M_{O_2}} \exp\left(\frac{4a_c F}{RT} \eta\right) \quad (3-10)$$

in which,  $C_{O_2}$  is the mass fraction of oxygen,  $M_{O_2}$  is the molecule weight of oxygen,  $Y_{O_2,ref}$  represents the reference oxygen molar concentration, and  $\eta$  is the cathode over-potential as a setting parameter. At this interface, oxygen is consumed. According to Eq. (3-1) and Faraday's law, its flux normal to the GDL-CL interface can be expressed as:

$$n_{O_2}|_{CL} = -\frac{j_c}{4F} M_{O_2} \quad (3-11)$$

Water vapor is introduced into the cathode electrode by water production and electro-osmotic drag (EOD), which are both proportional to the current density. In the absence of the membrane, a parameter called the net water transport coefficient is used to take into account the combined effects of EOD and water back diffusion. So, the water vapor flux normal to the interface can be written as:

$$n_{H_2O}|_{CL} = \frac{j_c(1 + 2a_{net})}{2F} M_{H_2O} \quad (3-12)$$

Finally, all other boundaries are assumed to be no-slip impermeable walls.

### 3.3.3 Numerical implementation

Several types of unstructured cells can be used to mesh this complicated geometry, as shown in Fig. 3-4a or Fig. 3-5. Here, the polyhedral mesh is generated through the commercially available software STAR-CCM+<sup>34</sup>. Our study shows that it is extremely difficult to obtain a completely mesh-independent solution for this complex fibrous structure. Nonetheless, literature study<sup>20, 23</sup> shows that the mesh resolution of 1.5  $\mu\text{m}$  is a reasonable choice for meeting requirements of computational efficiency and accuracy. Fig. 3-4b displays the generated polyhedral mesh with local refinements, including about 5 million polyhedral cells with a few tetrahedral ones. The governing equations (3-2)-(3-5) together with the applied boundary conditions are discretized by finite volume method with second-order schemes<sup>35</sup>. The SIMPLE (semi-implicit method for pressure-linked equations) algorithm is utilized to couple pressure and

velocity. The algebraic multi-grid (AMG) method, in conjunction with effective iteration scheme, is used to solve resultant nonlinear equations. In all numerical simulations presented in this work, the normalized residual values are less than  $10^{-6}$ .

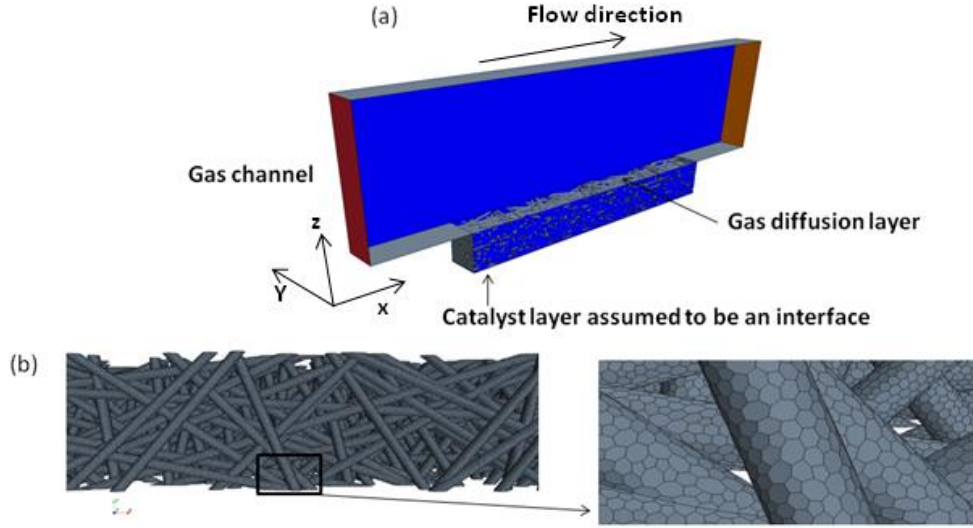


Figure 3-4: (a) the geometry used in pore-scale study, including GC, GDL and CL assumed to be an interface; (b) the corresponding mesh.

## 3.4 Results and discussion

### 3.4.1 Intrinsic permeability calculation

The well-known Darcy's law is always employed in the single-phase flow in porous media under low Reynolds numbers, which is given by (neglecting gravity effect):

$$\bar{q} = -\frac{\bar{k}}{\mu} \nabla p \quad (3-13)$$

in which,  $\bar{q}$  denotes the superficial velocity or Darcy's velocity,  $\mu$  is the dynamic viscosity of working fluid,  $\nabla p$  is the pressure gradient vector, and  $\bar{k}$  is called the intrinsic permeability tensor, expressed as:

$$\bar{k} = \begin{bmatrix} k_{xx} & k_{xy} & k_{xz} \\ k_{yx} & k_{yy} & k_{yz} \\ k_{zx} & k_{zy} & k_{zz} \end{bmatrix} \quad (3-14)$$

When the applied coordinate axes are aligned with the principle directions of flow, all the off-diagonal elements will be zero. In PEFCs, we always assume that two perpendicular in-plane

directions and through-plane direction are the principle directions of the carbon-paper GDL. Since the intrinsic permeability is a macroscopic material property in porous media, we should calculate this quantity for a selected REV to smooth out the local heterogeneities of GDL, such as the variation of porosity. Experimentally, it is much easier to use a big enough GDL for measuring its permeability. Therefore, we do not need to pay much attention to the REV concept. However, in numerical simulations, we should constrain the size of computational domain to save computational efforts. Schulz et al.<sup>19</sup> used LBM to confirm that the length along the in-plane direction should be larger than 0.38 mm to have representative domain of the essential geometric features of the carbon-paper GDL microstructure. However, Hao<sup>23</sup> and Wang<sup>20</sup> used much smaller domains to calculate the intrinsic permeability of GDL. In this work, we use a block with dimensions of 0.4mm×0.4mm×0.15mm along x, y and z directions, which is cut off from Fig. 3-3a. It is regarded to have the REV size for getting representative permeability. Fig. 3-5 displays the schematic of through-plane permeability calculation. It can be seen that two extensions on both sides of the GDL are used, where the velocity inlet boundary is imposed to stabilize the calculation. If we do not have extensions (i.e. uniform velocity profile is imposed on one side of the GDL), the calculated permeability would be underestimated dramatically. In the through-plane permeability calculation (see Fig. 3-5), we impose uniform inlet velocity of 0.002 m/s on one side and pressure on the outlet. Symmetric boundary conditions are applied to all the surrounding sides of computational domain. Since the flow is mainly in the through-plane direction and lateral flow can be negligible. No-slip wall boundary conditions are imposed on the fiber surfaces. Fig. 3-6 shows the pressure contours in the through-plane permeability calculation. Nearly uniform pressure distribution on each side of the GDL is obtained, which is consistent with the situation encountered in experimental measurements of permeability. For the in-plane permeability calculation, we have the same boundary settings expect for changing the flow direction to the in-plane one.

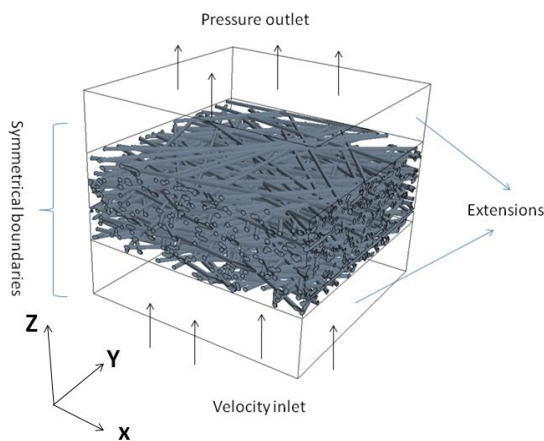


Figure 3-5: Schematic of through-plane permeability calculation including applied boundary conditions.

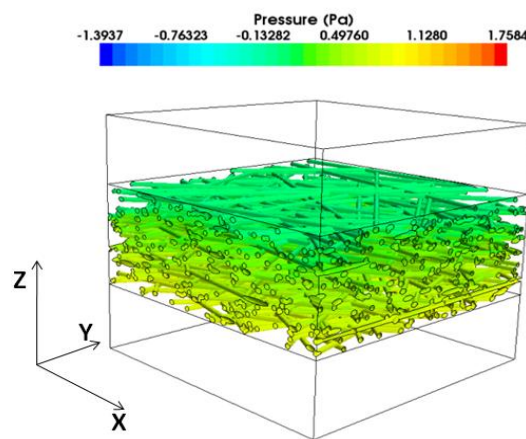


Figure 3-6: Pressure contours in the through-plane permeability calculation.

The famous Carman-Kozeny equation<sup>22</sup> can be employed to predict the permeability of fibrous porous media as a function of its porosity and fiber diameter, expressed as:

$$k = \frac{d_f^2 \varepsilon^3}{16k_{CK}(1-\varepsilon)^2} \quad (3-15)$$

Here,  $d_f$  is the fiber diameter,  $\varepsilon$  denotes the GDL porosity, and  $k_{CK}$  is the Carman-Kozeny constant depending on the type of porous media, which serves as a fitting parameter. Table 3-2 lists the permeability data obtained from literature and this work. In this work, the virtually-created GDL has the in-plane permeability of 9.84 Darcy (1 Darcy  $\approx 1.0 \times 10^{-12}$  m<sup>2</sup>) and through-plane permeability of 6.85 Darcy, which are of the same order as those given in Table 3-2. As indicated by the Carman-Kozeny equation, both fiber diameter and GDL porosity have impact on the obtained permeability. Therefore, we fit the Carman-Kozeny constant for the through-plane permeability to compare our data with the others listed in Table 3-2. It is seen that three numerical values from Navier-Stokes and LBM simulations are relatively close. The experimental measurement has the highest value of 7.53, which implies that numerical simulations overestimate the through-plane permeability of carbon-paper GDL. This can be explained by the fact that a real carbon-paper GDL contains lots of resin binder (see Fig. 3-2) for connecting fibers. The binder also contributes to the solid phase of GDL by a percentage of about 50% in terms of weight. However, in numerical simulations included in Table 3-2, just fibers are taken into account to reach the required GDL porosity. Therefore, we conclude that the GDL permeability can be overestimated without accounting for the binder effect.

From table 3-2, we also can see that the anisotropic factor for the in-plane and through-plane permeability of carbon-paper GDL from numerical calculations is close to 1.5. However, experimental measurement shows a much bigger anisotropic factor, up to 1.84. This discrepancy may be attributed to the binder effect as well. Without the consideration of binder, the anisotropic factor could be underestimated. Note that we find that the porosity of block 0.4mm×0.4mm×0.15mm (see Fig. 3-5) is 0.80 as shown in Table 3-2, even though the original GDL block (see Fig. 3-3) has a porosity of 0.82 (setting value). There is still a small variation of porosity by about 2.4%. However, we believe that this small variation of porosity does not detract our permeability calculation significantly.

Besides the Carman-Kozeny equation, a more complex model is developed by Tomadakis and Sotirchos (TS)<sup>37</sup>, which can be used to predict anisotropic permeability and evaluate numerical calculations. This model is based on the electric conduction principles to predict the permeability of randomly overlapping fiber structures:

$$\frac{k}{r^2} = \frac{\varepsilon}{8Ln^2\varepsilon(1-\varepsilon_p)^a \left[ (a+1)\varepsilon - \varepsilon_p \right]^2} (\varepsilon - \varepsilon_p)^{a+2} \quad (3-16)$$

in which,  $r$  is the fiber radius,  $\varepsilon$  is the porosity of fibrous porous media, and  $a$  and  $\varepsilon_p$  are constants determined by the orientation of fibers compared to the flow direction. The values of  $a$  and  $\varepsilon_p$  are given in Table 3-3 for different situations. The predicted values from TS model are 5.52 Darcy for the through-plane direction, and 8.38 Darcy for the in-plane direction. Compared to our simulation results, we can see that the TS model underestimates the permeability considerably. The deviation may be induced by boundary effect in permeability calculations. In

our numerical simulation, we used extensions to approximate the uniform pressure boundary conditions on both sides of the GDL. Note that the binder effect is also neglected in TS model.

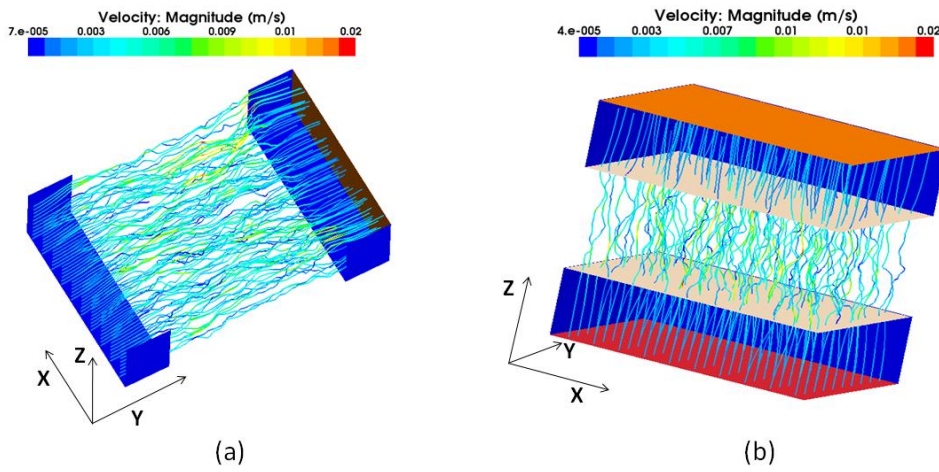


Figure 3-7: Streamline distributions: (a) along the in-plane direction; (b) along the through-plane direction.

Fig. 3-7 shows the tortuous streamlines along the through-plane and in-plane directions due to the complex structure of GDL. In macroscopic modeling, this characteristic is represented by the coefficient of tortuosity, which is reported to be a “transport-based” property<sup>20</sup>. It means that the value of tortuosity could be dependent on the variables of interest, such as pressure, temperature, and species concentration distributions. A simple way to obtain the approximate value of tortuosity is to calculate the ratio of the averaged length of the streamlines to the length of the domain of interest. Hao and Cheng<sup>23</sup> used this method to calculate the tortuosities as a function of porosity for the through-plane and in-plane directions, respectively. Their results showed that the tortuosities were nearly inversely proportional to the porosity, and the through-plane tortuosity had a slightly higher value than the in-plane one.

### 3.4.2 Pore-scale simulation

In this section, we discuss the results of pore-scale study of reactants transport in the cathode GDL. The operating parameters and geometric information are listed in Table 3-1. We consider two GC inlet velocities, namely 0.1 and 0.2 m/s, to study their effects on the species transport in the GDL and slip phenomenon at the GC-GDL interface.

Fig. 3-8 shows the velocity vector at the middle cross section of the GDL along the y direction at the GC inlet velocity of 0.1 m/s. According to Eq. (3-12), mass is added into the gas mixture in the cathode GDL under the assumption that the generated water is in water vapor form. So, the flow direction is towards the GC. However, it should be noted that if water is generated in liquid form (two-phase flow situation), the gas mixture flows towards the CL. From Fig. 3-8 it is seen that the gas mixture preferentially flows through big pore space, and the highest pore-scale velocity can reach about 0.01 m/s in the vicinity of the GC-GDL interface.

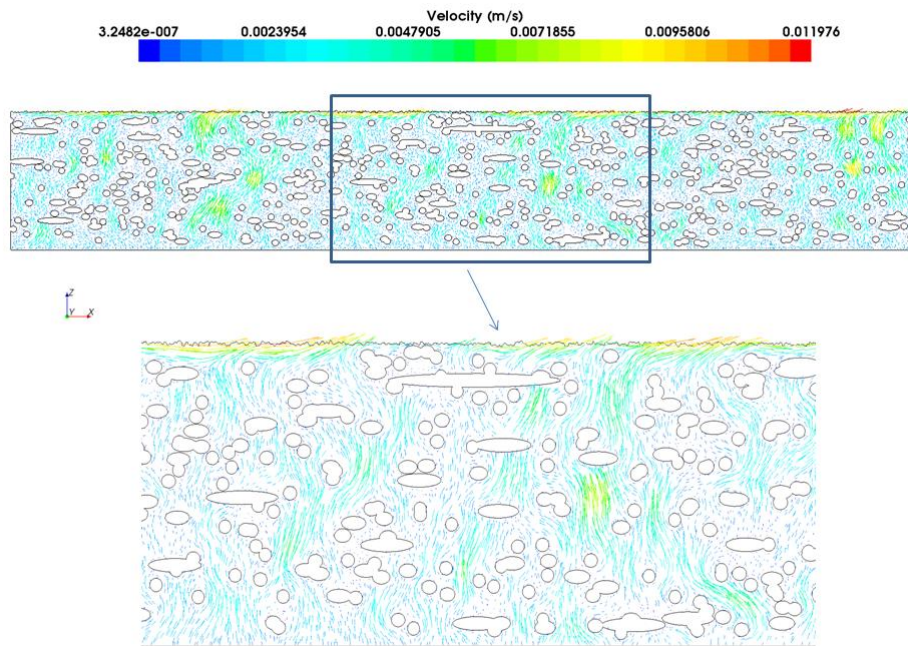


Figure 3-8: Velocity-vector field at the middle cross section ( $y=0.05$  mm) of the GDL at the GC inlet velocity of 0.1 m/s.

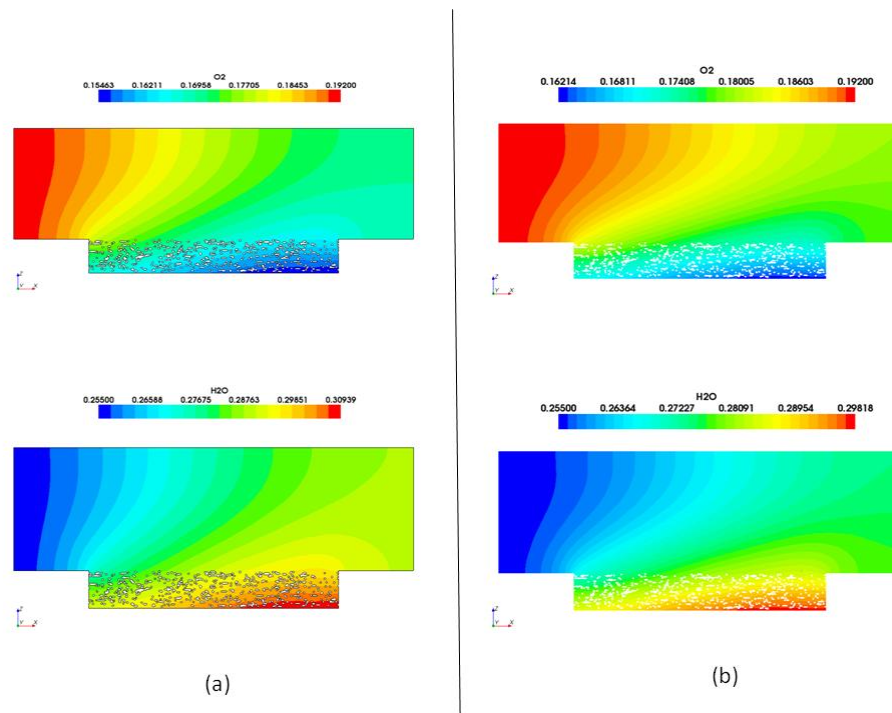


Figure 3-9: Mass fraction distributions of water vapor and oxygen at the middle cross section ( $y=0.05$  mm) of the GDL and GC at different GC inlet velocities: (a)  $v=0.1$  m/s; (b)  $v=0.2$  m/s.

Fig. 3-9 displays the mass fraction distributions of water vapor and oxygen at two different GC inlet velocities, namely 0.1 and 0.2 m/s. In fact, practically the gas inlet velocity at the cathode GC is determined by the applied stoichiometry based on the following expression:

$$\bar{u}_{in,c} \cdot \bar{n} = \frac{j_c A_m}{F} \frac{\xi_c}{4Y_{O_2} A_c} \quad (3-17)$$

where  $\xi_c$  is called the stoichiometric ratio,  $A_m$  is the reactive area of membrane,  $A_c$  denotes the cross-sectional area of cathode GC,  $Y_{O_2}$  is the inlet molar concentration of oxygen, and  $j_c$  the current density. In this work, we have a relatively small reactive area ( $10^{-7} \text{ m}^2$ ). So, small inlet velocities are employed to keep the stoichiometries in a reasonable range. As seen from Fig. 3-9, since more oxygen per unit time is introduced into reactive sites with the increase of GC inlet velocity, the lowest value of oxygen concentration at the right corner of the GDL is increased. In contrast, more water vapor is delivered out of the GC with enhanced convective transport. So, the highest value of water vapor mass fraction at the right corner of the GDL is decreased.

Fig. 3-10 shows the molar concentration distributions of oxygen at three different cross sections of the GDL along the y direction. Due to the random fibrous structure of GDL, we have three dissimilar cross sections in terms of geometric structure and pore-size distribution. Suppose we conduct species transport simulations based on these cross sections separately, considerable distinctions in species distributions among different cross sections can be expected. However, as shown in Fig. 3-10, only slight differences in molar concentration distributions of oxygen among these three cross sections are observed, which indicates that the carbon-paper GDL holds distinct three-dimensional structure, but this fibrous structure does not invoke large variations of species concentration distributions along the y direction. We note that results of two-dimensional pore-scale simulations of GDL should be interpreted with great care, as they could be misleading.

The molar concentration distributions of species at the bottom of GDL at two different inlet velocities are plotted in Fig. 3-11. As indicated in Fig. 3-9, more oxygen and less water vapor are expected at the bottom of GDL by increasing the GC inlet velocity. In macroscopic modeling of species transport, the oxygen molar concentration distribution at the GDL-CL interface (note that in this work this interface is represented by the bottom of GDL) is decreased along the positive-x direction. No variation could be observed along the y direction when symmetrical boundary conditions are imposed to the sidewalls of GC and GDL. In other words, a two-dimensional geometry can be used directly by macroscopic models. However, in our pore-scale simulations, we obtain some local variations of oxygen and water vapor molar concentrations at the GDL-CL interface. In particular, the local variations are relatively much stronger at the ending portion. Interestingly, the oxygen and water vapor molar concentrations show the almost same local variations, which are mainly caused by the fibrous structure of GDL. When the GC inlet velocity is increased to 0.2 m/s (see Fig. 3-11b), the local variations are a little changed, but the whole trend is similar.

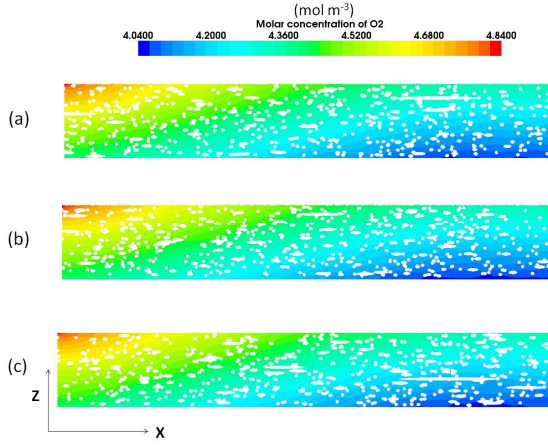


Figure 3-10: Molar concentration ( $\text{mol}/\text{m}^3$ ) distributions of oxygen at different cross sections of the GDL at the inlet GC velocity of 0.1 m/s: (a)  $y=0.0\text{mm}$ ; (b)  $y=0.05\text{mm}$ ; and (c)  $y=0.1\text{mm}$ .

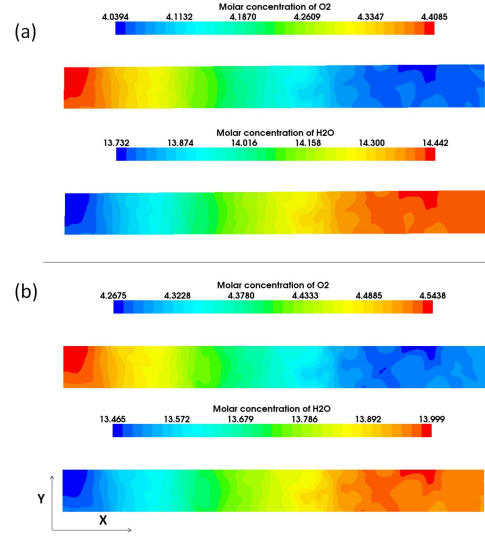


Figure 3-11: Molar concentration ( $\text{mol}/\text{m}^3$ ) distributions of species at the bottom of the GDL at different GC inlet velocities: (a)  $v=0.1\text{ m/s}$ ; (b)  $v=0.2\text{ m/s}$ .

Mass, momentum and heat transfers at the interface between a free fluid region and an adjacent porous medium play an important role in many applications<sup>38, 39</sup>. In the case of single-phase flow, macroscopically fluid flow in porous media is described by the Darcy's law, whereas N-S equations employed to describe the flow in a free fluid domain is of second order. This implies that additional interface conditions are needed for connecting the two domains mathematically. Up to date, it still has remained a challenge to derive appropriate interface conditions. Beavers and Joseph<sup>40</sup> were the first to introduce a jump condition for relating the derivative of the velocity in the free flow domain to the slip velocity at the interface:

$$\frac{du}{dy} = \frac{a}{\sqrt{k}}(u_s - u_d) \quad (3-18)$$

where  $u$  is the velocity in the direction tangential to the interface,  $y$  is normal to the interface,  $k$  is the intrinsic permeability of porous media,  $u_d$  is the Darcy velocity in the porous media,  $u_s$  is the slip velocity and  $a$  is a coefficient at the interface. However, in numerical simulations, the jump coefficient  $a$  should be determined in advance, which is considered as an intrinsic interfacial property. In numerical modeling of PEFCs, modified N-S equation with Darcy's source term or Brinkman equation is always adopted to describe the fluid flow in porous media for simplicity. The interface coupling between GDL and GC is solved automatically because of the same order of momentum equations in both GDL and GC. However, this simplified numerical implementation would be questionable. In Table 3-4, we list the magnitudes of the area-averaged velocities at the GC-GDL interface at two different GC inlet velocities, which can be used to

validate the abovementioned numerical implementations, modified N-S equation with Darcy's source term or Brinkman equation.

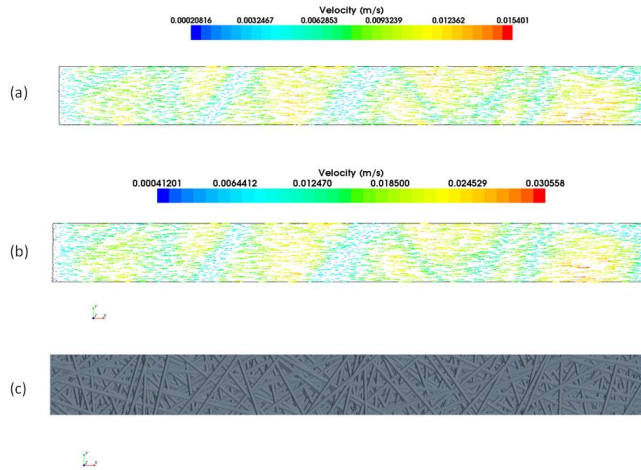


Figure 3-12: Velocity-vector fields at GC/GDL interface at different GC inlet velocities: (a)  $v=0.1$  m/s; (b)  $v=0.2$  m/s (c) pore-scale structure viewed from the top of the GDL.

Fig. 3-12a and Fig. 3-12b show the velocity-vector fields at the GC-GDL interface at two different GC inlet velocities. When the GC inlet velocity is doubled, the slip velocities at the interface are also almost doubled. There is nearly no change of the structure of slip velocity distribution. This could be explained by the fact that the slip velocity distribution is mainly dependent on the pore structure of the GDL in the vicinity of the GC-GDL interface. We also can see that near big pores, the slip velocities are relatively big. The highest value is up to about 0.03 m/s in Fig. 3-12b. Fig. 3-12c displays the pore structure of the GDL viewed from the top. In Table 3-4, we list the area-averaged velocities over the whole GC-GDL interface, which could be regarded as the superficial or Darcy velocities. As seen from Table 3-4, the area-averaged x-component slip velocities along the flow direction have the highest values, namely,  $8.199\text{e-}03$  m/s, and  $1.606\text{e-}02$  m/s for the 0.1 m/s and 0.2 m/s GC inlet velocities, respectively. The area-averaged x-component slip velocity is doubled when the GC inlet velocity is doubled. The area-averaged y-component slip velocities with the lowest values show the same trend as the x-component ones. As to the z-component velocities, their magnitudes are mainly affected by the mass flow rate from the CL to GC, and insensitive to the GC inlet velocity. As shown in Fig. 3-9, with the increase of the GC inlet velocity, more mass is delivered out of the GDL. Therefore, a little higher value of z-component velocity is expected, which is  $1.399\text{e-}03$  m/s at the GC inlet velocity of 0.2 m/s. When two-phase flow is modeled in PEFC modeling, the z-component velocity is expected to be negative.

### 3.5 Conclusions

In this chapter, first the pore structure of carbon-paper GDL is virtually constructed by means of stochastic method. Then we numerically calculate the in-plane and through-plane permeability of the GDL by solving N-S equations directly. The obtained permeability matches well with the existing numerical and experimental results in literature. The in-plane permeability has a higher value than the through-plane one. The anisotropic factor of permeability for carbon paper GDL is

found to be about 1.5, which is lower than experimental measurements mainly due to the absence of resin binder in our simulations. Furthermore, we conduct the pore-scale simulations of reactive species transport inside the cathode GDL. The slip phenomenon at the GC-GDL interface is explored. The results show that the carbon-paper GDL holds distinct three-dimensional structure, but this fibrous structure doesn't invoke intense variations of species concentration distributions locally. At the GDL-CL interface, the local variations are relatively much stronger at the ending portion. Regarding the slip phenomenon at the GC-GDL interface, the area-averaged x-component slip velocities tangential to the interface and along the flow direction have the highest values. Moreover, the x-component velocity is doubled when the GC inlet velocity is doubled. The area-averaged y-component velocities with the lowest values show the same tendency as the x-component ones. As to the z-component velocities, their magnitudes are mainly affected by the mass flow from the CL to GC, and insensitive to the GC inlet velocity.

## Nomenclature

$a$	charge transfer coefficient; net water flux per proton flux; TS constant; jump coefficient
$C$	species mass fraction
$d$	fiber diameter (m)
$D$	species diffusivity ( $\text{m}^2 \text{s}^{-1}$ )
$F$	Faraday's constant, 96487 ( $\text{C mol}^{-1}$ )
$j$	current density ( $\text{A m}^{-2}$ )
$k$	intrinsic permeability ( $\text{m}^2$ ); Carman-Kozeny constant
$M$	molecular weight ( $\text{kg mol}^{-1}$ )
$n$	mass flux ( $\text{kg m}^{-2} \text{s}^{-1}$ )
$P$	static pressure (Pa)
$r$	fiber radius (m)
$R$	universal gas constant 8.314 ( $\text{J mol}^{-1} \text{K}^{-1}$ )
$S$	source term ( $\text{kg m}^{-3} \text{s}^{-1}$ )
$T$	temperature (K)
$\bar{u}$	velocity ( $\text{m s}^{-1}$ )
$Y$	molar concentration ( $\text{mol m}^{-3}$ )

## Greek letters

$\mu$	dynamic viscosity of the gas mixture ( $\text{kg m}^{-1} \text{s}^{-1}$ )
$\eta$	over-potential (V)
$\alpha$	cathode catalyst specific area ( $\text{m}^2 \text{m}^{-3}$ )
$\rho$	density of the gas mixture ( $\text{kg m}^{-3}$ )
$\varepsilon$	porosity
$\xi$	stoichiometric ratio

## Subscripts and superscripts

$c$	cathode
$a$	anode

<i>i</i>	species index
<i>ref</i>	reference
<i>net</i>	net water flux
<i>CK</i>	Carman-Kozeny
<i>m</i>	membrane
<i>d</i>	Darcy
<i>s</i>	slip
<i>f</i>	fiber
<i>CL</i>	catalyst layer

## Abbreviations

GC	gas channel
GDL	gas diffusion layer
CL	catalyst layer
MEM	membrane
PEFC	polymer electrolyte fuel cell

## References

- [1] M.M. Mench, Fuel Cell Engines, John Wiley & Sons, 2008.
- [2] G. Hoogers, Fuel Cell Technology Handbook, CRC press, 2003.
- [3] C.Y. Wang, Fundamental models for fuel cell engineering, Chem. Rev. 104 (2004) 4727-4765.
- [4] M.A. Hickner, N.P. Siegel, K.S. Chen, D.S. Hussey, D.L. Jacobson, M. Arif, Understanding liquid water distribution and removal phenomena in an operating PEMFC via neutron radiography, J. Electrochem. Soc. 155 (3) (2008) B294-B302.
- [5] H. Li, Y. Tang, Z. Wang, A review of water flooding issues in the proton exchange membrane fuel cell, J. Power Sources 178 (2008) 103-117.
- [6] L. Cindrella, A.M. Kannan, J.F. Lin, K. Saminathan, Y. Ho, C.W. Lin, J. Wertz, Gas diffusion layer for proton exchange membrane fuel cells-A review, J. Power Sources 194 (2009) 146-160.
- [7] C. Qin, D. Rensink, S.M. Hassanizadeh, S. Fell, Two-phase flowing modeling for the cathode side of a polymer electrolyte fuel cell, J. Power Sources, 197 (2012) 136-144.
- [8] D. Natarajan, T.V. Nguyen, A two-dimensional, two-phase, multicomponent, transient model for the cathode of a proton exchange membrane fuel cell using conventional gas distributors, J. Electrochem. Soc. 148 (12) (2001) A1324-A1335.
- [9] J. Jang, W. Yan, H. Li, W. Tsai, Three-dimensional numerical study on cell performance and transport phenomena of PEM fuel cells with conventional flow fields, Int. J. Hydrogen Energy 33 (2008) 156-164.
- [10] J.E. Dawes, N.S. Hanspal, O.A. Family, A. Turan, Three-dimensional CFD modeling of PEM fuel cells: An investigation into the effects of water flooding, Chem. Eng. Sci. 64 (2009) 2781-2794.
- [11] Z.H. Wang, C.Y. Wang, K.S. Chen, Two-phase flow and transport in the air cathode of proton exchange membrane fuel cells, J. Power Sources 94 (2001) 40-50.

- [12] Q. Ye, T.V. Nguyen, Three-dimensional simulation of liquid water distribution in a PEMFC with experimentally measured capillary functions, *J. Electrochem. Soc.* 154 (12) (2007) B1242-B1251.
- [13] Y. Wang, Modeling of two-phase transport in the diffusion media of polymer electrolyte fuel cells, *J. Power Sources* 185 (2008) 261-271.
- [14] H. Wu, X. Li, P. Berg, On the modeling of water transport in polymer electrolyte membrane fuel cells, *Electrochim. Acta* 54 (2009) 6913-6927.
- [15] H. Ju, Analyzing the effects of immobile liquid saturation and spatial wettability variation on liquid water transport in diffusion media of polymer electrolyte fuel cells (PEFCs), *J. Power Sources* 185 (2008) 55-62.
- [16] Y.H. Cai, J. Hu, H.P. Ma, B.L. Yi, H.M. Zhang, Effects of hydrophilic/hydrophobic properties on the water behavior in the micro-channels of a proton exchange membrane fuel cell, *J. Power Sources* 161 (2006) 843-848.
- [17] A.Z. Weber, J. Newman, Modeling transport in polymer-electrolyte fuel cells, *Chem. Rev.* 104 (2004) 4679-4726.
- [18] G.F. Pinder, W.G. Gray, *Essentials of Multiphase Flow and Transport in Porous Media*, John Wiley & Sons, 2008.
- [19] V.P. Schulz, J. Becher, A. Wiegmann, P.P. Mukherjee, C.Y. Wang, Modeling of two-phase behavior in the gas diffusion medium of PEFCs via full morphology approach, *J. Electrochem. Soc.* 154 (4) (2007) B149-B426.
- [20] Y. Wang, S. Cho, R. Thiedmann, V. Schmidt, W. Lehnert, X. Feng, Stochastic modeling and direct simulation of the diffusion media for polymer electrolyte fuel cells, *Int. J. Heat Mass Transfer* 53 (2010) 1128-1138.
- [21] J.P. Feser, A.K. Prasad, S.G. Advani, Experimental characterization of in-plane permeability of gas diffusion layers, *J. Power Sources* 162 (2006) 1226-1231.
- [22] J.T. Gostick, M.W. Fowler, M.D. Pritzker, M.A. Ioannidis, L.M. Behra, In-plane and through-plane gas permeability of carbon fiber electrode backing layers, *J. Power Sources* 162 (2006) 228-238.
- [23] L. Hao, P. Cheng, Lattice Boltzmann simulation of anisotropic permeabilities in carbon paper diffusion layers, *J. Power Sources* 186 (2009) 104-114.
- [24] K. Schladitz, S. Peters, D. Reinel-Bitzer, A. Wiegmann, J. Ohser, Design of acoustic trim based on geometric modeling and flow simulation for non-woven, *Comput. Mater. Sci.* 38 (2006) 56-66.
- [25] S. Jaganathan, H.V. Tafreshi, B. Pourdeyhimi, A realistic approach for modeling permeability of fibrous media: 3-D imaging coupled with CFD simulation, *Chem. Eng. Sci.* 63 (2008) 244-252.
- [26] R. Thiedmann, F. Fleischer, C. Hartnig, W. Lehnert, V. Schmidt, Stochastic 3D modeling of the GDL structure in PEMFCs based on thin section detection, *J. Electrochem. Soc.* 155 (4) (2008) B391-B399.
- [27] F. Barbir, *PEM Fuel Cells: Theory and Practice*, Elsevier Academic Press, 2005.
- [28] N. Zamel, X. Li, J. Shen, J. Becker, A. Wiegmann, Estimating effective thermal conductivity in carbon paper diffusion media, *Chem. Eng. Sci.* 65 (2010) 3994-4006.
- [29] A.Z. Weber, M.A. Hickner, Modeling and high-resolution-imaging studies of water-content profiles in a polymer-electrolyte-fuel-cell membrane-electrode assembly, *Electrochim. Acta* 53 (2008) 7668-7674.

- [30] A. Bazylak, D. Sinton, N. Djilali, Dynamic water transport and droplet emergence in PEMFC gas diffusion layers, *J. Power Sources* 176 (2008) 240-246.
- [31] J.H. Nam, M. Kaviany, Effective diffusivity and water-saturation distribution in single- and two-layer PEMFC diffusion medium, *Int. J. Heat Mass Transfer* 46 (2003) 4595-4611.
- [32] H. Meng, Numerical investigation of transient responses of a PEM fuel cell using a two-phase non-isothermal mixed-domain model, *J. Power Sources* 171 (2007) 738-746.
- [33] J.S. Yi, T.V. Nguyen, Multicomponent transport in porous electrodes of proton exchange membrane fuel cells using the interdigitated gas distributors, *J. Electrochem. Soc.* 146 (1) (1999) 38-45.
- [34] User Guide, STAR-CCM+ Version 4.06.011, 2009, CD-adapco.
- [35] J.H. Ferziger, M. Perić, *Computational Methods for Fluid Dynamics*, 3rd ed., Springer-Verlag, 2002.
- [36] Z. Shi, X. Wang, A numerical study of flow crossover between adjacent flow channels in a proton exchange membrane fuel cell with serpentine flow field, *J. Power Sources* 185 (2008) 985-992.
- [37] M.M. Tomadakis, T.J. Robertson, Viscous permeability of random fiber structures: comparison of electrical and diffusional estimates with experimental and analytical results, *J. Comps. Mater.* 39 (2005) 163-188.
- [38] D. Jamet, M. Chandesris, On the intrinsic nature of jump coefficients at the interface between a porous medium and a free fluid region, *Int. J. Heat Mass Transfer* 52 (2009) 289-300.
- [39] B. Alazmi, K. Vafai, Analysis of fluid flow and heat transfer interfacial conditions between a porous medium and a fluid layer, *Int. J. Heat Mass Transfer.* 44 (2001) 1735-1749.
- [40] D.A. Nield, The Beavers-Joseph boundary condition and related matters: a historical and critical note, *Transp. Porous Media* 78 (2009) 537-540.

Table 3-1: Operating parameters and geometric information.

Parameters	Values
Channel width	0.1 mm
Channel height	0.5 mm
Channel length	1.6 mm
Thickness of GDL	0.15 mm
Operating temperature $T$	353.15 K
Inlet mass fraction of oxygen $C_{O_2}^{in}$	0.192 [36]
Inlet mass fraction of water vapor $C_{H_2O}^{in}$	0.255
Inlet velocity $u^{in}$	0.1 and 0.2 m s <sup>-1</sup>
Out-let pressure $p$	0 Pa
Dynamic viscosity of the gas mixture $\mu$	$2.03 \times 10^{-5}$ Pa s
Diffusivity of oxygen $D_{O_2}$	$2.930 \times 10^{-5}$ m <sup>2</sup> s <sup>-1</sup>
Diffusivity of water vapor $D_{H_2O}$	$3.302 \times 10^{-5}$ m <sup>2</sup> s <sup>-1</sup>
Transfer coefficient of oxygen reduction reaction $a_c$	0.5
Over-potential $\eta$	0.33 V
Net water transport coefficient of the membrane $a_{net}$	0.5
$ai_0^{ref} / Y_{O_2,ref}$	0.000001 A/m-mol O <sub>2</sub> [33]

Table 3-2: The permeability data of carbon paper GDL obtained from literature and this work.

Reference	In-plane permeability (Darcy)	Through-plane permeability (Darcy)	Anisotropy	Fiber diameter ( $\mu$ m)	PTFE	Porosity	Carman-Kozeny constant for the through-plane permeability	Applied Method
Schulz [19]	11.50	7.40	1.55	7.0	0	0.78	4.06	LBM
Hao [23]	11.00	7.63	1.44	7.5	0	0.79	5.15	LBM
Gostick [22]	16.56	8.99	1.84	9.2	0	0.80	7.53	experiment
This work	9.84	6.85	1.44	7.0	0	0.80	5.72	N-S

Table 3-3: Constants used in TS model for permeability calculation [22].

Dimension	Flow direction	$\varepsilon_p$	$a$
1D	Parallel	0	0
	Normal	0.33	0.707
2D	Parallel	0.11	0.521
	Normal	0.11	0.785
3D	Any direction	0.037	0.661

Table 3-4: Magnitudes of the area-averaged velocities at the GC/GDL interface at two different GC inlet velocities, 0.1 and 0.2m/s.

GC inlet velocity (m/s)	Area-averaged velocity at GC/GDL interface (m/s)		
	x-component	y-component	z-component
0.1	8.199e-03	1.333e-04	1.356e-03
0.2	1.606e-02	2.542e-04	1.399e-03

# Chapter 4 - Two-phase Flow Modeling for the Cathode Side of a Polymer Electrolyte Fuel Cell

---

## Abstract

*Liquid water flooding in micro gas channels is an important issue in the water management of polymer electrolyte fuel cells (PEFCs). However, in most previous numerical studies liquid water transport in the gas channels (GC) has been simplified by the mist flow assumption. In this chapter, we present a two-phase flow model for the cathode side of a PEFC. The GC is assumed to be a structured porous medium with the porosity of 1.0. The two-phase Darcy's law is applied to both diffusion layers and GC. Based on the developed model, the liquid water flooding in the GC and its impact on the liquid water distribution in the diffusion layers are explored in detail. Furthermore, we study the effect of the immobile saturation on the predicted liquid water distribution in the diffusion layers. The results show that neglecting the GC flooding leads to an incorrect prediction of liquid water distribution in the diffusion layers and an overestimation of the cell performance. The gas flow rate in the GC can be optimized to achieve the best cell performance. Finally, when considering the immobile saturation in the model, more liquid water is predicted in the diffusion layers.*

## 4.1 Introduction

In the pursuit of reduced dependence on fossil fuels, less pollution, as well as high efficiency, the polymer electrolyte fuel cell (PEFC) is regarded as one of the most promising alternative power sources in the future. It is expected to be widely employed in stationary, automotive and portable sections. However, before this can occur, several technical limitations of PEFCs must be overcome, such as cell durability, system power density, fuel storage, generation and delivery, as well as system cost<sup>1-3</sup>.

In a single PEFC unit, various transport processes are intricately coupled, along with electrochemical reactions in the catalyst layers. As a consequence, water and heat issues are always ineluctable. A typical PEFC consists of four distinct constituents, namely, bipolar plate (gas channels are grooved on both sides of bipolar plate), gas diffusion layer (including the micro porous layer), catalyst layer, and polymer electrolyte membrane. On one hand, the membrane should retain high water content to transport protons effectively with low ohmic resistance. Hence, gaseous reactants (e.g. H<sub>2</sub>, O<sub>2</sub>) are humidified before being fed into fuel cells. On the

other hand, excessive liquid water accumulating within fuel cells would block reactant pathways to reactive sites in catalyst layers, resulting in the so-called flooding situation. It is evident that there exist two conflicting requirements for liquid water. We need to have a delicate water balance inside fuel cells to ensure that the membrane is fully hydrated for high protonic conductivity, while severe flooding is avoided, especially on the cathode side. To be able to bring about this balance, a profound understanding of water transport inside fuel cells is indispensable<sup>4-7</sup>.

It is widely recognized that the flow of two immiscible phases (gas and liquid water) within PEFCs is challenging. While PEFCs are operating under certain conditions (e.g. high current densities, humid environments, and cold start-up), liquid water is simultaneously formed in all components. But, mechanisms affecting the liquid water transport are distinct in different layers. In general, the two-phase flow in PEFCs could be categorized into three sub-processes<sup>8, 9</sup>: (1) liquid water accumulation and transport in the CL, (2) two-phase flow in the GDL, along with interfacial coverage at the GC-GDL interface, and (3) water transport in the GC. These three sub-processes negatively impact the performance of PEFCs. For instance, in the CL, excessive liquid water would cover active catalyst sites, acting as an additional barrier to reactants transport. Based on the preceding descriptions of water transport we can see that a proper water management plays a central role in the development and commercialization of PEFCs.

Over the past two decades, the two-phase flow and flooding phenomena in PEFCs have been intensively investigated via both experimental<sup>10-15</sup> and numerical methods<sup>16-25</sup>. To date, several macroscopic computational fluid dynamics (CFD) models for the two-phase flow in PEFCs are available in literature, which are all based on the so-called two-phase Darcy's law<sup>26</sup>. He et al.<sup>27</sup> developed a two-phase flow model for the cathode GDL. They solved a steady-state transport equation of liquid water flow that derived from the two-phase Darcy's law. The equation strongly resembled a general scalar transport equation with convective and diffusive terms. The authors also assumed both capillary diffusivity and convective coefficient to be constants for numerical stability. Following He's method, Ye et al.<sup>29</sup> also derived a similar liquid water transport equation. Single-phase flow methodology was employed to model gas flow, and two phases were coupled by the phase change. The effect of the presence of liquid water on gas flow was taken into account only by correcting gaseous species diffusivities. Another popular two-phase model for PEFCs is called multiphase mixture ( $M^2$ ) model, which has been employed widely by fuel cell researchers<sup>30-34</sup>. Based on the two-phase Darcy's law, the  $M^2$  model for multiphase, multi-component transport in capillary porous media was firstly developed by Wang et al.<sup>35, 36</sup>. However, several researchers<sup>28, 37</sup> used volume-weighted mixture dynamic viscosity and mass-weighted mixture velocity to simplify the  $M^2$  model. So, the applications of this modified  $M^2$  model would be limited. Berning et al.<sup>38</sup> used the so-called multi-fluid model to study liquid water transport in the cathode porous layers. Since this model requires a multiphase solver, and needs to be capable of coupling species transport, phase change, and chemical reactions simultaneously, it entails lots of computational efforts and is prone to being numerically instable.

In an operating PEFC, liquid water emerges from the GDL into the GC, in the form of small droplets and slugs<sup>6</sup>. These droplets and slugs cover the GDL surface and block the GC, in turn, influence the flooding level inside the diffusion layers. In order to capture this important physical phenomenon, an interactive model of liquid water transport between the GC and GDL should be

developed. In most previous studies, a value of interfacial saturation or capillary pressure at the GC-GDL interface was specified. Normally, this value was assigned to zero, corresponding to the mist flow assumption in the GC. However, the mist flow assumption is only valid under high gas flow rates in the GC, which are not encountered in practice. So far, only a few researchers have numerically studied the water coverage effect on cell performance. Song et al.<sup>39</sup> developed a one-dimensional two-phase analytical model to address the effect of liquid water saturation at the GC-GDL interface on the transient behavior of liquid water transport inside the cathode GDL. Results showed that this parameter had a big impact on the calculated water saturation inside the GDL. A more elaborate interfacial coverage model was proposed by Meng et al.<sup>40</sup>. In their work, the interfacial liquid saturation at the GC-GDL interface was assumed to be a simple function of the GDL surface contact angle, current density, as well as gas inlet velocity. This was not based on a derivation and they also used the mist flow assumption in the GC. The results showed that the interfacial coverage led to higher flooding levels inside the GDL and CL. Berning<sup>38</sup> used the Hagen-Poiseuille equation to relate the interfacial water saturation with local pore velocity of liquid water in the GDL. Recently Basu et al.<sup>9</sup> proposed to apply the  $M^2$  model into the GC directly. In this approach, the GC was assumed to be a structured porous medium, and then the two-phase coupling between the GDL and GC became straightforward.

In this chapter, we develop a two-phase flow model for the cathode side of a PEFC. The GC is assumed to be a structured porous medium with the porosity of 1.0; then, the two-phase Darcy's law is applied to the GC. Based on this model, we study the liquid water flooding in the GC under different operating conditions, and also its impact on the liquid water distribution in the diffusion layers. Finally, we address the effect of the immobile saturation on the prediction of the liquid water distribution in the diffusion layers.

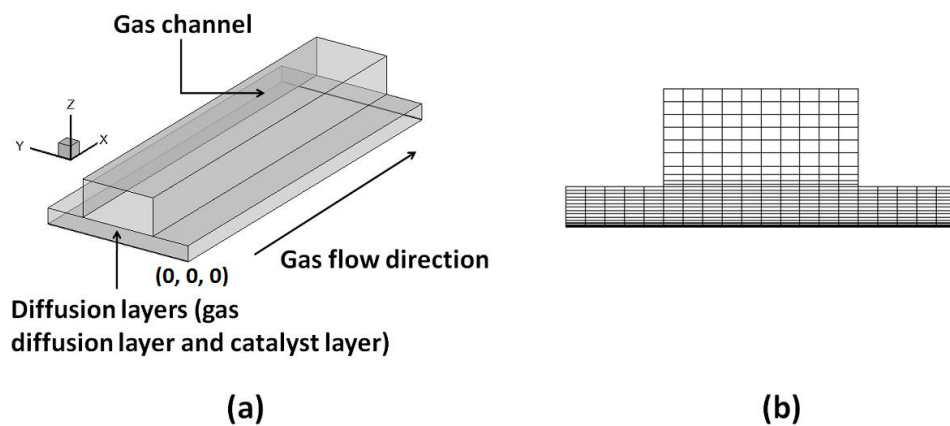


Figure 4-1: (a) Computational domain used in this work; (b) and the corresponding mesh in the Y-Z cross-section.

## 4.2 Two-phase flow model

Fig. 4-1 shows the three-dimensional computational domain and the corresponding mesh in the Y-Z plane. In this work, we focus on the liquid water flooding on the cathode side consisting

of the CL, GDL and GC. The typical cell length of 100 mm is used. In an operating PEFC, humidified air is delivered into the GC and diffuses through the GDL into the CL, where it combines with protons from the membrane, and electrons from the external circuit to form liquid water and heat. The following main assumptions are made in our model for numerical simplicity:

1. Ideal gas mixture
2. Isotropic and homogeneous diffusion layers
3. Laminar flow due to small Reynolds numbers and pressure gradients
4. Isothermal condition

#### 4.2.1 Governing equations of gas phase

The mass conservation equation of the gas mixture is given as follows:

$$\nabla \cdot (\rho_g \vec{V}_g) = S_g \quad (4-1)$$

where  $\vec{V}_g$  denotes the superficial or Darcy velocity of the gas phase,  $\rho_g$  is the density of the gas mixture, and  $S_g$  is the mass source term due to the chemical reaction and phase change.

The Darcy velocity is related to the intrinsic or pore-scale velocity by the following definition:

$$\vec{V}_g = (1-s)\varepsilon\vec{U}_g \quad (4-2)$$

where  $\vec{U}_g$  denotes the intrinsic velocity of the gas phase,  $\varepsilon$  is the porosity, and  $s$  represents the liquid water saturation defined as the volume fraction of the pores occupied by the liquid water.

The steady-state momentum equation of the gas phase can be derived based on the two-phase flow methodology<sup>42</sup>, which is given as:

$$\frac{1}{\varepsilon^2(1-s)^2} \nabla \cdot (\rho_g \vec{V}_g \vec{V}_g) = -\nabla p_g + \frac{1}{\varepsilon(1-s)} \nabla \cdot (\overline{\tau}) + S_m \quad (4-3)$$

where  $p_g$  is the gas phase pressure,  $\overline{\tau}$  is the stress tensor, and  $S_m$  represents the Darcy source term accounting for the viscous resistance imposed by the pore structure of porous media and the presence of liquid water in the pore space.

The above-listed mass and momentum conservation equations of the gas phase are applied to the whole computational domain. Since we regard the GC as a structured porous medium in this work, the porosity of the GC is assumed to be unity. It is worth noting that the two-phase Darcy's law for the gas phase can be obtained by neglecting the inertia and diffusive terms in Eq. 4-3. However, to keep the same order of the momentum equations used in the GC and diffusion layers, Eq. 4-3 is adopted in this work.

In automotive applications, we have water vapor, oxygen, and nitrogen species on the cathode side. The species transport equation can be expressed as:

$$\nabla \cdot (\rho_g C_i \bar{V}_g) = \nabla \cdot (\rho_g D_i^{eff} \nabla C_i) + S_i \quad (4-4)$$

in which  $C_i$  denotes the mass fraction of each component,  $D_i^{eff}$  is the effective diffusivity accounting for the presence of liquid water and the pore structure of porous media, and  $S_i$

represents the species source term owing to the oxygen reduction reaction (ORR) and phase change. In our calculations, nitrogen is regarded as an inert component.

#### 4.2.2 Liquid water transport equation

Liquid water is assumed to be a single-component phase, and the gaseous species diffusion in the liquid water is neglected. The mass conservation equation of the liquid water is given as:

$$\nabla \cdot (\rho_l \bar{V}_l) = S_l \quad (4-5)$$

where  $\rho_l$  is the liquid water density,  $S_l$  is the mass source term, and  $\bar{V}_l$  denotes the Darcy velocity of the liquid water, which can be given by the two-phase Darcy's law:

$$\bar{V}_l = -\frac{k_0 k_{rl}}{\mu_l} \nabla p_l \quad (4-6)$$

Recalling Eq. 4-3, we can safely drop the inertia and diffusive terms due to their extremely small magnitudes compared to the Darcy term. Then the two-phase Darcy equation for the gas phase is obtained as:

$$\bar{V}_g = -\frac{k_0 k_{rg}}{\mu_g} \nabla p_g \quad (4-7)$$

In Eq. 4-6 and 4-7,  $p_l$  denotes the liquid water pressure,  $k_0$  denotes the intrinsic permeability of porous media,  $\mu_l$  and  $\mu_g$  are the dynamic viscosities of the liquid water and gas, respectively,  $k_{rl}$  represents the relative permeability for the liquid phase, and  $k_{rg}$  represents the relative permeability for the gas phase. The primary difference between these two equations and the single-phase form stems from the presence of the relative permeability, which designates the influence of the reduced void space for each phase due to the existence of the other phase. Finally, the macroscopic capillary pressure is introduced to represent the pressure difference between the gas and liquid phases, given as:

$$p_c(s) = p_g - p_l \quad (4-8)$$

Eq. (4-5)-(4-8) can be combined, and after a few algebraic manipulations the liquid water transport equation is obtained as:

$$\nabla \cdot \left( \rho_l \frac{k_{rl}}{k_{rg}} \frac{\mu_g}{\mu_l} \bar{V}_g \right) = \nabla \cdot \left( -\rho_l \frac{k_0 k_{rl}}{\mu_l} \nabla p_c \right) + S_l \quad (4-9)$$

Here, the gas drag effect (the term on the left hand side) on the liquid water movement and the capillary diffusion (first term on the right hand side) are both included.

### 4.2.3 Constitutive correlations and source terms

To close the governing equations, several constitutive correlations are needed, such as state equation, capillary pressure-saturation and relative permeability-saturation relationships. Ideal gas mixture law is used to calculate the composition-dependent gas phase density as follows:

$$\rho_g = \frac{p_g}{RT \sum_i \frac{C_i}{M_i}} \quad (4-10)$$

in which,  $p_g$  refers to the gas pressure,  $C_i$  is the mass fraction of each component, and  $R$  is the universal gas constant. Due to the small pressure gradient, the mass density of the liquid water is assumed to be constant.

The multi-component diffusion in the gas phase can be described by Stefan-Maxwell equation. For simplicity, the Fick's law is commonly used<sup>43</sup>. Taking into account the presence of liquid water and the pore structure of porous media, the effective species diffusivity can be given based on Bruggeman correlation:

$$D_i^{eff} = (1-s)^n \varepsilon^{1.5} D_i \quad (4-11)$$

where  $D_i$  is the molecular diffusivity that depends on the temperature and pressure. For water vapor and oxygen, we have the following empirical expressions<sup>29</sup>:

$$D_{H_2O} = 0.2982 \times 10^{-4} (T/333)^{1.75} (101325/p_g) \quad (4-12)$$

$$D_{O_2} = 0.2652 \times 10^{-4} (T/333)^{1.75} (101325/p_g) \quad (4-13)$$

Regarding the capillary pressure, we know that it is dependent on the interface curvature at the micro scale. We traditionally presume that capillary pressure is solely a function of saturation at the macro scale, as expressed in Eq. 4-8. However, the hysteresis phenomenon of capillary pressure-saturation curves during consecutive drainage and imbibition processes in porous media indicates that other variables may also influence the capillary pressure. Hassanizadeh and Gray<sup>44</sup> claim that, based on a rigorous thermo-dynamical derivation the capillary pressure is not only a function of saturation but also of the specific areas of the three interfaces. However, to date, this model is still hard to be integrated with current CFD codes, since it involves several additional variables. There is also another weakness in the traditional capillary pressure-saturation relationship, which ignores the dynamic effect<sup>45</sup> in the pressure difference between two phases under unsteady state situations. In this work, we still follow the traditional approach, and use the well-known Leverett function, expressed as:

$$p_c = \sigma \cos \theta \left( \frac{\varepsilon}{k_0} \right)^{1/2} J(s) \quad (4-14)$$

$$J(s) = \begin{cases} 1.417(1-s) - 2.120(1-s)^2 + 1.263(1-s)^3 & \text{for } \theta \leq 90^\circ \\ 1.417s - 2.120s^2 + 1.263s^3 & \text{for } \theta > 90^\circ \end{cases} \quad (4-15)$$

As to the relative permeabilities, power-form correlations are commonly used in the absence of experimental data. They originally come from sand/rock-type porous media with a typical porosity of 0.1-0.4<sup>29</sup>. Therefore, the relative permeabilities for both gas and liquid phases can be expressed as:

$$k_{rg} = (1-s)^{n_2} \quad (4-16)$$

$$k_{rl} = \begin{cases} 0 & s < s_{im} \\ s_{eff}^{n_2} & s \geq s_{im} \end{cases} \quad (4-17)$$

$$s_{eff} = \frac{s - s_{im}}{1 - s_{im}} \quad (4-18)$$

In these equations,  $n_2$  is the material coefficient,  $s_{eff}$  is called the effective saturation, and  $s_{im}$  represents the immobile water saturation.

The liquid water flux is assumed to be zero, before it forms conducting pathways in the porous media of interest. As indicated in Eq. 4-17, when the liquid water saturation is less than the threshold value  $s_{im}$ , the relative permeability for the liquid phase is zero; thus, we obtain the zero water flux. Normally, the immobile saturation not only depends on the material properties of porous media, but also can be affected by the flow conditions (such as phase change, boundary condition, and flow history). Only a few researchers<sup>38, 46</sup> have investigated the impact of this parameter on the two-phase flow in the diffusion layers of a PEFC using one-dimensional simulations.

The simplified Tafel equation is employed to describe the relatively sluggish ORR in the cathode CL<sup>22</sup>:

$$j_c = (1-s)^{n_3} \alpha i_0^{ref} \frac{C_{O_2}}{Y_{O_2,ref}} \frac{\rho_g}{M_{O_2}} \exp\left(\frac{a_c F}{RT} \eta_c\right) \quad (4-19)$$

Here, the liquid water coverage effect is considered by the exponent  $n_3$ ,  $Y_{O_2,ref}$  denotes the reference molar concentration of oxygen, and  $\eta_c$  is the cathode overpotential.

The phase change between water vapor and liquid water is considered by a nonequilibrium phase change model<sup>47</sup>, which is expressed as:

$$R_l = k_{cond} \frac{\varepsilon(1-s)Y_{H_2O}M_{H_2O}}{RT} (Y_{H_2O}P_g - p_{H_2O}^{sat})q + k_{evap}\varepsilon s \rho_l (Y_{H_2O}P_g - p_{H_2O}^{sat})(1-q) \quad (4-20)$$

$$q = \frac{1 + |Y_{H_2O}P_g - p_{H_2O}^{sat}| / (Y_{H_2O}P_g - p_{H_2O}^{sat})}{2} \quad (4-21)$$

In Eq. 4-20,  $p_{H_2O}^{sat}$  denotes the water vapor pressure, which can be obtained from the following empirical formula as a function of temperature<sup>42</sup>:

$$\log_{10} \frac{p_{H_2O}^{sat}}{101325} = -2.1749 + 0.02953(T - 273.15) - 9.1837 \times 10^{-5}(T - 273.15)^2 + 1.4454 \times 10^{-7}(T - 273.15)^3 \quad (4-22)$$

The source terms of the conservation equations in different regions on the cathode side are listed in Table 4-1. Since the membrane is not included, the liquid water exchange between the CL and membrane is accounted for by means of the net water transfer coefficient. Note that the generated water in the CL is assumed to be in the liquid form due to the nanostructure of the CL. In this work, we assume the GC to be a structured porous medium associated with a given intrinsic permeability, which can be obtained from numerical experiments or Hagen-Poiseuille law<sup>48</sup>.

#### 4.2.4 Boundary conditions and numerical implementation

The gas inlet velocity on the cathode side can be determined by the specified stoichiometric ratio  $\xi_c$ , and the calculated average current density  $I_{ave}$ , as follows:

$$I_{ave} = \frac{\int_{CL} j_c dv}{A_m} \quad (4-23)$$

$$\vec{V}_{in,g} \cdot \vec{n} = \frac{I_{ave} A_m}{F} \frac{\xi_c}{4Y_{in,O_2} A_{gc}} \quad (4-24)$$

where  $A_m$  and  $A_c$  are the reactive and GC cross-sectional areas, respectively, and  $Y_{in,O_2}$  denotes the inlet molar concentration of oxygen, which is determined by the inlet relative humidity  $RH$  and local gas pressure, expressed as:

$$Y_{in,O_2} = 0.21 \times \frac{\rho_g}{M_g} \left( 1 - \frac{RH \cdot p_{H_2O}^{sat}}{P_g} \right) \quad (4-25)$$

The gas pressure at the GC outlet is assumed to be 2 atm. The symmetric boundary conditions are employed at the sidewalls of the GDL and CL due to the repeated structure in a PEFC stack. The slip and impermeable wall conditions are specified at the GC walls, since the GC is assumed to be a structured porous medium. The wall resistance is lumped into the Darcy's source term as

shown in Table 4-1. For the remaining boundaries, the conditions of no-slip and impermeable wall are imposed.

The set of steady-state governing equations and boundary conditions given above are discretized using finite volume method with second-order schemes based on the commercial CFD solver FLUENT. With the aid of user-defined functions, the liquid water transport equation, source terms and constitutive correlations are coupled with the general multi-component gas transport equations. The SIMPLE (semi-implicit method for pressure-linked equations) algorithm is utilized to couple pressure and velocity, and the AMG (algebraic multi-grid) method in conjunction with Gauss-Seidel type smoother is used to solve resultant nonlinear algebraic equations. In all simulations presented in the following section, the scaled values of the equation residuals are smaller than  $10^{-6}$ .

### 4.3 Results and discussion

Geometrical, physical, and operating parameters are summarized in Table 4-2. We assume uniform distribution of the cathode overpotential in the CL, and the average current density can be computed from Eq. 4-23. In what follows, we highlight the importance of modeling GC flooding in the numerical studies of PEFCs. And, its impact on the cell performance and liquid water distribution is explored in detail. At last, we address the effect of immobile saturation on the liquid water distribution in diffusion layers.

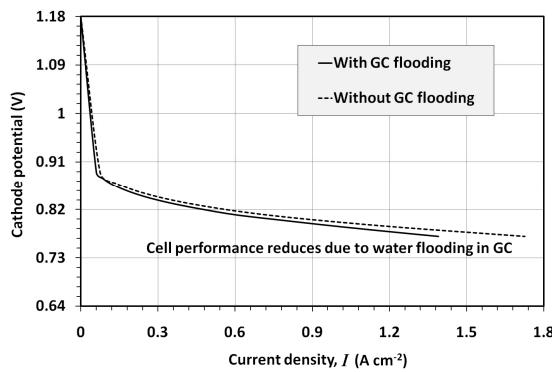


Figure 4-2: Polarization curves (cathode potential vs. current density) taking into account GC flooding, and neglecting GC flooding.

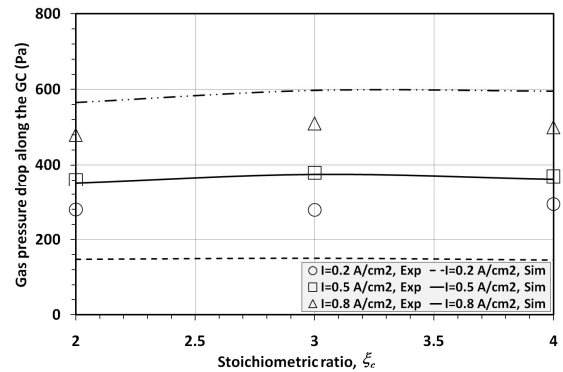


Figure 4-3: Gas pressure drop validation at different current densities and stoichiometric ratios (experimental data are extracted from Ref. [9]).

#### 4.3.1 Modeling of GC flooding

In the direct observations of operating PEFCs, we often observe lots of water droplets and slugs forming in the GC, which are finally removed out of the channel mainly under the gas drag force. Due to the complex flow dynamics, numerically two-phase flow in the GC was overwhelmingly simplified by the mist flow assumption in most previous studies. In this work, we apply the two-phase Darcy's law to the GC, and investigate its effect on the cell performance and

liquid water distribution. Fig. 4-2 shows two polarization curves (cathode potential vs. current density) under the situations of considering the GC flooding, and neglecting the GC flooding, separately. It can be seen that neglecting the GC flooding would overestimate the cell performance. We also validate our model against experimental data in terms of gas pressure drop in the GC as shown in Fig. 4-3. The excellent match is obtained at the current density of  $0.5 \text{ A cm}^{-2}$ . Increasing the stoichiometric ratio does not invoke obvious increase of the gas pressure drop, since more liquid water can be swept out of the channel under the higher gas flow rate. However, our model overpredicts the gas pressure drops at the current density of  $0.8 \text{ A cm}^{-2}$ , and underestimates the gas pressure drops at the low current density of  $0.2 \text{ A cm}^{-2}$ , respectively. This may be partly due to the unresolved water exchange between the cathode and anode sides in our half cell model. It also needs to point out that our channel flooding model is capable of predicting the tendency of gas pressure drop as increasing the stoichiometric ratio, as shown in Fig. 4-3.

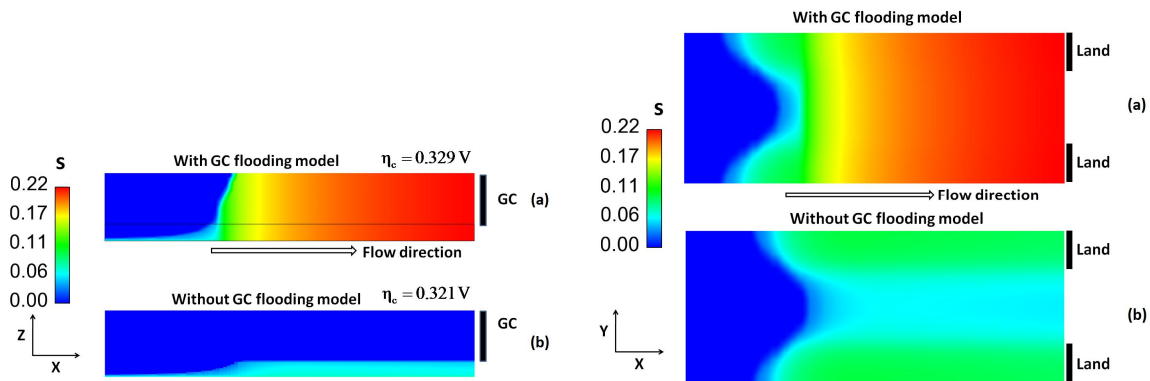


Figure 4-4: Distributions of the liquid water saturation at the middle cross-section ( $Y=1.0 \times 10^{-3} \text{ m}$ ) of the cathode side (operating conditions:  $RH = 66\%$ ,  $\xi_c = 2.0$ ,  $s_{im} = 0$ , and  $I_{ave} = 0.2 \text{ A cm}^{-2}$ ).

Figure 4-5: Distributions of the liquid water saturation at the middle cross-section ( $Z=9.0 \times 10^{-5} \text{ m}$ ) of the GDL (operating conditions:  $RH = 66\%$ ,  $\xi_c = 2.0$ ,  $s_{im} = 0$ , and  $I_{ave} = 0.2 \text{ A cm}^{-2}$ ).

Fig. 4-4 shows the comparison of the liquid water distributions at the middle cross-section ( $Y=1 \times 10^{-3} \text{ m}$ ) of the cathode side under two situations: considering the GC flooding (upper one), and neglecting the GC flooding (lower one). The corresponding operating conditions are as follows:  $RH = 66\%$ ,  $\xi_c = 2.0$ ,  $s_{im} = 0$ , and  $I_{ave} = 0.2 \text{ A cm}^{-2}$ . Much more liquid water is found in the diffusion layers due to the water coverage effect at the GC-GDL interface. The cathode overpotential increases to  $0.392 \text{ V}$  when taking into account the GC flooding. This indicates the decreased cell performance.

At the same operating conditions, the liquid water distributions at the middle cross-section ( $Z=9.0 \times 10^{-4} \text{ m}$ ) of the GDL are plotted in Fig. 4-5. The liquid water saturation at the inlet portions is zero due to the partially humidified air feeding. When neglecting the GC flooding (lower one) more liquid water is found under the land, this is because the liquid water under the land has to

travel a somewhat longer path to reach the GC. The liquid water saturation reduces slightly along the flow direction owing to the decreased current density. When the GC flooding model is included, the liquid water saturation increases along the flow direction (upper one). This opposite water distribution indicates that the GC flooding impacts the liquid water distribution in the diffusion layers considerably. Neglecting the GC flooding would lead to the incorrect prediction of liquid water distribution in the diffusion layers. In addition, the liquid water distribution in the transverse direction of the GC is more uniform, which is also caused by the presence of liquid water in the GC.

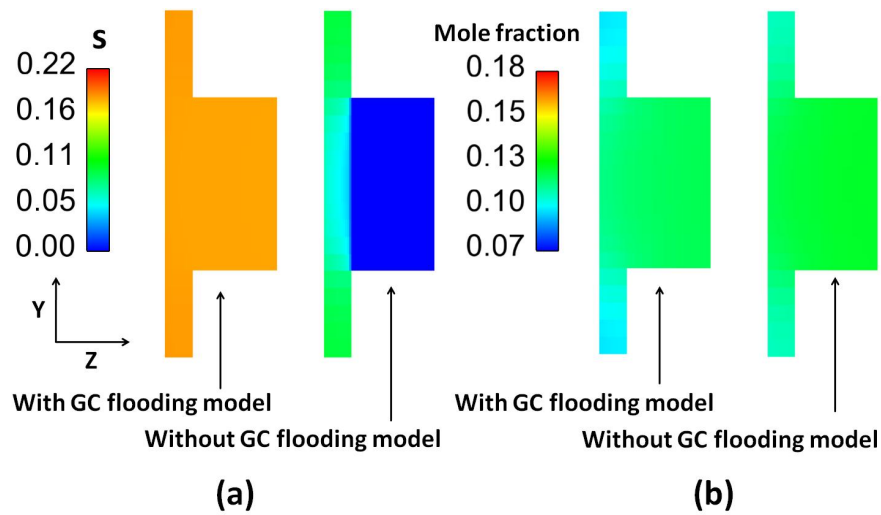


Figure 4-6: Distributions of (a) the liquid water saturation, (b) the mole fraction of oxygen at the middle cross-section ( $X=0.05$  m) of the cathode side (operating conditions:  $RH = 66\%$ ,  $\xi_c = 2.0$ ,  $s_{im} = 0$ , and  $I_{ave} = 0.2$  A  $cm^{-2}$ )

Fig. 4-6a shows the liquid water distributions at the middle cross-section ( $X=0.05$  m) of the cathode side. Liquid water flooding in the GC results in almost even distribution of the liquid water at the cross-section (left one). However, a distinct gradient of the liquid water saturation is found when we neglect the liquid water flooding in the GC (right one). Fig. 4-6b displays the distributions of the mole fraction of oxygen at the same cross-section. Lower oxygen concentrations are found under the land due to the transport limitation. When considering the GC flooding, much more liquid water is present in the diffusion layers (Fig. 4-6a). This gives rise to the higher oxygen diffusion resistance. Therefore, even lower oxygen concentration is observed (Fig. 4-6b, left one).

Fig. 4-7 illustrates the influence of the stoichiometric ratio on the liquid water distribution at the middle cross-section ( $Z=4.15 \times 10^{-4}$  m) of the GC. The operating conditions are:  $RH = 66\%$ ,  $s_{im} = 0$ , and  $I_{ave} = 0.5$  A  $cm^{-2}$ . When the applied stoichiometric ratio equals to 2.0, the highest liquid water saturation is predicted to be 0.23 at the end of the GC (Fig. 4-7a). We also can observe the water vapor front at which the water vapor reaches its saturated value. With the increase of the

stoichiometric ratio, the liquid water flooding is mitigated in the GC. This can be explained by the fact that more liquid water is removed out of the GC with the increase of the gas flow rate. Meanwhile, the water vapor front moves fast towards the end of the GC, which indicates that more water is transported out of the GC in the water vapor form. When the applied stoichiometric ratio equals to 4.0, only a little liquid water is left at the end of the GC. And, the cathode overpotential decreases to 0.348 V, indicative of the increased cell performance.

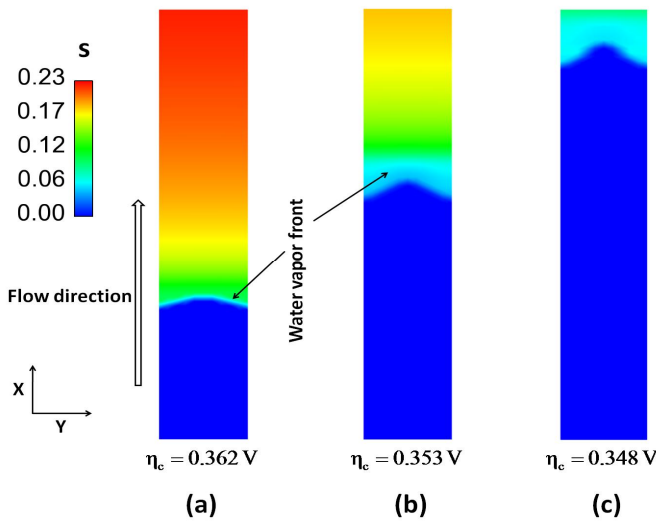


Figure 4-7: Distributions of the liquid water saturation at the middle cross-section ( $Z=4.15 \times 10^{-4}$ ) of the GC at different stoichiometric ratios: (a)  $\xi_c = 2.0$ , (b)  $\xi_c = 3.0$ , (c) and  $\xi_c = 4.0$  (operating conditions:  $RH = 66\%$ ,  $s_{im} = 0$ , and  $I_{ave} = 0.5 \text{ A cm}^{-2}$ ).

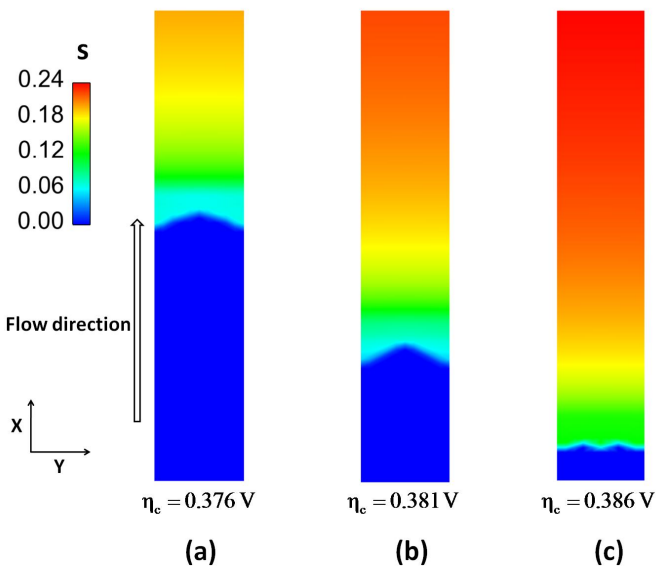


Figure 4-8: Distributions of the liquid water saturation at the middle cross-section ( $Z=4.15 \times 10^{-4}$ ) of the GC at different inlet relative humidity: (a)  $RH = 46\%$ , (b)  $RH = 66\%$ , (c) and  $RH = 86\%$  (operating conditions:  $\xi_c = 2.0$ ,  $s_{im} = 0$ , and  $I_{ave} = 0.8 \text{ A cm}^{-2}$ ).

Fig. 4-8 illustrates the influence of the inlet air relative humidity on the liquid water distribution at the middle cross-section ( $Z=4.15 \times 10^{-4}$  m) of the GC. Three different values of relative humidity are assigned, namely, 46%, 66%, and 86%. The operating conditions are:  $\xi_c = 2.0$ ,  $s_{im} = 0$ , and  $I_{ave} = 0.8 \text{ A cm}^{-2}$ . At the low relative humidity of 46% (Fig. 8a), only less than half GC is flooded by the liquid water, and most generated water is removed out of the GC in the

water vapor form as mentioned above. As a consequence, we get the minimum cathode overpotential of 0.376 V in all three cases. However, it is worth noting that low relative humidity would result in the membrane dehydration mainly at the inlet portion, which decreases the cell performance. From Fig. 4-8, we also can see that more and more liquid water accumulates in the GC with the increase of the inlet relative humidity. Although increasing the inlet relative humidity can slightly increase the gas flow rate at the same current density and stoichiometric ratio, the phase change dominates the liquid water flooding in the GC. Therefore, we obtain the maximum water saturation up to 0.24, when the inlet relative humidity equals to 86% (Fig. 8c). And, almost all the GC is flooded by the liquid water. Comparison between Fig. 8b and Fig. 4-7a shows that increasing the current density from 0.5 to 0.8 A cm<sup>-2</sup> gives the indiscernible change of the GC flooding. This is attributed to the fact that the high current density corresponds to the high gas flow rate, which can drag more liquid water out of the channel.

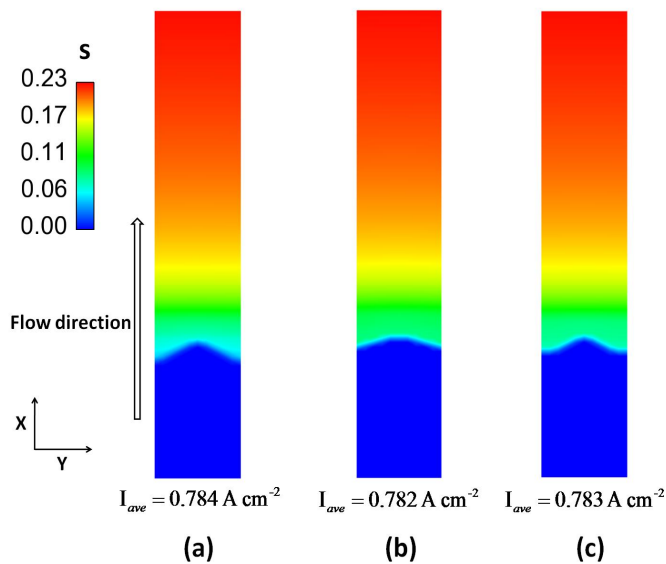


Figure 4-9: Distributions of the liquid water saturation at the middle cross-section ( $Z=4.15 \times 10^{-4}$ ) of the GC at different GC contact angles: (a)  $\theta = 60^\circ$ , (b)  $\theta = 80^\circ$ , and (c)  $\theta = 110^\circ$  (operating conditions:  $RH = 66\%$ ,  $\xi_c = 2.0$ ,  $s_{in} = 0$ , and  $\eta_c = 0.38$  V).

In this work, we apply Eq. 4-9 to track the liquid water flooding in the GC as a first attempt. By examining Eq. 4-9, we can see that two mechanisms determine the liquid water transport in the GC, namely, gas drag force and capillary action. However, their magnitudes strongly depend on the assumed material properties, such as GC contact angle and relative permeability for each phase. In what follows, we evaluate the sensitivity of the simulated GC flooding to these assumed material properties. Fig. 4-9 shows the contact angle effect on the liquid water distribution at the middle cross-section ( $Z=4.15 \times 10^{-4}$  m) of the GC. It needs to note that the real GC normally comprises of the hydrophilic sidewalls and is enclosed by the hydrophobic GDL surface. However, in this work, we lump all the wettability features to a GC contact angle. From Fig. 4-9 it can be seen that the liquid water flooding in the GC is insensitive to the contact angle at the fixed cathode overpotential of 0.38 V. This indicates that the capillary action is not the dominant mechanism of the liquid water transport in the GC.

Fig. 4-10 demonstrates the sensitivity of the liquid water flooding to the gas drag coefficient in the GC. According to Eq. 4-9, we can see that the gas drag effect is directly determined by the

relative permeabilities for both phases in the GC. By adjusting the exponent  $n_2$  in the definition of the relative permeability, we can evaluate the gas drag effect on the liquid water flooding in the GC. Fig. 4-10 shows that the GC flooding is very sensitive to the applied material property  $n_2$ . With the decrease of  $n_2$ , more and more liquid water is swept out of the channel by the gas flow. This indicates that proper estimation of the gas drag force is crucial to the GC flooding model used in this work. When the GC is assumed to be a structured porous media, the nominal relative permeability for each phase cannot be only a function of water saturation, but also of other variables (such as, gas flow rate and current density). Maybe experimental data can help fit an empirical formulation.

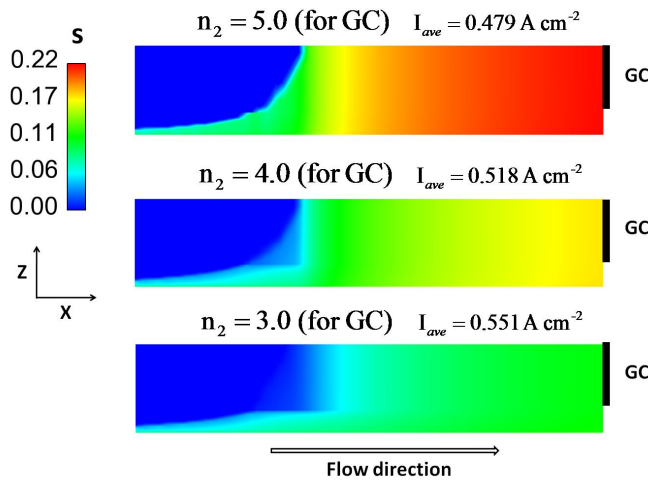


Figure 4-10: Impact of the gas drag coefficient on the water saturation distributions at the middle cross-section ( $Y=1.0 \times 10^{-3} \text{ m}$ ) of the cathode side (operating conditions:  $RH = 66\%$ ,  $\xi_c = 2.0$ ,  $s_{im} = 0$ , and  $\eta_c = 0.36 \text{ V}$ ).

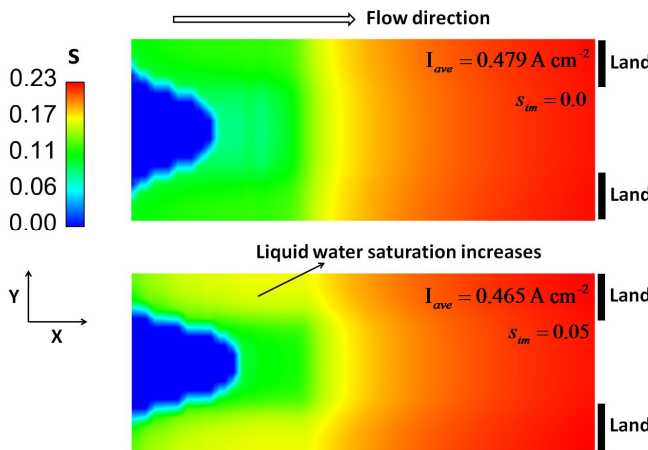


Figure 4-11: Effect of the immobile saturation on the liquid water distribution at the middle cross-section ( $Z=9.0 \times 10^{-5} \text{ m}$ ) of the GDL (operating conditions:  $RH = 66\%$ ,  $\xi_c = 2.0$ , and  $\eta_c = 0.36 \text{ V}$ ).

### 4.3.2 Immobile saturation effect

The immobile saturation could be an important parameter in the modeling of liquid water transport in the diffusion layers. Before the liquid water forms conducting pathways (i.e. the water saturation is less than  $s_{im}$ ), its relative permeability equals to zero; otherwise, the effective

saturation is employed in the relative permeability-saturation correlation. Since the gas phase is always continuous throughout the whole domain, its relative permeability is given by Eq. 4-16. Ju<sup>46</sup> used the effective saturation in the capillary pressure-saturation correlation. However, it is better to work with the actual water saturation  $s$  as shown in Eq. 4-15.

As stated earlier, the immobile saturation depends on the flow conditions and microstructure of porous media, normally an approximate value is assigned to it. In this work, we assign a constant value of 0.05 to the immobile saturation, and investigate its effect on the liquid water distribution in the diffusion layers. It needs to point out that when the immobile saturation is taken into account, the exponent  $n_2$  should be corrected to fit experimental data. However, due to the absence of experimental data, we keep it unchanged as a first attempt.

Fig. 4-11 shows the effect of the immobile saturation on the liquid water distribution at the middle cross-section ( $Z=9.0\times 10^{-5}$ ) of the GDL. The operating conditions are:  $RH=66\%$ ,  $\xi_c=2.0$ , and  $\eta_c=0.36$  V. When considering the immobile saturation (lower one), more liquid water resides in the diffusion layers. As a result, the current density decreases slightly. Unlike the GC flooding, the immobile saturation does not change the tendency of the liquid water distribution along the flow direction. It only increases the flooding level in the diffusion layers.

## 4.4 Conclusions

A two-phase flow model for the cathode side of a PEFC has been developed in this work. The salient feature is that we assume the GC to be a structured porous medium; then, the liquid water flooding in the GC can be modeled by the two-phase Darcy's law as a first attempt. We investigate the GC flooding under different operating conditions, and its impact on the liquid water distribution in the diffusion layers. We also study the effect of the immobile saturation on the predicted liquid water distribution in the diffusion layers. The main findings and conclusions are summarized in the following:

1. Neglecting the GC flooding leads to the incorrect prediction of the liquid water distribution in the diffusion layers, and also overestimates the cell performance.
2. Increasing the stoichiometric ratio does not invoke obvious increase of the gas pressure drop in the GC, since more liquid water can be removed out of the channel under the higher gas flow rate. This indicates that practically we can optimize the gas flow rate to achieve the best cell performance.
3. Decreasing the relative humidity of the inlet gas can mitigate the GC flooding, since more liquid is transported out of the channel in the water vapor form. However, a proper selection of relative humidity is needed to balance two requirements: preventing the membrane dehydration, and mitigating the GC flooding.
4. The gas flow is the main driving force for the liquid water transport in the GC. The liquid water flooding in the GC is insensitive to the capillary action.
5. When considering the immobile saturation in the model, more liquid water is predicted to be in the diffusion layers, and the cell performance decreases slightly.

## References

- [1] M.M. Mench, *Fuel Cell Engines*, John Wiley & Sons, 2008.
- [2] G. Hoogers, *Fuel Cell Technology Handbook*, CRC Press, 2003.
- [3] C.Y. Wang, Fundamental models for fuel cell engineering, *Chem. Rev.* 104 (2004) 4727-4765.
- [4] H. Li, Y. Tang, Z. Wang, A review of water flooding issues in the proton exchange membrane fuel cell, *J. Power Sources* 178 (2008) 103-117.
- [5] A.Z. Weber, J. Newman, Modeling transport in polymer-electrolyte fuel cells, *Chem. Rev.* 104 (2004) 4679-4726.
- [6] I.S. Hussaini, C.Y. Wang, Visualization and quantification of cathode channel flooding in PEM fuel cells, *J. Power Sources* 187 (2009) 444-451.
- [7] I. Manke, C. Hartnig, M. Grünerbel et al., Investigation of water evolution and transport in fuel cells with high resolution synchrotron x-ray radiography, *Appl. Phys. Lett.* 90, 174105 (2007).
- [8] Y. Wang, S. Basu, C.Y. Wang, Modeling two-phase flow in PEM fuel cell channels, *J. Power Sources* 179 (2008) 603-617.
- [9] S. Basu, J. Li, C.Y. Wang, Two-phase flow and maldistribution in gas channel of a polymer electrolyte fuel cell, *J. Power Sources* 187 (2009) 431-443.
- [10] I. Manke, C. Hartnig, N. Kardjilov et al., Characterization of water exchange and two-phase flow in porous gas diffusion materials by hydrogen-deuterium contrast neutron radiography, *Appl. Phys. Lett.* 92, 244101 (2008).
- [11] R. Satija, D.L. Jacobson, M. Arif, S.A. Werner, In situ neutron imaging technique for evaluation of water management systems in operating PEM fuel cells, *J. Power Sources* 129 (2004) 238-245.
- [12] T. Ous, C. Arcoumanis, Visualization of water accumulation in the flow channels of PEMFC under various operating conditions, *J. Power Sources* 187 (2009) 182-189.
- [13] F.Y. Zhang, X.G. Yang, C.Y. Wang, Liquid water removal from a polymer electrolyte fuel cell, *J. Electrochem. Soc.* 153 (2) A225-A232 (2006).
- [14] B. Gao, T.S. Steenhuis, Y. Zevi et al., Visualization of unstable water flow in a fuel cell gas diffusion layer, *J. Power Sources* 190 (2009) 493-498.
- [15] I.S. Hussaini, C.Y. Wang, Measurement of relative permeability of fuel cell diffusion media, *J. Power Sources* 195 (2010) 3830-3840.
- [16] B.R. Sivertsen, N. Djilali, CFD-based modeling of proton exchange membrane fuel cells, *J. Power Sources* 141 (2005) 65-78.
- [17] N. Djilali, Computational modeling of polymer electrolyte membrane (PEM) fuel cells: Challenges and opportunities, *Energy* 32 (2007) 269-280.
- [18] K.J. Lee, J.H. Nam, C.J. Kim, Pore-network analysis of two-phase water transport in gas diffusion layers of polymer electrolyte membrane fuel cells, *Electrochim. Acta* 54 (2009) 1166-1176.
- [19] L. Mao, C.Y. Wang, Y. Tabuchi, A multiphase model for cold start of polymer electrolyte fuel cells, *J. Electrochem. Soc.* 154 (3) B341-B351 (2007).
- [20] P. Zhou, C.W. Wu, Liquid water transport mechanism in the gas diffusion layer, *J. Power Sources* 195 (2010) 1408-1415.

- [21] P.K. Sinha, P.P. Mukherjee, C.Y. Wang, Impact of GDL structure and wettability on water management in polymer electrolyte fuel cells, *J. Mater. Chem.* 17 (2007) 3089-3103.
- [22] T. Berning, N. Djilali, A 3D, multiphase, multicomponent model of the cathode and anode of a PEM fuel cell, *J. Electrochem. Soc.* 150 (12) A1589-A1598 (2003).
- [23] X.D. Niu, T. Munekata, S.A. Hyodo, K. Suga, An investigation of water-gas transport processes in the gas-diffusion-layer of a PEM fuel cell by a multiphase-relaxation-time lattice Boltzmann model, *J. Power Sources* 172 (2007) 542-552.
- [24] X. Liu, W. Tao, Z. Li, Y. He, Three-dimensional transport model of PEM fuel cell with straight flow channels, *J. Power Sources* 158 (2006) 25-35.
- [25] Z. Shi, X. Wang, A numerical study of flow crossover between adjacent flow channels in a proton exchange membrane fuel cell with serpentine flow field, *J. Power Sources* 185 (2008) 985-992.
- [26] G.F. Pinder, W.G. Gray, *Essentials of Multiphase Flow and Transport in Porous Media*, John Wiley & Sons, 2008.
- [27] W. He, J.S. Yi, T.V. Nguyen, Two-phase flow model of the cathode of PEM fuel cells using interdigitated flow fields, *AIChE J.* 46 (2000) 2053-2064.
- [28] W. Yuan, Y. Tang, M. Pan, Z. Li, B. Tang, Model prediction of effects of operating parameters on proton exchange membrane fuel cell performance, *Renewable Energy* 35 (2010) 656-666.
- [29] Q. Ye, T.V. Nguyen, Three-dimensional simulation of liquid water distribution in a PEMFC with experimentally measured capillary functions, *J. Electrochem. Soc.* 154 (12) (2007) B1242-B1251.
- [30] V. Guran, R.V. Edwards, J.A. Mann et al, A look at the multiphase mixture model for PEM fuel cell simulations, *Electrochem. Solid-State Lett.* 11 (8) B132-B135 (2008).
- [31] C.Y. Wang, Comment on "A look at the multiphase mixture model for PEM fuel cell simulations", *Electrochem. Solid-State Lett.* 12 (8) S2-S3 (2009).
- [32] Y. Wang, Modeling of two-phase transport in the diffusion media of polymer electrolyte fuel cells, *J. Power Sources* 185 (2008) 261-271.
- [33] H. Meng, A three-dimensional mixed-domain PEM fuel cell model with fully-coupled transport phenomena, *J. Power Sources* 164 (2007) 688-696.
- [34] Y. Wang, C.Y. Wang, K.S. Chen, Elucidating differences between carbon paper and carbon cloth in polymer electrolyte fuel cells, *Electrochim. Acta* 52 (2007) 3965-3975.
- [35] C.Y. Wang, P. Cheng, A multiphase mixture model for multiphase multicomponent transport in capillary porous media-1. Model development, *Int. J. Heat Mass Transfer* 39 (1996) 3607-3618.
- [36] C.Y. Wang, C. Bechermann, A two-phase mixture model of liquid-gas flow and heat transfer in capillary porous media-1. Formulation, *Int. J. Heat Mass Transfer* 36 (1993) 2747-2758.
- [37] N. Khajeni-Hosseini-Dalasm, K. Fushinobu, K. Okazaki, Phase change in the cathode side of a proton exchange membrane fuel cell, *J. Power Sources* 195 (2010) 7003-7010.
- [38] T. Berning, M. Odgaard, S.K. Kær, A computational analysis of multiphase flow through PEMFC cathode porous media using the Multifluid approach, *J. Electrochem. Soc.* 156 (11) B1301-B1311 (2009).
- [39] D. Song, Q. Wang, Z.S. Liu, C. Huang, Transient analysis for the cathode gas diffusion layer of PEM fuel cells, *J. Power Sources* 159 (2006) 928-942.

- [40] H. Meng, C.Y. Wang, Model of two-phase flow and flooding dynamics in polymer electrolyte fuel cells, *J. Electrochem. Soc.* 152 (9) A1733-A1741 (2005).
- [41] H. Ju, Investigation of the effects of the anisotropy of gas-diffusion layers on heat and water transport in polymer electrolyte fuel cells, *J. Power Sources* 191 (2009) 259-268.
- [42] X. Liu, G. Lou, Z. Wen, Three-dimensional two-phase flow model of proton exchange membrane fuel cell with parallel gas distributors, *J. Power Sources* 195 (2010) 2764-2773.
- [43] J.E. Dawes, N.S. Hanspal, O.A. Family, A. Turan, Three-dimensional CFD modeling of PEM fuel cells: An investigation into the effects of water flooding, *Chem. Eng. Sci.* 64 (2009) 2781-2794.
- [44] S.M. Hassanizadeh, W.G. Gray, Mechanics and thermodynamics of multiphase flow in porous media including interface boundaries, *Adv. Water Res.* 13 (1990) 169-186.
- [45] S.M. Hassanizadeh, M.A. Celia, H.K. Dahle, Dynamic effect in the capillary pressure-saturation relationship and its impacts on unsaturated flow, *Vadose Zone J.* 1 (2002) 38-57.
- [46] H. Ju, Analyzing the effects of immobile liquid saturation and spatial wettability variation on liquid water transport in diffusion media of polymer electrolyte fuel cells (PEFCs), *J. Power Sources* 185 (2008) 55-62.
- [47] G. Lin, W. He, T.V. Nguyen, Modeling liquid water effects in the gas diffusion and catalyst layers of the cathode of a PEM fuel cell, *J. Electrochem. Soc.* 151 (12) A1999-A2006 (2004).
- [48] N.A. Mortensen, F. Okkels, H. Bruus, Reexamination of Hagen-Poiseuille flow: Shape dependence of the hydraulic resistance in microchannels, *Phys. Rev. E* 71, 057301 (2005).

Table 4-1: *Source terms of the conservation equations in different regions on the cathode side.*

Computational domain	$S_g$	$S_m$	$S_{O_2}$	$S_{H_2O}$	$S_l$
GC	$-R_l$	$-\frac{\mu_g}{k_{GC}k_{rg}}\vec{V}_g$	0	$-R_l$	$R_l$
GDL	$-R_l$	$-\frac{\mu_g}{k_{GDL}k_{rg}}\vec{V}_g$	0	$-R_l$	$R_l$
CL	$-R_l - \frac{j_c}{4F}M_{O_2}$	$-\frac{\mu_g}{k_{CL}k_{rg}}\vec{V}_g$	$-\frac{j_c}{4F}M_{O_2}$	$-R_l$	$R_l + \frac{j_c(1+2a)}{2F}M_{H_2O}$

Table 4-2: Geometrical, physical and operating parameters.

Parameter	Value
GC width/height/length	1.0/0.5/100 mm
Shoulder width	1.0 mm
GDL/CL thickness	0.15/0.015 mm
GC/GDL/CL porosity, $\varepsilon$	1.0/0.6/0.4
GC/GDL/CL intrinsic permeability, $k_0$	$1.4 \times 10^{-8}/3. \times 10^{-12}/3. \times 10^{-14}$ $\text{m}^2$
Cell temperature, $T$	353.15 K
Operating pressure, $P_{ref}$	2 atm
$n_1 / n_3$	2.0 / 2.0 [9]
GDL /CL /GC $n_2$	4.0/4.0/5.0 [9]
Liquid water density, $\rho_l$	972 $\text{kg m}^{-3}$
Dynamic viscosity of liquid water/gas mixture, $\mu$	$3.5 \times 10^{-4}/2.03 \times 10^{-5}$ Pa s [29]
Evaporation rate, $k_{evap}$	$5.0 \times 10^{-5}$ $\text{Pa}^{-1} \text{s}^{-1}$ [29]
Condensation rate, $k_{cond}$	$1.0 \text{ s}^{-1}$ [29]
GC/GDL/CL contact angle, $\theta$	60/120/110 °
Surface tension, liquid-water-air, $\sigma$	0.0625 $\text{N m}^{-1}$
Charge transfer coefficient, $a_c$	1.0
Reference current density $\times$ ratio of reaction surface to catalyst volume on cathode side, $\alpha i_{0,c}^{ref}$	$2.0 \times 10^4$ $\text{A m}^{-3}$
Reference oxygen molar concentration, $Y_{O_2}^{ref}$	40.88 $\text{mol m}^{-3}$
Net water transfer coefficient, $a$	0.0

# Chapter 5 - Polymer Electrolyte Fuel Cell Modeling with Emphasis on the Effect of Gas Diffusion Layer Anisotropy

---

## Abstract

*Numerical modeling can facilitate us to better understand the key transport processes happening in a polymer electrolyte fuel cell (PEFC). In this study, we develop a three-dimensional non-isothermal PEFC model to investigate the liquid water flooding in diffusion layers and the associated heat transfer. More importantly, we illustrate the necessity of considering GDL anisotropy in the PEFC modeling, which has been neglected in most previous numerical studies. Our case studies show that liquid water is absent on the anode side for fully humidified operations, because the water transfer through the membrane due to the electro-osmotic drag is more dominant than that due to the back diffusion. In the cathode diffusion layers, high water saturation locates underneath the land due to the large water transport resistance. When relatively small through-plane thermal conductivity instead of anisotropic value is used, the temperature variation along the through- or in-plane direction would be overpredicted considerably. This gives rise to the enhanced phase-change-driven removal of produced water. As a result, the liquid water distribution in the diffusion layers is changed. At last, we demonstrate that increasing the in-plane permeability of GDL can mitigate the liquid water flooding under the land. Consequently, the cell performance slightly increases mainly due to the enhanced mass transfer.*

## 5.1 Introduction

Polymer electrolyte fuel cells (PEFCs) directly converting chemical energy into electricity are attracting more and more attention due to their salient features, like high efficiency, low pollution, quick startup, and low operating temperatures<sup>1</sup>. In an operating PEFC, water plays a significant role in the proton migration through the membrane. However, excessive water accumulation would hamper the reactant diffusion and also covers the catalyst pellets, resulting in the reduced cell performance. So, it is essential to bring about a delicate water balance inside a PEFC<sup>2</sup>. On one hand, the membrane should keep high water content to transport protons effectively; on the other hand, severe liquid water flooding in both diffusion layers and gas channels can be avoided.

Several distinct mechanisms of water transport can be involved simultaneously in an operating PEFC. In the solid electrolyte (e.g. Nafion), three kinds of water transport coexist, namely, electro-osmotic drag (EOD) associated with proton migration, back diffusion owing to water concentration gradient, and hydraulic permeation driven by pressure gradient<sup>3, 4</sup>. To prevent the membrane dehydration, water vapor is commonly delivered into the fuel cell along with the reactants on both sides. In addition, some water is generated from the oxygen reduction reaction (ORR) in the cathode electrode. As a consequence, a complicated two-phase flow regime involving gas mixture and liquid water appears whenever the local water vapor pressure reaches its saturation value. It is worth pointing out that in PEFCs, water transport is intricately coupled with heat transport through phase change<sup>5</sup>.

Two-phase flow in a PEFC can occur in three different zones<sup>6</sup>: (1) transport in the catalyst layer (CL), (2) transport in the gas diffusion layer (GDL), and (3) transport in the micro gas channel (GC). The well-known two-phase Darcy's law<sup>7</sup> has been widely employed to describe the liquid water transport in the diffusion layers. However, some researchers argued that the two-phase Darcy's law is not applicable to the thin GDL, since it violates the concept of the representative elementary volume (REV) in the through-plane direction<sup>8</sup>. This means that a new mathematical description of the two-phase flow in the GDL should be developed, which may be an active research topic in the future. Liquid water dynamics is also quite complex in the GC due to its small dimensions and mixed-wettability. In particular, it is extremely hard to formulate the water dynamics in the GC at the macro scale, since several totally different flow patterns can coexist in the GC, such as corner film flow, slug and droplet movement, as well as channel clogging<sup>9, 10</sup>. Apart from water transport in the diffusion layers and GCs, attention should be paid to the interactive couplings of liquid water transport between different components, like the coupling at the GC-GDL interface<sup>11</sup>.

For better water management, both experimental and numerical studies have considerably contributed to the understanding of two-phase flow mechanisms in PEFCs. In what follows, we present a brief review of the developments in numerical modeling of PEFCs. For the reviews on experimental studies, one can refer to<sup>12, 13</sup>. He et al.<sup>14</sup> developed a two-dimensional two-phase flow model to study the liquid water transport on the cathode side. The authors simplified the two-phase Darcy's equation of the liquid water transport by introducing two constants, which represented the gas drag force and capillary action. Lin et al.<sup>15</sup> used unsaturated flow theory (UFT) to model the liquid water transport in the diffusion layers under isothermal conditions. Recently, Ye and Nguyen<sup>16</sup> presented a three-dimensional PEFC model with experimentally measured capillary functions. In this model, the authors implemented the major physical processes like charge transport, electrochemical reactions, and heat transfer. The liquid water transport equation was derived from the two-phase Darcy's law, and coupled with the gas mixture flow by a non-equilibrium phase change. Another model that has been extensively employed in the numerical modeling of PEFCs over the past decade is the multiphase mixture ( $M^2$ ) model<sup>17-20</sup>. It is claimed that the  $M^2$  model is equivalent to the two-phase Darcy's law in the context of capillary-dominated multiphase flow in porous media. By examining the  $M^2$  model, it can be seen that several definitions (e.g. mixture density and pressure) play an important role in its formulation. This model lumps water vapor with liquid water into one saturation variable, and recovers them in the post-processing, based on the local phase equilibrium assumption. Wang et al.<sup>21</sup> first implemented the  $M^2$  model for the cathode side of a PEFC, assuming the CL to be an interface.

The authors demonstrated that the  $M^2$  model was capable of capturing essential two-phase flow features in the GDL, and simulated the coexistence of single- and two-phase flow regimes. Pasaogullari and Wang<sup>22</sup> compared the  $M^2$  modeling with the UFT in a one-dimensional half cell model. They showed that the gas-driving force in the GDL impacted both oxygen concentration and liquid water distributions considerably. Wang<sup>23</sup> also applied the  $M^2$  model to a whole PEFC, and studied the liquid water flooding in the diffusion layers on both sides at low-humidity operating conditions.

The liquid water flooding in GCs, which is one of the most important issues in the water management of PEFCs, is a complex process and difficult to model. In the past few years, several interface-tracking techniques have been used to explore the fundamentals of water dynamics in GCs. Theodorakakos et al.<sup>24</sup> used the volume of fluid (VOF) method to study the detachments of water droplets from GDL surfaces. Zhu et al.<sup>25</sup> also adopted the VOF method in FLUENT to study the dynamic process of a water droplet emerging from a GDL pore. Hao and Cheng<sup>26</sup> used the Lattice Boltzmann Method (LBM) to study the formation and subsequent movement of a water droplet on GDL surface. Choi and Son<sup>27</sup> employed the level set method to investigate the droplet motion in a GC with different contact angles. However, these simulations only focused on the dynamics of a single droplet in a small part of GC, which are not ready to be extended into realistic applications due to the prohibitive computational efforts. On the other hand, it is not straightforward to couple them with the water flooding in diffusion layers due to the differences in scale. Most recently, Basu<sup>28</sup> proposed to apply the two-phase Darcy's law to the GC by assuming it to be a structured porous medium with unit porosity. This made the coupling of liquid water transport at the GC-GDL interface straightforward. They compared their modeling results with experimental data in terms of gas pressure drops and interfacial coverage ratios, and good matches were obtained.

In this chapter, we develop a three-dimensional non-isothermal PEFC model to explore the liquid water flooding in diffusion layers. In particular, we stress the effect of anisotropic GDL permeability and thermal conductivity on water and heat transfer, which has been neglected in most previous numerical studies. Up to now, only a few researches<sup>29, 30</sup> have investigated this influence. Pasaogullari et al.<sup>29</sup> were the first to implement anisotropic GDL in their half cell model, which included only cathodic GC and GDL. Ju<sup>30</sup> used the  $M^2$  model to study the effect of anisotropic thermal conductivity of the GDL on the water and heat transfer in a PEFC. The structure of this paper is given as follows: first, we describe the mathematical model; then, several case studies are conducted to elucidate the two-phase transport in a PEFC, as well as the effect of GDL anisotropy; finally, some concluding remarks are presented.

## 5.2 Mathematical model

Fig. 5-1a shows the computational domain used in this work, which represents a PEFC unit with two parallel GCs. In this section, we describe the mathematical model for simulating the electrochemical and transport mechanisms in all of the key components, such as the CLs and membrane. The main assumptions made in our model for numerical simplicity are as follows:

1. Ideal gas law is applicable to the gas mixture, and gaseous species diffusion in the liquid water is neglected.

2. The membrane and CLs are regarded to be isotropic and homogeneous.
3. The laminar flow is assumed due to small pressure gradients.
4. No liquid water exists in the GCs, corresponding to the mist flow assumption.
5. Local thermal equilibrium prevails in the whole domain.
6. Latent heat released from phase changes is neglected.

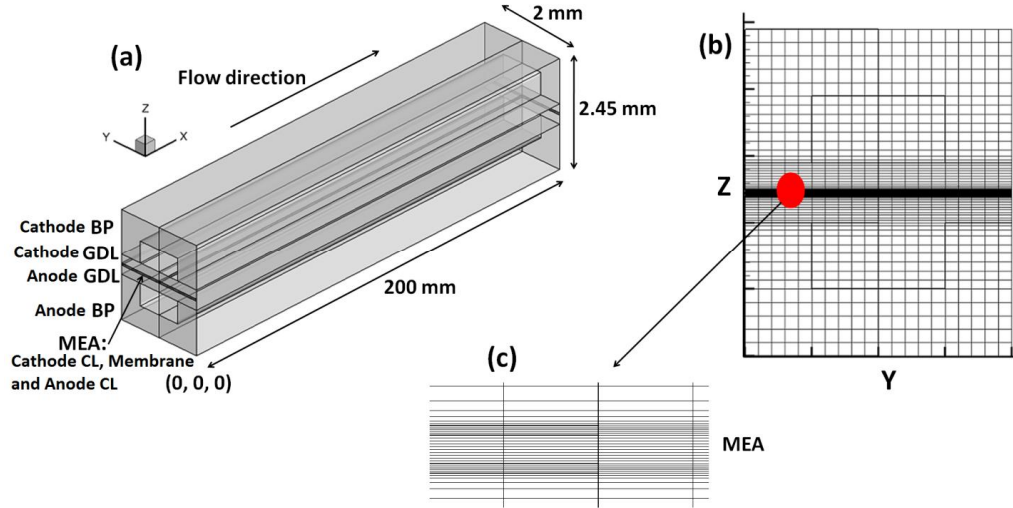
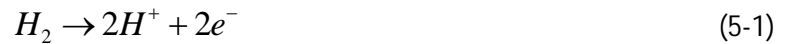


Figure 5-1: (a) Computational domain (i.e. single PEFC unit) used in this work,  $X$  denotes the flow direction,  $Y$  denotes the in-plane direction, and  $Z$  denotes the through-plane direction; (b) the corresponding mesh in the  $Y$ - $Z$  plane; (c) the MEA mesh.

### 5.2.1 Electrochemical kinetics

In an operating PEFC, humidified hydrogen and oxygen are delivered into the GCs on the anode and cathode sides, respectively. The hydrogen diffuses through the anode GDL into the CL, where each hydrogen molecule splits into two electrons and two protons according to the following reaction:



Eq. 5-1 is called the hydrogen oxidation reaction (HOR). The generated protons migrate into the cathode CL via the membrane, while the electrons have to travel through an external circuit to do useful work. On the cathode side, the oxygen also diffuses into the cathode CL, where it combines with the protons from the membrane and the electrons from the external circuit to form water and heat, expressed as:



Eq. 5-2 is referred to as the oxygen reduction reaction (ORR). Note that Eq. 5-1 and Eq. 5-2 are the main reaction steps, and a number of intermediate steps are neglected for simplicity.

The Tafel kinetics<sup>23</sup> is employed to describe the above two half reactions:

$$\text{HOR in the anode CL: } j_a = (1-s)^{n_1} ai_{0,a}^{ref} \left( \frac{C_{H_2}}{C_{H_2}^{ref}} \right)^{1/2} \left( \frac{\alpha_a + \alpha_c}{RT} F \eta \right) \quad (5-3)$$

$$\text{ORR in the cathode CL: } j_c = -(1-s)^{n_1} ai_{0,c}^{ref} \left( \frac{C_{O_2}}{C_{O_2}^{ref}} \right) \exp \left( -\frac{\alpha_c}{RT} F \eta \right) \quad (5-4)$$

Here,  $j_a$  and  $j_c$  denote the anode and cathode volumetric current densities, respectively, exponent  $n_1$  is used to account for the presence of liquid water, and  $\eta$  represents the surface overpotential, which is defined as<sup>23</sup>:

$$\eta = \phi_e - \phi_i - U_0 \quad (5-5)$$

where  $\phi_e$  is the electrical potential,  $\phi_i$  is the ionic potential, and  $U_0$  denotes the equilibrium potential. The equilibrium potential is zero in the anode, whereas in the cathode it is given by<sup>31</sup>:

$$U_0 = 1.23 - 9 \times 10^{-4} (T - 298.15) \quad (5-6)$$

In a PEFC, the ORR is sluggish, thus giving rise to high cathode overpotential. The temperature dependence of the ORR kinetic parameter can be approximated as<sup>30</sup>:

$$ai_{0,c}^{ref}(T) = ai_{0,c}^{ref}(353K) \cdot \exp \left[ -\frac{E_a}{R} \left( \frac{1}{T} - \frac{1}{353.15} \right) \right] \quad (5-7)$$

The electrical transport equation is used to describe the electron movement in a PEFC (i.e. BP, GDL, and CL), which is given as:

$$0 = \nabla \cdot (\sigma_e \nabla \phi_e) + S_e \quad (5-8)$$

where  $\sigma_e$  is the electrical conductivity, and  $S_e$  denotes the source/sink term in the CLs, due to the electron generation or consumption.

The ionic transport equation in the electrolyte can be given as:

$$0 = \nabla \cdot (\sigma_i \nabla \phi_i) + S_i \quad (5-9)$$

where  $\sigma_i$  is the ionic conductivity and  $S_i$  denotes the proton source/sink term. The ionic conductivity strongly depends on the water content in the electrolyte. In the Nafion, it can be given by the following expression measured by Springer et al.<sup>32</sup>:

$$\sigma_i = (0.5139\lambda - 0.326) \exp \left[ 1268 \left( \frac{1}{303} - \frac{1}{T} \right) \right] \quad (5-10)$$

In the CLs, the effective ionic conductivity can be approximated by Bruggeman correlation<sup>30</sup>:

$$\sigma_i^{eff} = \varepsilon_e^{1.5} \sigma_i \quad (5-11)$$

where  $\varepsilon_e$  denotes the ionomer volume fraction in the CLs.

## 5.2.2 Gas phase transport

In a PEFC, the gas transport equations are solved in the GCs, GDLs and CLs, and we neglect the species crossover in the membrane. First, the mass conservation of the gas phase is given as:

$$\nabla \cdot (\rho_g \bar{V}_g) = S_g \quad (5-12)$$

where  $\rho_g$  denotes the gas mixture density,  $\bar{V}_g$  is the superficial velocity of the gas phase, and  $S_g$  represents the source/sink term due to the phase change and chemical reactions. The ideal gas mixture law is used to calculate the composition-dependent gas phase density as follows:

$$\rho_g = \frac{p_g}{RT \sum_i \frac{w_i}{M_i}} \quad (i = O_2, H_2O, H_2, N_2) \quad (5-13)$$

where  $p_g$  is the gas pressure,  $R$  is the universal gas constant,  $w_i$  is the mass fraction of each species, and  $M_i$  denotes the molecular weight.

The gaseous species transport equation is given as:

$$\nabla \cdot (\rho_g w_i \bar{V}_g) = \nabla \cdot (\rho_g D_i^{eff} \nabla w_i) + S_i \quad (i = O_2, H_2O, H_2) \quad (5-14)$$

where  $S_i$  represents the source/sink term of each species, and  $D_i^{eff}$  is called the effective diffusivity, which can be given by Bruggeman correlation<sup>6</sup>:

$$D_i^{eff} = [(1-s)\varepsilon]^{1.5} D_i \quad (5-15)$$

where  $s$  is the liquid water saturation,  $\varepsilon$  is the porosity, and  $D_i$  denotes the molecular diffusivity, which is given as a function of temperature and pressure<sup>23</sup>:

$$D_i = D_i^{ref} \left( \frac{T}{353} \right)^{1.5} \left( \frac{101325}{p_g} \right) \quad (5-16)$$

In the CLs, the Knudsen diffusion due to the molecular-to-wall collision is taken into account. Therefore, the effective diffusivity is rewritten as<sup>33</sup>:

$$D_{i,CL}^{eff} = [(1-s)\varepsilon]^{1.5} \left( \frac{1}{D_i} + \frac{1}{D_i^k} \right)^{-1} \quad (5-17)$$

in which  $D_i^k$  is the Knudsen diffusion. According to the kinetic theory of gases, it can be computed by<sup>33</sup>:

$$D_i^k = \frac{2}{3} \left( \frac{8RT}{\pi M_i} \right)^{0.5} r_p \quad (5-18)$$

in which  $r_p$  denotes the characteristic pore length of the CLs.

The steady-state momentum equation for the gas phase is expressed as:

$$\rho_g \vec{V}_g \cdot \nabla \vec{V}_g = \nabla \cdot (\mu_g \nabla \vec{V}_g) - \nabla p_g + S_m \quad (5-19)$$

where  $\mu_g$  is the dynamic viscosity of the gas mixture, and  $S_m$  denotes the Darcy's source term accounting for the viscous resistance imposed by the pore structure of porous media and the presence of liquid water in the pore space. In the GCs, the Darcy's source term reduces to zero.

### 5.2.3 Water transport

Three forms of water can coexist in a PEFC, namely, water vapor, liquid water, and dissolved water. Normally, they are closely coupled by phase changes. The water vapor transport is described by Eq. 5-14. In this subsection, we focus on describing the liquid water transport in the diffusion layers and the dissolved water transport in the electrolyte.

The liquid water transport equation can be derived from the two-phase Darcy's law. For more detail, one can refer to our previous paper<sup>6</sup>. The governing equation is as follows:

$$\nabla \cdot \left( \rho_l \frac{k_{rl}}{k_{rg}} \frac{\mu_g}{\mu_l} \vec{V}_g \right) = \nabla \cdot \left( -\rho_l \frac{k_0 k_{rl}}{\mu_l} \nabla p_c \right) + S_l \quad (5-20)$$

Here,  $\rho_l$  is the liquid water density assumed to be constant,  $\mu_l$  is the dynamic viscosity of liquid water,  $k_{rl}$  and  $k_{rg}$  denote the relative permeabilities for the gas and liquid phases, respectively,  $k_0$  denotes the intrinsic permeability,  $S_l$  denotes the source/sink term due to the phase changes, and  $p_c$  represents the macroscopic capillary pressure, defined as:

$$p_c(s) = p_g - p_l \quad (5-21)$$

The capillary pressure can be further expressed as<sup>34</sup>:

$$p_c = \sigma \cos\theta \left( \frac{\varepsilon}{k_0} \right)^{0.5} J(s) \quad (5-22)$$

where  $\sigma$  is the surface tension between gas and liquid water,  $\theta$  is the static contact angle of the porous media of interest, and  $J(s)$  is the well-known Leverett function having the following form:

$$J(s) = \begin{cases} 1.417(1-s) - 2.120(1-s)^2 + 1.263(1-s)^3 & \theta \leq 90^\circ \\ 1.417s - 2.120s^2 + 1.263s^3 & \theta > 90^\circ \end{cases} \quad (5-23)$$

To solve Eq. 5-20, empirical correlations of the relative permeabilities for both phases are needed. Power-form expressions are commonly employed for the sake of simplicity:

$$k_{rg} = (1-s)^{n_2} \quad (5-24)$$

$$k_{rl} = s^{n_2} \quad (5-25)$$

Water transport in the dissolved form also occurs in the solid electrolyte. Three mechanisms govern the transport process, namely, the electro-osmotic drag (EOD), the back diffusion owing to the water concentration gradient, and the hydraulic permeation due to the pressure gradient. When the same operating pressure is used on both sides, we can safely neglect the hydraulic permeation effect. So, we write down the dissolved water transport in the electrolyte as follows:

$$\nabla \cdot \left( -\frac{n_d}{F} \sigma_i \nabla \phi_i \right) = \nabla \cdot \left( D_{H_2O}^{Naf} \frac{\rho_{Naf}}{EW} \nabla \lambda \right) + S_\lambda \quad (5-26)$$

where  $n_d$  denotes the electro-osmotic drag coefficient,  $F$  is the Faraday's constant,  $D_{H_2O}^{Naf}$  is the water diffusivity in the Nafion,  $\rho_{Naf}$  is the mass density of the Nafion,  $EW$  is the equivalent weight of the Nafion,  $\lambda$  is the water content defined as the moles of water per mole of sulfonic acid sites, and  $S_\lambda$  represents the water source/sink term due to the phase changes. Note that the water content and the molar concentration of dissolved water in the Nafion are related by:

$$\lambda = \frac{EW}{\rho_{Naf}} C_{H_2O}^{Naf} \quad (5-27)$$

The electro-osmotic drag coefficient is defined as the number of water molecules carried by each proton, which is dependent on the water content in the electrolyte, given by<sup>16</sup>:

$$n_d = \frac{2.5}{22} \lambda \quad (5-28)$$

The water diffusivity in the Nafion is also a function of water content, given by<sup>16</sup>:

$$D_{H_2O}^{Naf} = \begin{cases} 3.1 \times 10^{-7} \lambda (e^{0.28\lambda} - 1) e^{(-2463/T)} & 0 < \lambda \leq 3 \\ 4.17 \times 10^{-8} \lambda (161e^{-\lambda} + 1) e^{(-2463/T)} & \text{otherwise} \end{cases} \quad (5-29)$$

As stated above, three forms of water transport in a PEFC (refer to Eq. 5-14, 5-20, and 5-26) are coupled by phase changes. In the following, we introduce two non-equilibrium phase change models employed in this work. The first one is to describe the phase change between water vapor and liquid water<sup>15</sup>:

$$S_{phase} = k_{cond} \frac{\varepsilon(1-s)Y_{H_2O}M_{H_2O}}{RT} (Y_{H_2O}p_g - p_{sat})q + k_{evap} \varepsilon s \rho_l (Y_{H_2O}p_g - p_{sat})(1-q) \quad (5-30)$$

$$q = \frac{1 + |Y_{H_2O}p_g - p_{sat}|}{2(Y_{H_2O}p_g - p_{sat})} \quad (5-31)$$

Here,  $k_{cond}$  and  $k_{evap}$  are the condensation and evaporation coefficients, respectively,  $Y_{H_2O}$  is the mole fraction of water vapor,  $q$  is the switch function, and  $p_{sat}$  denotes the water vapor pressure, which can be obtained from the following empirical equation as a function of temperature<sup>34</sup>:

$$\log_{10} \frac{p_{H_2O}^{sat}}{101325} = -2.1749 + 0.02953(T - 273.15) - 9.1837 \times 10^{-5}(T - 273.15)^2 + 1.4454 \times 10^{-7}(T - 273.15)^3 \quad (5-32)$$

We also need to consider the phase change between dissolved water and water vapor and the phase change between dissolved water and liquid water. In the cathode CL, we can write down the source term of the dissolved water as follows:

$$S_{\lambda} = r_c \frac{\rho_{Naf}}{EW} (\lambda_{equi} - \lambda) + \frac{j_c}{2F} \quad (5-33)$$

In Eq. 5-33,  $r_c$  denotes the mass transfer coefficient with the unit of  $s^{-1}$ ,  $\lambda_{equi}$  denotes the equilibrium water content in the Nafion, and  $j_c$  denotes the volumetric current density. The equilibrium water content is determined by the local water activity<sup>16</sup>:

$$\lambda_{equi} = \begin{cases} 1.41 + 11.3a_{H_2O} - 18.8a_{H_2O}^2 + 16.2a_{H_2O}^3 & 0 \leq a_{H_2O} \leq 1 \\ 10.1 + 2.94(a_{H_2O} - 1) & 1 < a_{H_2O} \leq 3 \\ 16.0 & 3 < a_{H_2O} \end{cases} \quad (5-34)$$

where  $a_{H_2O}$  denotes the water activity, defined by:

$$a_{H_2O} = Y_{H_2O} \frac{p_g}{p_{sat}} + 2s \quad (5-35)$$

Now, we can explain the physical meaning of Eq. 5-33. The first term on the right hand side is due to the water exchange (i.e. phase change) between dissolved water and liquid water, and the second term means that the water generated by the chemical reaction is assumed to be in the dissolved form.

## 5.2.4 Heat transport

Based on the local thermal equilibrium assumption, we can write down the global heat transport equation applicable to the whole computational domain:

$$\nabla \cdot (\rho_g c_p T \bar{V}_g) = \nabla \cdot (k_T^{eff} \nabla T) + S_T \quad (5-36)$$

where  $c_p$  denotes the heat capacity of the gas mixture computed by the mixing-law  $c_p = \sum_i w_i c_{p,i}$ ,  $k_T^{eff}$  denotes the effective thermal conductivity, and  $S_T$  denotes the thermal source term due to the chemical reactions and ohmic losses.

In the diffusion layers, the effective thermal conductivity is obtained by:

$$k_T^{eff} = \varepsilon k_T^g + (1 - \varepsilon) k_T^s \quad (5-37)$$

where  $k_T^g$  is the thermal conductivity of the gas mixture, and  $k_T^s$  is the thermal conductivity of the solid material.

In the cathode CL, the heat is mainly generated from the entropy change and irreversible charge transfer:

$$S_T = j_c \left[ \frac{T(\Delta S)}{4F} + \eta \right] \quad (5-38)$$

In the anode CL, the heat is mainly generated from the irreversible charge transfer as:

$$S_T = j_a \eta \quad (5-39)$$

In the membrane, the heat source term is given by:

$$S_T = \frac{i_i^2}{\sigma_i} \quad (5-40)$$

where  $i_i$  denotes the current density in the membrane, computed by:

$$i_i = \sigma_i \frac{\partial \phi_i}{\partial Z} \quad (5-41)$$

Note that Z is the through-plane direction.

Finally, the governing equations solved in this work and the corresponding source/sink terms are summarized in Table 5-1 and Table 5-2, respectively.

### 5.3 Boundary conditions and implementation

As tabulated in Table 5-1, twelve partial differential equations (PDEs) in total are numerically solved associated with unknown variables,  $\vec{V}_g$  (three components),  $p_g$ ,  $w_i$  (three species),  $s$ ,  $T$ ,  $\lambda$ ,  $\phi_e$ , and  $\phi_i$ . In what follows, we describe the imposed boundary conditions.

The inlet gas velocities on both sides are given by:

$$\vec{V}_{in,a} \cdot \vec{n}|_{inlet} = \frac{\xi_a A_m}{C_{H_2} A_{gc}} \frac{I}{2F} \quad (5-42)$$

$$\vec{V}_{in,c} \cdot \vec{n}|_{inlet} = \frac{\xi_c A_m}{C_{O_2} A_{gc}} \frac{I}{4F} \quad (5-43)$$

where  $\xi_a$  and  $\xi_c$  are the stoichiometric ratios on the anode and cathode sides, respectively,  $A_m$  and  $A_{gc}$  are the cross-sectional areas of the membrane and GC, respectively,  $C_{H_2}$  is the inlet molar concentration of hydrogen, and  $C_{O_2}$  denotes the inlet molar concentration of oxygen. Note that the inlet molar concentrations are determined by the inlet gas pressure and relative humidity.

The inlet gas temperature on each side is assumed to be 353 K, and the isothermal boundary condition (353 K) is applied to the outer surfaces of both bipolar plates. At the GC outlet on each side, the pressure boundary condition is employed.

At the wall boundaries, the no-slip and impermeable wall (zero-flux) conditions are imposed.

The electrical potential on the outer surface of the anode bipolar plate is set to zero, while on the outer surface of the cathode bipolar plate, it is specified as:

$$\frac{\partial \phi_i}{\partial Z}|_{cathode} = \frac{I}{\sigma_e} \quad (5-44)$$

The set of steady-state governing equations and boundary conditions given above are discretized by finite volume method with second-order schemes based on the commercial software FLUENT. The well-known SIMPLE (semi-implicit pressure linked equation) algorithm is used for the pressure-velocity coupling, and the algebraic multi-grid (AMG) solver is to solve the resultant linear equations. Four user-defined scalars are implemented to represent the liquid water, electrical and ionic potentials, and dissolved water. In addition, a set of user-defined functions are employed to incorporate the source/sink terms and several material properties. About 152000 computational cells are used to capture the essential physical phenomenon happened in a PEFC. Fig. 5-2b shows the cross-sectional mesh in the Y-Z plane, and Fig. 5-2c shows the mesh density of the MEA. To ensure the numerical convergence, the scaled residual values of all the governing equations are required to be less than  $10^{-8}$ .

## 5.4 Results and discussion

A single PEFC with parallel GCs is chosen for the case studies in this work. Table 5-3 lists the main geometric, physical and operating parameters. The cell has a length of 200 mm to represent typical dimensions used in automotive applications. In order to highlight liquid water flooding in the diffusion layers, we employ the fully humidified inlet gas conditions on both sides, which is also the focused operation in the numerical studies of water flooding in PEFCs. Moreover, we suppress the possibility of liquid water flooding in the GCs by imposing the mist flow assumption. However, it needs to be noted that both liquid water flooding in GCs and coupling at the GC-GDL interface are crucial to a comprehensive PEFC model, to which more efforts should be paid in further studies.

In the first place, we validate our model against experimental data in terms of V-I (voltage vs. current density) curve as shown in Fig. 5-2. The operating conditions are as follows:  $p_0=2$  atm,  $\xi_{c/a}=2.0/1.5$ , and  $RH_{c/a}=100\%/100\%$ . It is seen that excellent agreement between numerical and experimental results is obtained except at the high current densities, where mass transport limitations, mainly owing to the liquid water flooding, dominate the cell polarization. Since the liquid water flooding in the GCs is ignored in this work, some deviations at high current densities are expected as seen in Fig. 5-2.

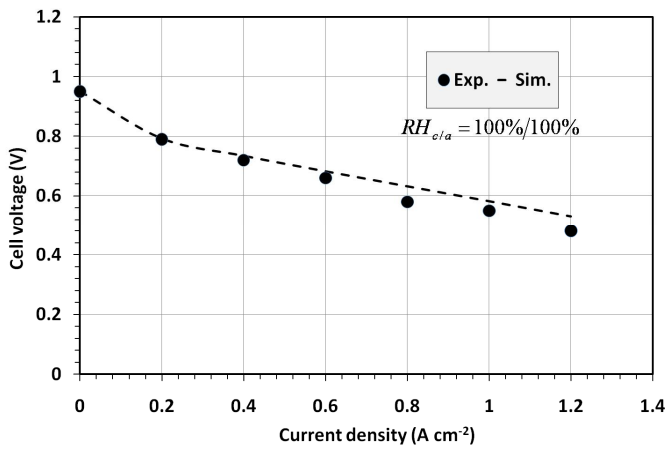


Figure 5-2: Model validation against experimental data (experimental data are extracted from Ref. [23]).

### 5.4.1 Base case study

At the middle cross section with  $Y=1$  mm, Fig. 5-3a shows the distributions of the mole fraction of oxygen at two different current densities, namely,  $0.2$  A cm<sup>-2</sup> and  $0.8$  A cm<sup>-2</sup>. The oxygen gradient along the through-plane direction is much steeper at the high current density, due to the higher oxygen consumption in the cathode CL. Fig. 5-3b shows the oxygen profiles at the middle cross section with  $X=100$  mm. In contrast to the low current density, much smaller mole fraction of oxygen is seen under the land at the current density of  $0.8$  A cm<sup>-2</sup>. This is because the oxygen has to travel a somehow long pathway to reach the region under the land.

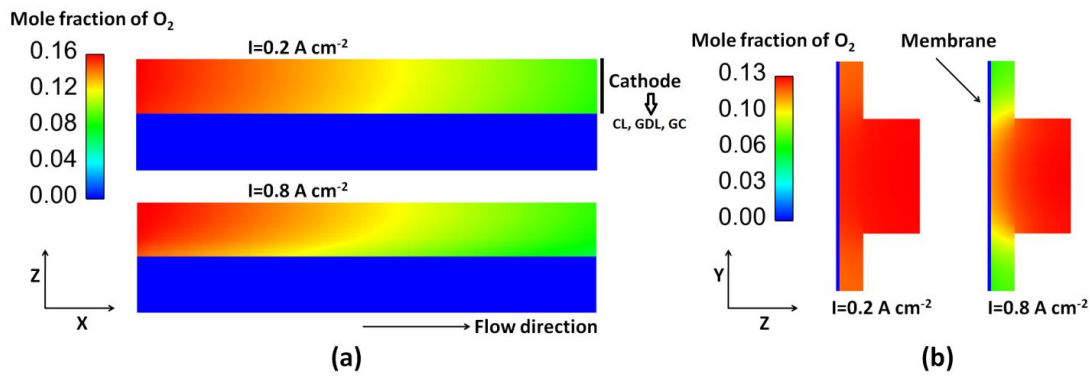


Figure 5-3: Distributions of the mole fraction of oxygen at two different current densities (a) at the middle cross section with  $Y=1 \text{ mm}$ , and (b) at the middle cross section with  $X=100 \text{ mm}$ .

Fig. 5-4 displays the water vapor distributions on both sides at the middle cross section with  $Y=1 \text{ mm}$ . The crossover of gaseous species through the membrane is neglected for simplicity. On the cathode side, the mole fraction of water vapor slightly increases along the flow direction due to the presence of the liquid water in the diffusion layers. We also note that the oversaturated water vapor in GCs has been observed in an operating PEFC [9]. At the low current density (see Fig. 5-4a) the mole fraction of water vapor on the anode side decreases slightly along the flow direction. This indicates that the net water transfer through the membrane is from the anode to the cathode sides. Although hydrogen is consumed in the anode CL, liquid water is absent on the anode side. At the high current density (see Fig. 5-4b), the water transport due to the EOD is more dominant than that due to the back diffusion. As a result, the mole fraction of water vapor on the anode side reduces considerably along the flow direction.

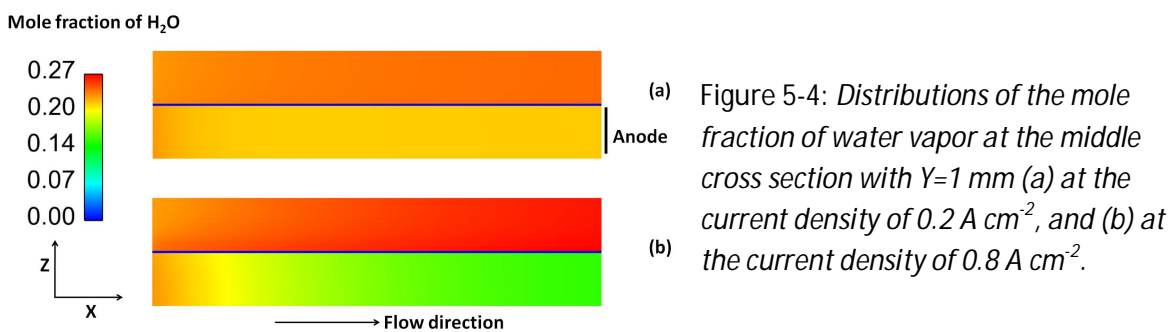


Fig. 5-5a displays the liquid water distributions at the middle cross section of the cathode CL with  $Z=1.245 \text{ mm}$ . The water saturation increases with the increase of current density, since more water is generated from ORR. High water saturation is found underneath the land due to the water transport limitation. Fig. 5-5b shows the liquid water distributions at the middle cross section of the cathode with  $X=100 \text{ mm}$ . At the current density of  $0.8 \text{ A cm}^{-2}$ , a distinct gradient of the water saturation is seen under the channel. However, it should be noted that water flooding in GCs can impact the liquid water distribution in the diffusion layers dramatically [6]. Due to the

absence of appropriate model for GC flooding, in this work we employ the mist flow assumption as mentioned earlier.

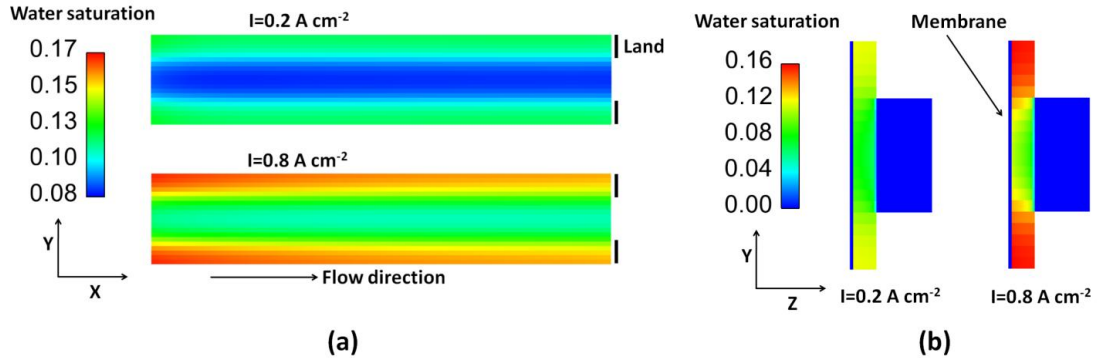


Figure 5-5: Distributions of the water saturation at two different current densities (a) at the middle cross section of the CL with  $Z=1.245 \text{ mm}$ , and (b) at the middle cross section of the cathode with  $X=100 \text{ mm}$ .

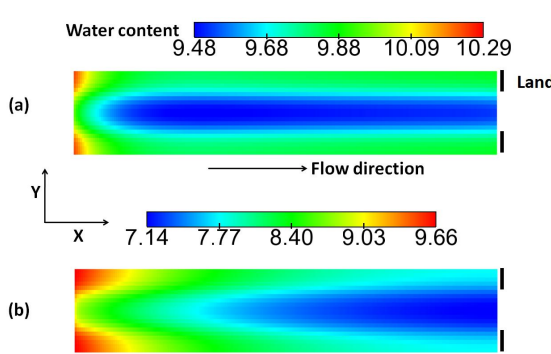


Figure 5-6: Water content distributions at the middle cross section of the membrane with  $Z=1.225 \text{ mm}$  (a) at the current density of  $0.2 \text{ A cm}^{-2}$ , and (b) at the current density of  $0.8 \text{ A cm}^{-2}$ .

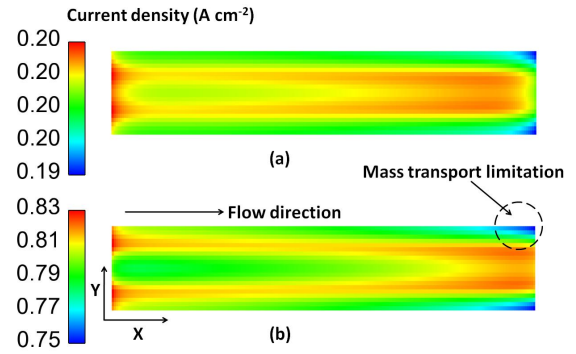


Figure 5-7: Distributions of the current density at the middle cross section of the membrane with  $Z=1.225 \text{ mm}$  (a) at the current density (average) of  $0.2 \text{ A cm}^{-2}$ , and (b) at the current density of  $0.8 \text{ A cm}^{-2}$ .

Fig. 5-6 shows the water content profiles at the middle cross section of the membrane with  $Z=1.225 \text{ mm}$ . In order to reduce the ohmic loss during proton migration, the membrane should be prevented from dehydration. The water content in the membrane mainly depends on the water activities in both CLs, as well as the operating current density. At the low current density of  $0.2 \text{ A cm}^{-2}$  (Fig. 5-6a), the water content decreases slightly along the flow direction owing to the decreased mole fraction of water vapor on the anode side (see Fig. 5-4a). In addition, it is found that the water content under the land is a little higher than that under the channel, which may be attributed to the liquid water distribution in the cathode CL (see Fig. 5-5a). At the high current density of  $0.8 \text{ A cm}^{-2}$  (Fig. 5-6b), the water content at the middle cross section of the membrane

decreases considerably due to the enhanced EOD effect. It indicates that the membrane is prone to being dehydrated at high current densities, especially near the anode side.

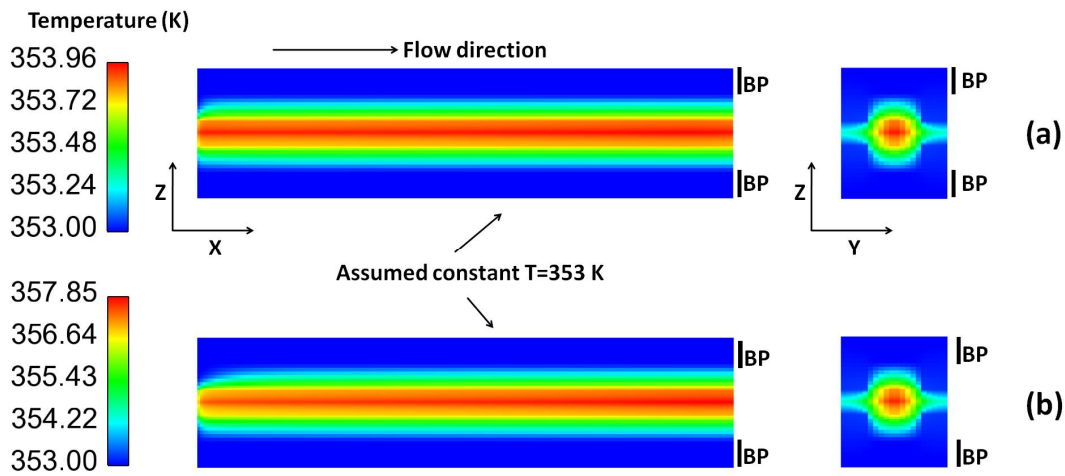


Figure 5-8: Temperature distributions at the middle cross sections with  $Y=1 \text{ mm}$  (left) and with  $X=100 \text{ mm}$  (right), (a) at the current density of  $0.2 \text{ A cm}^{-2}$ , and (b) at the current density of  $0.8 \text{ A cm}^{-2}$ .

For the low operating average current density of  $0.2 \text{ A cm}^{-2}$ , Fig. 5-7a shows the local current density distribution at the middle cross section of the membrane with  $Z=1.225 \text{ mm}$ . It is seen that the variation of the local current densities is quite small. With increasing the current density, however, the transport limitation starts to play an important role in the distribution of the local current densities. As shown in Fig. 5-7b, the electron transport limitation has a major effect on the distribution of the local current densities at the inlet region. As a result, the local current densities under the land are a little higher than those under the channel. In contrast, at the outlet region, the local current densities under the channel are much higher than those under the land due to the mass transport limitation.

Fig. 5-8 shows the temperature distributions at the middle cross sections with  $Y=1 \text{ mm}$  and  $X=100 \text{ mm}$  at two different current densities. In reality, coolant micro-channels are contiguous with bipolar plates (BPs). However, for simplicity we exclude the cooling system in our simulations by imposing a constant temperature of  $353 \text{ K}$  on the outer surfaces of both BPs. The temperature variation is less than  $1 \text{ K}$  at two cross sections at the low current density of  $0.2 \text{ A cm}^{-2}$  (Fig. 5-8a). High temperatures are found in the membrane electrode assemble (MEA) due to the local heat generation, whereas relatively low temperatures in each BP due to its large thermal conductivity. At the high current density of  $0.8 \text{ A cm}^{-2}$ , we have a similar temperature distribution pattern; however, the temperature variation increases considerably up to about  $4 \text{ K}$  at two cross sections (Fig. 5-8b).

## 5.4.2 Effect of GDL anisotropy

In this section, we discuss the effect of GDL anisotropy on the water and heat transfer in a PEFC. For the present, carbon-paper-based GDLs are preferred in automotive applications, which possess distinct anisotropic features in terms of thermal conductivity, permeability, electrical conductivity, and mass diffusivity. In what follows, we concentrate on the influences of anisotropic thermal conductivity and intrinsic permeability. Fig. 5-9 illustrates the effect of the anisotropy in thermal conductivity on the temperature distributions at the middle cross section of the membrane with  $Z=1.225$  mm. The operating current density is set to be  $0.8 \text{ A cm}^{-2}$ . When isotropic GDLs with the through-plane thermal conductivity of  $1.7 \text{ W m}^{-1} \text{ K}^{-1}$  (Table 5-3) are used, the temperature distribution is shown in Fig. 5-9a. The temperature variation at the middle cross section is up to 3.4 K, and relatively low temperature distributes under the land due to the large thermal conductivity of the BPs. In contrast, Fig. 5-9b shows the temperature distribution at the middle cross section of the membrane when GDLs with anisotropic thermal conductivity (in-plane:  $21 \text{ W m}^{-1} \text{ K}^{-1}$ ; and through-plane:  $1.7 \text{ W m}^{-1} \text{ K}^{-1}$ ) are considered<sup>29</sup>. It is clearly seen that the large in-plane thermal conductivity gives rise to almost uniform temperature distribution (about 354.5 K) at the cross section. Therefore, we conclude that it is essential to account for anisotropy in thermal conductivity of GDL to model the heat transfer in a PEFC. Otherwise, the temperature variation would be overpredicted, which in turn affect other transport processes.

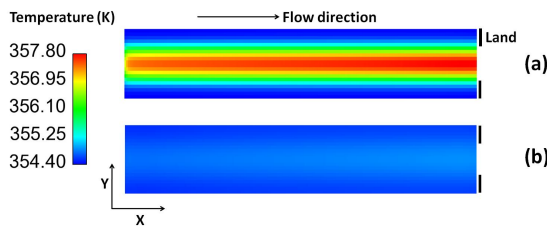


Figure 5-9: *Temperature distributions at the middle cross section of the membrane with  $Z=1.225$  mm, (a) when the through-plane thermal conductivity of the GDL is used, and (b) when the anisotropic thermal conductivity is used.*

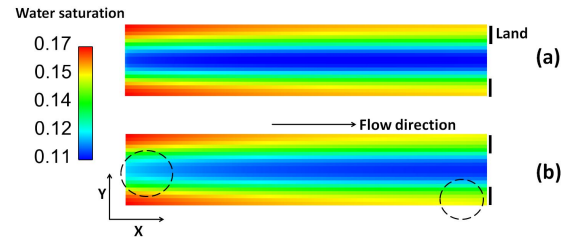


Figure 5-10: *Water saturation distributions at the middle cross section of the CL with  $Z=1.245$  mm at the current density of  $0.8 \text{ A cm}^{-2}$ : (a) when the through-plane thermal conductivity of the GDL is considered, and (b) when the anisotropic thermal conductivity is considered.*

Fig. 5-10 shows the effect of the anisotropic thermal conductivity on the liquid water distribution at the middle cross section of the CL with  $Z=1.245$  mm while the current density is  $0.8 \text{ A cm}^{-2}$ . It is known that phase change plays an important role in the connection between heat and water managements. Under some operating conditions, phase-change-driven removal of product water has been identified as another pivotal mechanism in the water management of PEFCs, besides the conventional view of capillary-driven removal of liquid water. When the through-plane thermal conductivity of the GDL is used, the temperature variations in both in-plane and through-plane directions can be up to around 4 K at high current densities (Fig. 5-8b).

As a result, the water vapor diffusion is enhanced, and the gradient of water saturation from the region under the land to that under the channel is relatively large as shown in Fig. 5-10a. In contrast, the saturation gradient in the in-plane direction decreases slightly while considering the anisotropic thermal conductivity (Fig. 5-10b); this is because the reduced temperature gradient weakens the water vapor diffusion [5]. However, we note that the heat pipe effect on the liquid water distribution in our study is not significant maybe due to two reasons: (1) up to now, non-equilibrium phase change between water vapor and liquid water hasn't been well described; (2) latent heat from phase change is not taken into account. Therefore, further work is still needed with respect to the coupling between heat and water transfer in PEFCs.

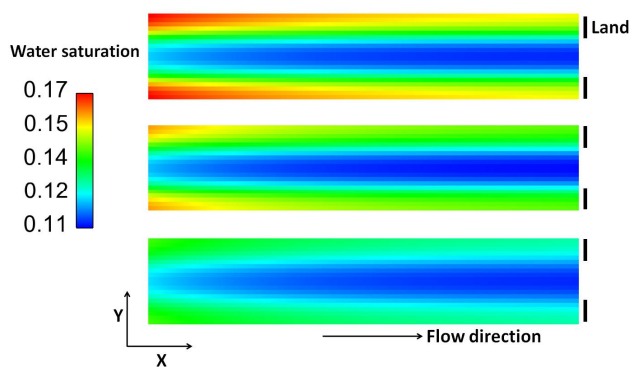


Figure 5-11: Effect of the GDL anisotropic permeability on the liquid water distributions at the middle cross section of the CL with  $Z=1.245$  mm at the current density of  $0.8 \text{ A cm}^{-2}$ : (a) anisotropic factor (i.e. ratio of in-plane to through-plane permeability), 1.0 (i.e. isotropic); (b) anisotropic factor, 2.0; (c) anisotropic factor, 10.0.

Intrinsic permeability of GDL is regarded as another anisotropic material property of importance, which has been mostly neglected in previous numerical studies of PEFCs. To highlight its effect on the liquid water distribution in the diffusion layers, herein we assign three different values of anisotropy factor (i.e. ratio of in-plane to through-plane permeability) to the GDLs, namely, 1.0 (i.e. isotropic), 2.0 and 10.0. Note that in all three cases the same through-plane permeability of  $3.0 \times 10^{-12} \text{ m}^2$  is used. Fig. 5-11 shows the influence of the GDL anisotropy factor on the liquid water distributions at the middle cross section of the CL with  $Z=1.245$  mm at the current density of  $0.8 \text{ A cm}^{-2}$ . It is evident that increasing the in-plane permeability can mitigate the liquid water flooding under the land considerably. As a result, the cell performance slightly increases mainly due to the enhanced mass transport.

## 5.5 Conclusions

Numerical modeling plays an important role in understanding several key transport processes in PEFCs. In this study, we develop a three-dimensional non-isothermal full PEFC model to explore the water and heat transfer in a cell unit. We obtain an excellent agreement between numerical and experimental results in terms of V-I curve, except at the high current densities. This is probably attributed to the fact that the liquid water flooding in the GCs is neglected. Furthermore, we illustrate the importance of considering the GDL anisotropy in the PEFC modeling. We obtain the following main conclusions based on the conducted cases in this work, all with fully humidified gas inlet on both sides:

1. The net water transfer through the membrane is from the anode to the cathode side. No liquid water is found on the anode side, since the water transfer due to the EOD is more dominant than that due to the back diffusion. As a result, the mole fraction of water vapor on the anode side reduces considerably along the flow direction at high current densities.
2. With the increase of the operating current density, transport limitation begins to impact the distribution of the local current densities in the membrane. At the inlet region, the local current densities under the land are a little higher than those under the channel due to the electron transport limitation. However, at the outlet region, the local current densities under the channel are much higher than those under the land owing to the mass transport limitation.
3. It is essential to account for anisotropy in thermal conductivity of GDL in modeling the heat transfer in a PEFC. Otherwise, the temperature variation would be overpredicted if a relatively small through-plane thermal conductivity is used, which would in turn affect other transport processes.
4. We demonstrate that increasing the in-plane permeability of GDL can mitigate the liquid water flooding under the land; as a result, the cell performance slightly increases mainly due to the enhanced mass transfer.

## Nomenclature

$a$	effective catalyst area per unit volume ( $\text{m}^2 \text{m}^{-3}$ ); water activity
$A$	cross-sectional area ( $\text{m}^2$ )
$C$	molar concentration ( $\text{mol m}^{-3}$ )
$C_p$	specific heat capacity of gas mixture ( $\text{J kg}^{-1} \text{K}^{-1}$ )
$D$	species diffusivity ( $\text{m}^2 \text{s}^{-1}$ )
$E_a$	activation energy for ORR ( $\text{J mol}^{-1}$ )
$EW$	equivalent weight of Nafion ( $\text{kg mol}^{-1}$ )
$F$	Faraday's constant ( $\text{C mol}^{-1}$ )
$i_0$	exchange current density ( $\text{A m}^{-2}$ )
$j$	volumetric current density ( $\text{A m}^{-3}$ )
$J$	Leverett function
$k_{rg}$	relative permeability for gas phase
$k_{rl}$	relative permeability for liquid phase
$k_T$	thermal conductivity ( $\text{W m}^{-1} \text{K}^{-1}$ )
$k_0$	intrinsic permeability ( $\text{m}^2$ )
$k_{cond}$	condensation coefficient in phase change ( $\text{s}^{-1}$ )
$k_{evap}$	evaporation coefficient in phase change ( $\text{Pa}^{-1} \text{s}^{-1}$ )
$M$	molecular weight ( $\text{kg mol}^{-1}$ )
$n_1$	catalyst coverage coefficient due to liquid water
$n_2$	relative permeability coefficient
$n_d$	EOD coefficient
$p$	pressure (Pa)

$p_c$	capillary pressure (Pa)
$p_{sat}$	water vapor pressure (Pa)
$q$	switch function in phase change
$r$	water transfer coefficient ( $s^{-1}$ )
$r_p$	characteristic pore length of CL (m)
$R$	universal gas constant ( $8.314 \text{ J mol}^{-1} \text{ K}^{-1}$ )
$RH$	relative humidity
$s$	liquid water saturation
$S$	source term
$T$	temperature (K)
$U_0$	equilibrium potential (V)
$\bar{V}$	velocity vector ( $\text{m s}^{-1}$ )
$w$	species mass fraction
$Y$	mole fraction

## Greek letters

$\alpha$	transfer coefficient
$\eta$	surface overpotential (V)
$\sigma$	surface tension ( $\text{N m}^{-1}$ ); electrical or ionic conductivity ( $\text{S m}^{-1}$ )
$\phi$	potential (V)
$\lambda$	water content in Nafion
$\rho$	density ( $\text{kg m}^{-3}$ )
$\varepsilon$	porosity
$\varepsilon_e$	ionomer volume fraction in CLs
$\mu$	dynamic viscosity (Pa s)
$\theta$	contact angle ( $^\circ$ )
$\xi$	stoichiometric flow ratio

## Superscripts and subscripts

	anode
$a$	
$c$	cathode
$e$	electrical phase
$eff$	effective value
$equi$	equilibrium situation
$H_2O$	water vapor
$i$	species index; ionic phase
$g$	gas phase
$gc$	gas channel
$k$	Knudsen
$l$	liquid phase
$m$	membrane
$Naf$	Nafion
$ref$	reference value

## References

- [1] M.M. Mench, *Fuel Cell Engines*, John Wiley & Sons, 2008.
- [2] H. Li, Y. Tang, Z. Wang, Z. Shi, S. Wu, D. Song et al., A review of water flooding issues in the proton exchange membrane fuel cell, *J. Power Sources* 178 (2008) 103-117.
- [3] A.Z. Weber, J. Newman, Modeling transport in polymer-electrolyte fuel cells, *Chem. Rev.* 104 (2004) 4679-4726.
- [4] J.E. Dawes, N.S. Hanspal, O.A. Family, A. Turan, Three-dimensional CFD modeling of PEM fuel cells: An investigation into the effects of water flooding, *Chem. Eng. Sci.* 64 (2009) 2781-2794.
- [5] S. Basu, C.Y. Wang, K.S. Chen, Phase change in a polymer electrolyte fuel cell, *J. Electrochem. Soc.*, 156 (6) (2009) B748-B756.
- [6] C.Z. Qin, D. Rensink, S. Fell, S.M. Hassanizadeh, Two-phase flow modeling for the cathode side of a polymer electrolyte fuel cell, *J. Power Sources* 197 (2012) 136-145.
- [7] G.F. Pinder, W.G. Gray, *Essential of Multiphase Flow and Transport in Porous Media*, John Wiley & Sons, 2008.
- [8] M. Rebai, M. Prat, Scale effect and two-phase flow in a thin hydrophobic porous layer: Application to water transport in gas diffusion layers of proton exchange membrane fuel cells, *J. Power Sources* 192 (2009) 534-543.
- [9] X.G. Yang, F.Y. Zhang, A.L. Lubawy, C.Y. Wang, Visualization of liquid water transport in a PEFC, *Electrochem. Solid-State Lett.* 7 (11) (2004) A408-A411.
- [10] F.Y. Zhang, X.G. Yang, C.Y. Wang, Liquid water removal from a polymer electrolyte fuel cell, *J. Electrochem. Soc.* 153 (2) (2006) A225-A232.
- [11] T. Berning, M. Odgaard, S.K. Kær, A computational analysis of multiphase flow through PEMFC cathode porous media using the multifluid approach, *J. Electrochem. Soc.* 156 (11) (2009) B1301-B1311.
- [12] R. Mukundan, R.L. Borup, Visualising liquid water in PEM fuel cells using neutron imaging, *Fuel Cells* 9 (5) (2009) 499-505.
- [13] A. Bazylak, Liquid water visualization in PEM fuel cells: A review, *Int. J. Hydrogen Energy* 34 (9) (2009) 3845-3857.
- [14] W. He, J.S. Yi, T.V. Nguyen, Two-phase flow model of the cathode of PEM fuel cells using interdigitated flow fields, *AIChE J.* 46 (2000) 2053-2064.
- [15] G. Lin, W. He, T.V. Nguyen, Modeling liquid water effects in the gas diffusion and catalyst layers on the cathode of a PEM fuel cell, *J. Electrochem. Soc.* 151 (12) (2004) A1999-A2006.
- [16] Q. Ye, T.V. Nguyen, Three-dimensional simulation of liquid water distribution in a PEMFC with experimentally measured capillary functions, *J. Electrochem. Soc.* 154 (12) (2007) B1242-B1251.
- [17] C.Y. Wang, C. Bechermann, A two-phase mixture model of liquid-gas flow and heat transfer in capillary porous media-1. Formulation, *Int. J. Heat Mass Transfer* 36 (1993) 2747-2758.

- [18] C.Y. Wang, P. Cheng, A multiphase mixture model for multiphase, multicomponent transport in capillary porous media-1. Model development, *Int. J. Heat Mass Transfer* 39 (1996) 3607-3618.
- [19] S. Basu, J. Li, C.Y. Wang, Two-phase flow and maldistribution in gas channels of a polymer electrolyte fuel cell, *J. Power Sources* 187 (2009) 431-443.
- [20] H. Meng, C.Y. Wang, Model of two-phase flow and flooding dynamics in polymer electrolyte fuel cells, *J. Electrochem. Soc.* 152 (9) (2005) A1733-A1741.
- [21] Z.H. Wang, C.Y. Wang, K.S. Chen, Two-phase flow and transport in the air cathode of proton exchange membrane fuel cells, *J. Power Sources* 94 (2001) 40-50.
- [22] U. Pasaogullari, C.Y. Wang, Two-phase transport and the role of micro-porous layer in polymer electrolyte fuel cells, *Electrochim. Acta* 49 (2004) 4359-4369.
- [23] Y. Wang, Modeling of two-phase transport in the diffusion media of polymer electrolyte fuel cells, *J. Power Sources* 185 (2008) 261-271.
- [24] A. Theodorakakos, T. Ous, M. Gavaises, J.M. Nouri, N. Nikolopoulos, H. Yanagihara, Dynamics of water droplets detached from porous surfaces of relevance to PEM fuel cells, *J. Colloid Interface Sci.* 300 (2006) 673-687.
- [25] X. Zhu, P.C. Sui, N. Djilali, Three-dimensional numerical simulations of water droplet dynamics in a PEMFC gas channel, *J. Power Sources* 181 (2008) 101-115.
- [26] L. Hao, P. Cheng, Lattice Boltzmann simulations of liquid droplet dynamic behavior on a hydrophobic surface of a gas flow channel, *J. Power Sources* 190 (2009) 435-446.
- [27] J. Chio, G.H. Son, Numerical study of droplet motion in a microchannel with different contact angles, *J. Mech. Sci. Technol.* 22 (2008) 2590-2599.
- [28] S. Basu, Channel two-phase flow and phase change in polymer electrolyte fuel cells, PhD thesis, 2008, The Pennsylvania State University.
- [29] U. Pasaogullari, P.P. Mukherjee, C.Y. Wang, K.S. Chen, Anisotropic heat and water transport in a PEFC cathode gas diffusion layer, *J. Electrochem. Soc.* 154 (8) (2007) B823-B834.
- [30] H. Ju, Investigation of the effects of the anisotropy of gas-diffusion layers on heat and water transport in polymer electrolyte fuel cells, *J. Power Sources* 19 (2009) 259-268.
- [31] L. Mao, C.Y. Wang, Analysis of cold start in polymer electrolyte fuel cells, *J. Electrochem. Soc.* 154 (2) (2007) B139-B146.
- [32] T.E. Springer, T.A. Zawodzinski, S. Gottesfeld, *J. Electrochem. Soc.* 138 (1991) 2334-2342.
- [33] H. Ju, Analyzing the effects of immobile liquid saturation and spatial wettability variation on liquid water transport in diffusion media of polymer electrolyte fuel cells (PEFCs), *J. Power Sources* 185 (2008) 55-62.
- [34] X. L, G. Lou, Z. Wen, Three-dimensional two-phase flow model of proton exchange membrane fuel cell with parallel gas distributors, *J. Power Sources* 195 (2010) 2764-2773.

Table 5-1: Governing equations

Equations	Descriptions
$\nabla \cdot (\rho_g \vec{V}_g) = S_g$	Mass equation of gas phase
$\rho_g \vec{V}_g \cdot \nabla \vec{V}_g = \nabla \cdot (\mu_g \nabla \vec{V}_g) - \nabla p_g + S_m$	Momentum equation of gas phase
$\nabla \cdot (\rho_g w_{O_2} \vec{V}_g) = \nabla \cdot (\rho_g D_{O_2}^{eff} \nabla w_{O_2}) + S_{O_2}$	Oxygen transport equation
$\nabla \cdot (\rho_g w_{H_2O} \vec{V}_g) = \nabla \cdot (\rho_g D_{H_2O}^{eff} \nabla w_{H_2O}) + S_{H_2O}$	Water vapor transport equation
$\nabla \cdot (\rho_g w_{H_2} \vec{V}_g) = \nabla \cdot (\rho_g D_{H_2}^{eff} \nabla w_{H_2}) + S_{H_2}$	Hydrogen transport equation
$\nabla \cdot \left( \rho_l \frac{k_{rl} \mu_g}{k_{rg} \mu_l} \vec{V}_g \right) = \nabla \cdot \left( -\rho_l \frac{k_{rl} k_0}{\mu_L} \nabla p_c \right) + S_l$	Liquid water transport equation
$\nabla \cdot (\rho_g c_p T \vec{V}_g) = \nabla \cdot (k_T^{eff} \nabla T) + S_T$	Heat transport equation
$\nabla \cdot \left( -\frac{n_d}{F} \sigma_i \nabla \phi_i \right) = \nabla \cdot \left( D_{H_2O}^{Naf} \frac{\rho_{Naf}}{EW} \nabla \lambda \right) + S_\lambda$	Dissolved water transport in the membrane
$0 = \nabla \cdot (\sigma_e \nabla \phi_e) + S_e$	Electrical transport equation
$0 = \nabla \cdot (\sigma_i \nabla \phi_i) + S_i$	Ionic transport equation

Table 5-2: Source terms

Source term	Units	Description
$S_g = S_{O_2} + S_{H_2} + S_{H_2O}$	$\text{kg m}^{-3} \text{s}^{-1}$	Mass source term of gas phase
$S_m = -\frac{\mu_g}{k_{rg} k_0} \bar{V}_g$	$\text{Pa m}^{-1}$	Darcy's source term of gas phase
$S_{O_2} = -\frac{j_c}{4F} M_{O_2}$	$\text{kg m}^{-3} \text{s}^{-1}$	Mass source term of oxygen
$S_{H_2} = -\frac{j_a}{4F} M_{H_2}$	$\text{kg m}^{-3} \text{s}^{-1}$	Mass source term of hydrogen
$S_{H_2O} = \begin{cases} -S_{phase} - S_\lambda M_{H_2O} & (\text{in ACL}) \\ -S_{phase} & (\text{otherwise}) \end{cases}$	$\text{kg m}^{-3} \text{s}^{-1}$	Mass source term of water vapor
$S_l = \begin{cases} S_{phase} + \left(\frac{j_c}{2F} - S_\lambda\right) M_{H_2O} & (\text{in CCL}) \\ S_{phase} & (\text{otherwise}) \end{cases}$	$\text{kg m}^{-3} \text{s}^{-1}$	Mass source term of liquid water
$S_T = \begin{cases} j \left( \eta + \frac{T\Delta S}{nF} \right) & (\text{in CLs}) \\ \frac{i_i^2}{\sigma_i} & (\text{in membrane}) \end{cases}$	$\text{J m}^{-3} \text{s}^{-1}$	Heat source term
$S_\lambda = \begin{cases} r_c \frac{\rho_{Naf}}{EW} (\lambda_{equi} - \lambda) + \frac{j_c}{2F} & (\text{in CCL}) \\ r_a \frac{\rho_{Naf}}{EW} (\lambda_{equi} - \lambda) & (\text{in ACL}) \end{cases}$	$\text{mol m}^{-3} \text{s}^{-1}$	Mass source term of dissolved water
$S_e = \begin{cases} j_c & (\text{in CCL}) \\ -j_a & (\text{in ACL}) \end{cases}$	$\text{A m}^{-3}$	Electrical source term
$S_i = \begin{cases} -j_c & (\text{in CCL}) \\ j_a & (\text{in ACL}) \end{cases}$	$\text{A m}^{-3}$	Ionic source term

Table 5-3: Geometrical, physical and operating parameters used for the base case.

Parameter	Value
GC width/height/length	1.0/0.5/200 mm
Shoulder width/BP thickness	0.5/1.0 mm
GDL/CL/MEM thickness	0.2/0.01/0.03 mm
GDL/CL porosity, $\varepsilon$	0.6/0.6
Characteristic length of pore space in CL,	$1.0 \times 10^{-7}$ m
Ionomer volume fraction in CL, $\varepsilon_e$	0.2
GDL/CL intrinsic permeability, $k_0$	$3.0 \times 10^{-12} / 3.0 \times 10^{-14}$ m <sup>2</sup>
Operating temperature, $T$	353 K
Operating pressure, $p_0$	2 atm
$n_1 / n_2$	2.0/4.0
Liquid water/Nafion density, $\rho_l / \rho_{Naf}$	972/2000 kg m <sup>-3</sup>
Dynamic viscosity of liquid water/gas mixture, $\mu$	$3.5 \times 10^{-4} / 2.03 \times 10^{-5}$ Pa s
Evaporation rate, $k_{evap}$	$9.8 \times 10^{-6}$ Pa <sup>-1</sup> s <sup>-1</sup>
Condensation rate, $k_{cond}$	100 s <sup>-1</sup>
Water transfer coefficients, $r_a / r_c$	1.3/1.3 s <sup>-1</sup>
GDL/CL contact angel, $\theta$	110/110 °
Surface tension, liquid-water-air, $\sigma$	0.0625 N m <sup>-1</sup>
Charge transfer coefficient, $a_c / a_a$	1.0/1.0
Reference current density $\times$ ratio of reaction surface to catalyst volume, $\alpha i_{0,c}^{ref} / \alpha i_{0,a}^{ref}$	$1.0 \times 10^4 / 1.0 \times 10^9$ A m <sup>-3</sup>
Activation energy for oxygen reduction reaction, $E_a$	73269 J mol <sup>-1</sup>
Reference molar concentration, $C_{O_2}^{ref} / C_{H_2}^{ref}$	40.88/40.88 mol m <sup>-3</sup>
Equivalent weight of Nafion, $EW$	1.1 kg mol <sup>-1</sup>
Electrical conductivity of BP/GDL/CL	2000/1000/500 S m <sup>-1</sup>
Thermal conductivity of BP/GDL/CL/MEM	20/1.7/1.0/0.95 W m <sup>-1</sup> K <sup>-1</sup> [16]
Entropy change of oxygen reduction reaction, $\Delta S$	326.36 J mol <sup>-1</sup> K <sup>-1</sup>
Inlet relative humidity, $RH_c / RH_a$	100%/100%
Stoichiometric ratio on cathode /anode side, $\xi_c / \xi_a$	2.0/1.5

# Chapter 6 - Direct Simulation of Liquid Water Dynamics in the Gas Channel of a Polymer Electrolyte Fuel Cell

---

## Abstract

*For better water management in gas channels (GCs) of polymer electrolyte fuel cells (PEFCs), a profound understanding of the liquid water dynamics is needed. In this study, we propose a novel geometrical setup to conduct a series of direct simulations of the liquid water dynamics in a GC. The conducting pathways in the gas diffusion layer (GDL) are simplified by three cylindrical pipes connected to a liquid water reservoir representing the catalyst layer (CL). The droplet dynamics, corner film dynamics, and the competition between the film and droplet flows in the GC are explored in detail. The results show that the three-phase contact line plays an important role in resisting the gas drag force for a droplet movement in the GC. The gas drag force can dominate the film flow along the GC corners, and a proper selection of the contact angle of the GC sidewalls is necessary to balance two requirements: increasing the film removal ability and removing the water clogging fast. The competing mechanisms of the droplet and film flows give us the possibility to regulate liquid water flow into GCs, and maybe lead to a better water management in GCs. Finally, the results from this work also serve to provide insights into the development of a phenomenological model for the liquid water flooding in GCs.*

## 6.1 Introduction

Water plays an important role in the operation of polymer electrolyte fuel cells (PEFCs). In order to reduce ohmic resistance, the membrane needs to keep high water content. However, too much water accumulating in PEFCs would hinder reactants diffusion towards reactive sites. This is known as “water flooding”. Water flooding in PEFCs gives rise to reactant starvation, increases parasitic pressure loss along the gas channel (GC), and also accelerates cell degradation<sup>1-4</sup>.

In the manufacture of PEFCs, GCs are normally grooved on both sides of bipolar plates (BPs). They have the following two main functions: (1) delivering gaseous reactants into catalyst layers (CLs), (2) providing pathways for excessive water to go out of cells. A typical GC is composed of hydrophilic sidewalls, and enclosed by the surface of a hydrophobic gas diffusion layer (GDL). At

high current densities, the cathode side of a PEFC is prone to being flooded, since liquid water is generated from the oxygen reduction reaction (ORR) in the cathode CL, and some water is also transported from the anode to the cathode under the electro-osmotic drag (EOD). Then, the liquid water penetrates into the GCs, and consequently forms small droplets on the GDL surface, and film slugs at the corners. Fig. 6-1 shows various stages of emergence and disappearance of water droplets in a GC observed during operation [5]. At the beginning, two small droplets preferentially emerged on the GDL surface, and later grew up. After two droplets coalesced, the liquid water wicked onto the hydrophilic GC sidewalls, and joined the film flow along the corners.

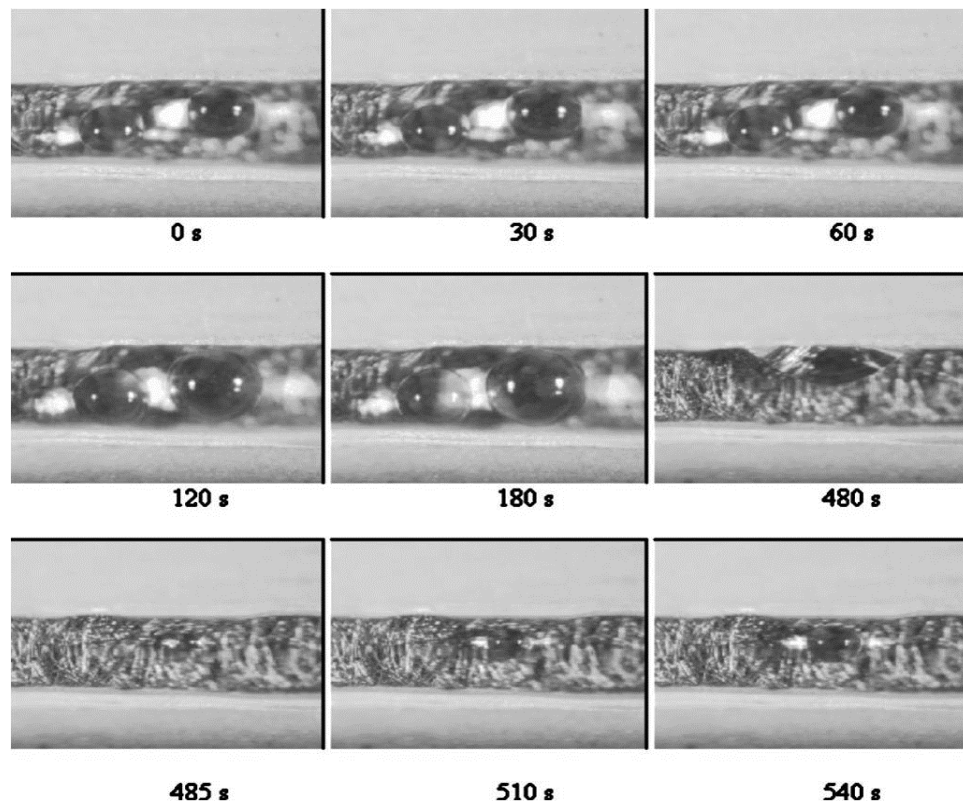


Figure 6-1: *Dynamics of water droplets in a gas channel observed in experiments at the current density of  $0.82 \text{ A cm}^{-2}$  and the temperature of  $70 \text{ }^\circ\text{C}$  (reference 5, reproduced by permission of ECS-The Electrochemical Society).*

Water flooding in GCs always has a detrimental impact on the cell performance. It prevents reactants from reaching reactive sites; it increases the flooding levels in diffusion layers and the pressure losses along channels; and it facilitates transport of ionic impurities<sup>6</sup>. Several engineering parameters can affect the liquid water removal and distribution in GCs. These include channel geometries and dimensions, wettabilities of channel sidewalls and GDL surfaces, as well as gas flow rates. In order to promote the water removal ability, a profound understanding of the liquid water dynamics in GCs is indispensable.

Because of its micro structure and mixed-wettability, the liquid water dynamics in a GC is quite complicated and sensitive to cell operating conditions. Over the past few years, both

experimental and numerical studies have contributed to understanding this dynamics. Optical photography using transparent fuel cells has been widely employed to investigate the liquid water dynamic behaviors in GCs. This technique has excellent spatial and temporal resolutions depending upon the combination of optics and recording systems<sup>7,8</sup>. However, it often requires the modification of GCs in order to facilitate optical observations. This modification results in different material properties, which in turn affects the cell performance and water distribution. Additionally, it is rather difficult to quantify the liquid water distribution in GCs, particularly for the film flow. Ge and Wang<sup>9</sup> optically observed the liquid water formation and transport in anode GCs, and found that condensed water could wick into the hydrophilic GDL and mitigated the anode channel flooding. Yang et al.<sup>5</sup> found that water droplets emerged from preferential locations on the GDL surface under oversaturation of water vapor, and surface tension played a dominant role in the water removal out of the GC. When the GC sidewalls were highly hydrophilic, coalescence of water droplets and flow along the GC sidewalls were regarded as the main water removal mechanism. Zhang et al.<sup>10</sup> also presented two models of water removal in the GC based on the magnitude of gas inlet velocity. When the gas velocity was high, the water droplet size was small and mainly swept by the drag force. At the low gas flow rate, emerged droplets would grow to a critical size comparable to the channel dimensions, and then wicked into the sidewalls under the capillary forces. In addition, the authors fitted a semi-empirical relationship between the droplet detachment diameter and the gas velocity. Most recently, Hussaini and Wang<sup>11</sup> presented a flow map illustrating various two-phase flow patterns in GCs. They introduced a parameter called wetted area ratio to quantify the liquid water coverage effect on the GDL surface, which would affect the liquid water distribution and transport inside the GDL, as well as hinder reactants diffusion into reactive sites.

Numerically, several interface-tracking methods can be conveniently employed to investigate the liquid water behaviors in micro GCs. Theodorakakos et al.<sup>12</sup> used the volume of fluid (VOF) method to study the detachments of water droplets from different porous material surfaces used in PEFCs. Cai et al.<sup>13</sup> utilized the VOF method in FLUENT package to study the water droplet and film behaviors in the gas channels of a PEFC. It was reported that a hydrophilic channel side wall with a hydrophobic MEA surface could avoid water accumulation on the GDL surface. Rensink et al.<sup>14</sup> utilized VOF method to investigate the behavior of a water droplet in the GC and its interaction with channel walls under pure capillary action. Zhu et al.<sup>15</sup> also adopted the VOF method in FLUENT to study the dynamic process of a water droplet emerging from a GDL pore. Various parametric simulations including the effects of gas flow velocity, water injection velocity and dimensions of the pore were performed with a highlight on the effect of the wettabilities of GDL surface and micro channel sidewalls. Besides the widely applied VOF method, Lattice Boltzmann Method (LBM) is another effective numerical approach to study the two-phase flow phenomena in micro gas channels. Hao and Cheng<sup>16</sup> used the multiphase free-energy LBM to study the formation and subsequent movement of a water droplet on the GDL surface. Recently Choi and Son<sup>17</sup> employed the level set method to investigate the droplet motion in a micro channel with different contact angles.

Aside from extensive experimental and numerical studies, a few researchers<sup>6, 18</sup> proposed some simplified analytical models to predict the onset of liquid water droplet instability in a GC. However, they all ignored the effect of the GC width in the approximation of the velocity profile

over the droplet. So, the results from these analytical models would overestimate the water droplet instabilities.

Most of previous numerical studies only focused on the droplet dynamics in GCs. However, at low gas flow rates, the film flow could be the main transport mechanism for the liquid water along GC corners. If water droplets emerge in the vicinity of the hydrophilic sidewalls of a GC, the film flow at the corners would form immediately under the capillary force. On the other hand, for the droplets emerged near the center of the GC, most of them would grow up and coalesce with each other to reach a critical size, and finally wicked onto the hydrophilic sidewalls. So it is very important to investigate the film dynamics in GCs, which is explored in this work in detail.

Since the GDL has complex fibrous structure, it is difficult and time-consuming to simulate the water movement inside the GDL at the pore scale. Lattice-Boltzmann method can resolve liquid water dynamics in the realistic GDL. However, to reduce computational efforts and stabilize calculations, arbitrary values have been used for both water density and viscosity in previous numerical studies<sup>31, 32</sup>, which may impact interpretations of obtained numerical results. Hence, most researchers<sup>15-17</sup> simply “planted” certain number of droplets inside GCs or imposed a water inlet boundary condition at a small region of GDL surface. They did not include the GDL in their simulations. So, the receding phenomenon of the liquid water at the GC-GDL interface could not be modeled numerically<sup>19, 20</sup>.

In this chapter, we account for the presence of GDL in a simple fashion. We assume that liquid water is transported from a water reservoir to the GC by three cylindrical pipes. These pipes are regarded as the formed conducting pathways for the liquid water transport through the GDL, and the water reservoir could be assumed to be the CL providing constant water flow rates. Based on this novel geometrical setup, we also investigate the competition between the droplet and film flows inside the GC, which often occurs in an operating PEFC.

The objective of this chapter is three-fold: (1) to explore the water droplet and film dynamics in a GC, addressing the effects of gas flow rate and wettabilities of channel sidewalls and GDL surface on the liquid water distribution and water removal; (2) to illustrate the competing mechanisms of the liquid water flow from three distinct water conducting pathways in the GDL to the GC; (3) to provide insights into the development of a phenomenological model for the water flooding in GCs.

## 6.2 Numerical method

### 6.2.1 Computational domain

In order to make the direct simulation of water dynamics in a GC feasible, we need to simplify the CL and GDL considerably. Up to now, the exact liquid water transport mechanism in the GDL is still unclear mainly due to its complex pore-structure and mixed-wettability. Nam and Kaviany<sup>21</sup> first proposed the branching-type flow structure, which is composed of larger main streams and smaller ones, connected to homogeneously distributed condensation sites. Later, Litster et al.<sup>22</sup> used a novel fluorescence microscopy technique to visualize the liquid water transport in the GDL, and concluded that the water transport was dominated by fingering and channeling, not a converging capillary tree. Recently, Hartnig et al.<sup>20</sup> also observed a similar transport process in

the GDL based on the high-resolution synchrotron X-ray radiography. So, in this work, it is quite reasonable to simplify the formed conducting pathways in the GDL by means of three capillary channels (i.e. pipes) as shown in Fig. 6-2. Two cylindrical pipes are located in the vicinity of two sidewalls of the GC for simulating the film flow along the corners, and the third cylindrical pipe is mounted at the centre for the droplet dynamic study. The exact positions of these three pipes are marked in Fig. 6-2a.

The CL is simplified by a water reservoir for providing the liquid water. We do not consider the coalescence of droplets in the GC, and the dynamics of only one droplet is studied in this work. Therefore, we use a relatively short channel with the length of 1 mm to reduce computational efforts. At last, we note that liquid water dynamics in the GC also depends on the surface texture of the GDL. This is not included in the present work for simplicity, which could be our further studies.

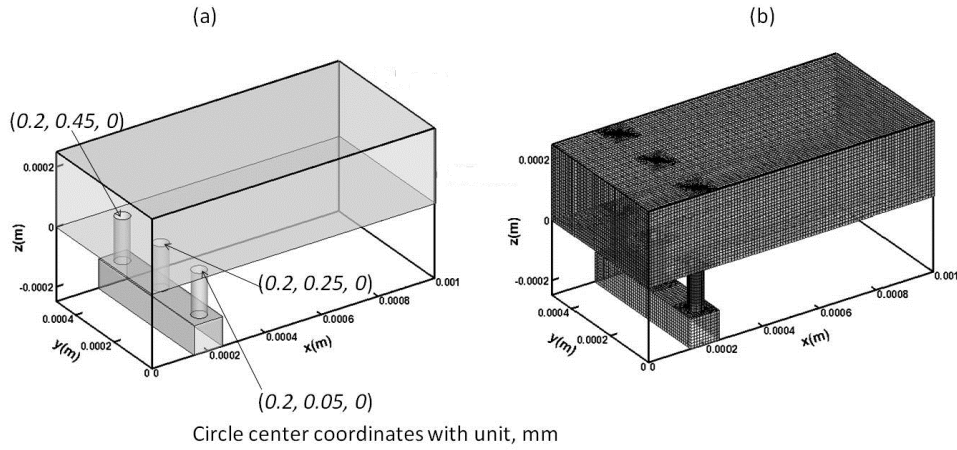


Figure 6-2: (a) Computational domain and (b) the corresponding mesh.

## 6.2.2 Governing equations

The VOF method<sup>23, 24</sup> is used in this work to explicitly track the interface between the gas and liquid water. We assume to have unsteady-state, isothermal, laminar three-dimensional flow in the GC and no phase change. The densities of both phases are assumed to remain constant due to the small pressure gradients.

In the VOF method, each computational element may have only one or both fluid phases. So, we introduce a phase indicator  $a$  with the definition:

$$a = \frac{V_l}{V_{cv}} \quad (6-1)$$

where  $V_l$  is the volume of the liquid phase in a computational element, and  $V_{cv}$  is the volume of the computational element.

Based on the averaging theorem<sup>25, 26</sup>, we can write down the governing equations as follows:

$$\nabla \cdot \bar{\mathbf{v}} = 0 \quad (6-2)$$

$$\frac{\partial(\rho\bar{\mathbf{v}})}{\partial t} + \nabla \cdot (\rho\bar{\mathbf{v}}\bar{\mathbf{v}}) = -\nabla p + \mu\nabla^2\bar{\mathbf{v}} + \frac{1}{\delta V_{cv}} \int_{\delta S} (p_l - p_g) \bar{\mathbf{n}}_l ds_\xi \quad (6-3)$$

$$\frac{\partial a}{\partial t} + \bar{\mathbf{v}} \cdot \nabla a = 0 \quad (6-4)$$

Here,  $\rho$ ,  $\mu$ , and  $p$  are called mixture density, mixture viscosity and mixture pressure, respectively. They have the following definitions:

$$\rho = a\rho_l + (1-a)\rho_g \quad (6-5)$$

$$\mu = a\mu_l + (1-a)\mu_g \quad (6-6)$$

$$p = ap_l + (1-a)p_g \quad (6-7)$$

where subscripts  $l$  and  $g$  stand for liquid and gas, respectively.

Eq. 6-3 is the momentum equation of the mixture gas-water flow. The gravity is neglected due to the quite small Bond number ( $Bo = (\rho_l - \rho_g)gL^2/\sigma$ ). The last term in Eq. 6-3 represents the effect of the capillary force at the interface between gas and liquid water,  $\delta S$  denotes the interface area,  $\bar{\mathbf{n}}_l$  is the unit normal vector pointing outwards the liquid phase. Brackbill et al.<sup>27</sup> first assumed that the interface between phases could be represented by a transition region with finite thickness, and the indicator  $a$  varied continuously across this region. Then they used the continuum method to convert the capillary force to a volumetric force, as follows:

$$F = \frac{1}{\delta V_{cv}} \int_{\delta S} (p_l - p_g) \bar{\mathbf{n}}_l ds_\xi = \frac{2\sigma\rho k \nabla a}{\rho_l + \rho_g} \quad (6-8)$$

where  $\sigma$  is the surface tension,  $\rho$  is the mixture density, and  $k$  denotes the converted curvature, which is defined as:

$$k = \nabla \cdot \bar{\mathbf{n}} = \nabla \cdot \left( \frac{\nabla a}{|\nabla a|} \right) \quad (6-9)$$

where  $\bar{\mathbf{n}}$  is the unit vector normal to the indicator field.

The wall adhesion is also considered in this work; the unit normal vector at the cell next to the wall is given as<sup>28</sup>:

$$\bar{\mathbf{n}} = \bar{\mathbf{n}}_w \cos\theta + \bar{\mathbf{t}}_w \sin\theta \quad (6-10)$$

where  $\vec{n}_w$  and  $\vec{t}_w$  denote the unit vectors normal and tangential to the solid wall, respectively, and  $\theta$  is the contact angle of the solid wall.

Note that, in the derivation of governing equations, both phases are assumed to share the same velocity in each computational element. Therefore, the VOF method neglects the slip phenomenon between the gas and liquid water. We restrict our studies to the water dynamics in GCs in automotive applications<sup>2</sup>. The corresponding physical parameters for typical operating conditions are listed in Table 6-1. The densities and viscosities of both phases are given at a typical operating temperature of 353.15 K.

### 6.2.3 Boundary and initial conditions

Uniform gas inlet velocities normal to the GC inlet ( $x=0.0$  mm) are specified for different cases shown in Table 6-2. They are related to the corresponding Reynolds numbers as follows:

$$v_{in} = \text{Re} \frac{\mu_g}{\rho_g D_{gc}} \quad (6-11)$$

Here,  $\text{Re}$  is the Reynolds number, and  $D_{gc}$  is the hydraulic diameter of the GC, defined as:

$$D_{gc} = \frac{4A_{gc}}{L_{gc}} \quad (6-12)$$

where  $A_{gc}$  is the cross-sectional area of the GC and  $L_{gc}$  is the wetted perimeter of the cross-section.

A pressure outlet boundary condition is imposed at the GC outlet ( $x=1$  mm). At the inlet boundary of the CL reservoir ( $z=-0.25$  mm), a constant mass flow rate of liquid water is specified. The contact angle in the reservoir is assumed to be zero. For the rest of the boundaries, the no-slip wall condition with a specified static contact angle is employed.

Before the calculation of each case, we use the inlet velocity to initialize the flow field, and the pipes are fully filled with liquid water to reduce computational efforts.

### 6.2.4 Mesh and numerical implementation

Adequate mesh density is essential to capture sharp interfaces and reduce smeared regions in VOF simulations<sup>23</sup>. The basic mesh used in this work is shown in Fig. 6-2b. They are mainly cubic cells with dimensions of  $10 \times 10 \times 10 \mu\text{m}$  except for the refined regions nearby the pipes. The mesh independency study is also done by increasing and decreasing the cell size by 20% and 40%, respectively<sup>15</sup>. The obtained results for water dynamics and flow field are found to be quite similar.

The set of transient governing equations and boundary conditions given above are discretized by finite volume method with second-order schemes based on a commercial CFD solver FLUENT 12.0.16. Eq. 6-4 describes the evolution of the volume fraction of liquid water, which is a

hyperbolic partial differential equation (PDE). So, its discretization is crucial to the VOF simulation. In this work, we use the geometric reconstruction scheme, which represents the interface between both phases by a piecewise-linear curve. It works quite well on the orthogonal cells.

For transient VOF simulations, the selected time step can affect the numerical results and computational efforts much. A big time step would give rise to smeared interfaces and even unreliable results, while a small time step increases computational efforts. In this work, in order to balance the two effects, we choose time steps such that the global Courant number<sup>28</sup> is less than 0.6. For all the simulated cases, the scaled residuals of all the equations are less than  $10^{-5}$ .

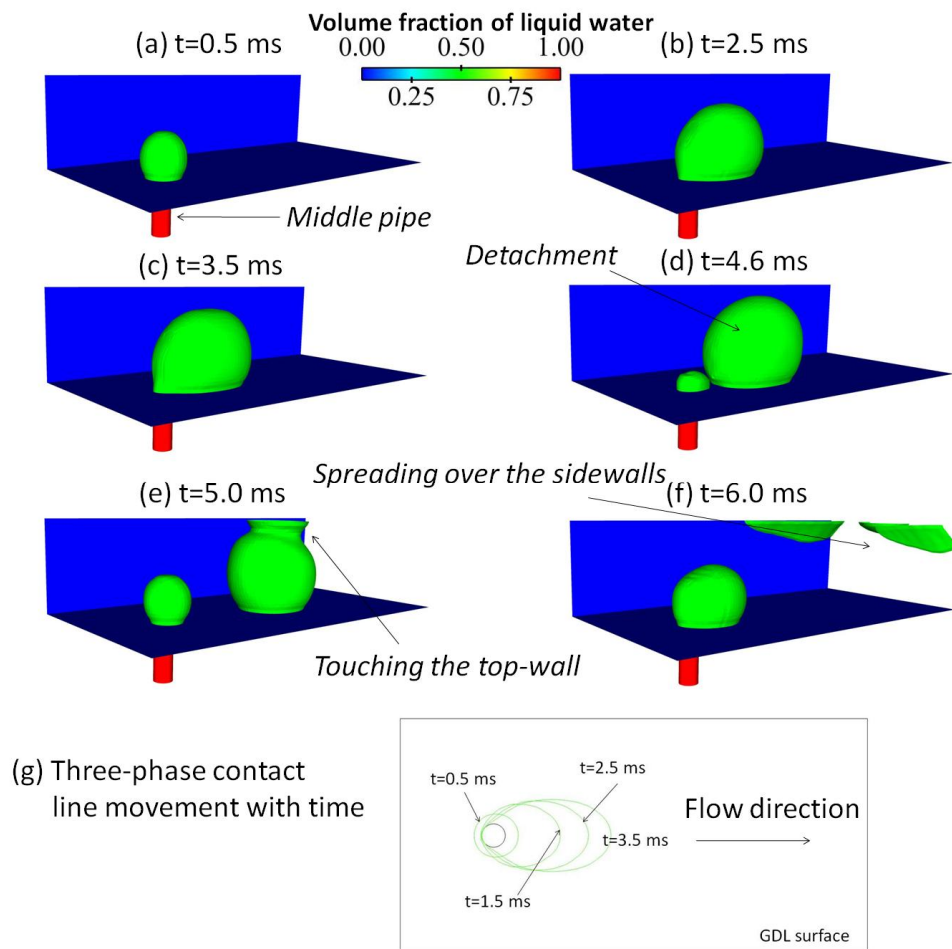


Figure 6-3: *Dynamic progress of one water droplet emergence, growth, detachment, and touching the top wall (case 1: gas Re number, 150; water flow rate,  $2.0 \times 10^{-6} \text{ kg s}^{-1}$ ; sidewall contact angle,  $40^\circ$ ; GDL surface contact angle,  $140^\circ$ ; middle pipe diameter,  $50 \mu\text{m}$ ).*

## 6.3 Results and discussion

Seventeen different cases are conducted in this work to explore the liquid water dynamics in a GC. The corresponding boundary conditions and pipe diameters are given in Table 6-2. Cases (1-7) are used to study the water droplet dynamics including the effects of the gas flow rate

represented by Reynolds (Re) number, and the contact angle of GDL surface. Cases (8-14) are used to study the film dynamics in the GC taking into account the effects of the Re number and the contact angle of GC sidewalls. The remaining cases are meant to illustrate the competing mechanisms of the droplet and film flows. Note that in PEFCs a practical gas inlet velocity of 5 m/s can be used, which corresponds to a Re number of about 164 in this study. Based on the simulations in this work, we attempt to answer the following questions:

1. What is the role of the three-phase contact line in a droplet detachment?
2. Can increasing the hydrophobicity of the GDL surface enhance the water removal ability?
3. How do the gas drag and surface tension forces affect the film flow along the GC corners?
4. Is decreasing the hydrophilicity of the GC sidewalls beneficial to the water removal?
5. How do the conducting pathways formed in the GDL compete to transport liquid water into the GC?

We should point out that the liquid water flow rate used in this work is too large compared to real situations. But, up to now, this has been unavoidable in all interface-tracking VOF simulations in the context of PEFC applications. In order to reduce computational efforts, the mass flow rate has to be enlarged dramatically to make numerical study feasible. However, in the film flow of case 14, we reduce the mass flow of the liquid water four times to address its effect on the film dynamics in the GC.

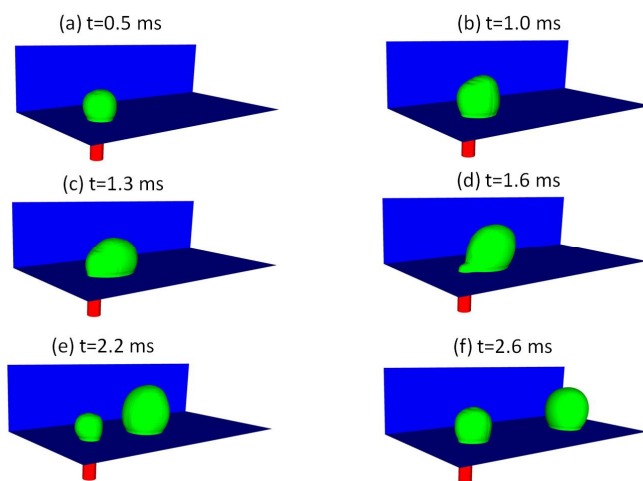


Figure 6-4: *Dynamic progress of one water droplet emergence, growth and detachment (case 3: gas Re number, 250; water flow rate,  $2.0 \times 10^{-6} \text{ kg s}^{-1}$ ; sidewall contact angle,  $40^\circ$ ; GDL surface contact angle,  $140^\circ$ ; middle pipe diameter,  $50 \mu\text{m}$ ).*

### 6.3.1 Droplet dynamics

Fig. 6-3 shows the dynamic process of one water droplet movement along the GC (case 1). Since only one droplet is focused here, the two side pipes are not included in the simulation. At  $t=0.5 \text{ ms}$  (Fig. 6-3a), a small droplet forms on the hydrophobic GDL surface. Due to the relatively small gas drag force, the deformation of the droplet is initially very small. With the continuous water filling through the pipe, the droplet becomes bigger and more deformable (Fig 6-3b, 6-3c). The length of three-phase contact line along the GC increases with time until the detachment of the droplet occurs (Fig 6-3g). This leads to an increase of adhesion force, which resists the increased gas drag force. Another parameter, called droplet contact angle hysteresis, also

increases the adhesion force along the contact line. The contact angle hysteresis may depend on gas flow rate, droplet size, roughness of the GDL surface, and channel dimensions in a complex way<sup>6</sup>. We have chosen to neglect this effect, and only a fixed static contact angle is assumed in this work. As a result, the increased adhesion force comes only from the contact line deformation as shown in Fig 6-3g. At about  $t=4.6$  ms (Fig. 6-3d), we observe the detachment of the droplet. Note that we claim that the droplet is detached by the gas drag force in this work, when the droplet contact line totally separates from the pipe inlet circumference at the GDL surface. At  $t=5.0$  ms (Fig 6-3e) the detached droplet suddenly touches the GC top wall, and we also find that the deformation of the droplet is much smaller than in Fig. 6-3c. After touching the hydrophilic top wall of the GC, the liquid water wicks into the corners and the top wall under the surface tension force. So, when water clogging happens in GCs of an operating PEFC, highly hydrophilic sidewalls are preferred to spread out liquid water quickly.

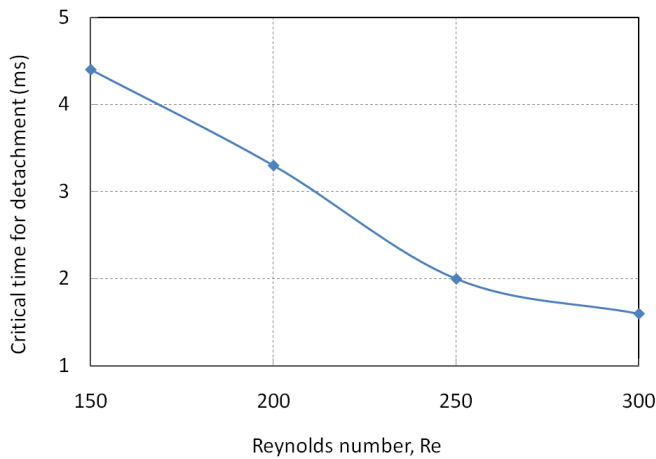


Figure 6-5: *Critical time for the detachment of a water droplet vs. Reynolds number.*

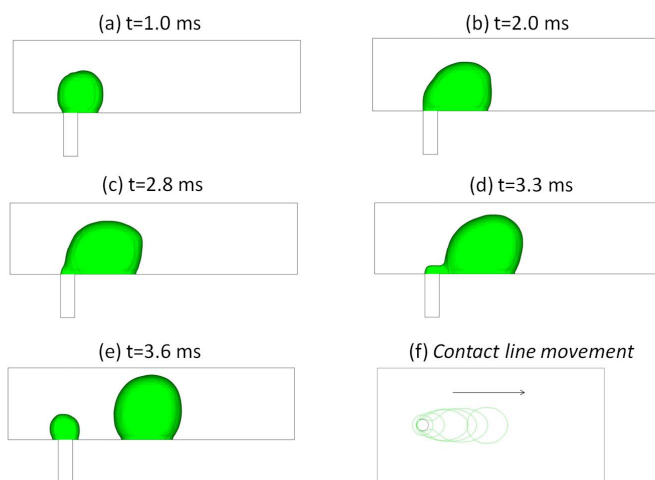


Figure 6-6: *Droplet dynamics and its contact line movement with time in the cross-section ( $y=0.25$ mm) of the GC (case 2: gas Re number, 200; water flow rate,  $2.0 \times 10^{-6}$  kg  $s^{-1}$ ; sidewall contact angle,  $40^\circ$ ; GDL surface contact angle,  $140^\circ$ ; middle pipe diameter,  $50 \mu m$ ).*

When the gas flow rate is increased (case 3), the droplet dynamic process is shown in Fig. 6-4. The detachment of the droplet occurs much earlier than in Fig. 6-3. In Fig. 6-4d, a small water tail behind the droplet is observed, which may be related to the increased gas flow rate. From the

comparison of Fig. 6-3 and Fig. 6-4, we conclude that the droplet deformation increases with an increase of the gas flow rate. The critical times at which the detachments of droplets occur are plotted in Fig. 6-5 for four different Re numbers. Since a constant water flow rate is assumed, the critical time directly represents the critical droplet size in the GC. As seen from Fig. 6-5, increasing the gas flow rate can assist in the droplet removal in the GC. However, this effect becomes much weaker after the Re number is larger than 250, which means that the force balance for a droplet<sup>18</sup> is highly nonlinear.

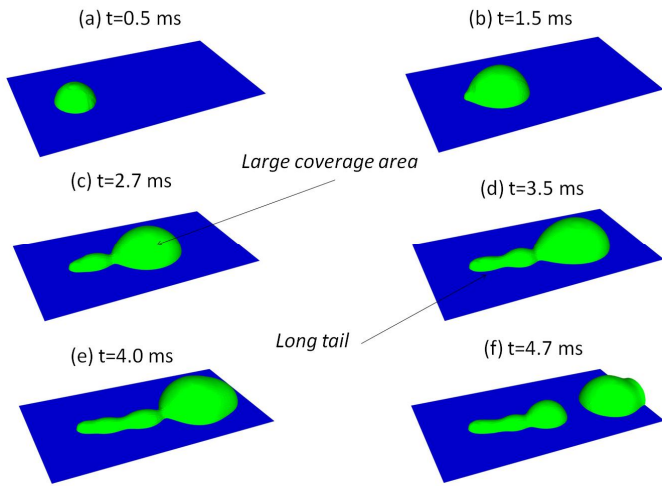


Figure 6-7: Droplet dynamics on a slightly hydrophilic GDL surface (case 5: gas Re number, 150; water flow rate,  $2.0 \times 10^{-6} \text{ kg s}^{-1}$ ; sidewall contact angle,  $40^\circ$ ; GDL surface contact angle,  $80^\circ$ ; middle pipe diameter,  $50 \mu\text{m}$ ).

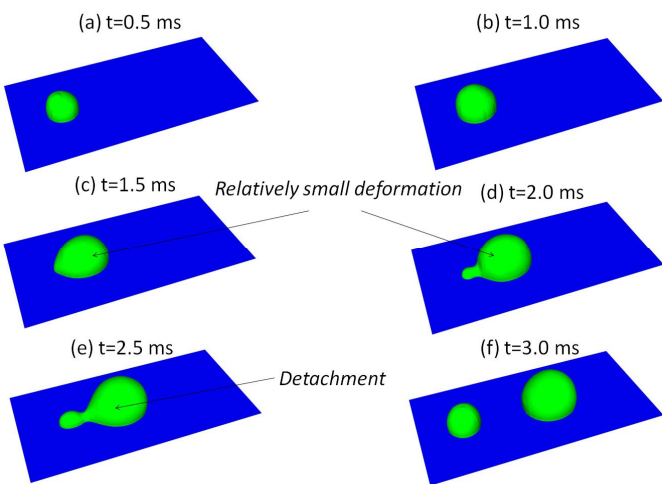


Figure 6-8: Dynamic progress of one water droplet emergence, growth and detachment (case 6: gas Re number, 150; water flow rate,  $2.0 \times 10^{-6} \text{ kg s}^{-1}$ ; sidewall contact angle,  $40^\circ$ ; GDL surface contact angle,  $110^\circ$ ; middle pipe diameter,  $50 \mu\text{m}$ ).

Fig. 6-6 shows the droplet dynamics and its contact line evolution with time in the cross-section ( $y=0.25 \text{ mm}$ ) of the GC for case 2. Before the droplet detachment (Fig. 6-6a, 6-6b, 6-6c), the gas drag force exerted on the droplet becomes bigger and bigger due to the increase of the droplet size. This force is resisted by the adhesion along the contact line, which extends in both longitudinal and transversal directions (Fig. 6-6f). In addition, the droplet deforms more and more. After the detachment (Fig. 6-6e), the gas drag force imposed on the droplet decreases

dramatically due to the fast movement of the droplet along the GC. As a result, the contact line shape approaches a circle (Fig. 6-6f), indicative of the reduced adhesion force.

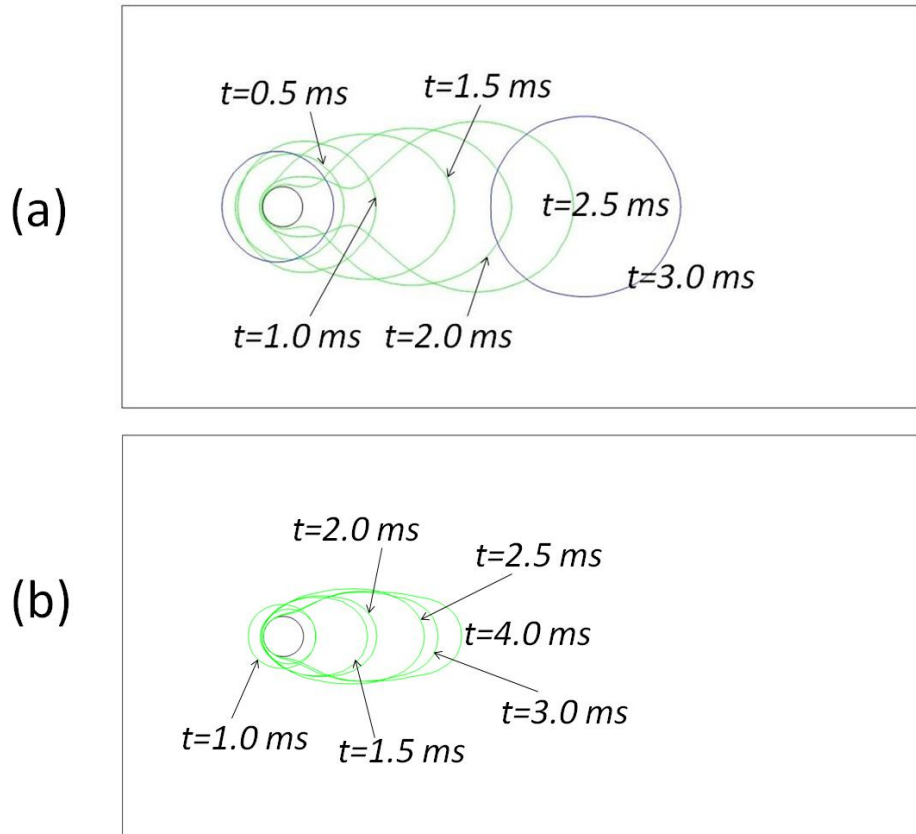


Figure 6-9: (a) Contact line movement with time (case 6: gas Re number, 150; water flow rate,  $2.0 \times 10^{-6}\text{ kg s}^{-1}$ ; sidewall contact angle,  $40^\circ$ ; GDL surface contact angle,  $110^\circ$ ; middle pipe diameter,  $50\text{ }\mu\text{m}$ ); (b) Contact line movement with time (case 7: gas Re number, 150; water flow rate,  $2.0 \times 10^{-6}\text{ kg s}^{-1}$ ; sidewall contact angle,  $40^\circ$ ; GDL surface contact angle,  $170^\circ$ ; middle pipe diameter,  $50\text{ }\mu\text{m}$ ).

Fig. 6-7 shows the droplet dynamics on a hydrophilic GDL surface (case 5). As expected, large water coverage is found during the whole process. No distinct droplet detachment can be identified. In fact it behaves more like a film flow spreading over the surface. Therefore, hydrophobic GDLs are commonly used in PEFCs to circumvent heavy water accumulation and large water coverage. Fig. 6-8 illustrates the droplet dynamics on a slightly hydrophobic GDL (case 6). It is interesting to find that the critical time for the droplet detachment ( $t=2.5\text{ ms}$ ) is much shorter compared to that in Fig. 3 ( $t=4.4\text{ ms}$ ). This can be explained by the fact that the contact line deformation on this slightly hydrophobic GDL is very small as it cannot resist the increased gas drag force (Fig. 6-9a). As a result, the droplet is detached at a quite early stage. Fig. 6-9 shows the contact line comparison between case 5 (contact angle of GDL surface,  $110^\circ$ ) and case 7 ( $170^\circ$ ). It is evident that the contact area in case 5 is bigger than in case 7 at the same moment due to its slightly hydrophobic GDL. In addition, we find that the contact line

deformation in case 7 is much larger than in case 5, which has the ability to resist the increased gas drag force. We conclude that the smaller the contact angle of the hydrophobic GDL surface, the smaller the contact line deformation under the same flow condition will be. However, as mentioned above, in this study we do not consider the effect of contact angle hysteresis due to the VOF model limitation. Recently, Kumbur et al.<sup>6</sup> has experimentally demonstrated that the contact angle hysteresis of one droplet in the GC increased as increasing the GDL hydrophobicity. Since the contact angle hysteresis also contributes to increasing the droplet adhesion force, we could state that a slightly hydrophobic GDL is favorable to droplet detachment. It needs to be pointed out that the hydrophobic GDL with a smaller contact angle results in large water coverage over the surface, which is disadvantageous to reactants diffusion into reactive sites. When the contact angle of the GDL surface is increased to 170 degrees (case 7), the critical time is found to be about 4.5 ms, which is quite close to the critical time for the detachment in Fig. 6-3 (4.4 ms). This means that highly hydrophobic GDL surface is unnecessary for the droplet removal in the GC. However, it can reduce the water coverage over the GDL surface.

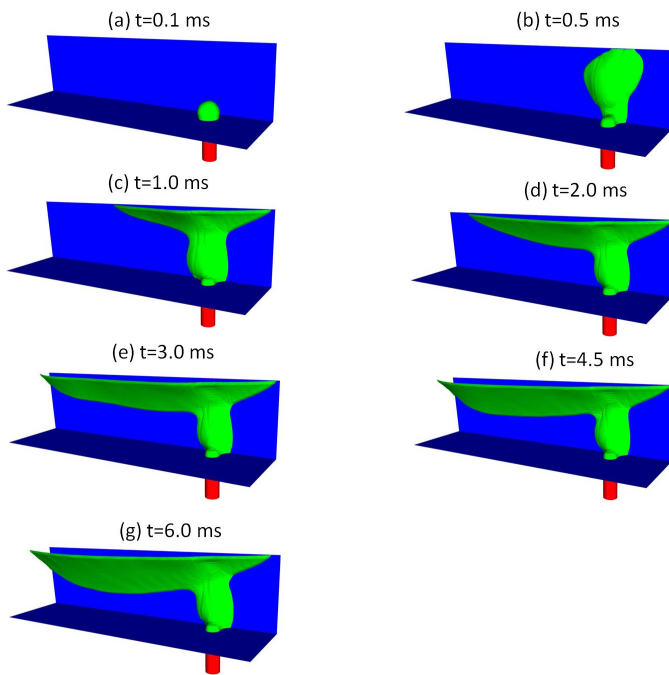


Figure 6-10: Dynamics of film flow along the corner of the GC (case 8: gas  $Re$  number, 150; water flow rate,  $2.0 \times 10^{-6} \text{ kg s}^{-1}$ ; sidewall contact angle,  $40^\circ$ ; GDL surface contact angle,  $140^\circ$ ; side pipe diameter,  $50 \mu\text{m}$ ).

### 6.3.2 Film dynamics

At low gas flow rates, film flow could be the main transport mechanism for the liquid water removal in GCs. As shown in Fig. 6-3f, when the droplet reaches its critical size comparable to the GC dimensions, it joins the film flow along the corners. There is another mechanism that contributes to the film filling, namely, the capillary force of the hydrophilic sidewalls of the GC. This contribution is discussed in this section. In order to reduce the computational efforts, we take advantage of the symmetrical film flow in the GC, and use only half of the GC as our computational domain. In these computations, the middle pipe pertaining to the droplet formation is neglected. At  $t=0.1 \text{ ms}$  (Fig. 6-10a), a small water droplet forms on the hydrophobic

GDL surface nearby the sidewall. When the droplet grows, at some critical size, it touches the GC sidewall, and spreads over the sidewall quickly with the help of the surface tension force (Fig. 6-10b). With further feeding of the liquid water into the GC, the film flow forms along the corner of the GC as shown in Fig.6-10 d. From the water inlet position (side pipe), the water spreads towards the GC outlet and the GC inlet, with the film thickness reducing in both directions. This is attributed to the fact that the surface tension dominates the film flow at the early stage. However, the gas drag force plays a more and more important role as more and more liquid water accumulates in the GC. Finally, we get a totally different film shape from the water inlet position to the GC outlet, which is from the thin to the thick. This indicates that the gas drag force begins to dominate the film flow compared with the surface tension force (Fig. 6-10g). Note that, at the outlet region, the film shape changes a little, perhaps due to the boundary effect.

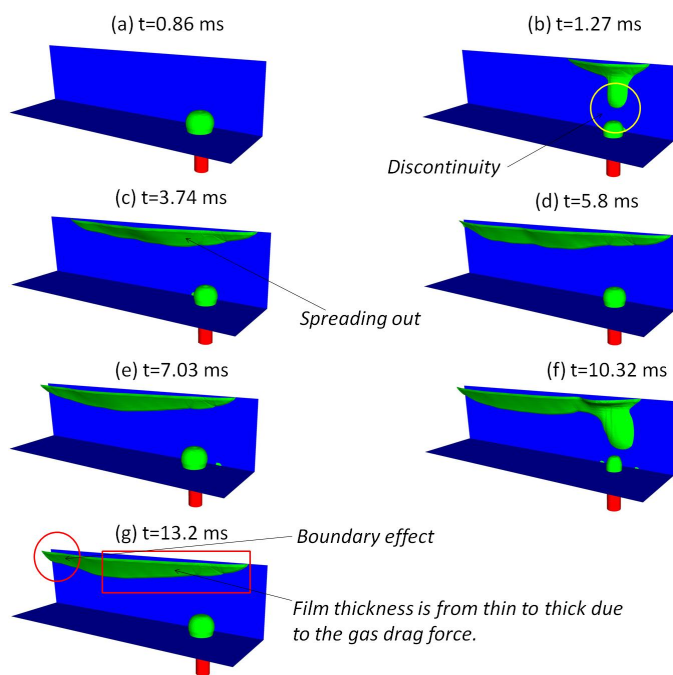


Figure 6-11: Dynamics of film flow along the corner of the GC (case 14: gas  $Re$  number, 150; water flow rate,  $5.0 \times 10^{-7} \text{ kg s}^{-1}$ ; sidewall contact angle,  $40^\circ$ ; GDL surface contact angle,  $140^\circ$ ; side pipe diameter,  $50 \mu\text{m}$ ).

As mentioned earlier, in our simulations, we specify a much larger liquid water flow rate ( $2e-06 \text{ kg s}^{-1}$ ) from the CL than in real situations. This unrealistic water flow rate may render our numerical results unrealistic. In order to address this issue, we reduce the water flow rate by a factor four and the obtained film dynamic process is shown in Fig. 6-11. As expected, in comparison to the results shown in Fig. 6-10, the water filling time is much longer for reaching a certain value of water saturation in the whole GC. The second difference can be seen from Fig. 6-11b. After the grown-up droplet touches the sidewall of the GC, the discontinuity of the water flow is observed due to the slow water filling rate from the side pipe (i.e. small water flow rate). The isolated water film at the corner flows towards the GC outlet under the gas drag and surface tension forces (Fig. 6-11e). The film shape distribution also shows the same tendency as in Fig. 6-10g, which implies that the gas drag force plays a dominant role in the film flow. When the second water droplet reaches its critical size, it also touches the sidewall and fills the film flow again as shown in Fig. 6-11f. This water refilling phenomenon demonstrates that the film flow at

the corner has a periodic feature at the low water flow rate. This periodic flow feature is not present when the water flow rate is large. In contrast, a continuous conducting pathway for the liquid water flow is formed along the GC corner as shown in Fig. 6-10f. So, we conclude that the periodic feature of the film flow at the GC corners cannot be captured with a high water flow rate. However, both Fig. 6-10 and Fig. 6-11 show that the gas drag force is quite important for the film flow, as it enhances the liquid water removal. So, when formulating governing equations for water flow in the GC, the gas drag force has to be taken into account besides the capillary forces.

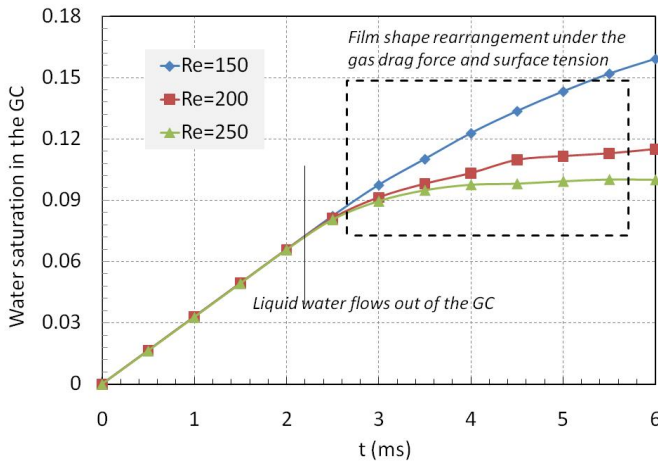


Figure 6-12: Effect of the Gas flow rate on the film flow at the corner of the GC (water saturation in the GC vs. flow time; case 8-10).

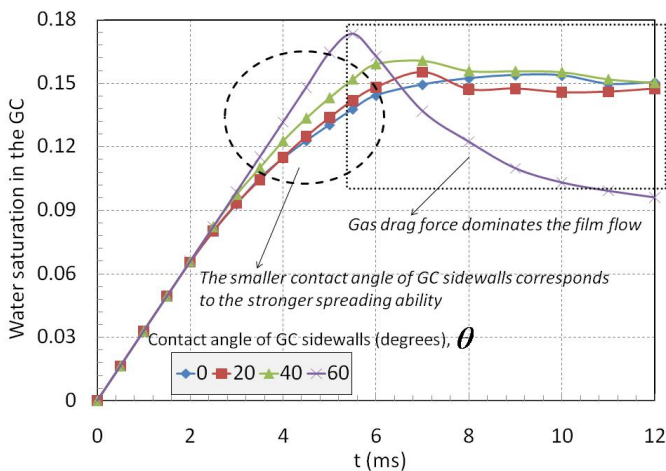


Figure 6-13: Effect of the sidewall contact angle on the film flow along the corner of the GC (water saturation in the GC vs. flow time; case 8 and case 11-13).

Since higher gas flow rate corresponds to larger gas drag force for the same film flow condition, practically, we can increase the gas flow rate to enhance the film removal along the GC corners. The effect of the gas flow rate on the film flow along the GC corner is present in Fig. 6-12 in terms of the water saturation in the whole GC as a function of time. Three gas flow rates are used with Re numbers of 150, 200, and 250, respectively. Before the liquid water flows out of the GC, we have the same water saturation for the three cases due to the same water flow rate from the side pipe. After the breakthrough of the liquid water at the GC outlet, there is a distinct difference between the three cases; the saturation increase is slower for higher Re number. This is because the film shape is rearranged differently under the gas drag and surface tension forces

for each case. One should note that the flow conditions are still unsteady even at  $t=6$  ms. For the lower two curves ( $Re=200, 250$ ), the flow conditions can be assumed to be very close to the steady state according to the water saturation tendency. It is obvious that increasing the gas flow rate can mitigate the film flooding at the GC corners. However, it needs to keep in mind that higher gas flow rate gives rise to higher pressure loss along the GC, which means a lower cell efficiency.

A similar study is performed for determining the effect of sidewall contact angle on the water flooding in the GC. Results are shown in Fig. 6-13 in terms of change of water saturation in the whole GC with time for four different sidewall contact angles, namely, 0, 20, 40, and 60 degrees. For the contact angle of 60 degrees, the water saturation in the GC reaches its peak value of 0.17 at about  $t=5.5$  ms. After that, it starts to go down quickly, the curve slope becomes smaller and smaller. This whole process indicates that the gas drag force suppresses the increase of the film thickness, and tries to balance the viscous resistance from the sidewall. At the end of the simulation, the water saturation in the GC approaches a certain value. From the region enclosed by a dashed circle in Fig. 6-13, we can see that the water saturation in the GC is significantly affected by the sidewall contact angle. The water saturation in the GC decreases with the decrease of the sidewall contact angle. This is attributed to the fact that the GC sidewall with a smaller contact angle can spread out the liquid water faster. So, for the GC sidewall with the contact angle of zero, it can spread most liquid water out of the GC, leading to the smallest water saturation. The flow region enclosed by a dashed rectangle denotes the regime that the gas drag force dominates the film flow; the film shapes are also rearranged during this period (Fig. 6-10g). At the same time, the capillary force starts to resist the water film flow along the GC corner. The contact angle of 60 degrees corresponds to a small capillary force; as a result, the water saturation in the GC reduces considerably with time as shown in Fig. 6-13. In contrast, the water saturation for the other three contact angles does not change much with time. We also find that the water saturation evolution for the contact angle of 60 degrees is quite different from the others, which may be explained by the fact that the film flow is very unstable when the contact angle of the sidewall is larger than 45 degrees in the rectangular corner of the GC (Concus and Finn condition<sup>29</sup>). In PEFC applications, normally the water removal ability is evaluated over a large time scale (i.e. several hours). Based on this point, we conclude that a sidewall with less hydrophilicity is advantageous to reducing the film flooding along the GC corners (Fig. 6-13). However, we must note that a sidewall with less hydrophilicity is incapable of removing the water clogging (Fig. 6-3e) immediately maybe occurred in the GCs of an operating PEFC. This would result in the non-uniform distributions of the reactants in the cell [30], and reduce the cell performance. So, in practice, a proper contact angle of the GC sidewalls should be selected to balance both requirements, namely, increasing the film removal ability (less hydrophilicity) and removing the water clogging fast (higher hydrophilicity).

### 6.3.3 Competition between film and droplet flows

Under the water flooding situation of the cathode side of a PEFC, several conducting pathways for the liquid water transport are formed in the fibrous GDL. It has been observed experimentally that small droplets preferentially emerge from certain pores on the GDL surface. Depending on the locations of such pores, we could have both film and droplet flows. On the other hand, these conducting pathways in the GDL are not isolated, but maybe connected by several water

reservoirs inside the GDL and CL. So, it is obvious that these conducting pathways would compete to feed the liquid water into the GC. As stated above, we simplify the conducting pathways by three cylindrical pipes, which are connected to the same water reservoir within the CL (Fig.6-2a).

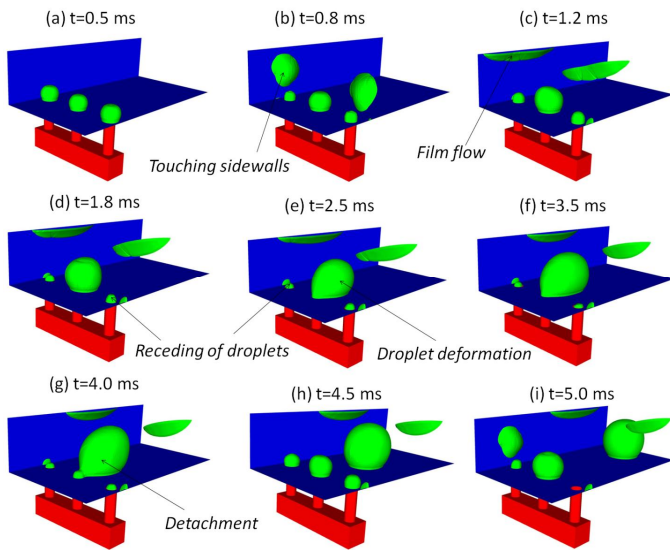


Figure 6-14: *Water dynamics in the GC, filling by three pipes with the same diameter (case 15: gas Re number, 150; water flow rate,  $2.0 \times 10^{-6} \text{ kg s}^{-1}$ ; sidewall contact angle,  $40^\circ$ ; GDL surface contact angle,  $140^\circ$ ; side pipes diameter,  $50 \mu\text{m}$ ; middle pipe diameter,  $50 \mu\text{m}$ ).*

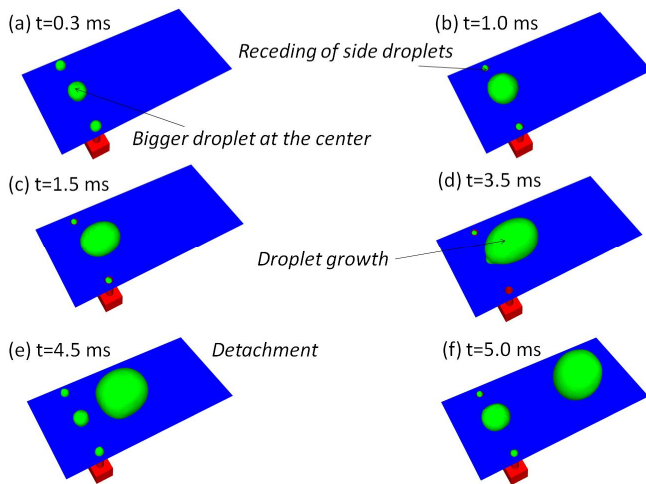


Figure 6-15: *Water dynamics in the GC, filling by three pipes with different diameters (case 16: gas Re number, 150; water flow rate,  $2.0 \times 10^{-6} \text{ kg s}^{-1}$ ; sidewall contact angle,  $40^\circ$ ; GDL surface contact angle,  $140^\circ$ ; side pipes diameter,  $40 \mu\text{m}$ ; middle pipe diameter,  $50 \mu\text{m}$ ).*

Fig. 6-14 shows the liquid water dynamics in the GC. The liquid water is delivered by three cylindrical pipes with the same diameter of  $50 \mu\text{m}$ . At  $t=0.5 \text{ ms}$ , three droplets with the same size form on the hydrophobic GDL surface. After a while, when two side droplets are big enough to touch the sidewalls, the water spreads out quickly and forms the film flow along the corners as shown in Fig. 6-14b and 6-14c. Due to the small water flow rate from the side pipes, we observe the discontinuities of the water flow at the corners, which is already discussed in the section on film dynamics. From Fig. 6-14c to Fig.6-14f, we observe that the middle droplet becomes bigger and bigger, while two side droplets recede back into the pipes. This receding phenomenon implies that more liquid water is filled into the GC through the middle pipe, since three pipes are connected together with the fixed water flow rate from the CL. In Fig. 6-14b, after wicking into the film at the corners, the two side droplets become much smaller than the middle one. As a result, the bigger middle droplet has much smaller capillary pressure over the interface. If we

assume the same gas pressure around three droplets and uniform liquid water pressure inside each droplet, we can conclude that the liquid water pressure inside the middle droplet is much smaller than those in two side droplets. So, the driving force for the water flow through the middle pipe is biggest, and this can explain the aforementioned receding phenomenon. At  $t=4.0$  ms (Fig. 6-14g), the middle droplet reaches its critical size, and is detached by the gas drag force. From  $t=4.5$  ms (Fig. 6-14h), a second water flow cycle starts as shown in Fig. 6-14i. So, for this kind of conducting pathway settings, we could have the droplet detachment, side droplets receding, and film filling at the corners cyclically. To some extent, this numerical study resembles the processes observed in some experiments<sup>19, 20</sup>.

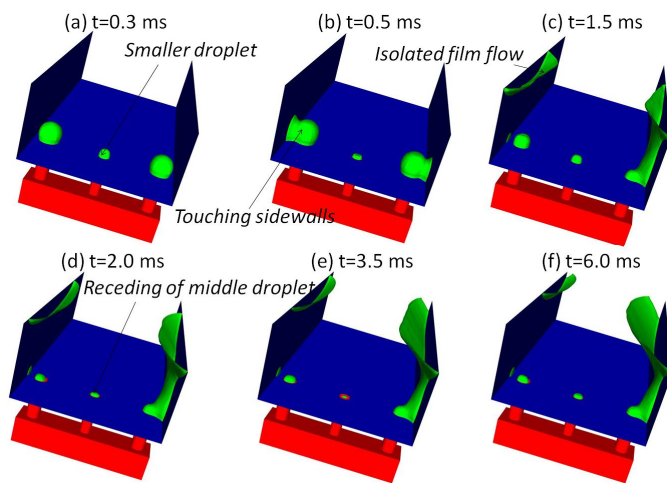


Figure 6-16: *Water dynamics in the GC, filling by three pipes with different diameters (case 17: gas Re number, 150; water flow rate,  $2.0 \times 10^{-6} \text{ kg s}^{-1}$ ; sidewall contact angle,  $40^\circ$ ; GDL surface contact angle,  $140^\circ$ ; side pipes diameter,  $50 \mu\text{m}$ ; middle pipe diameter,  $40 \mu\text{m}$ ).*

In the GDL, the sizes of the conducting pathways are randomly formed maybe due to the random structure of the GDL. In what follows, we investigate the effect of the sizes of the conducting pathways on the competing water filling into the GC. In Fig. 6-15, we reduce the diameter of the side pipes to  $40 \mu\text{m}$ , while the middle pipe has an unchanged diameter of  $50 \mu\text{m}$ . At the beginning, a relatively bigger middle droplet is observed as expected due to the smaller flow resistance (Fig. 6-15a). With the increase of the middle droplet, the driving force for the water flow through the middle pipe is bigger and bigger, compared to that through the side pipes. So, the two side droplets recede back into the pipes quickly, whereas the middle droplet grows up with time. At about  $t=4.5$  ms, the middle droplet is detached by the gas flow, and later the second cycle starts. For this case, the film flow along the corners does not occur because of the higher flow resistance for the two side pipes. Only periodic droplet detachment is found. In Fig. 6-16, we change the middle pipe diameter to  $40 \mu\text{m}$ , and the diameter of the side pipe is set to  $50 \mu\text{m}$ . Then, a totally different water dynamics in the GC is observed. In contrast to Fig. 6-15a, two bigger droplets form nearby the sidewalls due to the smaller water flow resistance as shown in Fig. 6-16a. After touching the hydrophilic sidewalls, the surface tension force assists in the water flow from the side pipes, while the middle droplet recedes back into the pipe immediately. It is interesting to find that the isolated film flow at the left corner is formed, while a conducting pathway for the water transport along the right corner is established. This may be caused by the highly unstable flow condition in the GC. It must be noted that in real water flooding of PEFC

applications, we never obtain continuous conducting pathways for the liquid water transport along the GC corners, since the water flow rate is extremely low. This is also explained in the section on film dynamics. After a conducting pathway is formed as in Fig. 6-16c, the liquid water flow through the remaining two pipes (middle and left ones) is totally suppressed, because the surface tension effect on the film flow at the right corner is much larger, resulting in a quite big driving force for the water flow through the right pipe. In addition, we obtain asymmetrical water dynamics in the GC as shown in Fig. 6-16, even though the GC with symmetrical structure is used. We attribute it to the physical phenomenon of liquid water dynamics in the GC, due to its transient and unstable flow features. However, as demonstrated in Fig. 6-11, due to the small water flow rate in an operating PEFC, we cannot have continuous conducting pathways for the liquid water transport along the GC corners. Instead, periodic film flow (or slugs) at both corners can be expected, meanwhile droplet dynamics is always suppressed in this case.

## 6.4 Conclusions

In this work, based on a novel geometrical setup, a series of direct simulations (VOF) are conducted to explore in detail the liquid water dynamics in GCs, including the droplet dynamics, film dynamics, and the competition between the film and droplet flows. The main findings and conclusions are summarized as follows:

With the increase of the droplet size in the GC, the three-phase contact line extends along both the gas flow and transverse directions to resist the increased gas drag force. For the same flow conditions of a droplet, before its detachment, the contact line deformation increases with increasing the gas flow rate, and decreases as reducing the hydrophobicity of the GDL surface. A slightly hydrophobic GDL surface could lead to an early droplet detachment. However, it results in large water coverage over the GDL surface, which would hinder reactants diffusion into the reactive sites. We also find that too highly hydrophobic GDL surface is unnecessary for the droplet removal in the GC.

As filling the liquid water into the GC through the side conducting pathway (nearby one hydrophilic GC sidewall), the film flow forms along the GC corner with the help of the surface tension force. At the beginning, the surface tension dominates the film flow, so, the liquid water spreads over the corner quickly. The film thickness distribution is from the thick to the thin, from the inlet position to the GC outlet. With more and more liquid water accumulating in the GC, the gas drag force starts to play an importance role. Finally, we get an opposite film thickness distribution, which is from the thin to the thick along the GC corner. Increasing the gas flow rate can mitigate the film flooding at the GC corner. However, it generates high pressure loss along the GC. Practically, a proper contact angle of the GC sidewalls should be selected to balance two requirements, namely, increasing the film removal ability (less hydrophilicity) and removing the water clogging fast (higher hydrophilicity).

The sizes of conducting pathways formed in the GDL have a big impact on the water dynamics in the GC. For different combinations of pipe diameters, we could have the droplet detachment, droplet receding, and isolated film flow at the corner cyclically, or only have the film flow at the corners and the droplet flow at the center. The surface tension forces from the hydrophilic sidewalls and the interface between the droplet and gas both play important roles in the

competing water flow from the conducting pathways into the GC. These competition mechanisms could give us the possibility to regulate liquid water flow into GCs, and contribute to the water management in GCs.

## References

- [1] M.M. Mench, *Fuel Cell Engines*, John Wiley & Sons, 2008.
- [2] G. Hoogers, *Fuel Cell Technology Handbook*, CRC Press, 2003.
- [3] C.Y. Wang, Fundamental models for fuel cell engineering, *Chem. Rev.* 104 (2004) 4727-4765.
- [4] H. Li, Y.H. Tang, Z.W. Wang, et al., A review of water flooding issues in the proton exchange membrane fuel cell, *J. Power Sources* 178 (2008) 103-117.
- [5] X.G. Yang, F.Y. Zhang, A.L. Lubawy, C.Y. Wang, Visualization of liquid water transport in a PEFC, *Electrochem. Solid-State Lett.* 7 (2004) A408-A411.
- [6] E.C. Kumbur, K.V. Sharp, M.M. Mench, Liquid droplet behavior and instability in a polymer electrolyte fuel cell flow channel, *J. Power Sources* 161 (2006) 333-345.
- [7] A. Bazylak, Liquid water visualization in PEM fuel cells: A review, *Int. J. Hydrogen Energy* 34 (2009) 3845-3857.
- [8] R. Mukundan, R.L. Borup, Visualising liquid water in PEM fuel cells using neutron imaging, *Fuel Cells* 9 (2009) 499-505.
- [9] S.H. Ge, C.Y. Wang, Liquid water formation and transport in the PEFC anode, *J. Electrochem. Soc.* 154 (2007) B998-B1005.
- [10] F.Y. Zhang, X.G. Yang, C.Y. Wang, Liquid water removal from a polymer electrolyte fuel cell, *J. Electrochem. Soc.* 153 (2006) A225-A232.
- [11] I.S. Hussaini, C.Y. Wang, Visualization and quantification of cathode channel flooding in PEM fuel cells, *J. Power Sources* 187 (2009) 444-451.
- [12] A. Theodorakakos, T. Ous, M. Gavaises, J.M. Nouri, N. Nikolopoulos, H. Yanagihara, Dynamics of water droplets detached from porous surfaces of relevance to PEM fuel cells, *J. Colloid Interface Sci.* 300 (2006) 673-687.
- [13] Y.H. Cai, J. Hu, H.P. Ma, B.L. Yi, H.M. Zhang, Effects of hydrophilic/hydrophobic properties on the water behavior in the micro-channels of a proton exchange membrane fuel cell, *J. Power Sources* 161 (2006) 843-848.
- [14] D. Rensink, J. Roth, S. Fell, Liquid water transport and distribution in fibrous porous media and gas channels, *Proc. 6<sup>th</sup> Int. ASME Conf. On Nanochannels, Microchannels and Minichannels* (2008), ICNMM2008-62087.
- [15] X. Zhu, P.C. Sui, N. Djilali, Three-dimensional numerical simulations of water droplet dynamics in a PEMFC gas channel, *J. Power Sources* 181 (2008) 101-115.
- [16] L. Hao, P. Cheng, Lattice Boltzmann simulations of liquid droplet dynamic behavior on a hydrophobic surface of a gas flow channel, *J. Power Sources* 190 (2009) 435-446.
- [17] J. Chio, G.H. Son, Numerical study of droplet motion in a microchannel with different contact angles, *J. Mech. Sci. Technol.* 22 (2008) 2590-2599.

- [18] K.S. Chen, M.A. Hickner, D.R. Noble, Simplified models for predicting the onset of liquid water droplet instability at the gas diffusion layer/gas flow channel interface, *Int. J. Energy Res.* 29 (2005) 1113-1132.
- [19] A. Bazylak, D. Sinton, N. Djilali, Dynamic water transport and droplet emergence in PEMFC gas diffusion layers, *J. Power Sources* 176 (2008) 240-246.
- [20] C. Hartnig, I. Manke, R. Kuhn, S. Kleinau, J. Goebbels, J. Banhart, High-resolution in-plane investigation of the water evolution and transport in PEM fuel cells, *J. Power Sources* 188 (2009) 468-474.
- [21] J.H. Nam, M. Kaviany, Effective diffusivity and water-saturation distribution in single- and two-layer PEMFC diffusion medium, *Int. J. Heat Mass Transf.* 46 (2003) 4595-4611.
- [22] S. Lister, D. Sinton, N. Djilali, Ex situ visualization of liquid water transport in PEM fuel cell gas diffusion layers, *J. Power Sources* 154 (2006) 95-105.
- [23] O. Ubbink, R.I. Issa, A method for capturing sharp fluid interfaces on arbitrary meshes, *J. Comput. Phys.* 153 (1999) 26-50.
- [24] C.W. Hirt, B.D. Nichols, Volume of fluid (VOF) method for the dynamics of free boundaries, *J. Comput. Phys.* 39 (1981) 201-225.
- [25] K. Jiao, B. Zhou, P. Quan, liquid water transport in parallel serpentine channels with manifolds on cathode side of a PEM fuel cell stack, *J. Power Sources*, 154 (2006) 124-137.
- [26] S. Whitaker, *The method of volume averaging*, Kluwer Academic Publishers, 1999.
- [27] J.U. Brackbill, D.B. Kothe, C. Zemach, A continuum method for modeling surface tension, *J. Comput. Phys.* 100 (1992) 335-354.
- [28] FLUNET6.3, *User's Guide*, Fluent Inc., 2006.
- [29] P.K. Sinha, C.Y. Wang, Pore-network modeling of liquid water transport in gas diffusion layer of a polymer electrolyte fuel cell, *Electrochim. Acta* 52 (2007) 7936-7945.
- [30] S. Basu, J. Li, C.Y. Wang, Two-phase flow and maldistribution in gas channels of a polymer electrolyte fuel cell, *J. Power Sources* 187 (2009) 431-443.
- [31] L. Hao, P. Cheng, Lattice Boltzmann simulations of water transport in gas diffusion layer of a polymer electrolyte membrane fuel cell, *J. Power Sources* 195 (2010) 3870-3881.
- [32] P.P. Mukherjee, C.Y. Wang, Q. Kang, Mesoscopic modeling of two-phase behavior and flooding phenomena in polymer electrolyte fuel cells, *Electrochim. Acta* 54 (2009) 6861-6875.

Table 6-1: Geometrical and physical parameters.

Parameters	Values
GC width/height/length	0.5/0.25/1.0 mm
Height of pipes	0.15 mm
Bath width/height/length	0.5/0.1/0.1 mm
Gas density, $\rho_g$	2.0016 kg m <sup>-3</sup>
Liquid water density, $\rho_l$	972 kg m <sup>-3</sup>
Gas dynamic viscosity, $\mu_g$	2.03×10 <sup>-5</sup> kg m <sup>-1</sup> s <sup>-1</sup>
Liquid water dynamic viscosity, $\mu_l$	3.5×10 <sup>-4</sup> kg m <sup>-1</sup> s <sup>-1</sup>
Surface tension, $\sigma$	0.0625 N m <sup>-1</sup>

Table 6-2: Simulated cases in this work.

Case name	Gas inlet Re number	Mass flow rate of liquid water (kg s <sup>-1</sup> )	Contact angle of GC sidewalls (degrees)	Contact angle of GC down wall (degrees)	Diameter of side pipes (μm)	Diameter of middle pipe (μm)
Case1_droplet	150	2.0×10 <sup>-6</sup>	40	140	None	50
Case2_droplet	200	2.0×10 <sup>-6</sup>	40	140	None	50
Case3_droplet	250	2.0×10 <sup>-6</sup>	40	140	None	50
Case4_droplet	300	2.0×10 <sup>-6</sup>	40	140	None	50
Case5_droplet	150	2.0×10 <sup>-6</sup>	40	80	None	50
Case6_droplet	150	2.0×10 <sup>-6</sup>	40	110	None	50
Case7_droplet	150	2.0×10 <sup>-6</sup>	40	170	None	50
Case8_film	150	2.0×10 <sup>-6</sup>	40	140	50	None
Case9_film	200	2.0×10 <sup>-6</sup>	40	140	50	None
Case10_film	250	2.0×10 <sup>-6</sup>	40	140	50	None
Case11_film	150	2.0×10 <sup>-6</sup>	0	140	50	None
Case12_film	150	2.0×10 <sup>-6</sup>	20	140	50	None
Case13_film	150	2.0×10 <sup>-6</sup>	60	140	50	None
Case14_film	150	5.0×10 <sup>-7</sup>	40	140	50	None
Case15_both	150	2.0×10 <sup>-6</sup>	40	140	50	50
Case16_both	150	2.0×10 <sup>-6</sup>	40	140	40	50
Case17_both	150	2.0×10 <sup>-6</sup>	40	140	50	40

# Chapter 7 - One-dimensional Phenomenological Model for Liquid Water Flooding in Cathode Gas Channel of a Polymer Electrolyte Fuel Cell

---

## Abstract

*The mathematical description of the liquid water flooding in the gas channel (GC) of a polymer electrolyte fuel cell (PEFC) at the macro scale has remained a challenge up to now. The mist flow assumption in the GC has been commonly used in previous numerical studies. In this chapter, a one-dimensional (down-the-channel) macroscale phenomenological model for the liquid water flooding in the cathode GC is developed based on several reasonable assumptions. We focus on the operating conditions with fully humidified inlet air on the cathode side. Some simplifications are introduced to obtain a manageable numerical model. A series of case studies are conducted to investigate the effects of droplet population and various operating parameters on the liquid water flooding in the GC. The results show that the gas drag force at the film-gas interface significantly enhances the film flow along the GC corners. The droplet size distribution also plays an important role in the GC water flooding. A proper selection of the GC sidewall contact angle is found to be critical to a better water management in the GC.*

## 7.1 Introduction

Water management plays a critical role in the development of polymer electrolyte fuel cells (PEFCs). The proton exchange membrane needs to attain high water content for effective ionic conduction. On the other hand, too much liquid water accumulating inside porous layers results in reactant starvations and cell degradations. Such a situation is referred to as “flooding” in PEFCs. In order to balance both water requirements, a deep understanding of liquid water transport in the whole PEFC is needed<sup>1-5</sup>.

The cathode side of a PEFC is prone to being flooded first, since water is generated in the cathode catalyst layer (CL) due to electrochemical reactions. Then, excessive liquid water penetrates through the porous layers into gas channels (GCs). Typically, a GC is confined by three walls from the bipolar plate which are hydrophilic, and the surface of the gas diffusion layer (GDL)

which is hydrophobic. When liquid water breaks through the GDL-GC interface, water droplets and film slugs form on the GDL surface and along hydrophilic GC corners<sup>6-9</sup>, respectively. It is obvious that under flooding situations, liquid water transport on the cathode side can occur in both porous layers and micro GCs simultaneously.

Experimentally, several techniques have been employed to visualize liquid water evolution and transport inside porous layers, such as synchrotron X-ray<sup>10-12</sup>, neutron radiography<sup>13-16</sup> and tomography, magnetic resonance imaging<sup>17</sup>, as well as fluorescence microscope<sup>18, 19</sup>. As a result, a new liquid water transport mechanism through fibrous GDL is proposed, which is termed as “fingering and channeling” flow<sup>18, 20</sup>. Liquid water dynamics in the GC is quite complex due to its microstructure and mixed-wettability. Over the past few years, optical photography using transparent fuel cells<sup>7, 8, 21, 36</sup> have been widely used to study liquid water flow in the GC and droplet dynamics. As for computational fluid dynamics (CFD) simulations of the liquid water transport in a PEFC, two major challenges lie in how to effectively mimic the liquid water transport in the GC, and how to couple the liquid water transport between the GDL and GC. Even though some interface tracking methods<sup>22-24</sup> have been extensively used to investigate water dynamics in the GC, they all suffer from heavy computational efforts, and cannot be applied to a large level. In addition, these methods are based on a much smaller spatial scale than that in the GDL, where the averaged two-phase Darcy’s law<sup>25</sup> is commonly employed to describe the liquid water transfer. To date, there are only a few works addressing the interfacial coupling effect<sup>26-28</sup> on the liquid water transport in the porous layers, often based on some simplified models.

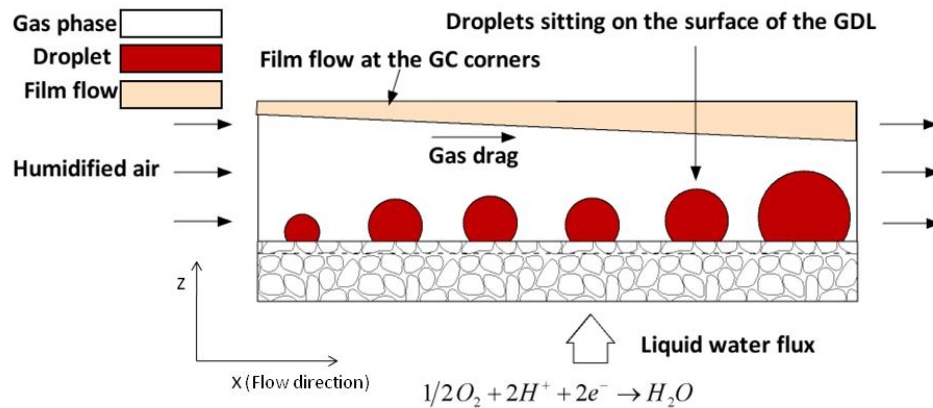


Figure 7-1: Two-dimensional schematic of liquid water flooding in the GC.

In this chapter, we mainly contribute to the first challenge mentioned above, and try to describe the liquid water transport in the GC at a macroscopic scale. We develop a model that is very computationally effective. Fig. 7-1 shows the schematic water flooding in the GC. With continuous liquid water filling from the GDL, film flow forms along the GC corners, and droplets sit on the GDL surface. Note that the isolated GC is our study domain to avoid the GDL-GC interface treatment as a first attempt.

In what follows, we first list the main assumptions used in the model development. Then, the detailed mathematical derivations are given. Finally, several case studies are conducted to investigate the effects of various engineering and operating parameters on the liquid water flooding in the GC, and some useful conclusions are obtained.

## 7.2 Physical model

In this section, we first give the main assumptions adopted in this work. Then the governing equations of the phenomenological model for the water flooding in the GC are derived in detail.

### 7.2.1 Assumptions

To make mathematical descriptions of water flooding in the GC feasible, and based on physical considerations, the following main assumptions are used in the model development:

1. The dynamic evolution of individual droplets in the GC can be described by the following sequential processes: emergence, growth, detachment, coalescence and finally wicking into the hydrophilic sidewalls of the GC (as shown in Fig. 7-2). In other words, droplets in the GC are not tracked explicitly.
2. The liquid water coming from the GDL, and condensed from water vapor flows out of the GC only via the film forming along the GC corners. This is a reasonable assumption under low gas flow rates<sup>8, 9, 29</sup>.

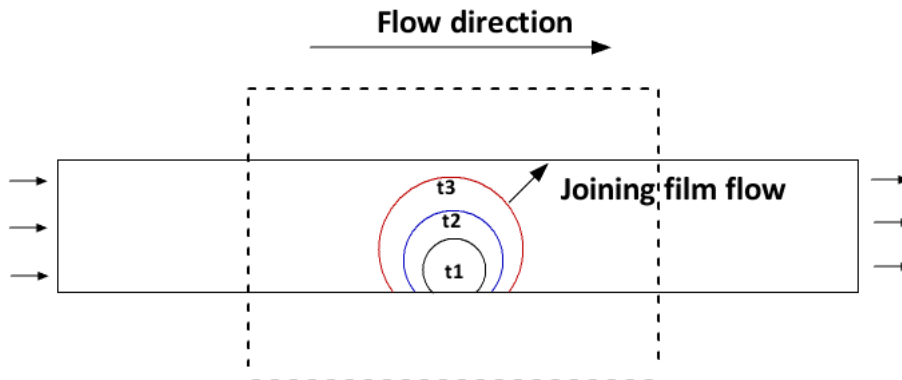


Figure 7-2: Schematic of the growth of a water droplet with time in the GC (Finally, this droplet reaches to a critical size comparable to the GC dimensions, and joins the film flow along the GC corners).

### 7.2.2 Governing equations

Fig. 7-3 depicts the assumed idealized liquid water distribution at the GC cross section, which is separated into film (including two symmetric parts) forming at the hydrophilic GC corners, as well as droplet sitting on the hydrophobic GDL surface (i.e. GC down wall in this work). Since droplet dynamics is not considered here, we focus on the derivations of governing equations for

the gas and film flows in what follows. The droplet effect in the GC is accounted for in terms of one parameter called droplet area in the GC cross-section,  $A_d$ , which could be a function of  $x$  coordinate (flow direction along the GC), and other flow variables.

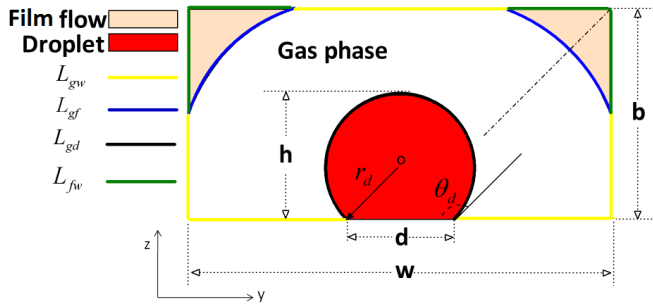


Figure 7-3: Assumed liquid water distribution at the GC cross section, including the film at the corners and the water droplet sitting at the center.

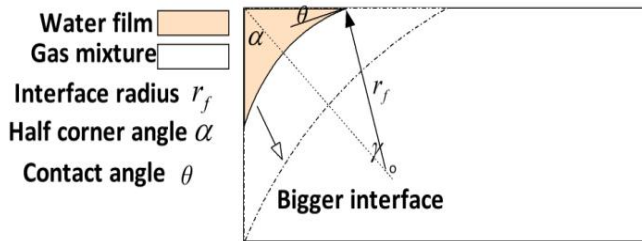


Figure 7-4: Schematic of the film configuration at a GC corner.

### 7.2.2.1 Gas phase

We integrate the microscopic continuity equation for the gas phase over the GC cross section shown in Fig. 7-3, and get:

$$\frac{d(A_g \rho_g v_g)}{dx} = S_g \quad (7-1)$$

where  $A_g$  is the area of the gas phase in the GC cross section,  $\rho_g$  is the gas mass density,  $v_g$  denotes the area-averaged gas velocity, and  $S_g$  represents the source/sink term of the gas phase owing to the oxygen consumption and phase change between water vapor and liquid water. The gas flow direction is in the positive  $x$ .

On the cathode side of a PEFC, humidified air is delivered into the GC. We have the following averaged species transport equations for both water vapor and oxygen:

$$\frac{d(A_g \rho_g C_{O_2} v_g)}{dx} = \frac{d}{dx} \left( A_g \rho_g D_{O_2} \frac{dC_{O_2}}{dx} \right) + S_{O_2} \quad (7-2)$$

$$\frac{d(A_g \rho_g C_{H_2O} v_g)}{dx} = \frac{d}{dx} \left( A_g \rho_g D_{H_2O} \frac{dC_{H_2O}}{dx} \right) + S_{H_2O} \quad (7-3)$$

Here,  $C_{O_2}$  and  $C_{H_2O}$  denote the mass fractions of oxygen and water vapor, respectively,  $D_{O_2}$  and  $D_{H_2O}$  are the diffusivities of oxygen and water vapor, respectively,  $S_{O_2}$  is the oxygen sink term, and  $S_{H_2O}$  is the water vapor sink/source term.

The relation between the gas velocity and gas pressure gradient along the GC is approximated by the well-known Hagen-Poiseuille equation<sup>30</sup>, which is given as:

$$v_g = -K_g (\mu_g, A_g) \frac{dp_g}{dx} \quad (7-4)$$

where  $p_g$  is the gas pressure, and  $K_g$  is called the flow conductivity of the gas phase, which is a function of gas dynamic viscosity, and gas flow area. With the help of the hydraulic diameter for the gas flow, the gas flow conductivity is specified as follows:

$$K_g = \frac{D_H^2}{32\mu_g} = \frac{1}{32\mu_g} \left( \frac{4A_g}{L_{no-slip}} \right)^2 \quad (7-5)$$

$$L_{no-slip} = L_{gw} + L_{gf} + L_{gd} \quad (7-6)$$

In Eq. 7-5,  $D_H = 4A_g / L_{no-slip}$  is the hydraulic diameter for the gas flow, and  $L_{no-slip}$  is the wetted perimeter of the gas flow area as shown in Fig. 7-3, which is given in Eq. 7-6.  $L_{gw}$ ,  $L_{gf}$ , and  $L_{gd}$  denote the lengths of gas-wall interface, gas-film interface, as well as gas-droplet interface, respectively.

Isothermal condition is assumed in this work, no energy equation for gas or film phase is needed. In addition, we have the following three complementary equations for the gas phase:

$$A_g + A_f + A_d = A_{gc} \quad (7-7)$$

$$C_{O_2} + C_{H_2O} + C_{N_2} = 1 \quad (7-8)$$

$$\rho_g = \frac{P_g}{RT \sum_i \frac{C_i}{M_i}} \quad (7-9)$$

Eq. 7-7 means that the summation of the gas phase area, film area, and droplet area is equal to the GC cross-sectional area, which can be seen in Fig. 7-3. Eq. 7-8 shows the summation of species mass fractions equals to unity. Finally, Eq. 7-9 is the state equation for an ideal gas

mixture, where  $C_i$  is the species mass fraction,  $M_i$  is the molecular weight of each species,  $R$  is the universal gas constant, and  $T$  denotes the cell operating temperature.

### 7.2.2.2 Film phase

The averaged continuity equation for the film phase is given as:

$$\frac{d(A_f \rho_f v_f)}{dx} = S_f \quad (7-10)$$

where  $v_f$  is the average velocity of the film phase, and  $S_f$  denotes the source term due to water flux from the GDL as well as phase change between water vapor and film.

Based on the average process, the film flow equation can be expressed as follows:

$$v_f = -\frac{r_f^2}{\mu_f \beta} \frac{dp_f}{dx} + F_{drag} \frac{r_f \tau}{\mu_f} \quad (7-11)$$

where  $r_f$  is the radius of the curvature of gas-film interface,  $\mu_f$  is the dynamic viscosity of liquid water,  $p_f$  denotes the film pressure,  $\tau$  represents the gas shear stress at the gas-film interface,  $\beta$  is called dimensionless viscous resistance, and  $F_{drag}$  can be called dimensionless gas drag coefficient. Greater detail on the derivation of Eq. 7-11 is given in Appendix 7A.

We can find the approximate expressions for  $\beta$  and  $F_{drag}$  by means of numerical simulations. Particularly, extensive studies on the dimensionless viscous resistance are available in literature<sup>32</sup>. The two pressures for the gas and film phases are coupled through the capillary pressure:

$$p_c = p_g - p_f = \frac{\sigma}{r_f} \quad (7-12)$$

Here,  $\sigma$  represents the surface tension between gas and liquid water, and we assume that the radius of the curvature of gas-film interface along the GC is infinite.

### 7.2.2.3 Geometrical information

In order to close the governing equations derived above, some additional equations are required which can be obtained based on the geometrical information shown in Fig. 7-3 and 7-4. The Concus and Finn condition<sup>33</sup> should be satisfied in this work to ensure a stable film distribution along the GC corners:

$$\alpha + \theta < \pi/2 \quad (7-13)$$

The film area in the GC cross section can be written as a function of the radius of the curvature of gas-film interface:

$$A_f = r_f^2 \left[ \sin(2\gamma) + \frac{2 \sin^2 \gamma}{\tan \alpha} - 2\gamma \right] \quad (7-14)$$

where  $r_f$  is the radius of the curvature of gas-film interface,  $\alpha$  is the upper half corner angle of the GC, and  $\gamma$  is expressed as:

$$\gamma = \frac{\pi}{2} - \alpha - \theta \quad (7-15)$$

where  $\theta$  denotes the static contact angle of the GC sidewalls.

The areas of droplet and GC cross sections are given as:

$$A_d = r_d^2 \left[ \theta_d - \frac{\sin(2\theta_d)}{2} \right] \quad (7-16)$$

$$A_{gc} = b \sin(\pi - 2\alpha) [w - b \cos(\pi - 2\alpha)] \quad (7-17)$$

in which,  $\theta_d$  denotes the static contact angle of the GDL surface, and  $r_d$  is the droplet radius shown in Fig. 7-3. In Eq. 7-17,  $b$  is the side edge length of the GC cross section, and  $w$  is the down edge length of the GC cross section.

As shown in Fig. 7-3, the lengths of the gas-film interface, gas-wall interface, gas-droplet interface, and film-wall interface are given as:

$$L_{gf} = 4r_f \gamma \quad (7-18)$$

$$L_{gd} = 2r_d \theta_d \quad (7-19)$$

$$L_{gw} = 2w + 2b[1 - \cos(\pi - 2\alpha)] - 2r_d \sin(\pi - \theta_d) - \frac{4r_f \sin \gamma}{\sin \alpha} \quad (7-20)$$

$$L_{fw} = \frac{4r_f \sin \gamma}{\sin \alpha} \quad (7-21)$$

## 7.3 Numerical model

### 7.3.1 Simplifications of governing equations

As a first attempt, we make some simplifications of the governing equations derived above for numerical studies. First, we focus on the fully humidified air inlet on the cathode side. Therefore, we just need to consider the water vapor condensation along the GC. And, constant molar density of the gas phase is assumed in the GC due to the relatively small pressure drop, which is given as:

$$\widehat{\rho}_g = \frac{p_0}{RT} \quad (7-22)$$

where  $\widehat{\rho}_g$  designated by the caret is the molar density of the gas phase, and  $p_0$  is the gas inlet pressure.

We also neglect the species diffusion in the GC and simplify the transport equations 7-2 and 7-3 as follows:

$$\frac{d(A_g \widehat{\rho}_{O_2} v_g)}{dx} = \widehat{S}_{O_2} \quad (7-23)$$

$$\frac{d(A_g \widehat{\rho}_{H_2O} v_g)}{dx} = \widehat{S}_{H_2O} \quad (7-24)$$

Here,  $\widehat{\rho}_{O_2}$  and  $\widehat{\rho}_{H_2O}$  represent the molar densities of oxygen and water vapor, respectively, and  $\widehat{S}_{O_2}$  and  $\widehat{S}_{H_2O}$  are the molar source/sink terms (mol/m/s).

Since the inlet gas is fully humidified, we can write the molar density of water vapor as:

$$\widehat{\rho}_{H_2O} = \frac{p_{sat}}{RT} \quad (7-25)$$

where  $p_{sat}$  is the saturated water vapor pressure, given by the following empirical expression [34]:

$$\log_{10} \frac{p_{sat}}{10^{1325}} = -21794 + 0.02953(T - 27315) - 9.1837 \times 10^{-5}(T - 27315)^2 + 14454 \times 10^{-7}(T - 27315)^3 \quad (7-26)$$

After several algebraic manipulations on Eq. (7-22)-(7-25), the molar sink term of water vapor is expressed as:

$$\widehat{S}_{H_2O} = \frac{p_{sat}}{p_0 - p_{sat}} \widehat{S}_{O_2} \quad (7-27)$$

So, the gas phase averaged continuity equation can be obtained as:

$$\frac{d(A_g v_g)}{dx} = \left( \frac{RT}{p_0 - p_{sat}} \right) \widehat{S}_{O_2} \quad (7-28)$$

The molar sink term of oxygen is given as:

$$\widehat{S}_{O_2} = -\frac{I(x)w}{4Ft} \quad (7-29)$$

where  $I(x)$  is the cell current density as a function of  $x$  coordinate,  $F$  is the Faraday constant,  $w$  is the down edge length of the GC cross section, and  $t$  denotes the ratio of the area of the GC down wall to the reactive area in the membrane.

For the film phase, the continuity equation (7-10) may be rewritten as:

$$\frac{d(A_f v_f)}{dx} = \frac{S_f}{\rho_f} = \frac{M_{H_2O}}{\rho_f} \left[ \frac{(1+2a)I(x)w}{2Ft} - \widehat{S}_{H_2O} \right] \quad (7-30)$$

In Eq. 7-30, the film density is assumed to be constant,  $M_{H_2O}$  denotes the molecular weight of water vapor, and  $a$  is the net water transfer coefficient.

Substituting Eq. 7-12 into Eq. 7-11, we get the film flow equation as:

$$v_f = -\frac{r_f^2}{\mu_f \beta} \frac{dp_g}{dx} - \frac{\sigma}{\mu_f \beta} \frac{dr_f}{dx} + F_{drag} \frac{r_f \tau}{\mu_f} \quad (7-31)$$

A simplified expression for the dimensionless viscous resistance  $\beta$ , based on an analytical solution, is available in the literature<sup>35</sup>, which is given as:

$$\beta = \frac{12 \sin^2 \alpha (1-B)^2 (\psi_1 - B\psi_2) \psi_3^2}{(1 - \sin \alpha)^2 B^2 (\psi_1 - B\psi_2)^3} \quad (7-32)$$

$$B = \left( \frac{\pi}{2} - \alpha \right) \tan \alpha \quad (7-33)$$

$$\psi_1 = \cos^2(\alpha + \theta) + \cos(\alpha + \theta) \sin(\alpha + \theta) \tan \alpha \quad (7-34)$$

$$\psi_2 = 1 - \frac{\theta}{\frac{\pi}{2} - \alpha} \quad (7-35)$$

$$\psi_3 = \frac{\cos(\alpha + \theta)}{\cos \alpha} \quad (7-36)$$

The gas shear stress at the gas-film interface can be formulated as:

$$\tau = -f_\tau \frac{A_g}{L_{no-slip}} \frac{dp_g}{dx} \quad (7-37)$$

In Eq. 7-37,  $f_\tau$  denotes the effect of the gas flow configuration on the shear stress distribution, which can be obtained based on numerical experiments<sup>31</sup>:

$$f_\tau = 1 - \exp \left[ \frac{-13 r_f}{D_H} \left( \cos \gamma + \frac{\sin \gamma}{\tan \alpha} - 1 \right) \right] \quad (7-38)$$

We also can employ numerical simulations to obtain values for the dimensionless gas drag coefficient, which is given in Table 7-2. Note that the effect of the contact angle of the GC sidewalls is neglected here.

### 7.3.2 Boundary conditions and numerical implementation

Based on the adopted simplifications in Section 7.3.1, five first-order ordinary differential equations (ODEs) are obtained, namely, Eq. 7-28, Eq. 7-23, Eq. 7-4, Eq. 7-30, and Eq. 7-31, associated with five unknown variables,  $v_g$ ,  $\hat{\rho}_{O_2}$ ,  $P_g$ ,  $v_f$ , and  $r_f$ . In the following, we describe the applied boundary conditions.

The inlet gas velocity is decided by averaged current density, stoichiometric ratio, reactive area, as well as GC cross-section, expressed as:

$$v_g \Big|_{x=0} = \frac{\xi_c I_a A_m}{4F \hat{\rho}_{O_2} A_g} = \frac{\xi_c A_m}{4LF (\hat{\rho}_{O_2} \Big|_{x=0}) A_g} \int_0^L I(x) dx \quad (7-39)$$

where  $\xi_c$  is the stoichiometric ratio on the cathode side,  $L$  is the GC length,  $I_a$  is the averaged current density along the GC, and  $A_m$  denotes the reactive area.

The inlet oxygen molar density is dependent on the inlet gas pressure, and relative humidity:

$$\hat{\rho}_{O_2} \Big|_{x=0} = \frac{0.21 p_0}{RT} \left( 1 - \frac{P_{sat}}{p_0} RH \right) \quad (7-40)$$

where  $RH$  represents the relative humidity of the inlet air, and it is 100% in this work.

A constant inlet gas pressure is specified as:

$$P_g \Big|_{x=0} = P_0 \quad (7-41)$$

The film velocity at the GC inlet is set to be zero:

$$v_f \Big|_{x=0} = 0 \quad (7-42)$$

For the radius of the curvature of the gas-film interface, we assume a fully developed boundary condition at the GC out, expressed as:

$$\frac{dr_f}{dx} \Big|_{x=L} = 0 \quad (7-43)$$

Since the five ODEs are highly nonlinear and coupled, MATLAB 2010 is employed to solve them numerically. Note that, good initial guesses of unknown variables are essential to solve the ODEs with boundary conditions in this work.

## 7.4 Results and discussion

Table 7-1 lists the geometrical, physical and operating parameters for the base case. Note that we assume that droplets are absent in the base case. Fig. 7-5 shows the effects of the half corner angle of the GC and the contact angle of the GC sidewalls on the dimensionless viscous resistance,  $\beta$ . Generally speaking, the dimensionless viscous resistance increases with the increase of the GC half corner angle. For a given half corner angle, no obvious change of the dimensionless viscous resistance can be found with the change in the contact angle of the GC sidewalls, as long as the contact angle is smaller than 15 degrees. While the contact angle is larger than 15 degrees, the dimensionless viscous resistance increases dramatically as increasing the contact angle.

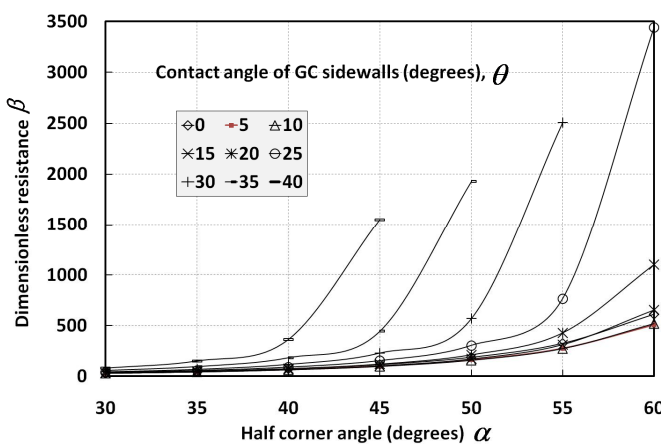


Figure 7-5: Effects of the half corner angle of the GC and the contact angle of the GC sidewalls on the dimensionless resistance.

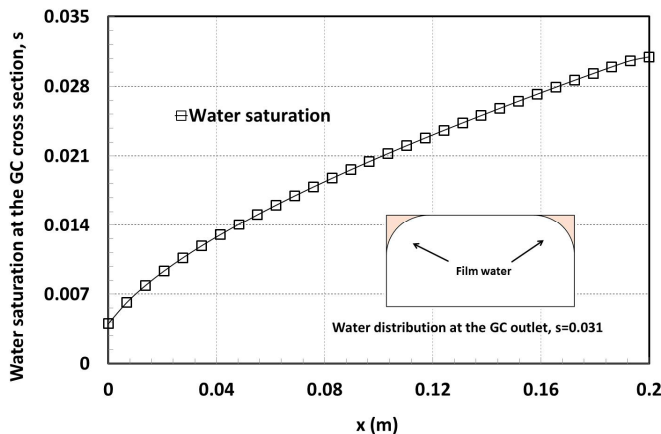


Figure 7-6: Distribution of liquid water saturation along the GC (Insertion: liquid water distribution at the GC outlet).

### 7.4.1 Base case study

In the base case study, we suppress the appearance of droplets in the GC. This may be done by regulating liquid water flow into the GC. For more detail, one can refer to the reference<sup>29</sup>. We note that low water saturation in GCs is beneficial to the performance of PEFCs due to low water coverage at the GDL-GC interface and small pressure losses along GCs. Fig. 7-6 shows the

distribution of liquid water saturation along the flow direction. As a uniform water flux is provided through the bottom of the GC, more and more liquid water accumulates along the GC corners. As a result, the distribution of the film thickness along the GC is from thin to thick. Since no droplet is considered here, the liquid water saturation is quite small, only up to 0.031 at the end of the GC (see the insertion in Fig. 7-6).

The gas phase velocity decreases along the flow direction as shown in Fig. 7-7 (left). This can be explained by the fact that while the change of the gas flow area is quite small, the gas phase loses considerable mass along the GC due to the water vapor condensation and oxygen consumption. Fig. 7-7 (right) shows that the film velocity increases along the GC from 0 to about 0.024 m/s. This is due to the water vapor condensation and uniform liquid water flux from the GDL. It is seen that the film velocity is much smaller compared to that of the gas phase, which results in large gas drag force at the film-gas interface. This gas drag force assists the film flow along the GC corners considerably<sup>29</sup>. Therefore, very low water saturation is found in the GC (see Fig. 7-6).

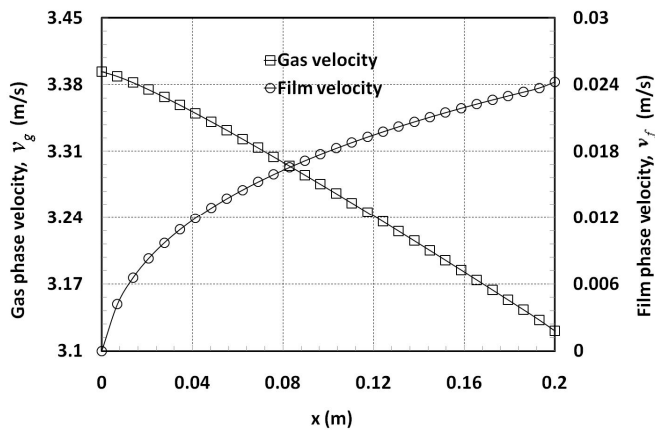


Figure 7-7: Left: gas phase velocity distribution along the GC (decreasing); right: film phase velocity distribution along the GC (increasing).

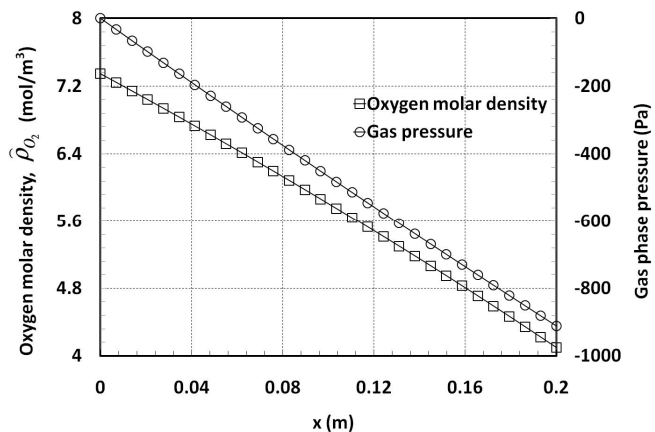


Figure 7-8: Left: oxygen molar density distribution along the GC; right: gas pressure drop along the GC.

Fig. 7-8 (left) displays the oxygen molar density reduction along the GC. For the base case, the stoichiometric ratio is 2.0, and the molar density of oxygen at the GC outlet is a little higher than

half of that at the GC inlet mainly due to the decrease of gas phase velocity along the GC (Fig. 7-7). Fig. 7-8 (right) shows the gas pressure distribution along the GC relative to the inlet pressure (1.5 bar). The total pressure drop is about 911 Pa, which is quite close to that for single-phase flow in the GC. This indicates that film flow along the GC corners has little impact on gas pressure loss due to its small saturation.

#### 7.4.2 Effect of droplets in the GC

It has been assumed that droplets in the GC join in the film flow along the GC corners through a series of dynamic processes. However, at any time droplets can be always observed in the GC under flooding situations. For comprehensiveness, the effect of droplets should be taken into account in the present steady-state GC flooding model. Since droplets are not explicitly tracked, we introduce a parameter called droplet radius (see Eq. 7-16) in our model development. In addition, the droplet radius at the GC cross section (Fig. 7-3) can be expected to be a function of several variables such as Reynolds number of gas flow, current density, and contact angle of the GDL surface, as well as pore-structure of the GDL. We can illustrate it as follows:

$$r_d = f(\text{Re}, \theta_d, I, \text{etc}) \quad (7-44)$$

Up to now, it is still difficult to derive a general explicit expression for droplet distribution along the GC. It should be possible, however, to obtain some empirical expressions by means of experimental observations. As a first attempt, we propose a simple empirical model for calculating the droplet radius at the GC cross section:

$$r_d = k \frac{A_{gc}}{A_g v_g} I(x) \quad (7-45)$$

In Eq. 7-45, we take into account two major factors influencing the magnitude of droplet radius: local water flux from the GDL denoted by local current density  $I(x)$  and local gas drag force approximated by gas flow rate. In addition, we note that the coefficient  $k$  serves as a fitting parameter, which should be calibrated by experimental data. In principal, the coefficient  $k$  should also be a dependent parameter. However, for simplicity in this work it is set to a constant of  $1.0 \times 10^{-7}$  due to the absence of experimental data.

Fig. 7-9 shows the droplet effect on gas pressure drops along the GC for different stoichiometric ratios. Note that expect for droplet radius and stoichiometry, all other parameters are the same as for the base case. It is seen that the gas pressure loss is almost linearly proportional to the applied stoichiometry when droplets are absent, which corresponds to the mist flow assumption used by most previous PEFC models<sup>26, 34</sup>. By incorporating the droplet model of Eq. 7-45, we obtain the totally different gas pressure losses along the GC as shown by the upper curve in Fig. 7-9. At the stoichiometry of 2.0, the gas pressure loss is up to about 2790 Pa, which is about three times as large as that without droplet effect. As increasing the stoichiometry the gas pressure loss reduces first due to the enhanced gas drag force on the droplets. As a consequence, smaller droplets are expected in the GC. Later on the gas pressure loss increases slightly because of the enlarged gas flow rate, which starts to dominate the gas

pressure loss along the GC. The same phenomenon was also observed in experiments<sup>39</sup> which can be captured very well by the present GC flooding model.

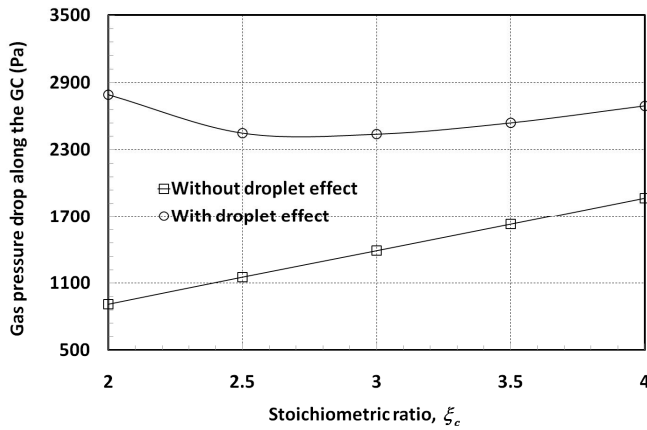


Figure 7-9: Droplet effect on gas pressure losses along the GC for different stoichiometric ratios.

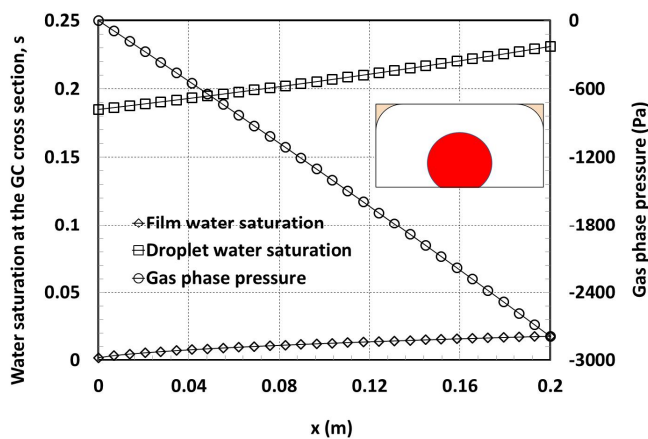


Figure 7-10: Distributions of water saturation and gas pressure along the GC at the stoichiometry of 2.0 (Insertion: liquid water distribution at the GC outlet, including both film and droplet).

Fig. 7-10 shows the water saturation and gas pressure distributions along the GC at the stoichiometry of 2.0. The water saturation at the GC cross section includes two contributions: film water and droplet water. It can be seen obviously that the droplet water saturation is much bigger than the film one, which increases slightly due to the decreased gas drag force. The gas pressure drops almost lineally along the GC mainly owing to the small variation of liquid water saturation in the GC. The insertion in Fig. 7-10 displays the liquid water distribution at the GC outlet with the film water saturation of about 0.02 and droplet water saturation of about 0.23. It is evident that droplets in the GC are not only the main contributions to gas pressure loss, but also cover the GDL-GC interface blocking reactant diffusion into reactive sites. Therefore for better water management in GCs, we should depress the emergence of droplets, and enhance the film flow along GC corners.

### 7.4.3 Effect of operating conditions

In this subsection, we examine the influences of several operating parameters plus the GC sidewall contact angle on liquid water flooding in the GC. Fig. 7-11 shows the effect of stoichiometric ratio on liquid water saturation distributions along the GC. It is seen that with the increase of stoichiometry, the droplet water saturation first reduces dramatically due to the enhanced gas drag force, and later on it reduces slowly due to the increased gas flow area at the GC cross section. This indicates that in practice the stoichiometry can be optimized to achieve a compromise between reducing droplet water saturation and decreasing gas pressure loss. The film water saturation for each stoichiometry is also plotted in Fig. 7-11. Interestingly we find no obvious difference among these film saturation distributions along the GC, which means that increasing stoichiometry has little influence on film flow along GC corners.

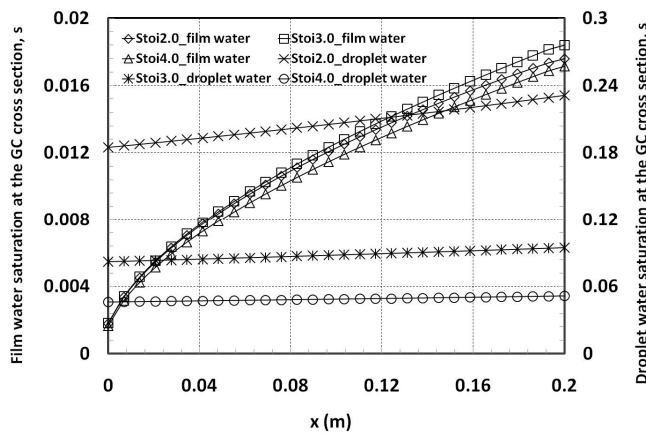


Figure 7-11: Distributions of water saturation (i.e. film water saturation and droplet water saturation) along the GC for different stoichiometric ratios.

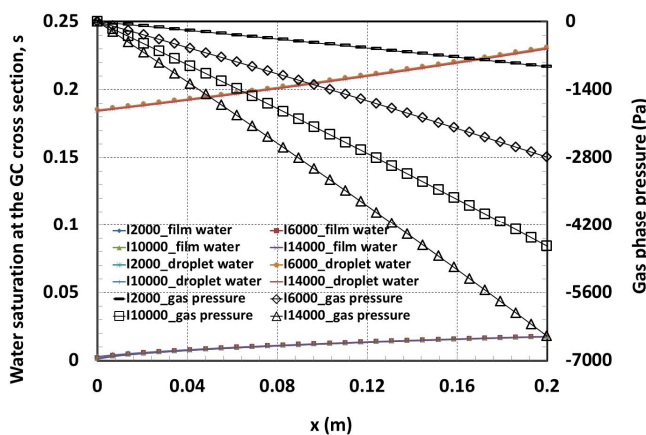


Figure 7-12: Distributions of water saturation and gas pressure along the GC for different operating current densities.

Fig. 7-12 displays the effect of operating current density on the water saturation and gas pressure distributions along the GC. The same parameters as for the base case are employed except for varied current density and inclusion of droplet model. Interestingly, no discernible difference in either droplet water saturation or film water saturation distributions can be observed, although increasing current density means more liquid water is introduced into the GC.

We can explain this phenomenon by the fact that the inlet gas flow rate increases as increasing the operating current density at a fixed stoichiometry of 2.0. Thus, the resultant gas drag force can always hold the GC water flooding at a certain level. The corresponding gas pressure loss along the GC as shown in Fig. 7-12 is directly proportional to the applied operating current density.

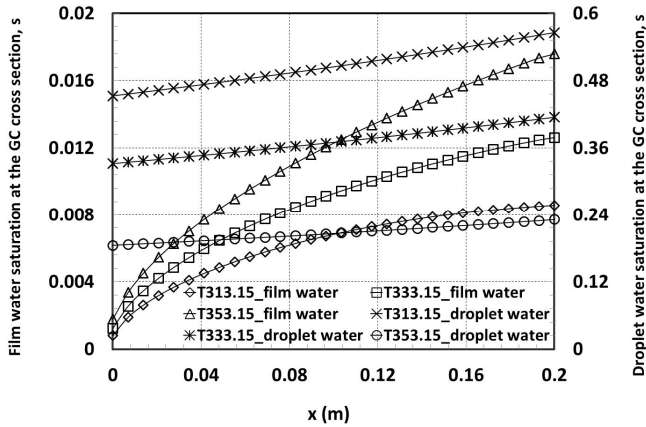


Figure 7-13: Distributions of water saturation (i.e. film water saturation and droplet water saturation) along the GC for different operating temperatures.

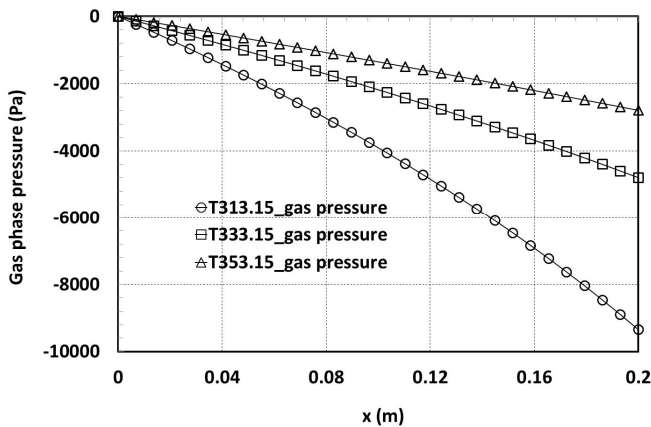


Figure 7-14: Effect of the operating temperature on the gas pressure drop along the GC.

Fig. 7-13 displays the effect of operating temperature on the distributions of water saturation and gas pressure along the GC. As increasing the operating temperature, the oxygen molar density decreases for the fully humidified inlet air. In order to satisfy the fixed stoichiometric ratio of 2.0, the inlet gas flow rate increases with the increase of the operating temperature at the fixed current density of  $6000 \text{ A/m}^2$ . As a result, the droplet water saturation decreases as increasing the operating temperature as shown in Fig. 7-13. However, the film water saturation increases as increasing the operating temperature. This is attributed to the fact that water vapor condensation dominates the film water flooding along the GC corners (more and more water can be condensed from water vapor as increasing the operating temperature). Since droplet water flooding plays a dominant role in the gas pressure loss along the GC, the largest gas pressure loss of about 9300 Pa is found at the operating temperature of 313.15 K, as shown in Fig. 7-14. Therefore, we conclude that liquid water flooding in GCs can be considerably mitigated by

increasing the cell operating temperature, which in addition gives rise to small gas pressure loss along GCs.

We also investigate the effect of the contact angle of the GC sidewalls on the water removal ability of the GC in the absence of droplet influence. Qin et al.<sup>29</sup> studied the effect of the sidewall contact angle on the film flow at the GC corners by means of direct simulations. They concluded that larger contact angle of the hydrophilic sidewalls was beneficial to the film removal at the GC corners. However, less hydrophilic sidewalls were incapable of removing the water clogging in the GC efficiently. Based on our phenomenological model in this work, we also find that the water saturation at the GC cross section decreases with the increase of the contact angle of the GC sidewalls, as shown in Fig. 7-15. This is attributed to the fact that a larger contact angle of the hydrophilic sidewalls corresponds to smaller adhesion force on the film flow; in turn, less liquid water can be held in the GC. However, it should be pointed out that in practice a proper contact angle of the GC sidewalls should be selected to balance two requirements<sup>37, 38</sup>: increasing the film removal ability (less hydrophilicity), and removing the water clogging fast (higher hydrophilicity).

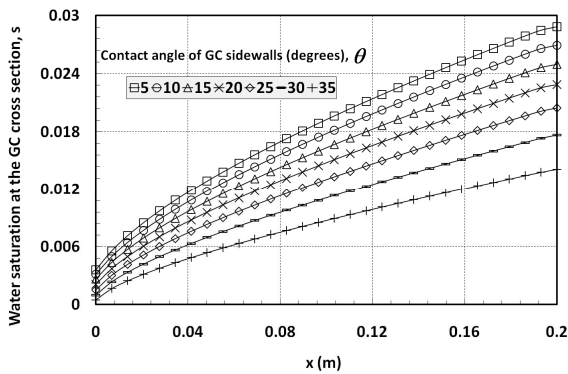


Figure 7-15: Effect of the sidewall contact angle of the GC on the film water distribution along the GC corners.

At last we note that the steady- state GC flooding model presented in this work is still at its early stage. Further improvements are still ongoing. For instance, a non-equilibrium phase change model needs to be introduced to consider the operation of partially humidified gas inlet. The model should be capable of modeling liquid water flooding in a large-scale flow field, probably including the effect of channel bends. Most importantly, extensive experimental data are needed to calibrate the droplet model proposed by the present work.

## 7.5 Conclusions

In this work, we first propose an idealized liquid water distribution at the GC cross section. Water droplets are assumed to form on the GDL surface, and water film resides at the GC corners. As a first attempt, we do not model the droplet dynamics explicitly, but we assume that droplets in the GC join the film flow along the GC corners through a series of dynamic processes. This assumption is quite reasonable under low gas flow rates. Then, we develop a phenomenological channel flooding model and a number of simulations are conducted to investigate the effects of

droplets and several operating parameters on liquid water flooding in the GC. The following main conclusions are obtained:

1. The film water flow velocity in the GC is much smaller than that of the gas phase, which results in large gas drag force at the film-gas interface. This gas drag force assists in the film flow along GC corners considerably; thus playing a dominant role in the water removal along GC corners. In addition, the film flow along GC corners has little impact on gas pressure loss due to its small saturation.
2. With the presence of droplets in the GC, the gas pressure loss is about three times as large as that without droplet effect at the stoichiometry of 2.0. As increasing the stoichiometry the gas pressure loss reduces first due to the enhanced gas drag force on the droplets. Later on the gas pressure loss increases slightly due to the enlarged gas flow rate, which begins to dominate the gas pressure loss along the GC. We find that droplets in the GC are the main contributions to the gas pressure loss and liquid water flooding. For better water management in GCs, we should depress the emergence of droplets, and enhance the film flow along GC corners.
3. In practice the stoichiometry can be optimized to obtain a compromise between reducing droplet water saturation and decreasing gas pressure loss. Particularly increasing stoichiometry has little influence on film flow along GC corners.
4. No discernible difference in either droplet water distribution or film water distribution can be found for different operating current densities. The gas pressure loss is directly proportional to the applied current density.
5. The liquid water in GCs can be considerably mitigated by increasing the cell operating temperature, which in addition gives rise to small pressure loss along GCs.
6. A proper contact angle of the GC sidewalls should be chosen to balance two requirements: increasing the film removal ability (less hydrophilicity), and removing the water clogging fast (higher hydrophilicity).

## References

- [1] Z. Weber and J. Newman, *Chem. Rev.*, 104, 4679 (2004).
- [2] N. Djilali, *Energy*, 32, 269 (2007).
- [3] S. S. Zhang, X. Z. Yuan, J. N. C. Hin, H. J. Wang, K. A. Friedrich and M. Schulze, *J. Power Sources*, 194, 588 (2009).
- [4] M. M. Mench, *Fuel Cell Engines*, John Wiley & Sons, Inc (2008).
- [5] Y. Wang, *Chem. Rev.*, 104, 4727 (2004).
- [6] A. Bazylak, D. Sinton and N. Djilali, *J. Power Sources*, 176, 240 (2008).
- [7] Spornjak, A. k. Prasad and S. G. Advani, *J. Powers Sources*, 170, 334 (2007).
- [8] X. G. Yang, F. Y. Zhang, A. L. Lubawy and C. Y. Wang, *Electrochem. Solid-State Lett.*, 7, A408 (2004).
- [9] F. Y. Zhang, X. G. Yang and C. Y. Wang, *J. Electrochem. Soc.*, 153, A225 (2006).
- [10] P. K. Sinha, P. Halleck and C. Y. Wang, *Electrochem. Solid-State Lett.*, 9, A344 (2006).
- [11] Hartnig, I. Manke, R. Kuhn, N. Kardjilov, J. Banhart and W. Lehnert, *Appl. Phys. Lett.*, 92, 134106 (2008).

- [12] S. J. Lee, N. Y. Lim, S. Kim, G. G. Park and C. S. Kim, *J. Power Sources*, 185, 867 (2008).
- [13] M. A. Hickner, N. P. Siegel, K. S. Chen, D. S. Hussey, D. L. Jacobson and M. Arif, *J. Electrochem. Soc.*, 155, B294 (2008).
- [14] M. A. Hickner, N. P. Siegel, K. S. Chen, D. S. Hussey, D. L. Jacobson and M. Arif, *J. Electrochem. Soc.*, 155, B427 (2008).
- [15] K. Yoshizawa, K. Ikezoe, Y. Tasaki, D. Kramer, E. H. Lehmann and G. G. Scherer, *J. Electrochem. Soc.*, 155, B223 (2008).
- [16] Y. Wang and K. S. Chen, *J. Electrochem. Soc.*, 157, B1878 (2010).
- [17] K. Teranishi, S. Tsushima and S. Hirai, *J. Electrochem. Soc.*, 153, A664 (2006).
- [18] S. Lister, D. Sinton and N. Djilali, *J. Power Sources*, 154, 95 (2006).
- [19] A. Bazylak, *Liquid Water Transport in Fuel Cell Gas Diffusion Layers*, Ph.D. Thesis, University of Victoria, 2008.
- [20] C. Hartnig, I. Manke, R. Kuhn, S. Kleinau, J. Goebbels and J. Banhart, *J. Power Sources*, 188, 648 (2009).
- [21] Z. Lu, S. G. Kandlikar, C. Rath, M. Grimm, W. Domigan, A. D. White, M. Hardbarger, J. P. Owejan and T. A. Trabold, *Int. J. Hydrogen Energy*, 34, 3445 (2009).
- [22] Y. H. Cai, J. Hu, H. P. Ma, B. L. Yi and H. M. Zhang, *J. Power Sources*, 161, 843 (2006).
- [23] X. Zhu, P. C. Sui and N. Djilali, *J. Power Sources*, 181, 101 (2008).
- [24] J. Y. Chio and G. H. Son, *J. Mech. Sci. Technol.*, 22, 2590 (2008).
- [25] G. F. Pinder and W. G. Gray, *Essentials of Multiphase Flow and Transport in Porous Media*, John Wiley & Sons, 2008.
- [26] T. Berning, M. Odgaard and S. K. Kær, *J. Electrochem. Soc.* 156, B1301 (2009).
- [27] S. Basu, J. Li, C. Y. Wang, *J. Power Sources*, 187, 431 (2009).
- [28] C. Z. Qin, D. Rensink, S. Fell, S. M. Hassanizadeh, *J. Power Sources*, 197, 136 (2012).
- [29] C. Z. Qin, D. Rensink, S. M. Hassanizadeh, S. Fell, *Direct simulations of liquid water dynamics in the gas channel of a polymer electrolyte fuel cell*, submitted to *J. Electrochem. Soc.*, 159, B434 (2012).
- [30] V. Joekar-Niasar, *the Immiscibles: Capillary Effect in Pours Media – Pore-network Modeling*, Ph.D. Thesis, Utrecht University, 2011.
- [31] A. Caulk, *J. Fuel Cell Sci. Technol.*, 7, 031013 (2010).
- [32] T. C. Ransohoff and C. J. Radke, *J. Colloid Interface Sci.*, 121, 392 (1988).
- [33] P. K. Sinha and C. Y. Wang, *Electrochim. Acta* 52, 7936 (2007).
- [34] Q. Ye and T. V. Nguyen, *J. Electrochem. Soc.*, 154, B1242 (2007).
- [35] D. Zhou, M. Blunt and F. M. Orr, *J. Colloid Interface Sci.*, 187, 11 (1997).
- [36] E. Kimball, T. Whitaker, Y. G. Kevrekidis, and J. B. Benziger, *AIChE J.*, 54, 1313 (2008).
- [37] H. Y. Tang, A. Santamaria, J. W. Park, C. Lee, W. Hwang, *J. Power Sources*, 196, 9373 (2011).
- [38] A. Turhan, S. Kim, M. Hatzell, M. M. Mench, *Electrochim. Acta*, 55, 2734 (2010).
- [39] I. S. Hussaini, C. Y. Wang, *J. Power Sources*, 187, 444 (2009).

## Appendix 7A

### Derivation of film flow equation

Gas drag force plays a dominant role<sup>29</sup> in the film flow along GC corners, which must be included in the derivation of momentum equation. First, the point momentum equation for the film flow is given by Stokes equation:

$$\mu \nabla^2 \bar{v} = \nabla p \quad (7A-1)$$

where  $\mu$  is the dynamic viscosity of liquid water,  $\bar{v}$  is the velocity vector at the microscopic scale, and  $p$  is the pressure. We assume that the y- and z- components of the water velocity and the second derivative of x-component along the GC are zero. The pressure variation in the GC cross-section is neglected. So, we get the film flow equation only in the channel direction:

$$\mu_f \left( \frac{\partial^2 v_x}{\partial y^2} + \frac{\partial^2 v_x}{\partial z^2} \right) = \frac{dp_f}{dx} \quad (7A-2)$$

Here,  $\mu_f$  is the dynamic viscosity of liquid water,  $v_x$  represents the film velocity along the GC (point velocity), and  $p_f$  is the film pressure. We also can write down the corresponding boundary conditions as:

At the GC sidewalls:

$$v_x = 0 \quad (7A-3)$$

At the gas-film interface:

$$\mu_f \frac{\partial v_x}{\partial \bar{n}} = \tau \quad (7A-4)$$

Eq. 7A-3 shows the no slip boundary condition at the GC sidewalls. In Eq. 7A-4,  $\tau$  denotes the gas shear stress, and  $\bar{n}$  is the unit vector normal to the gas-film interface pointing towards the gas phase. Then, we separate Eq. 7A-2 into two new partial different equations (PDEs) associated with their boundary conditions<sup>31</sup>:

$$\begin{cases} \mu_f \left( \frac{\partial^2 v_1}{\partial y^2} + \frac{\partial^2 v_1}{\partial z^2} \right) = \frac{dp_f}{dx} \\ \mu_f \left( \frac{\partial^2 v_2}{\partial y^2} + \frac{\partial^2 v_2}{\partial z^2} \right) = 0 \end{cases} \quad (7A-5)$$

At the GC sidewalls:

$$\begin{cases} v_1 = 0 \\ v_2 = 0 \end{cases} \quad (7A-6)$$

At the gas-film interface:

$$\begin{cases} \frac{\partial v_1}{\partial \bar{n}} = 0 \\ \mu_f \frac{\partial v_2}{\partial \bar{n}} = \tau \end{cases} \quad (7A-7)$$

$$v_x = v_1 + v_2 \quad (7A-8)$$

In Eq. 7A-8, Film velocity along the GC is divided into two components:  $v_1$  arising from the pressure gradient and  $v_2$  due to the gas drag force.

To make Eq. 7A-5 dimensionless, we define:

$$v_1 = -\frac{r_f^2}{\mu_f} \frac{dp_f}{dx} v_1^* \quad (7A-9)$$

$$y = r_f y^*, \quad z = r_f z^* \quad (7A-10)$$

$$v_2 = \frac{r_f \tau}{\mu_f} v_2^* \quad (7A-11)$$

So, the dimensionless equations are obtained as:

$$\begin{cases} \frac{\partial^2 v_1^*}{\partial (y^*)^2} + \frac{\partial^2 v_1^*}{\partial (z^*)^2} = -1 \\ \mu_f \left( \frac{\partial^2 v_2^*}{\partial (y^*)^2} + \frac{\partial^2 v_2^*}{\partial (z^*)^2} \right) = 0 \end{cases} \quad (7A-12)$$

At the GC sidewalls:

$$\begin{cases} v_1^* = 0 \\ v_2^* = 0 \end{cases} \quad (7A-13)$$

At the gas-film interface:

$$\begin{cases} \frac{\partial v_1^*}{\partial \bar{n}} = 0 \\ \frac{\partial v_2^*}{\partial \bar{n}} = 1 \end{cases} \quad (7A-14)$$

Based on the above derivations of the film flow at the microscopic scale, we integrate the point velocity  $v_x$  over the film flow area at the GC cross section, and get:

$$A_f v_f = \int_{A_f} (v_1 + v_2) ds = \int_{A_f} \left( -\frac{r_f^2}{\mu_f} \frac{dp_f}{dx} v_1^* + \frac{r_f \tau}{\mu_f} v_2^* \right) ds = -\frac{r_f^2}{\mu_f} \frac{dp_f}{dx} \int_{A_f} v_1^* ds + \frac{r_f \tau}{\mu_f} \int_{A_f} v_2^* ds \quad (7A-15)$$

where  $v_f$  is the average film flow velocity along the GC, and  $A_f$  is the film flow area in the GC cross section. Next, we introduce two dimensionless parameters with the following definitions:

$$\frac{1}{\beta} = \frac{1}{A_f} \int_{A_f} v_1^* ds, \quad F_{drag} = \frac{1}{A_f} \int_{A_f} v_2^* ds \quad (7A-16)$$

in which,  $\beta$  is called dimensionless viscous resistance, and  $F_{drag}$  can be called dimensionless gas drag coefficient. Obviously, both dimensionless coefficients are related to the GC half corner angle and the contact angle of sidewalls. Finally we obtain the following film flow equation:

$$v_f = -\frac{r_f^2}{\mu_f \beta} \frac{dp_f}{dx} + F_{drag} \frac{r_f \tau}{\mu_f} \quad (7A-17)$$

## List of Symbols

$a$	net water transfer coefficient
$A$	area, m <sup>2</sup>
$b$	side edge length of GC cross section, m
$C$	mass fraction
$D$	molecular diffusivity, m <sup>2</sup> s <sup>-1</sup>
$D_H$	hydraulic diameter for gas flow, m
$f_t$	effect of gas flow configuration on shear stress distribution
$F$	Faraday's constant, C mol <sup>-1</sup>
$F_{drag}$	dimensionless gas drag coefficient
$I$	current density, A m <sup>-2</sup>
$L$	interface length, m
$M$	molecular weight, kg mol <sup>-1</sup>
$P$	pressure, Pa
$P_0$	cell operating pressure (i.e. gas inlet pressure), Pa
$P_{sat}$	saturated water vapor pressure, Pa
$r_f$	radius of curvature of gas-film interface, m
$R$	universal gas constant, 8.314 J mol <sup>-1</sup> K <sup>-1</sup>
$RH$	relative humidity
$S$	mass source term, kg m <sup>-1</sup> s <sup>-1</sup>
$\hat{S}$	molar source term, mol m <sup>-1</sup> s <sup>-1</sup>
$t$	ratio of GC down wall to reactive area
$T$	temperature, K
$v$	velocity, m s <sup>-1</sup>

$w$	down edge length of GC cross section, m
$x$	flow direction, m

## Greek letters

$\rho$	mass density, kg m <sup>-3</sup>
$\bar{\rho}$	molar density, mol m <sup>-3</sup>
$\mu$	dynamic viscosity, Pa s
$\beta$	dimensionless viscous resistance
$\tau$	shear stress, Pa
$\sigma$	gas-liquid surface tension, N m <sup>-1</sup>
$\alpha$	upper half corner angle of GC, radian
$\theta$	contact angle of GC sidewalls, radian
$\theta_d$	contact angle of GDL surface, radian
$r_d$	droplet radius, radian
$\xi_c$	cathodic stoichiometry

## Superscripts and Subscripts

$g$	gas phase
$f$	film phase
$d$	droplet
$gc$	gas channel
$O_2$	oxygen
$H_2O$	water vapor
$gw$	gas-wall
$gf$	gas-film
$gd$	gas-droplet
$no - slip$	wetted perimeter of gas flow area
$m$	membrane

Table 7-1: Geometrical, physical and operating parameters for base case.

Parameter	Value
GC width/height/length	1.0/0.5/200 mm
Droplet radius at the GC cross section, $r_d$	None
Contact angle of the bottom wall of the GC, $\theta_d$	$7\pi/9$ radian
Contact angle of the GC sidewalls, $\theta$	0 radian
Half angle of the GC corner, $\alpha$	$\pi/4$ radian
Averaged current density, $I_a$	6000 A m <sup>-2</sup>
Dimensionless viscous resistance, $\beta$	113.38
Dimensionless gas drag coefficient, $F_{drag}$	0.065
Cell temperature, $T$	353.15 K
Inlet gas mixture pressure (or cell operating pressure), $p_0$	1.5 bar
Liquid water density, $\rho_l$	972 kg m <sup>-3</sup>
Dynamic viscosity of liquid water/gas mixture, $\mu$	$3.5 \times 10^{-4} / 2.03 \times 10^{-5}$ Pa s
Surface tension, liquid water-air, $\sigma$	0.0625 N m <sup>-1</sup>
Ratio of GC to reactive areas, $t$	0.5
Net water transfer coefficient, $a$	0.2
Stoichiometric ratio, $\xi_c$	2.0

Table 7-2: Dimensionless gas drag coefficients for different GC upper half corner angles (adapted from the reference<sup>31</sup>).

Half corner angle, $\alpha$ (radian)	Dimensionless gas drag coefficient, $F_{drag}$
$\pi/6$	0.086
$7\pi/36$	0.08
$2\pi/9$	0.073
$\pi/4$	0.065
$5\pi/18$	0.055
$11\pi/36$	0.045
$\pi/3$	0.035

# Chapter 8 - Numerical study on liquid water flooding in gas channels used in polymer electrolyte fuel cells

---

## Abstract

*Water management plays an important role in the development of low-temperature polymer electrolyte fuel cells (PEFCs). The lack of a macroscopic gas channel (GC) flooding model constrains the current prediction of PEFC modeling under severe flooding situations. In this chapter, we have extended our previously developed channel flooding model for including phase change and water flooding on the anode side. Several case studies are conducted to explore the effects of inlet relative humidity, net water transfer coefficient and GC shape on water film flooding in the GCs on both sides with the assumption that, both GCs are free from water droplets for simplicity. We demonstrate that the present model is capable of capturing key phenomenon of liquid water flooding in GCs. Our primary results show that gas drag force prevents liquid water accumulation in GCs, which dominates the liquid water removal. Both inlet relative humidity and stoichiometry can influence the liquid water flooding in GCs dramatically. At last, it is shown that increasing the upper half corner angle of the GC can mitigate the film water flooding in GCs.*

## 8.1 Introduction

Polymer electrolyte fuel cells (PEFCs), converting chemical energy directly into electricity via electrochemical reactions, are widely recognized as the most promising alternative power sources in the 21<sup>st</sup> century for automobiles<sup>1,2</sup>. Water management plays an important role in the development of PEFCs, which is closely coupled with heat management in terms of phase change between water vapor and liquid water. Under severe flooding situations, liquid water transfer can be involved in both diffusion layers and micro gas channels (GCs) simultaneously<sup>3-5</sup>. To avoid membrane dehydration and mass transport limitations, we need to deeply understand the liquid water evolution inside a whole PEFC.

Over the past decade, tremendous efforts have been paid to the numerical modeling of liquid water flooding in the diffusion layers of a PEFC<sup>6-10</sup>, especially on the cathode side. At the representative elementary volume (REV) scale, liquid water transport in the diffusion layers is described by the so-called two-phase Darcy's law<sup>11</sup>. However, some researchers argue that

extremely thin gas diffusion layer (GDL), about five times pore-size in the through-plan direction, violates the REV concept embedded in the formulation of two-phase Darcy's law<sup>12, 13</sup>. On the other hand, pore-scale models<sup>14-17</sup> such as pore-network (PN), Lattice Boltzmann (LB) have been extensively employed to illustrate the exact liquid water transport mechanisms through fibrous GDL. Sinha and Wang<sup>14</sup> developed a dynamic pore-network model to study the liquid water movement and flooding in a GDL. They represented the GDL by a three-dimensional random tetragonal pore-network structure with cubic pores and throats of square cross-section. Most recently, Luo et al.<sup>15</sup> developed a steady-state topologically equivalent pore network model. The salient feature was that they extracted pore networks directly from GDL microstructures. They found that GDL morphology affected water transport characteristics strongly.

Besides flooding in diffusion layers, liquid water also accumulates in GCs. It prevents reactants from transporting into reactive sites, increases the flooding levels in diffusion layers and pressure losses along GCs, and also provides facilitated transport of ionic impurities<sup>18</sup>. Several explicit interface tracking models<sup>19, 20</sup> have been used to study water dynamics in GCs. Zhu et al.<sup>19</sup> utilized volume of fluid (VOF) method to investigate water droplet dynamics in GCs, with an emphasis on channel geometry effect. Qin et al.<sup>20</sup> conducted a series of direct simulations of liquid water dynamics (i.e. water droplet and film dynamics) in GCs based on a proposed novel geometrical setup. They simplified the GDL by means of three connected water conducting pathways, which was supported by experimental observations. They also studied the competing mechanism of liquid water flow from conducting pathways in the GDL to the GC. However, these interface-tracking simulations all suffer from extremely heavy computational efforts. Therefore, it is prohibitive to apply them into the full scale of GCs.

With the purpose of computational effectiveness, a channel flooding model should be formulated at a macro scale, which is comparable to the REV scale used by the two-phase Darcy's law in diffusion layers. If so, the interface treatment between GC and GDL would be simple and straightforward. A few researchers assumed GCs to be structured porous media with assigned nominal permeability<sup>10, 21, 22</sup>. The two-phase Darcy's law then can be applied into GCs directly associated with assumed constitutive correlations (e.g. capillary pressure vs. saturation). Basu et al. used this type of channel flooding model to simulate liquid saturation distribution in parallel channels as well as predict two-phase pressure drop. However, it is worth noting that complicated water dynamics in GCs ranging from mist flow to droplet and film flows cannot really be simulated by the Darcy's law properly. The validation of this methodology is still pending. Most recently, Qin et al.<sup>23</sup> derived a phenomenological model for liquid water flooding in cathode GC, based on several reasonable assumptions. The droplet sitting above the hydrophobic GDL surface and film flow along GC corners were both taken into account. They conducted several cases to study the effects of various engineering and operating parameters on the liquid water flooding in GCs.

In this chapter, we introduce a non-equilibrium phase change model into our previously developed one-dimensional channel flooding model<sup>23</sup>, which enables the consideration of partially humidified inlet gas. In addition, we extend this model into the anode side, and connect the channel flooding on both sides by the so-called net water transfer coefficient. This parameter determines the water exchange between cathode and anode sides, which plays an important role in the water management of PEFCs. In what follows, we first give the developed mathematical

channel flooding model; then, several case studies are conducted to investigate the effects of inlet relative humidity, net water transfer coefficient, and GC shape on the liquid water flooding in the GCs on both sides.

## 8.2 Mathematical model

In this section, we briefly present the applied mathematical channel flooding model. For greater detail, one can refer to chapter 7. Fig. 8-1 shows the two-dimensional schematic of liquid water flooding in the cathode GC. It is assumed that we have idealized water film flow along the hydrophilic GC corners, as well as droplets sitting on the hydrophobic GDL surface. Fig. 8-2 shows the two-dimensional schematic of a PEFC; and the computational domains in this work are enclosed by dashed red lines, including the cathode and anode GCs.

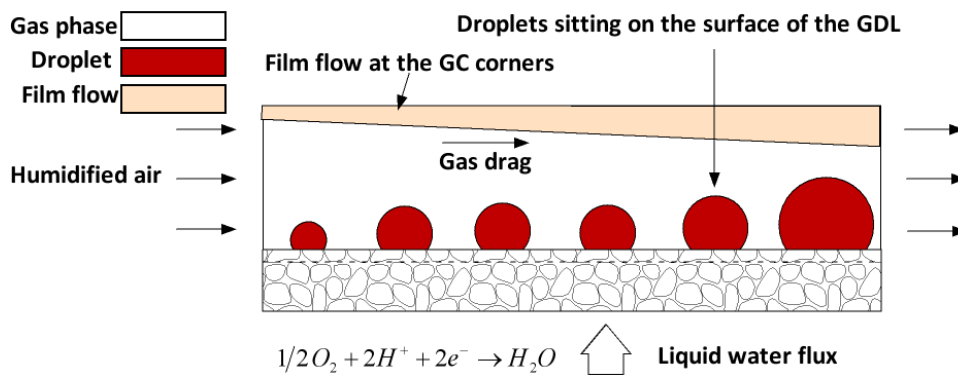


Figure 8-1: Two-dimensional schematic of liquid water flooding in the cathode GC (it includes the film flow along the hydrophilic GC corners, as well as droplets on the hydrophobic GDL surface).

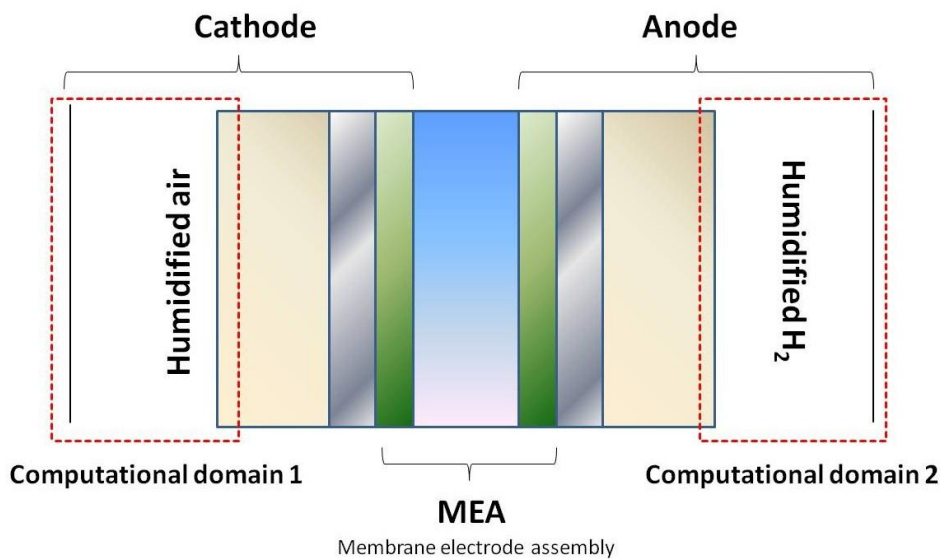


Figure 8-2: Two-dimensional schematic of a PEFC (the computational domains in this work are enclosed by dashed red lines).

## 8.2.1 Governing equations

We integrate the microscopic continuity equation for the gas phase over the GC cross-section as shown in Fig. 8-3, and get:

$$\frac{d(A_g \widehat{\rho}_g v_g)}{dx} = \widehat{S}_g \quad (8-1)$$

where  $A_g$  is the flow area of the gas phase in the GC cross-section,  $\widehat{\rho}_g$  is the molar density of the gas phase,  $v_g$  denotes the area-averaged gas velocity, and  $\widehat{S}_g$  represents the molar source term of the gas phase due to chemical reactions and phase change. Note that the transverse velocities are assumed to be zero, and the gas flow is in the x direction.

In automotive applications, partially humidified air is delivered into flow fields on the cathode side, while partially humidified hydrogen is delivered on the anode side. Under normal operating conditions, the Péclet number is much bigger than unity for species transport in the GCs. Therefore, we can neglect the species diffusion safely and simplify the transport equation as follows:

$$\frac{d(A_g \widehat{\rho}_i v_g)}{dx} = \widehat{S}_i \quad (i = O_2, H_2, H_2O) \quad (8-2)$$

where  $\widehat{\rho}_i$  denotes the species molar density, and  $\widehat{S}_i$  is the species molar source term (mol/m/s).

The Hagen-Poiseuille equation is used to relate the gas velocity and gas pressure gradient along the GC, which is given as:

$$v_g = \frac{-1}{32\mu_g} \left( \frac{4A_g}{L_{gw} + L_{gf} + L_{gd}} \right) \frac{dp_g}{dx} \quad (8-3)$$

Here,  $\mu_g$  is the dynamic viscosity of the gas phase,  $p_g$  is the gas phase pressure, and  $L_{gw}$ ,  $L_{gf}$ , and  $L_{gd}$  denote the lengths of gas-wall interface, gas-film interface, as well as gas-droplet interface, respectively (see Fig. 8-3).

Similar to the gas phase, the averaged mass equation for the water film is given as:

$$\frac{d(A_f \rho_f v_f)}{dx} = S_f \quad (8-4)$$

where  $A_f$  denotes the film flow area,  $\rho_f$  is the mass density of liquid water,  $v_f$  is the averaged film velocity, and  $S_f$  represents the mass source/sink term of the film phase (kg/m/s). Taking into account the gas drag force, the film flow equation is formulated as:

$$v_f = -\frac{r_f^2}{\mu_f \beta} \frac{dp_f}{dx} + F_{drag} \frac{r_f \tau}{\mu_f} \quad (8-5)$$

where  $\mu_f$  is the dynamic viscosity of liquid water,  $r_f$  is the radius of the curvature of gas-film interface,  $\tau$  denotes the gas shear stress at the interface between gas and film,  $\beta$  denotes the dimensionless viscous resistance, and  $F_{drag}$  can be called dimensionless gas drag coefficient.

Finally, the gas and film pressures are coupled by the capillary pressure, defined as:

$$p_c = p_g - p_f = \frac{\sigma}{r_f} \quad (8-6)$$

Here, we assume that the radius of the curvature of gas-film interface along the GC is infinite, and  $\sigma$  denotes the surface tension between gas and liquid water.

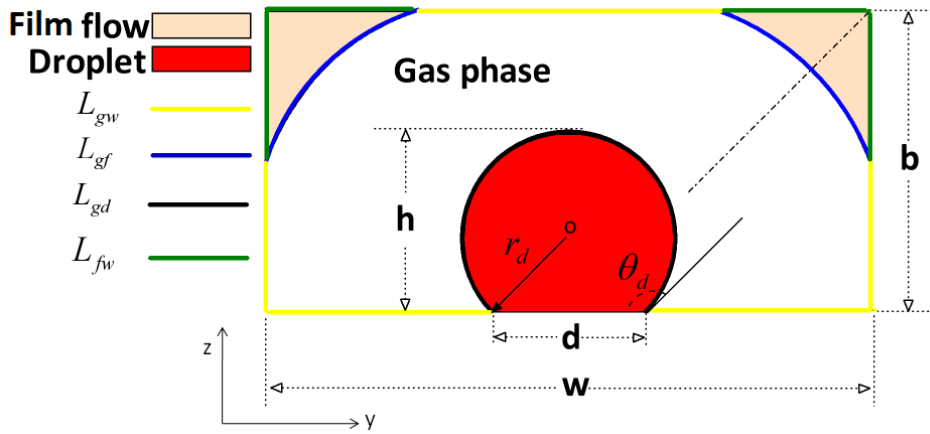


Figure 8-3: Assumed liquid water distribution in the GC, including the film flow at the corners, and the water droplet sitting at the center.

## 8.2.2 Source terms and geometrical information

The source terms are summarized in Table 8-1, wherein,  $I(x)$  represents the current density distribution along the GC;  $F$  is the Faraday's constant (96487 C/mol),  $w$  is the down edge length of the GC cross-section, and  $t$  denotes the ratio of the area of the GC down wall to the reactive area in the membrane;  $a$  is the net water transfer coefficient, which determines the water exchange between cathode and anode sides;  $\widehat{S}_{phase}$  denotes the molar source term due to the phase change between water vapor and liquid water, which is given by the following non-equilibrium phase change model:

$$\widehat{S}_{phase} = \begin{cases} k_{evap} \frac{\Delta p A_f \rho_f}{M_{H_2O}} & \text{if } \Delta p = (p_g X_{H_2O} - p_{sat}) < 0 \\ k_{cond} \frac{\Delta p A_g X_{H_2O}}{RT} & \text{if } \Delta p = (p_g X_{H_2O} - p_{sat}) \geq 0 \end{cases} \quad (8-7)$$

where  $k_{evap}$  and  $k_{cond}$  denote the water evaporation and condensation rates, respectively,  $X_{H_2O}$  represents the mole fraction of water vapor,  $M_{H_2O}$  is the molecular weight of water vapor,  $R$  is the universal gas constant,  $T$  is the cell operating temperature, and  $p_{sat}$  represents the saturated water vapor pressure, given by the following empirical expression:

$$\log_{10}^{p_{sat}/101325} = -2.1794 + 0.02953(T - 27315) - 9.1837 \times 10^{-5}(T - 27315)^2 + 1.4454 \times 10^{-7}(T - 27315)^3 \quad (8-8)$$

Since we assume an idealized liquid water distribution in the GC cross-section, some additional equations can be obtained based on the geometrical information shown in Fig. 8-3. The film area in the GC cross-section is a function of the radius of the curvature of gas-film interface, which is given as:

$$A_f = r_f^2 \left[ \sin(2\gamma) + \frac{2 \sin^2 \gamma}{\tan \alpha} - 2\gamma \right] \quad (8-9)$$

$$\gamma = \frac{\pi}{2} - \alpha - \theta \quad (8-10)$$

Here,  $\alpha$  is the upper half corner angle of the GC, and  $\theta$  denotes the static contact angle of the GC sidewalls.

The areas of both droplet and GC cross-section can be expressed as:

$$A_{gc} = b \sin(\pi - 2\alpha) [w - b \cos(\pi - 2\alpha)] \quad (8-11)$$

$$A_d = r_d^2 \left[ \theta_d - \frac{\sin(2\theta_d)}{2} \right] \quad (8-12)$$

Here,  $b$  is the side edge length of the GC cross-section,  $w$  is the down edge length of the GC cross-section,  $r_d$  is the droplet radius, and  $\theta_d$  denotes the static contact angle of the GDL surface.

The lengths of the gas-film interface, gas-wall interface, gas-droplet interface, as well as film-wall interface are given as:

$$L_{gf} = 4r_f \gamma \quad (8-13)$$

$$L_{gd} = 2r_d \theta_d \quad (8-14)$$

$$L_{gw} = 2w + 2b[1 - \cos(\pi - 2\alpha)] - 2r_d \sin(\pi - \theta_d) - \frac{4r_f \sin \gamma}{\sin \alpha} \quad (8-15)$$

### 8.2.3 Closure equations

To close the governing equations, several constitutive correlations are needed as follows:

$$A_g + A_f + A_d = A_{gc} \quad (8-16)$$

$$\widehat{\rho}_g = \begin{cases} \widehat{\rho}_{O_2} + \widehat{\rho}_{H_2O} + \widehat{\rho}_{N_2} & \text{cathode GC} \\ \widehat{\rho}_{H_2} + \widehat{\rho}_{H_2O} & \text{anode GC} \end{cases} \quad (8-17)$$

Eq. 8-16 indicates that the summation of the gas phase, film, and droplet areas is equal to unity, Eq. 8-17 means that the summation of species molar densities on each side equals to the molar density of gas mixture.

The dynamic viscosities of gas mixture and liquid water are both assumed to be constants, and the liquid water density is also presumed to be constant. For the gas mixture, we assume the constant molar density owing to the small gas pressure drop along the GC, which is given as:

$$\widehat{\rho}_g = \frac{p_0}{RT} \quad (8-18)$$

where  $p_0$  denotes the inlet pressure of gas mixture.

The gas shear stress at the gas-film interface can be approximated as:

$$\tau = -f_\tau \frac{A_g}{L_{gw} + L_{gf} + L_{gd}} \frac{dp_g}{dx} \quad (8-19)$$

In Eq. 8-19, factor  $f_\tau$  is used to correct the shear stress at the gas-film interface. It can be fitted based on numerical experiments<sup>23, 24</sup>:

$$f_\tau = 1 - \exp\left[\frac{-13r_f}{D_H} \left(\cos \gamma + \frac{\sin \gamma}{\tan \alpha}\right) - 1\right] \quad (8-20)$$

$$D_H = \frac{4A_g}{L_{gw} + L_{gf} + L_{gd}} \quad (8-21)$$

where  $D_H$  denotes the hydraulic diameter for the gas flow.

The expressions of dimensionless coefficients  $\beta$  and  $F_{drag}$  in Eq. 8-5 are presented in the reference<sup>23</sup>.

### 8.3 Boundary conditions

In what follows, we describe the applied boundary conditions for both cathode and anode GCs. The inlet gas mixture velocity is determined by average current density, stoichiometry, reactive area, as well as gas flow area. Therefore, both inlet gas velocities can be expressed as:

$$v_g^{cathode} \Big|_{x=0} = \frac{\xi_c A_m}{4LFA_g(\rho_{O_2}|_{x=0})} \int_0^L I(x) dx \quad (8-22)$$

$$v_g^{anode} \Big|_{x=0} = \frac{\xi_a A_m}{2LFA_g(\rho_{H_2}|_{x=0})} \int_0^L I(x) dx \quad (8-23)$$

Here,  $\xi_c$  and  $\xi_a$  denote the cathode and anode stoichiometric ratios, respectively,  $L$  denotes the GC length, and  $A_m$  is the reactive area.

A constant gas inlet pressure on each side is specified as:

$$p_g \Big|_{x=0} = p_0 \quad (8-24)$$

The inlet oxygen, hydrogen and water vapor molar densities are given as:

$$\widehat{\rho}_{O_2} \Big|_{x=0} = \frac{0.21p_0}{RT} \left( 1 - \frac{p_{sat}}{p_0} RH_c \right) \quad (8-25)$$

$$\widehat{\rho}_{H_2} \Big|_{x=0} = \frac{p_0}{RT} \left( 1 - \frac{p_{sat}}{p_0} RH_a \right) \quad (8-26)$$

$$\widehat{\rho}_{H_2O} = \frac{p_{sat}}{p_0} RH_{c/a} \quad (8-27)$$

where  $RH$  represents the relative humidity of the inlet gas.

On each side, the film velocity at the GC inlet is set to zero, as:

$$v_f \Big|_{x=0} = 0 \quad (8-28)$$

For the radius of the curvature of gas-film interface, we assume a fully developed boundary condition at the GC out, expressed as:

$$\frac{dr_f}{dx} \Big|_{x=L} = 0 \quad (8-29)$$

## 8.4 Results and discussion

### 8.4.1 Base case

Table 8-2 lists the main geometrical, physical and operating parameters for the base case. The cell current density is set to  $6000 \text{ A/m}^2$ ; the operating pressure is at 1.5 bars on each side; and fully humidified air and hydrogen are delivered on the cathode and anode sides, respectively. We note that for coupling three phases (gas, film, droplet) an empirical droplet model in GCs is needed. However, due to the absence of experimental data, we assume that both GCs are free from water droplets in this work, and concentrate on the film flow along GC corners.

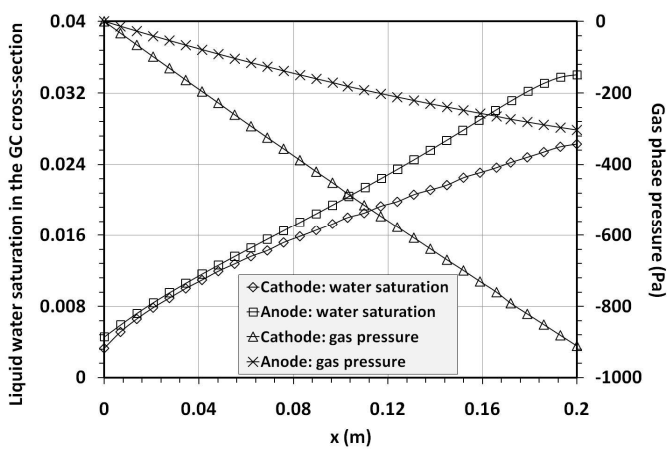


Figure 8-4: Water saturation distribution and gas pressure drop along the GC for the base case.

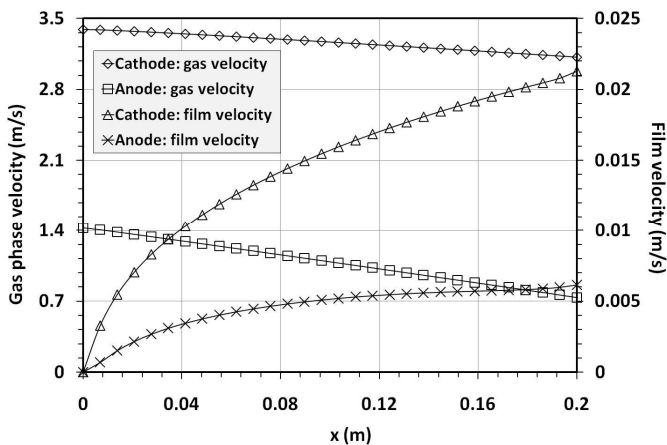


Figure 8-5: Distributions of gas and film velocities along the GCs for the base case.

Fig. 8-4 shows the water saturation distributions and gas pressure drops along the GCs (both sides) for the base case. Since the net water transfer coefficient is supposed to be zero, the liquid water on the anode side is purely generated from the water vapor condensation owing to the hydrogen consumption. In the cathode GC, we not only have the condensed liquid water, but also the water filling from the diffusion layers owing to the oxygen reduction reaction (ORR). Although the water generation rate on the cathode side is higher than that on the anode side, severer

water flooding in the anode GC is found (Fig. 8-4, Left). This can be explained by the gas pressure drops along the GCs (Fig. 8-4, Right). On the cathode side, fully humidified air is delivered into the GC instead of pure oxygen. Therefore, in order to satisfy the specified stoichiometric ratio (Table 8-2), much higher gas flow rate is required compared to that on the anode side. Higher gas flow rate corresponds to larger gas pressure drop; as a result, more liquid water can be swept out of the channel on the cathode side. This indicates that gas drag force prevents liquid water accumulation in GCs, which plays an important role in liquid water removal.

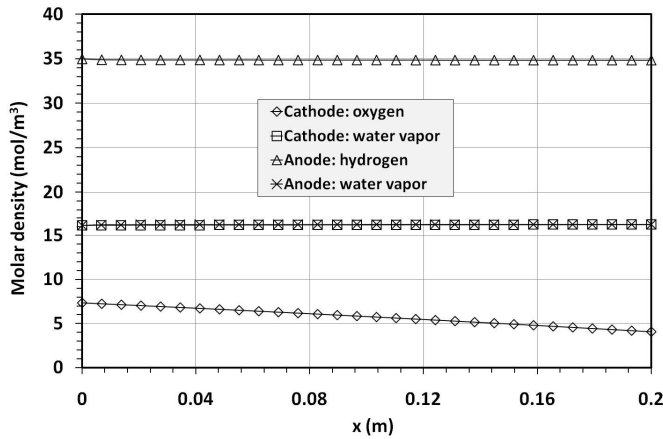


Figure 8-6: Distributions of molar densities of oxygen and hydrogen along the GCs for the base case.

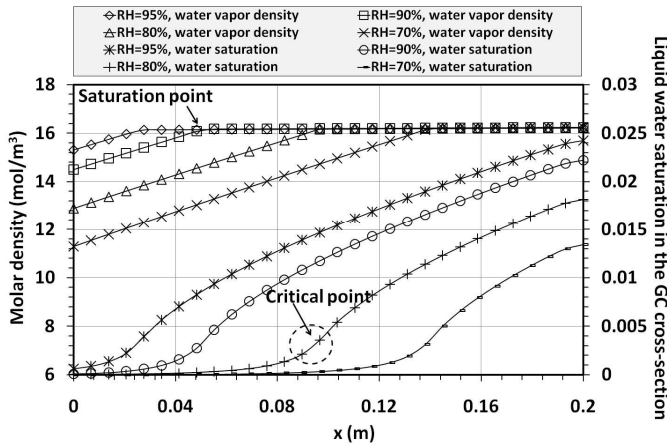


Figure 8-7: Molar density distributions of water vapor for different inlet relative humidity (Left); inlet relative humidity effect on the water flooding in the cathode GC (Right).

Fig. 8-5 shows the distributions of gas and film velocities along the GCs for the base case. On each side, the gas velocity decreases along the GC due to the mass loss and almost unchanged gas flow area. The cathode gas velocity is much higher than that on the anode side, corresponding to the larger pressure drop as shown in Fig. 8-4. As stated above, more liquid water is introduced into the cathode GC; consequently, the film flow at the cathode GC corners has much higher velocity up to about 0.021 m/s.

Fig. 8-6 shows the distributions of molar densities of oxygen and hydrogen along the GCs for the base case. On the anode side, hydrogen keeps saturated along the GC with the water vapor molar density of about  $15.4 \text{ mol/m}^3$ . The hydrogen molar density has almost horizontal

distribution along the GC. This is because the anode gas velocity reduces to the half inlet one approximately, and also the anode stoichiometric ratio of 2.0 is specified for the base case. On the cathode side, air also keeps saturated as in the anode GC, the oxygen molar density reduces from  $7.3 \text{ mol/m}^3$  at the GC inlet to  $4.1 \text{ mol/m}^3$  at the outlet.

### 8.4.2 Effect of relative humidity

Fig. 8-7 and Fig. 8-8 demonstrate the inlet relative humidity effect on the water flooding in the cathode and anode GCs, respectively. Four values of relative humidity are used, namely, 95%, 90%, 80%, and 70%. On the cathode side, the partially humidified air gains water from the film at the inlet region by means of phase change. It reaches the full humidity at about  $x=0.027 \text{ m}$  as the inlet relative humidity equals to 95% (Fig. 8-7, Left). With the decrease of the inlet relative humidity, the “saturation point” shifts to the GC outlet more and more. The liquid water flooding in the cathode GC deteriorates as increasing the inlet relative humidity as shown in Fig. 8-7 (Right), since more water vapor condenses into the liquid water. We also observe that the slope of the water saturation distribution along the GC has a “critical point” for each inlet relative humidity, at which it starts to descend. In addition, this critical point coincides with the saturation point of water vapor. It is worth noting that zero water saturation at the GC inlet cannot be obtained in this work for two reasons: one is due to the applied non-equilibrium phase change model (Eq. 8-7); the other is caused by the capillary action on the film flow along the GC corners (Eq. 8-6). On the anode side, we have the similar tendency of the distributions of water vapor molar density as well as water saturation, except that the water flooding in the anode GC is severer because of the small gas drag force.

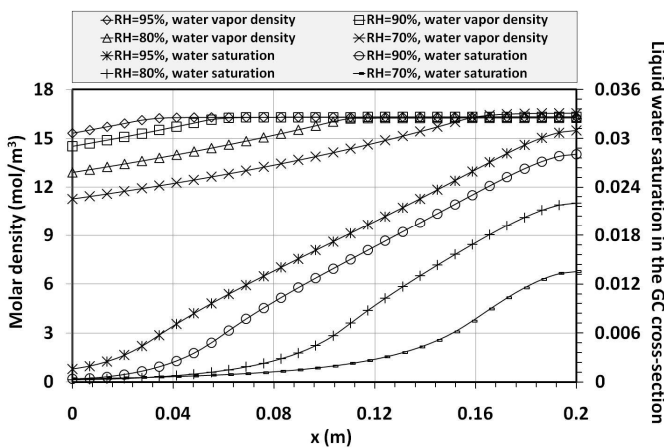


Figure 8-8: Molar density distributions of water vapor for different inlet relative humidity (Left); inlet relative humidity effect on the water flooding in the anode GC (Right).

### 8.4.3 Effect of net water transfer coefficient

In the water management, we divide a PEFC unit into the cathode and anode sides, which are connected by the membrane (Fig. 8-2); thus, the water exchange between two sides can be quantified by the net water transfer coefficient. In this subsection, we explore the effect of net water transfer coefficient on the water flooding in the GCs. Fig. 8-9 shows the effect of net water transfer coefficient on the water flooding in the cathode GC (Left), as well as the corresponding

gas pressure drops along the GC (Right). With the increase of this parameter, more and more water is transported from the anode to cathode via the membrane; as a result, we have the severest water flooding in the GC as the net water transfer coefficient equals to 0.5 (Fig. 8-9, Left). Note that no discernible difference can be found in the gas pressure drops, since the liquid water saturation in the GC is quite low with limited influence on the gas flow. Fig. 8-10 illustrates the effect of net water transfer coefficient on the water flooding in the anode GC. On the anode side, liquid water condenses from the water vapor; meanwhile, some water is transported into the cathode side represented by the net water transfer coefficient. Therefore, it is evident that less and less liquid water accumulates at the GC corners with the increase of net water transfer coefficient, as shown in Fig. 8-10.

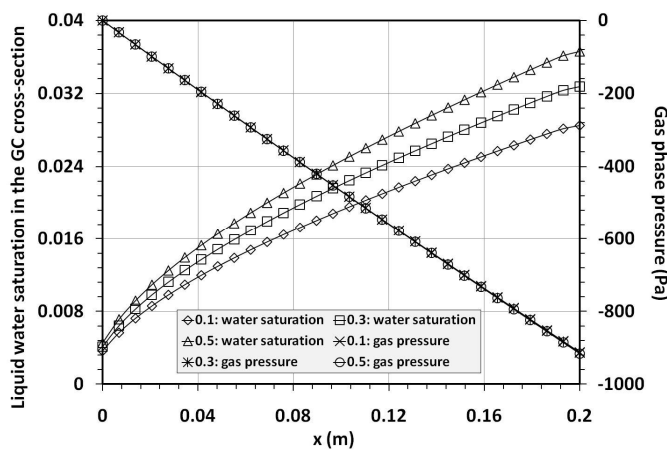


Figure 8-9: Effect of net water transfer coefficient on the water flooding in the cathode GC (Left); corresponding gas pressure drops along the GC (Right).

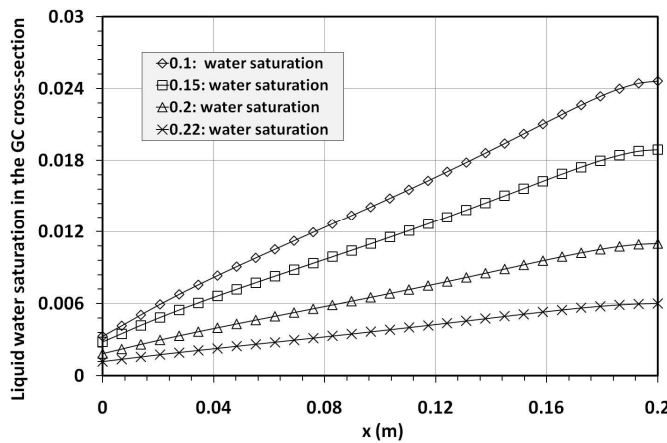


Figure 8-10: Effect of net water transfer coefficient on the water flooding in the anode GC.

Due to the high inlet concentration of hydrogen on the anode side, in practice, a low stoichiometric ratio of 1.2 is normally applied. In Fig. 8-11, we illustrate the combined effect of net water transfer coefficient and stoichiometric ratio on the water flooding in the anode GC. While the stoichiometric ratio is set to 1.2 with the net water transfer coefficient of 0.1, the water saturation at the GC outlet reaches its maximum value of about 0.06. After increasing the stoichiometric ratio to be 2.0, the water saturation decreases dramatically with the maximum value of about 0.025 at the GC outlet. We also can see that the gas pressure drop along the GC increases considerably with the decrease of the stoichiometric ratio, which can be explained by

the fact that the gas flow rate is directly proportional to the applied stoichiometric ratio as indicated in Eq. 8-24. While the stoichiometric ratio is set to be 1.2 with the net water transfer coefficient of 0.2, only maximum water saturation of 0.027 is found at the GC outlet. This is because most of water is transported into the cathode side.

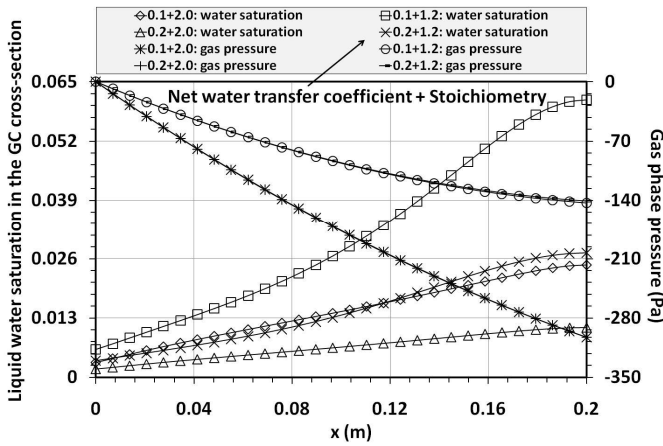


Figure 8-11: Effects of net water transfer coefficient and stoichiometric ratio on the water flooding in the anode GC (Left); corresponding gas pressure drops along the GC (Right).

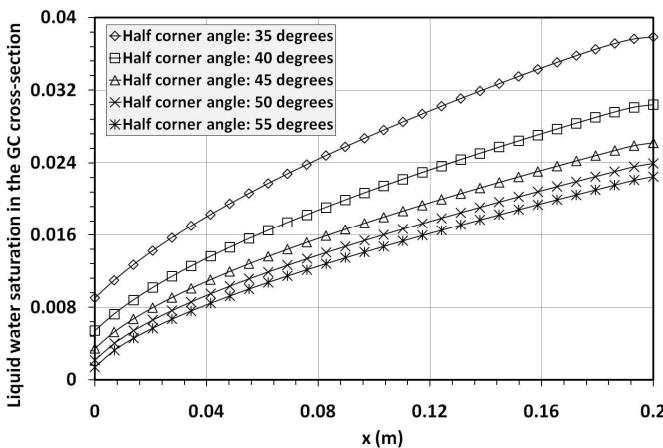


Figure 8-12: Influence of half corner angle on the water flooding in the cathode GC.

#### 8.4.4 Effect of half corner angle

The upper half corner angle determines the shape of the GC cross-section. We fix the area of the GC cross-section to be the same as the base case ( $5 \times 10^{-7} \text{ m}^2$ ), and vary the value of half corner angle to investigate its effect on the water flooding in the cathode GC. Fig. 8-12 shows the liquid water saturation distributions along the GC for different half corner angles. It is seen that increasing the upper half corner angle can mitigate the water flooding in the cathode GC; however, this influence becomes weaker and weaker. The gas pressure drops for five half corner angles are plotted in Fig. 8-13 (Right). It is found that the gas pressure drop increases slightly with the decrease of the half corner angle. Since the effect of a little film at the GC corners on the gas pressure drop is limited, the main cause should come from the change of the GC cross-section. In turn, the hydraulic diameter for the gas flow is altered as indicated in Eq. 8-21. The film velocity for each half corner angle is shown in Fig. 8-13 (Left). Since the same amount of water is added

into the GC for each case, the film velocity is only inversely proportional to the water saturation along the GC according to the mass conservation. Therefore, we obtain the highest film velocity up to 0.025 m/s at the half corner angle of 55 degrees. Now, we go back to explain why increasing half corner angle can mitigate the water flooding. In general, we have two ways to enhance the film removal along the GC corners: one way is to increase the gas pressure gradient (i.e. pressure drop); the other way is to increase the interface area between the gas and film (i.e. increasing the gas drag force). While increasing the half corner angle, the gas pressure drops decreases slightly as shown in Fig. 8-13 (Right). However, it is evident that increasing the half corner angle can enlarge the interface area between the gas and film noticeably; as a result, more liquid water is removed out of the GC. Therefore, we conclude that the mitigation of the water flooding dominantly arises from increased gas drag force exerted on the film flow.

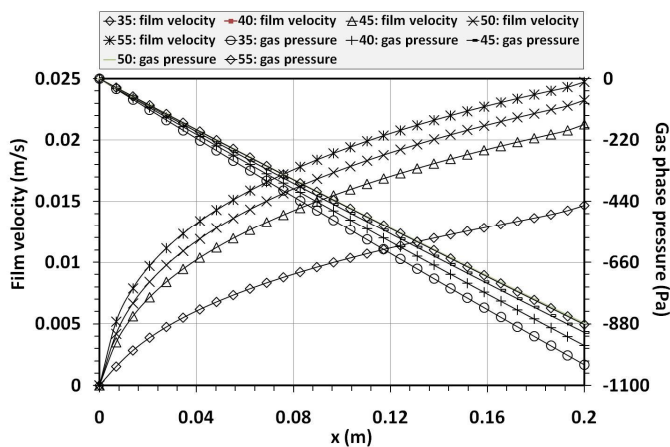


Figure 8-13: *Film velocity distributions for different half corner angles of the GC (Left); corresponding gas pressure drops along the GC (Right).*

## 8.5 Conclusions

In this work, we extend our previously developed channel flooding model to include the phase change and liquid water flooding in the anode GC. Consequently, we can consider the partially humidified gas inlet, and also connect the water flooding in the GCs on both sides by means of net water transfer coefficient. In addition, it needs to point out that the channel flooding model presented in this work possesses the capability of considering the water droplets influence on the channel flooding. However, droplet population should be described in advance, which should be a function of gas flow rate, operating current density, GDL pore morphology, and GDL contact angle, etc. Maybe an empirical expression for droplet population can be fitted based on direct optical observations experimentally. On the other hand, we also can attempt to track droplet dynamics explicitly, which requires lots of efforts to come true. Finally, we draw the main conclusions in this study:

1. In the base case study, severer water flooding in the anode GC is found, even though the water generation rate on the cathode side is higher than that on the anode side. This is because the gas flow rate is much higher on the cathode side; as a result, more liquid water can be removed out of the channel. This indicates that gas drag force prevents liquid water accumulation in GCs, which plays an important role in the liquid water removal.

2. The slope of the water saturation distribution along the GC has a “critical point” for each inlet relative humidity, at which it starts to descend. In addition, this critical point coincides with the saturation point of water vapor.
3. Net water transfer coefficient plays an important role in the water flooding in both GCs. In practice, we can influence the water flooding on both sides by adjusting this parameter.
4. Increasing the upper half corner angle of the GC can enlarge the interface area between the gas and film noticeably; as a result, more liquid water is removed out of the GC.

## List of Symbols

$A$	area, m <sup>2</sup>
$a$	net water transfer coefficient
$b$	side edge length of GC cross-section, m
$D_H$	hydraulic diameter for gas flow, m
$F$	Faraday’s constant, C mol <sup>-1</sup>
$F_{drag}$	dimensionless gas drag coefficient
$I$	current density, A m <sup>-2</sup>
$L$	interface length; GC length, m
$M$	molecular weight, kg mol <sup>-1</sup>
$p$	pressure, Pa
$p_0$	cell operating pressure (i.e. gas inlet pressure), Pa
$R$	universal gas constant, 8.314 J mol <sup>-1</sup> K <sup>-1</sup>
$RH$	relative humidity
$r_f$	radius of curvature of gas-film interface, m
$r_d$	droplet radius
$S$	mass source term, kg m <sup>-1</sup> s <sup>-1</sup>
$\hat{S}$	molar source term, mol m <sup>-1</sup> s <sup>-1</sup>
$T$	temperature, K
$t$	ratio of GC down wall to reactive area
$v$	velocity along flow direction, m s <sup>-1</sup>
$w$	down edge length of GC cross-section, m
$X$	mole fraction
$x$	flow direction, m

## Greek letters

$\beta$	dimensionless viscous resistance
$\mu$	dynamic viscosity, Pa s
$\rho$	mass density, kg m <sup>-3</sup>
$\hat{\rho}$	molar density, mol m <sup>-3</sup>
$\tau$	shear stress, Pa
$\sigma$	surface tension, N m <sup>-1</sup>
$\alpha$	upper half corner angle of GC
$\xi$	stoichiometric ratio

## Subscripts and superscripts

<i>g</i>	gas phase
<i>f</i>	water film
<i>a</i>	anode side
<i>c</i>	capillary; cathode side
<i>i</i>	species index
<i>sat</i>	saturation
$H_2O$	water vapor
$H_2$	hydrogen
$O_2$	oxygen
$N_2$	nitrogen
<i>d</i>	droplet
<i>gc</i>	gas channel
<i>gf</i>	gas-film interface
<i>gd</i>	gas-droplet interface
<i>gw</i>	gas-wall interface
<i>m</i>	membrane

## References

- [1] M. M. Mench, Fuel Cell Engines, John Wiley & Sons, 2008.
- [2] Gregor Hoogers, Fuel Cell Technology Handbook, CRC Press, 2003.
- [3] A. Bazylak, D. Sinton and N. Djilali, J. Power Sources, 176, 240 (2008).
- [4] F. Y. Zhang, X. G. Yang and C. Y. Wang, J. Electrochem. Soc., 153, A225 (2006).
- [5] C. Hartnig, I. Manke, R. Kuhn, S. Kleinau, J. Goebbels and J. Banhart, J. Power Sources, 188, 468 (2009).
- [6] Y. Wang, J. Power Sources, 185, 261 (2008).
- [7] C. Y. Wang, Chem. Rev. (Washington, D.C.), 104, 4727 (2004).
- [8] C. Z. Qin, S. M. Hassanizadeh, D. Rensink and S. Fell, Polymer electrolyte fuel cell modeling with emphasis on the effect of gas diffusion layer anisotropy, Electrochim. Acta (under review).
- [9] H. Wu, Mathematical Modeling of Transient Transport Phenomena in PEM Fuel Cells, PhD thesis, University of Waterloo, 2009.
- [10] C. Z. Qin, D. Rensink, S. Fell and S. M. Hassanizadeh, J. Power Sources, 197, 136 (2012).
- [11] G. F. Pinder and W. G. Gray, Essentials of Multiphase Flow and Transport in Porous Media, John Wiley & Sons, 2008.
- [12] M. Rebai and M. Prat, J. Power Sources, 192, 534 (2009).
- [13] O. Chapuis, M. Prat, M. Quintard, E. Chane-Kane, O. Guillot and N. Mayer, J. Power Sources, 178, 258 (2008).
- [14] P. K. Sinha and C. Y. Wang, Electrochim. Acta, 52, 7936 (2007).
- [15] G. Luo, Y. Ji, C. Y. Wang and P. K. Sinha, Electrochim. Acta, 55, 5332 (2010).
- [16] P. K. Sinha, P. P. Mukherjee and C. Y. Wang, J. Mater. Chem., 17, 3053 (2007).
- [17] K. Moriyama and T. Inamuro, Commun. Comput. Phys., doi: 10.4208/cicp.311009.081110s.

- [18] S. Zhang, X. Yuan, J. Hin, H. Wang, K. A. Friedrich and M. Schulze, J. Power Sources, 194, 588 (2009).
- [19] X. Zhu, P. C. Sui and N. Djilali, J. Power Sources, 181, 101 (2008).
- [20] C. Z. Qin, D. Rensink, S. M. Hassanizadeh and S. Fell, Direct Simulation of Liquid Water Dynamics in the Gas Channel of a Polymer Electrolyte Fuel Cell, J. Electrochem. Soc., 159, B434 (2012).
- [21] S. Basu, C. Y. Wang and K. S. Chen, Chem. Eng. Sci., 65, 6145 (2010).
- [22] S. Basu, J. Li and C. Y. Wang, J. Power Sources, 187, 431 (2009).
- [23] C. Z. Qin, S. M. Hassanizadeh, D. Rensink and S. Fell, One-dimensional Phenomenological Model for Liquid Water Flooding in Cathode Gas Channel of a Polymer Electrolyte Fuel Cell, J. Electrochem. Soc., 159, B737 (2012).
- [24] D. A. Caulk, J. Fuel Cell Sci. Technol. 7, 031013-1 (2010).

Table 8-1: Source terms in this work.

Source term	Description
$\widehat{S}_g = \begin{cases} \widehat{S}_{O_2} + \widehat{S}_{H_2O} & \text{cathode GC} \\ \widehat{S}_{H_2} + \widehat{S}_{H_2O} & \text{anode GC} \end{cases}$	Molar source term of the gas phase on each side
$\widehat{S}_{O_2} = -\frac{I(x)w}{4Ft}$	Molar source term of oxygen due to oxygen reduction reaction
$\widehat{S}_{H_2} = -\frac{I(x)w}{2Ft}$	Molar source term of hydrogen due to hydrogen oxidation reaction
$\widehat{S}_{H_2O} = \begin{cases} \frac{(1+2a)I(x)w}{2Ft} - \widehat{S}_{phase} & \text{cathode GC} \\ -\frac{aI(x)w}{Ft} - \widehat{S}_{phase} & \text{anode GC} \end{cases}$	Phase change between water vapor and liquid water
$S_f = \widehat{S}_{phase} M_{H_2O}$	Mass source term of the film phase

Table 8-2: Geometrical, physical and operating parameters for the base case.

Parameter	Value
GC width/height/length	1.0/0.5/200 mm
Droplet radius in the GC cross section, $r_d$	no droplet
Contact angle of the bottom wall of the GC, $\theta_d$	$7\pi/9$ radian
Contact angle of the GC sidewalls, $\theta$	0 radian
Half angle of the GC corner, $\alpha$	$\pi/4$ radian
Averaged current density, $I_a$	$6000 \text{ A m}^{-2}$
Dimensionless viscous resistance, $\beta$	113.38
Dimensionless gas drag coefficient, $F_{drag}$	0.065
Cell temperature, $T$	353.15 K
Inlet gas humidity, $RH_c / RH_a$	100%/100%
Inlet gas mixture pressure (or cell operating pressure), $p_0$	1.5 bar
Liquid water density, $\rho_l$	$972 \text{ kg m}^{-3}$
Dynamic viscosity of liquid water/gas mixture, $\mu$	$3.5 \times 10^{-4} / 2.03 \times 10^{-5} \text{ Pa s}$
Surface tension, liquid water-air, $\sigma$	$0.0625 \text{ N m}^{-1}$
Ratio of GC to reactive areas, $t$	0.5
Net water transfer coefficient, $a$	0.0
Stoichiometric ratio, $\xi_c / \xi_a$	2.0/2.0

# Chapter 9 - Summary and future works

---

## 9.1 Summary

Numerical modeling plays an important role in understanding various transport processes in PEFCs. It can not only provide insights into the development of new PEFC architectures, but also optimize operating conditions for better cell performance. In this thesis, we focus on modeling liquid water transport in a PEFC unit and its impact on the cell performance. First, a two-phase flow model for the cathode side of a PEFC is developed. The GC is assumed to be structured porous media with the porosity of 1.0. The two-phase Darcy's law is applied to both diffusion layers and GC. We find that neglecting liquid water flooding in the GC leads to an incorrect prediction of liquid water distribution in the diffusion layers and an overestimation of cell performance. Then, we extend the half cell model into a full PEFC including heat transfer. We illustrate the necessity of considering the GDL anisotropy in the PEFC modeling. We also demonstrate that increasing the in-plane permeability of GDL can mitigate the liquid water flooding under the land. Consequently, the cell performance slightly increases mainly due to the enhanced mass transfer.

To explore in detail liquid water dynamics in a GC, we propose a novel geometric setup to conduct a series of direct simulations. The conducting pathways in the GDL are simplified by three cylindrical pipes connected to a liquid water reservoir. The results show that the three-phase contact line plays an important role in resisting the gas drag force for a droplet movement in the GC. The gas drag force can dominate the film flow along the GC corners, and a proper selection of the contact angle of the GC sidewalls is necessary to balance two requirements: increasing the film removal ability and removing the water clogging fast. The competing mechanisms of the droplet and film flows give us the possibility to regulate liquid water flow into GCs, and maybe lead to a better water management in GCs.

Even though direct simulations (e.g. VOF and LBM) have the potential to provide fundamentals of water dynamics in GCs, they cannot be applied to large-scale flow fields due to prohibitive computational efforts. With the purpose of computational effectiveness, we develop a one-dimensional macroscopic GC flooding model, which is an essential part of a full PEFC model. To avoid explicit tracking of droplet dynamics, we presume that the droplet size can be determined by local water flux from the GDL as well as local gas drag force. Several cases are conducted to investigate the effects of droplets and various operating parameters on the liquid water flooding in the GC. The results show that the gas drag force at the film-gas interface significantly enhances the film flow along the GC corners. Droplets in the GC are the main contributions to the gas pressure loss and liquid water flooding. For better water management in

GCs, we should depress the emergence of droplets, and enhance the film flow along GC corners. A proper selection of the GC sidewall contact angle is found to be critical to balance two requirements: increasing the film removal ability (less hydrophilicity) and removing the water clogging fast (higher hydrophilicity).

Later on, we introduce a non-equilibrium phase change model into the GC flooding model mentioned above. This enables the consideration of partially humidified gas inlet. In addition, we extend this model to the anode side, and connect the GC flooding on both sides by the so-called net water transfer coefficient. We show that gas drag force prevents liquid water accumulation in GCs, which plays an important role in the liquid water removal. Increasing the upper half corner angle of the GC can enlarge the interface area between the gas and film noticeably; as a result, more liquid water is removed out of the GC.

## 9.2 Future works

The present thesis has contributed to the understanding of liquid water flooding in PEFCs and its impact on cell performance. In addition, we attempt to describe liquid water flooding in the GC at a macro scale. A reliable and comprehensive macro GC flooding model is an essential part of a full PEFC model, since liquid water has to travel out of the cell via GCs. On the other hand, a macro GC flooding model is strongly required due to its computational efficiency for engineering applications. To this end, some further works are expected, which are outlined as follows:

1. Improving the present GC flooding model: either to provide droplet population data based on experiments or to track droplet dynamics explicitly for a more comprehensive GC flooding model.
2. Extending the present GC flooding model to large-scale flow fields, including channel bends effect.
3. Incorporating the GC flooding to diffusion layers for a full PEFC model, including a proper GC-GDL interface treatment.

# Samenvatting

---

Numeriek modelleren speelt een belangrijke rol bij het begrijpen van verschillende transportprocessen in (polymer electrolyte fuel cells) PEFC's. Het kan niet alleen inzicht opleveren in de ontwikkeling van nieuwe PEFC-constructies, maar ook de omstandigheden optimaliseren voor een betere prestatie van de cellen. In dit proefschrift wordt de aandacht gericht op het modelleren van het transport van vloeibaar water in een PEFC-eenheid en het gevolg daarvan voor het gedrag van de cellen. In de eerste plaats is een tweefasenstroming model ontwikkeld voor de cathode kant van een PEFC. De Gas Channel (GC) wordt verondersteld te zijn opgebouwd uit gestructureerde poreuze media met een porositeit van 1.0. De wet van Darcy met betrekking tot de tweefasenstroming is toegepast op zowel de diffusielagen als op de GC. Vastgesteld werd dat het verwaarlozen van het water dat de GC binnenstroomt leidt tot een incorrecte voorspelling van de waterverdeling in de diffusielagen en een overschatting van de prestatie van de cel. Vervolgens wordt het halve celmodel uitgebreid tot een volledige PEFC en wordt warmteoverdracht ingebracht. De noodzaak van het rekening houden met de anisotropie van de Gas Diffusion Layer (GDL) wordt geïllustreerd in de PEFC-modellering. Tevens wordt gedemonstreerd dat het vergroten van de permeabiliteit in het vlak van GDL het stromen van water onder het dichte kant van de GC kan versoepelen. Als gevolg hiervan nemen de prestaties van de cellen iets toe, voornamelijk door de verhoogde massa-overdracht.

Om gedetailleerd onderzoek te doen naar de dynamica van water in een GC wordt een nieuwe geometrische opstelling geïntroduceerd waarin een serie van directe simulaties wordt uitgevoerd. De conductieve paden in de GDL worden geïdealiseerd als drie cilindrische pijpen die GC verbinden met een waterreservoir in Catalyst Layer (CL). De resultaten laten zien dat de driefasen contactlijn een belangrijke rol speelt in het weerstaan van de gastegenkracht voor de beweging van een druppel in de GC. De gastegenkracht kan de stroming van de film langs de hoeken van de GC beïnvloeden. Een juiste selectie van de contacthoek van de zijanten van de GC is noodzakelijk om twee vereisten in evenwicht te houden: een toename in de mogelijkheid om film te verwijderen en het snel weghalen van waterverstopping. De concurrerende mechanismen van de stromende druppels en film geven ons de mogelijkheid de vloeibare waterstroom te reguleren in GC's, wat een beter waterbeheer in GC's tot gevolg zou kunnen hebben.

Hoewel directe simulaties (e.g. VOF en LBM) voor fundamentele aspecten van water dynamica in GC-s kunnen zorgen, kunnen ze, door beperkingen bij de computerberekeningen, niet worden toegepast op stroming op grotere schaal. Om een grotere effectiviteit in de computerberekeningen te bereiken, werd een 1-dimensionaal macroscopisch GC overstromingsmodel ontwikkeld. Dit model vormt een essentieel deel van een volledig PEFC-model. Een expliciete speurtocht op het gebied van de druppeldynamica wordt vermeden door ervan uit te gaan dat de druppelgrootte vastgesteld kan worden door de plaatselijke

waterstroom via de GDL en de lokale gastegenkracht. Verschillende proeven zijn uitgevoerd om het effect van druppels en verschillende parameters die van kracht zijn op het vloeibare water dat de GC overstroomt te onderzoeken. De resultaten laten zien dat de gastegenkracht op de film-gas interface de filmstroming langs de hoeken van de GC aanzienlijk verbetert. Druppels in de GC zijn de belangrijkste veroorzakers van verhoogde gasdruk en overstroming van vloeibaar water in de GC. Ten aanzien het waterbeheer in de GC's te verbeteren, zou het ontstaan van druppels onderdrukt moeten worden en het stromen van de film langs GC hoeken gestimuleerd. Een juiste keuze van de contacthoek van de GC-zijwand is de kritieke factor om de twee vereisten met elkaar in balans te brengen: de mogelijkheid om de film te verwijderen te laten toenemen (minder hydrofiliciteit) en het snel weghalen van waterverstopping (hogere hydrofiliciteit).

Later wordt een non-equilibrium faseveranderingsmodel geïntroduceerd in het hierboven genoemde GC overstromingsmodel. Hierdoor wordt het mogelijk om de invloed van het binnenlaten van gedeeltelijk bevochtigd gas te bestuderen. Verder wordt het model uitgebreid aan de kant van de anode en wordt de overstroming binnen de GC aan beide zijden in contact gebracht met de zogenaamde "netto watertransfer coëfficiënt". Aangetoond wordt dat de gastegenkracht voorkomt dat vloeibaar water zich verzamelt in GC's, dit speelt een belangrijke rol bij het verwijderen van vloeibaar water. Het vergroten van de hoek van de GC in de bovenste helft kan het gebied van de film-gas interface aanmerkelijk vergroten; meer vloeibaar water kan zo uit de GC worden verwijderd.

